Methanol Oxidation on Molybdenum oxide Catalysts

Ibrahim Garba Wawata

School of Chemistry, Cardiff University

2015

DECLARATION

This work has not been submitted in substance for any other degree or award at this or any other university or place of learning, nor is being submitted concurrently in candidature for any degree or other award.

Signed …… (candidate) Date ……

STATEMENT 1

This thesis is being submitted in partial fulfillment of the requirements for the degree of ……(insert MCh, MD, MPhil, PhD etc, as appropriate)

Signed …… (candidate) Date ……

STATEMENT 2

This thesis is the result of my own independent work/investigation, except where otherwise stated.

Other sources are acknowledged by explicit references. The views expressed are my own.

Signed …… (candidate) Date ……

STATEMENT 3

I hereby give consent for my thesis, if accepted, to be available online in the University's Open Access repository and for inter-library loan, and for the title and summary to be made available to outside organisations.

Signed …… (candidate) Date ……

STATEMENT 4: PREVIOUSLY APPROVED BAR ON ACCESS

I hereby give consent for my thesis, if accepted, to be available online in the University's Open Access repository and for inter-library loans **after expiry of a bar on access previously approved by the Academic Standards & Quality Committee.**

Signed …… (candidate) Date ……

Abstract

Molybdenum oxide based catalysts were prepared by a variety of methods and characterized using nitrogen adsorption, X-ray diffraction, temperature programmed desorption, alongside other spectroscopic and microscopic techniques. Methanol oxidation over the catalysts was measured using temperature programmed reaction in a CATLAB pulsed flow micro reactor.

The prepared MoO_3 revealed high activity and selectivity for methanol oxidation to formaldehyde at low temperature in comparison to commercial MoO_3 sample, due to high surface area and exposure of Lewis acid sites. However, potassium doping neutralizes the Lewis acids sites and modifies the surface work function of MoO_3; therefore, lowering the reducibility of the Mo^{6+} sites selective to formaldehyde at higher temperature, and suppresses secondary oxidation of CO to CO_2.

Methanol oxidation on iron molybdates catalysts indicates amorphous MoOx species on top of the stoichiometric ratio (1.5) material as the active phase, with excess crystalline MoO_3 on 2.2:1 Mo: Fe ratio acting as a reservoir for replenishment of volatile MoOx species to maintain catalytic activity as well as selectivity to formaldehyde.

Nanodiamond (ND) is thermally unstable, and burns completely at 600 ^{o}C. The supported catalysts revealed both monomeric and polymeric MoOx species at low coverage but crystalline polymeric MoO_3 at high coverage. Methanol oxidation on MoO_3/ND produces DME and formaldehyde from acid and redox sites respectively. A synergistic effect observed on 90 % MoO_3/ND catalyst due to metal-support interaction, prevents complete reducibility of Mo^{6+} sites. $\gamma - Al_2O_3$ is highly selective to DME due to acid sites, which are completely titrated at 2wt % MoO_3 loading. Formaldehyde selectivity increases with increasing MoO_3 loading on both supported MoO_3 catalysts.

MoO_3 and $Fe_2(MoO_4)_3$ films were successfully synthesised on α-Al_2O_3 (0001) single crystal via a novel wet chemical deposition method. These films revealed varying particle sizes at different monolayer coverage, with Mo and Fe in high oxidation state of Mo^{6+} and Fe^{2+}.

Dedication

This Thesis is dedicated to my Parent, wife and son for their prayers, patience and support throughout my entire PhD programme.

Acknowledgement

I wish to express my profound gratitude to my supervisor Prof. Michael Bowker for given me the opportunity to undergo PhD programme in his Research group, and my co-supervisor Dr Albert F. Carley, mentor Prof. Gary Attard, Examiner Stuart H. Taylor and Phil R. Davis for their useful critique and advice.

I am as well obliged to be thankful to Kebbi State University of Science and Technology Aliero (KSUSTA) in collaboration with Tertiary Education Trust Fund (TETFund) formally called Education Trust Fund (ETF) Nigeria for funding my study at Cardiff University.

However, challenges are encountered during research work. At this juncture, I wish to appreciate the support of Mr Alun Davis and Steve Morris of the School workshop for support with trouble – shooting and repair of the reactor, Dr Mahmud Akhtar for financial advice, Dr David Morgan for XPS analysis, Catherine Brookes for running some samples at the Laboratory in Harwell and the entire members of Bowker's research group.

Lastly, my gratitude goes to the entire member of the Wawata family, friends and well-wishers for prayers and support throughout this work.

Glossary

AFM – Atomic force microscopy

AHM – Ammonia hepta molybdate

BET – Brunauer-Emmett-Teller

BDH – British drug house

COx – Carbon oxides

CPS – Capillary power supply

DC – Direct current

DEE – Di-ethyl ether

DFT – Density functional theory

DLD – Delay-line-detector

DME – Di-methyl ether

DMM – Dimethoxy methane

DRIFT – Diffuse reflectance infrared spectroscopy

DSC – Differential scanning calorimetry

Ea – Activation energy

EDX – Energy dispersive X-ray

EHT – electron high tension

EPR – Electron paramagnetic resonance

FTIR – Fourier transform infrared

FWHM – Full width half maximum

HPHT – High-pressure high temperature

IR – Infrared

JCPDS – Joint committee on powder diffraction standard

LEED – Low energy electron diffraction

MS – Mass spectrometry/spectrometer

MSIU – Mass spectrometer interface unit

ML – Mono layer

NMR – Nuclear magnetic resonance

PC- Personal computer

PECVD – Plasma enhanced chemical vapour deposition

QIC – Quartz inlet capillary

RF – Radio frequency

RT – Room temperature

SEM – Scanning electron microscopy/microscope

SFG – Sum frequency generation

STM – Scanning tunnelling microscopy

TEM – Transmission electron microscopy/microscope

TGA – Thermogravimetry analysis

TOF – Turn over frequency

TPD – Temperature programmed desorption

TPR – Temperature programmed reaction/reduction

Tm – Peak maximum temperature

UHV – Ultra high vacuum

UV – Ultraviolet

WAXS – Wide – angle – X –ray scattering

XAFS – Extended – X-ray absorption fine structure

XPS – X-ray photoelectron spectroscopy

XRD – X-ray diffraction

Contents

List of Figures

List of Tables

Chapter 1 Introduction and Literature Review

Contents

1.1 Catalysis

Background

Catalysis is an essential phenomenon in the industrialization of global economy and environmental protection, which is of immense importance to the functioning of life in general. It accounts for virtually most process happening around us: ranging from production of industrially important chemicals and materials to reduction of pollution via the use of catalytic converters, as well as complex biochemical reactions occurring in living matter (using enzymes) such as conversion of carbohydrate to glucose, and photosynthesis in plants using chlorophyll.

Humans have used catalysis since 8000 years ago in ancient Egypt and Mesopotamia (modern Iraq), especially using yeast as a catalyst in the fermentation process, for the conversion of sugar in fruits (grape) or grains into ethyl alcohol [1, 2].

The first work on heterogeneous catalysis was reported in 1813 by Louis Thénard, where he observed decomposition of ammonia to hydrogen and nitrogen over red-hot metals arranged in decreasing order of reactivity Fe > Cu > Ag > Au > Pt. Humphrey Davy was first to report catalytic oxidation reactions, with coal gas (CO and H_2) oxidation, without the action of flame in the presence of Pt [3]. This led to the manufacture of the miner's safety lamp (Davy lamp), which alerts miners when in dangerous zones. Later his cousin Edmond Davy, demonstrated catalytic oxidation of alcohol at room temperature over finely divided Pt catalysts [4].

Catalyst

A catalyst is a body or substance which causes or accelerates the rate of formation of product using a lower energetic pathway, and which is not consumed at the end of the reaction. In essence, it does not change the thermodynamics of the reaction, but rather enhances the attainment of chemical equilibrium (kinetics). The process by which this occurs was first termed *catalysis* by Berzelius in 1836 [5]. He proposed the existence of a catalytic force in the catalyst which differs from chemical affinity, but leads to decomposition of bodies into new compounds [5].

There are two broad classifications of industrial catalysis namely;

Heterogeneous catalysis – In this process, the catalyst exists in a different phase to the reactants and products; example of which is production of formaldehyde from methanol using silver (Ag) or iron molybdate ($Fe_2(MoO_4)_3$) catalysts.

Homogeneous catalysis – In this process the catalyst, reactants, and products exist in the same phase; for example the destruction of ozone layer (O_3) catalysed by chlorine radical species (Cl*) in gas phase reaction.

The Table 1. 1 below outlines some of the first applications of industrial catalytic processes:

Table 1. 1 ***First applications of industrial catalytic processes [1, 2, 5-7]***

Founder	Year	Process
Peregrine Phillips	1875	Contact process for the synthesis of sulfuric acid (H_2SO_4) over V_2O_5 catalysts
Wilhelm Ostwald	1902	Oxidation of ammonia to NO over Pt foil, used in the synthesis of nitric acid (HNO_3)
Paul Sabatier	1902	Hydrogenation of alkenes using Pt catalysts
Fritz Haber and Bosch	1914	Haber – Bosch process for the synthesis of ammonia using promoted Fe catalysts
Fischer and Tropsch	1925	Fischer – Tropsch synthesis of hydrocarbon from water gas (CO and H_2) using Fe or Co catalysts
Mittasch and Schiller	1926 to 1930	Steam reforming of hydrocarbons using Ni catalysts

Catalytic cycle on metal oxides

The reaction on metal oxides surfaces occurs in a continuous cycle which includes: activation of substrates on active sites, production and desorption of products, and regeneration of actives sites.

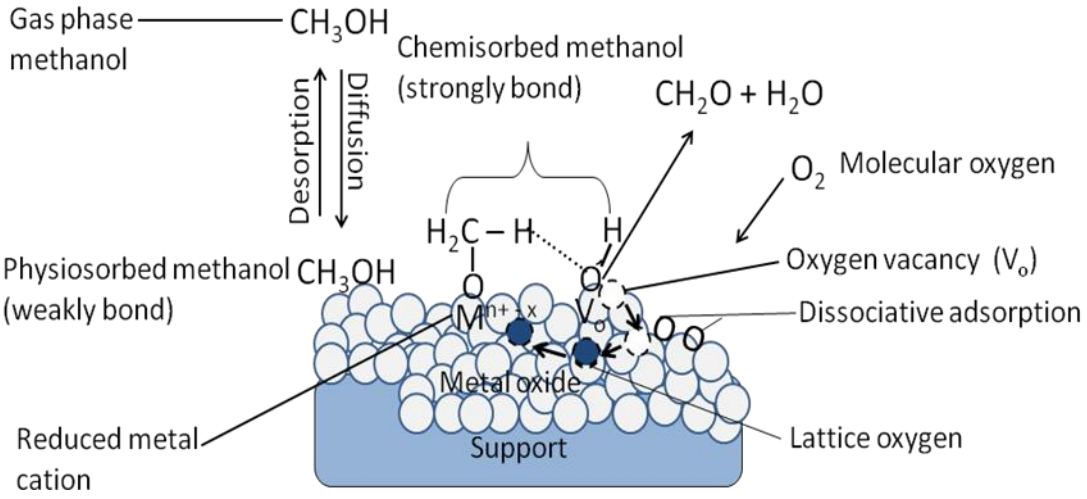

Fig. 1. 1 ***Catalytic cycle of methanol oxidation to formaldehyde over supported metal oxide***

The catalyst surface is the most crucial arena for molecular and atomic interaction between reactants to form products. A typical example of a catalytic cycle is the selective oxidation of methanol (CH_3OH) to formaldehyde (CH_2O) over supported heterogeneous metal oxides as shown in Fig. 1. 1 above. In this process, gas phase CH_3OH is adsorbed on the surface forming weakly bonded molecular CH_3OH (physisorption), or chemically bonded methoxy and hydroxyl species (chemisorption). The physisorbed methanol is liable to desorb as intact methanol at low temperature, whereas abstraction of β – hydrogen from the adsorbed methoxy species results in the formation of CH_2O. Furthermore, recombination of surface hydroxyl with hydrogen or hydroxyl species results in water formation, which desorbs from the surface leaving behind an oxygen vacancy Vo, and reduced metal centre $M^{n+ - x}$; where x = 1 and n = any positive integer. The gas phase molecular oxygen dissociates and binds on the catalyst surface by sequential acceptance of electrons, which later diffuses into the bulk metal oxide. The reduced metal centre is re-oxidized by diffuse lattice oxygen to complete the cycle.

1.2 Selective Oxidation Catalysis using Metal Oxides

Metal oxide

Metal oxides are one of the vital and readily utilized classes of heterogeneous catalysts, used as either active phase or support in selective oxidation processes. Their application in selective oxidation catalysis underpins three basic properties which include: (i) the ease of oxidation – reduction (redox property) (ii) surface coordination environment (iii) oxidation state of the surface atom. Among the metal oxides, transition metals are widely used in selective oxidation and related reactions [8]. They possess small ionic radii, which are usually located in octahedral and tetrahedral holes among oxygen atom in close packed arrangement. Their oxides exhibit high electrical conductivity, which enhances electron transfer as well as diffusion of lattice oxygen within the bulk to re-oxidize the reduced metal sites. Moreover, metal oxide surfaces consist basically of two types of oxygen species: either electrophilic oxygen (such as peroxide O_2^{2-} , superoxide O_2^{-}), or the ionic radical, (O^{-}) or nucleophilic oxygen (O^{2-}) (in form of lattice terminal M=O or bridging M – O – M), with the former supporting complete oxidation, and the latter leading to selective oxidation products [9-11].

Metal oxide surfaces undergo two mutually dependent reactions, which includes acid – base reaction and oxidation – reduction (redox) reaction.

Redox reaction occurring on metal oxide surfaces has been proposed to follow the Mars – van Krevelen [12] mechanism as exemplified in equation 1.1 and 1.2 below:

$$A^{cat} – O + Red \rightarrow A^{cat} + Red – O \qquad \text{Equation 1. 1}$$

Oxidation of substrate by lattice oxygen

$$A^{cat} + O – O \rightarrow \quad A^{cat} – O + O \qquad \text{Equation 1. 2}$$

where A^{cat} is a metal cation and Red is a reducing substrate

The re-oxidation of reduced metal cationic sites by lattice oxygen from the bulk, generated by dissociation of molecular oxygen on the surface, regenerates the selective sites.

Metal oxides consist of defects, terraces, steps, and edges. Bond breakage between metal and oxygen atoms results in the exposure of very unstable sites, which have high energy. These exposed coordinative unsaturated cationic sites act as Lewis acids with their exposed oxygen atom species representing potential basic sites, whereas exposed surface hydroxyl groups formed from chemisorbed water molecules could act as

Bronsted acid or basic sites. However, CO_2 from the atmosphere could bond to high energy sites to form carbonate species, if out-gassing or pre-treatment temperature is insufficient to cause their decomposition [13]. Most covalent solid oxides such as P_4O_{10}, CrO_3 , MoO_3, and V_2O_5 exhibit external forces or surface energy resulting from the breakage of the van der Waals forces within the structure, but not the covalent metal – oxygen bonding. A typical study of layered covalent solids (MoO_3 and V_2O_5) reported by Busca et al [14], revealed that breakage of the van der Waals forces on (100) and (010) phases of α – MoO_3 and V_2O_5 leads to formation of coordinated unsaturated sites on the (001) and defect, and basal plane respectively.

However, Cavani and Trifiro [15] listed a number of major factors for controlling catalytic performance and product distribution on bulk and surfaces of heterogeneous metal oxides catalyst which include:

i. Nature of the active sites (comprising of density of active sites, acid/base properties, and multi functionality of the surface)
ii. Orientation of the crystal phase, and their ability to change under reaction conditions
iii. Structure of the catalyst (including redox properties and metal – oxygen bond strength)
iv. Synergy effect of different phases in enhancing catalyst performance
v. The significance of metal – support interaction, in enhancement of the properties of the active metal oxide phase

Selective oxidation of lower molecular weight alkanes and alcohols using metal oxide catalysts is an important industrial process for synthesis of valuable chemicals. This reaction occurs via redox and radical mechanism on transition metal oxides and non – reducible metal oxides (alkaline and alkaline earth metals) respectively. The former reaction follows the Mars van Krevelen mechanism, while the latter is based on the activation of molecular O_2 on the surface. Activation of molecules (alkanes or alcohols) on metal oxide occurs on the acid – base pairs, with basic sites abstracting hydrogen, whereas the alkyl or alkoxy group bond to metal acid sites. Subsequently, the removal of hydrogen or addition of oxygen into the activated molecules results in formation of alkenes and oxygenated carbon product (alcohol, aldehydes, or carboxylic acid). However, reactivity and selectivity of the process is guided by the

structure of the molecule (C – chain length, position of functional group), type of active sites, and process conditions.

Ozkan and co-workers [16, 17], reported that M=O sites are active for partial oxidation of methane (CH_4) to formaldehyde (CH_2O) on bulk crystal MoO_3, and the M – O – M sites support complete oxidation to CO_2. Moreover, Spencer and Pereira [18] reported direct oxidation of CH_4 to C1 – oxygenates on V_2O_5 and MoO_3 supported over SiO_2. The authors found correlation between CH_2O selectivity and MoO_3 structure, with direct oxidation of CH_4 to CO_2 at higher temperature, which was observed on MoO_3/SiO_2 in contrast to sequential oxidation of CH_2O to CO, then CO_2 revealed on V_2O_5/SiO_2 catalyst. Banares and Fierro [19] investigated the effect of MoOx species on SiO_2 support on activity and selectivity towards partial oxidation of CH_4. They observed decline in CH_2O selectivity with increasing reaction temperature, and residence time at constant temperature, with activity increasing with increase in temperature. However, Suzuki et al [20] attributed better activity of MoO_3/SiO_2 catalyst in partial oxidation of CH_4 to well dispersed MoOx species on the SiO_2 support. Isotopic study of selective oxidation of CH_4 over MoO_3/SiO_2 reported by Baranes et al [21] evidenced CH_2O as primary product formed from oxidation of CH_4 by lattice oxygen via Mars van Krevelen mechanism, whereas oxidation of CH_2O to CO at high temperature is supported by molecular oxygen.

Other valuable industrial oxidation processes include: selective oxidation and oxidative dehydrogenation (ODH) of alkanes. In the case of selective oxidation of propane and n – butane to acrylic acid and maleic anhydride respectively, using PVO or V or Mo – based mixed metal oxides, Gai Boy [22] highlighted the significance of higher oxidation state of Mo and V cationic centre in enhancing selectivity towards desired products. The authors concluded that the reduced metal centres (basic sites), favour complete oxidation of reactant to CO_2.

However, Mo – based mixed oxides (Mo, V, Nb) were reported by Chen et al [23], Botella et [24], and Osawa et al [25] as active and selective catalyst for ODH of ethane to ethene, with 100 % [23] and 60 – 65 % [24] ethene selectivity, by 10 % and 22 % at 559 K and 637 K respectively. The authors concluded Mo as the active sites in the mixed oxide for ODH reaction, while Nb enhances selectivity to ethene by inhibiting further oxidation of ethene to CO_2. The use of alkali metals as dopants on active catalysts such as MgO and CaO were reported by Velle et al [26] to create defect site

on catalysts surface, which are capable of activation of molecular oxygen used in the ODH reaction.

In addition, Hargreaves et al [27] studied partial oxidation of CH_4 to CH_3OH on a wide range of metal oxides. They reported high activity and selectivity of the reaction over mixed (1:1) Ga_2O_3 and MoO_3 catalyst. In a similar study of CH_4 oxidation to CH_3OH over wide range of screen metal oxides, which are activators of CH_4, O_2 and CH_3OH, but do not combust methanol reported by Taylor et al [28], revealed selective advantage of methanol production over Cu doped MoO_3 at 450 ^oC. Furthermore, the authors observed high activity and selectivity for CH_4 conversion to CH_3OH over mixed Ga_2O_3/MoO_3 catalyst, consequently indicating a synergy effect of the individual oxide component.

1.3 Methanol and Formaldehyde; Properties and uses

Methanol

Methanol or methyl alcohol is a colourless, volatile and flammable liquid which is highly miscible in water. It was first synthesized by Robert Boyle in 1661 via pyrolysis of wood, as such known as wood alcohol [29]. Methanol is the simplest member of the alcohol group with chemical formula CH_3OH and molecular weight of 32.4 g/mol. It has a density of 0.79 g/mol at 25 ^oC, and a melting and boiling points of -97.6 ^oC (-143.7 ^oF) and 64.96 ^oC (148 ^oF) respectively. It burns in air with pale blue non – luminous flame to give carbon dioxide and water as in equation 1.3 below:

$$2\ CH_3OH_{(g)} + 3\ O_{2(g)} \rightarrow 2\ CO_{2\ (g)} + 4\ H_2O_{(g)} \qquad \text{Equation 1.3}$$

Methanol is produced by varieties of bacteria through anaerobic metabolism and is present in a minute amount in the atmosphere [30].

Industrial production of methanol from synthesis gas occurs by reacting carbon monoxide and hydrogen over mixed copper, zinc oxide, and alumina ($Cu/ZnO/Al_2O_3$) catalyst [31]. Recently, Liu et al [32] and Pontzen et al [33], reported Methanol synthesis via CO and CO_2 hydrogenation; currently at the laboratory and pilot plant stage. These reactions are represented in equation 1.4 and 1.5 below:

$$CO_{(g)} + 2H_{2\ (g)} \rightarrow CH_3OH_{\ (g)} \qquad \text{Equation 1.4}$$

$$CO2_{\ (g)} + 3H_{2\ (g)} \rightarrow CH_3OH_{(g)} + H_2O_{(g)} \qquad \text{Equation 1.5}$$

Methanol ingestion causes metabolic acidosis (acidity of blood plasma) , neurologic sequelae (result from damaged neurons), blindness and even death [34].

Methanol is widely used as:

- Starting material for synthesis of valuable chemicals such formaldehyde
- Anti – freezing agent
- Fuel for internal combustion engine

Formaldehyde

Formaldehyde is a colourless and irritating gas with molecular formula CH_2O. It has a molar mass of 30.039 g/mol and density of 0.8153 g/cm^3 at (-20 ^oC), with melting and boiling points of -92 ^oC (-134 ^oF) and -19 ^oC (-2 ^oF) respectively. It also occurs in two different forms: as trimer in the case of 1, 3, 5 – trioxane $(CH_2O)_3$, and as white solid paraformaldehyde $OH(CH_2O)_nH$, where n = 8 – 100 units [35].

Formaldehyde was first discovered by a Russian chemist Aleksandr Butlerov in (1859) [36], but only chemically identified by August Wilhelm Von Hofmann in 1869 [37]. It occurs in the atmosphere due to combustion of methane and other carbon compounds from vehicular exhaust, forest fire, and tobacco smoke [35].

Formaldehyde is produced industrially from selective oxidation of methanol using either silver or mixed oxide catalysts as in equation 1.6 below:

$$2\ CH_3OH + O_2 \rightarrow 2\ CH_2O + 2\ H_2O \qquad \text{Equation 1.6}$$

Formaldehyde use:

Major application of formaldehyde is in the manufacture of resins such as urea formaldehyde resin, melamine resin, phenol formaldehyde resin used in textile, plastics, automobile, and furniture industries for the production of the following:

Thermosetting plastics, particleboards, fibreglass, floor laminates, furniture finishing, oriented strand board, dashboards, and automobile parts. It is also used as a fixative and embalmment agent for preservation of tissues and organs.

Formaldehyde is toxic, allergic, and recently classified as a potential carcinogen [38].

1.4 Methanol Oxidation; Thermodynamics and Kinetics

Industrial process

Methanol oxidation to formaldehyde is commercially carried out via two major routes: silver (Ag) and the oxide routes. The Ag route involves reaction of 50 % v/v methanol / air mixture above methanol explosion limit (net reducing mixture) over Ag catalyst at atmospheric pressure between 560 – 650 ^{o}C, yielding between 37 – 56 % concentration of CH_2O in water (formalin) [39, 40]. However, the silver route is based on two major processes: the methanol ballast process operated by Degussa using methanol and air as the only feedstock, and water ballast process practiced by BASF and Dynea using mixture of methanol, air and water, thereby achieving a higher methanol conversion [40-42]. On the other hand, the oxides route mostly practiced by Formox (Johnson Matthey) reacts methanol in excess air, below methanol explosion limit (net oxidizing mixture) over iron and molybdenum or vanadium mixed oxides catalyst between 300 – 400 ^{o}C [39, 43]. The choice of process depends on formaldehyde end usage. Currently, there are hybrid plants that operate using both silver and oxides routes.

Thermodynamics

The major reactions in formaldehyde synthesis from methanol involve oxidative dehydrogenation as in the equation below:

Dehydrogenation

$CH_3OH \rightarrow HCHO + H_2$ $\Delta H^{\Theta} = +85$ kJ/mol Equation 1.7

$CH_3OH \rightarrow CO + 2\,H_2$ $\Delta H^{\Theta} = +97$ kJ/mol Equation 1.8

Oxidative dehydrogenation

$CH_3OH + \frac{1}{2}\,O_2 \rightarrow HCHO + H_2O$ $\Delta H^{\Theta} = -159$ kJ/mol Equation 1.9

Combustion

$CH_3OH + 1\frac{1}{2}\,O_2 \rightarrow CO_2 + 2H_2O$ $\Delta H^{\Theta} = -674$ kJ/mol Equation 1.10

$CH_3OH + O_2 \rightarrow CO + 2H_2O$ $\Delta H^{\Theta} = -389$ kJ/mol Equation 1.11 [44]

where ΔH^{Θ} is the standard enthalpy at 298 K and 1 atm.

In the silver process, both equations 1.7 and 1.9 occur resulting in a net exothermic reaction, while the mixed oxide synthesis occurs via oxidative dehydrogenation as in equation 1.9 above. However, oxidative dehydrogenation methanol to formaldehyde is

greatly affected by combustion reaction as in equations 1.10 and 1.11, which are highly thermodynamically favoured.

Mechanism

The proposed reaction mechanism for selective oxidation of methanol to formaldehyde over single oxides and mixed oxide catalyst by Bowker's group [44-46] and others [47-49] are outlined below:

$CH_3OH_{(g)} + a \rightarrow CH_3OHa$ Equation 1.12

$CH_3OHa \rightarrow CH_3OH_{(g)} + a$ Equation 1.13

$CH_3OH + Oa \rightarrow CH_3Oa + OHa$ Equation 1.14

$CH_3Oa + Oa \rightarrow CH_2O + OHa$ Equation 1.15

$2OHa \rightarrow H_2O + Oa + Vo$ Equation 1.16

$O_{2(g)} + 2Vo \rightarrow 2Oa$ Equation 1.17

$CH_3OHa + O^*a \rightarrow CH_2O + H_2O$ Equation 1.18

$CH_3Oa + OHa \rightarrow CH_3OH + Oa + Vo$ Equation 1.19

Where g, a, Xa, X*, and Vo represent, gas phase species, surface sites, adsorbed molecule, radical species, and oxygen vacancies respectively. Molecular gas phase methanol is adsorbed on the surface as in Equation 1.12; this species could desorb as intact methanol from the surface at a low temperature in Equation 1.13. The dissociative adsorption of methanol on the catalyst surface resulting from abstraction of α – hydrogen from methanol by lattice oxygen in Equation 1.14, leads to formation of surface hydroxyl and methoxy species; further abstraction of β – hydrogen from the surface methoxy species as in Equation 1.15 produces formaldehyde and surface hydroxyl species. This step is often considered the rate-determining step, as formaldehyde desorption from the surface is temperature dependent. The recombination of surface hydroxyl species leads to desorption of water leaving behind adsorbed O atom and a vacancy (Vo) as in Equation 1.16, which is regenerated by dissociative adsorption of gas phase molecular oxygen as in Equation 1.17. However, Routray et al [49] proposed the plausible mechanism involving reactive surface O* radical species in formaldehyde formation at low temperature in Equation 1.18, while surface methoxy and hydroxyl species could recombine to give methanol adsorbed O

atom and a vacancy (Vo) as in Equation 1.19. However, non selective reaction products such as dimethyl ether $(CH_3)_2O$, methyl formate $(HCOOCH_3)$, dimethoxy methane $(CH_2(OCH_3)_2$, and carbon monoxide (CO) were produced during reaction.

1.5 Selective Oxidation of Methanol over Mo – oxide based catalysts

Molybdenum trioxide (MoO_3)

Methanol selective oxidation over molybdenum trioxide (MoO_3) conducted by Tatibouet and Germain [50] revealed the reaction to be structure – sensitive. The authors inferred formation of formaldehyde and dimethyl ether (DME) on basal (010), side (100), and apical (001 and 110) surface planes respectively. Abon et al [51] held a different view that the truncated (100) phase leading to formation of more stable (012) phase (step atomic structure) is the active phase, owing to the presence of mild acidic sites on the molybdenum (Mo^{6+}- Mo^{5+}) bonded to terminal oxygen. In addition, Vedrine [52] reported the presence of both redox and Lewis acid sites on MoO_3 (101 and 001) plane, which promotes electron transfer and activation of methanol and molecular oxygen.

However, isotopic labelling [47], temperature programmed desorption (TPD), temperature programmed reaction, in-situ Infra-red [53], and reduction/microbalance reactor studies [47, 53, 54] of methanol oxidation to formaldehyde over MoO_3 was reported to proceed via dissociative chemisorption of methanol on partially oxidized molybdenum site (oxygen vacancies) and hydroxyl group (from α-hydrogen abstraction by the Mo=O site). The abstraction of β-hydrogen from the surface methoxy intermediate species was accepted by Chung et al [55] and others [47, 53] as the rate-limiting step in formaldehyde production. Ab-initio quantum chemical calculation conducted by Allison and Goddard [56], suggested that the presence of dual adjacent surface di-oxo sites are responsible for the activation and abstraction of H from methanol, but Sleight et al [47] and Gai-Boyes [22] attributed methanol activation and formaldehyde production to unsaturated molybdenum (under-coordinated) sites on MoO_3 catalyst. Furthermore, Cheng [57] reported competitive adsorption of water, methanol, and formaldehyde on the same catalytic site of MoO_3 during methanol oxidation reaction. The author attributed high selectivity of formaldehyde during methanol oxidation reaction to adsorption of water on sites

responsible for further oxidation of formaldehyde to carbon oxides. Chung et al [55], revealed that Mo=O terminal vacancy sites are responsible for formaldehyde and carbon oxide production, while high-order products; dimethoxymethane (DMM), dimethyl ether (DME) are produced on Mo-O-Mo bridge vacancy.

Bowker et al [58], highlighted the significance of Mo oxidation state in selective oxidation of methanol to formaldehyde. They reported a contrasting behaviour of the Mo^{6+} and Mo^{4+} valence states in methanol oxidation, with Mo^{6+} state highly selective to formaldehyde, while the reduced Mo^{4+} produces CO in presence of oxygen. A TPD study of methanol oxidation on MoO_3 by Sleight et al [47] and Vedrine et al [59] indicated that the reaction follows the Mars-van Krevelen mechanism, which involves lattice oxygen exchange between bulk catalyst and its surface replenished by gaseous oxygen. However, in-situ Raman spectroscopic study of MoO_3 conducted by Mestl [60], explains the significance role played by MoO_3 defects (oxygen vacancy) in promoting oxygen exchange between gas phase and catalyst bulk.

Moreover, alkali and alkali earth metal promotion of Mo – oxide based catalysts neutralizes acidic sites, decreases reducibility of cationic sites, and enhances electron transfer on metal oxides surface. K doping mediates the adsorption and dissociation of gas phase oxygen on the catalyst surface. Temperature programmed desorption and steady state reaction study of transient isotopic labelling oxygen of methane coupling over alkali promoted molybdates ($MnMoO_4$), reported by Driscoll and Ozkan and Driscoll et al [61, 62], revealed the influence of K in providing easy pathway for dissociative adsorption of gas phase oxygen on $MnMoO_4$. This controls mobility and exchange of gas phase oxygen with the catalyst surface or subsurface lattice. Most reports on methanol oxidation over MoO_3 catalyst are based on single crystal studies. This study seeks to investigate the effect of acid sites as well as alkaline metal (K) promotion on catalytic activity in methanol oxidation to formaldehyde, over bulk MoO_3 surface on bulk metal oxide surface.

Iron Molybdates ($Fe_2(MoO_4)_3$)

Selective oxidation of methanol using iron molybdates ($Fe_2(MoO_4)_3$) was first reported by Adkins and Peterson [63] in 1931. Their work attracted much interest in the investigation of catalytic active and selective sites for methanol oxidation to

formaldehyde. Currently, there are an array of techniques employed in the synthesis of $Fe_2(MoO_4)_3$ such as co precipitation reported by Adkins and Peterson [63], Sun-Kuo et al [64], Soares et al [65] and House et al [66], wet-mixing reported by Li et al [67], and sol-gel reported by Soares et al [68]. Other methods include: thermal spreading reported by Huang et al [69], hydrothermal reported by Beale et al [70], and incipient wetness impregnation reported by Bowker et al [71] and Brookes et al [72], with iron and molybdenum species in their highest oxidation state. The evolution of the $Fe_2(MoO_4)_3$ phase begins between 250 – 400 ^oC, with segregation of MoO_3 over bulk $Fe_2(MoO_4)_3$ observed above 400 ^oC, usually influenced by increasing Mo content. Moreover, Li et al [67] and Soares et al [68] reported better thermal stability with good reaction reproducibility for wet-mixing and sol-gel synthesized catalysts, than co-precipitation and thermal spreading catalysts respectively. In addition, Bowker's group [66, 72] reported higher activity and selectivity to formaldehyde over co-precipitation and incipient wetness impregnation catalysts.

However, the nature of active phase in $Fe_2(MoO_4)_3$ catalyst remains debatable in the field of catalysis, material and surface science. Okamoto et al [73] revealed that the bulk $Fe_2(MoO_4)_3$ with excess Mo (1.7 ratio) as the active phase, with excess Mo species dispersed on defective Fe – O – Mo sites, responsible for electron transfer and enhancement of catalytic activity. However, Sun-Kou et al [64] argued a much higher Mo ratio (> 1.7) to be the active phase. In a comprehensive review by Soares and Farinha-Portela [48], they concluded that the stoichiometric phase (1.5) is the active phase, whereas excess Mo is required for preventing the exposure of Fe-rich site during reaction. Recently, Soderhjelm et al [74] reported synergic effect between Mo and $Fe_2(MoO_4)_3$ phase. The authors surmised that the amorphous MoOx species on bulk $Fe_2(MoO_4)_3$ as active and selective phase for formaldehyde production during methanol oxidation reaction. However, Routray et al [49], and Wachs and Routray [75] disputed the existence of a synergic effect between crystalline MoO_3 and bulk $Fe_2(MoO_4)_3$, due to similar catalytic activity observed for both stoichiometric and Mo excess $Fe_2(MoO_4)_3$ during CH_3OH-TPSR (methanol-temperature programmed surface reaction) study on the catalysts. The authors confirmed the presence of MoOx mono layer on crystalline $Fe_2(MoO_4)_3$ as the active phase, while crystalline excess MoO_3

phase on $Fe_2(MoO_4)_3$ serves as a reservoir for maintaining the activity and replenishment of volatile Mo species during reaction.

Furthermore, a temperature programmed reaction study of methanol oxidation over $Fe_2(MoO_4)_3$ by Bowker's group [66, 71, 72, 76], revealed increasing formaldehyde selectivity with increasing Mo loading on both co precipitation and impregnated catalysts, with maximum selectivity > 90 % at 90 % conversion recorded for 2.2 Mo ratios. The decline in formaldehyde selectivity was due to CO formation from surface exposed isolated Mo and Fe sites. A steady-state kinetic study of methanol oxidation over industrial $Fe_2(MoO_4)_3$ between 230 ^oC – 360 ^oC using a differential reactor by Deshmukh et al [77], revealed that the reaction is first order at low methanol concentration, but independent at higher concentration showing Langmuir-Hinshel-wood type dependency on oxygen due to saturation of actives site by methanol. They attributed CO formation to secondary oxidation of formaldehyde.

Soares et al [68] evidenced the deactivation of co precipitation and sol-gel $Fe_2(MoO_4)_3$ by water, a reaction product which forms volatile $MoO_2(OH)_2$ species, thus preventing surface re-oxidation of Mo +4 sites. They attribute surface reduction (deactivation) of stoichiometric co precipitation $Fe_2(MoO_4)_3$ to lack of excess Mo reservoir to replenish the lost Mo species, whereas irreversible reduction of the sol-gel prepared $Fe_2(MoO_4)_3$ is attributable to loss of surface lattice oxygen during calcination. However, Andersson et al [78] argued that lost of excess Mo is caused by methanol reaction, leading to deactivation of the active phase via the mechanism below:

Reaction of methanol over iron molybdate:

$$CH_3OH + Fe_2(MoO_4)_3 \rightarrow CH_2O + H_2O + 2FeMoO_4 + MoO_3 \qquad \text{Equation 1.20}$$

Reoxidation of iron molybdate in excess Mo:

$$2FeMoO_4 + MoO_3 + ½\ O_2 \rightarrow Fe_2(MoO_4)_3 \qquad \text{Equation 1.21}$$

Reoxidation in Mo scarcity:

$$3FeMoO_4 + ¾\ O_2 \rightarrow Fe_2(MoO_4)_3 + ½\ Fe_2O_3 \qquad \text{Equation 1.22}$$

Mitov et al [79] proposed that deactivation of $Fe_2(MoO_4)_3$ during reaction with methanol proceeds via formation of anion vacancies during steady state reaction, leading to disruption of subsurface layer at 300 ^oC, which increases at higher temperature. However, Jacques et al [80] contested the concept of anion mobility due to rapid reoxidation kinetics of β $FeMoO_4$ to $Fe_2(MoO_4)_3$, and inferred that H_2O formed during reaction blocks the active site for H abstraction on $Fe_2(MoO_4)_3$. In a separate in-situ multi-technique study, Jacques et al [81] revealed that surface reduction of $Fe_2(MoO_4)_3$ in methanol proceeded via the disappearance of MoO_3 and $Fe_2(MoO_4)_3$, and appearance of MoO_2, amorphous material, and MoC at 350 ^oC. They observed that the rates of reduction in methanol and oxidation in O_2 were faster for the catalyst with excess Mo, which was ascribed to either surface area effect, or promotion effect, or possible substitution of Fe^{3+} by Mo^{6+} ion. However, they maintain the view that excess Mo is essential for maintaining both, structural stability and selectivity during reaction.

Recently Pradhan et al [82], reported participation of non-lattice oxygen in selective oxidation of decane to oxygenated aromatics at lower temperature (< 350 ^oC) over $Fe_2(MoO_4)_3$ catalyst, indicating possible implication of non lattice surface oxygen in selective oxidation catalysis. Although $Fe_2(MoO_4)_3$ is extensively researched, this work seeks to understand the nature of the active and selective sites during methanol selective oxidation to formaldehyde.

Supported Mo – oxide based catalysts

Selective oxidation of methanol over Mo – oxide based catalysts has been widely attributed to either increase in the surface area of the active phase, or enhanced catalytic performance of the catalyst. Methanol oxidation on MoO_3 supported over graphite as reported by Tatibouet et al [83, 84] and Machiels et al [53], reveal structure sensitivity of the surface due to the presence of both redox (basal face) and acidic (apical face) sites, which makes formaldehyde and dimethyl ether respectively. Castillo et al [85], reported a synergistic effect between mechanically mixed (50 % equal amount) MoO_3 and α – Sb_2O_4 phase during methanol reaction, revealing a selectivity of 99.5 % formaldehyde at 94 % conversion. They attributed the high selectivity to a spill over effect of α – Sb_2O_4 phase, which supplies

reduced Mo sites with oxygen to maintain high oxidation state of + 6. In addition, XPS study revealed that single oxide MoO_3 reduces easily in comparison to the mechanically mixed MoO_3 and $\alpha - Sb_2O_4$ catalyst. Furthermore, Briand et al [86] reported complete independence between catalytic activity of methanol reaction and nature of surface MoOx species (tetrahedral or octahedral) on MoO_3 supported on variety of supports at mono layer coverage, but revealed the influence of polymeric and isolated surface Mo species at high coverage due to increase in surface Mo density. In the case of SiO_2 supported MoO_3, the isolated Mo species show high activity in comparison to polymeric Mo species. However, they observed a strong correlation between specific activity of the catalysts with electronegativity of the metal cation of the support, which increases in the following order: $ZrO_2 > MnO > TiO_2 > Nb_2O_5 > Cr_2O_3 > Al_2O_3 \sim NiO > SiO_2$. This effect influences the electron density of the metal support cation, as such controlling adsorption, reaction, and desorption rate of reactants and products. In a separate study of MoO_3/ Ta_2O_5 catalyst reported by Chen and Wachs [87], they revealed the presence of both redox and acidic sites responsible for the formation of formaldehyde and DME respectively. They evidenced the presence of polymeric distorted MoO_6 species over 1 % MoO_3/ Ta_2O_5 catalyst. Moreover, Matsouka et al [88] reported increase in turn over frequency (TOF) of methanol oxidation over $MoO_3/\gamma - Al_2O_3$ with increasing Mo loading, due to strong dependence on MoO_3 support interaction. In addition, Hu and Wachs [89] reported an in – situ Raman study of methanol oxidation in aerobic and anaerobic conditions; they reported reduction of Mo=O vibration bands from 1004 – 995 cm^{-1} for 20 wt% in anaerobic condition, and recovery of 70 % of the bands by 530 K. The author indicated that structural morphology of $MoO_3/\gamma–Al_2O_3$ does not affect formaldehyde selectivity, but increases the activity of polymeric tetrahedral/octahedral MoOx species by a factor of 2 – 4 in comparison to isolated tetrahedral MoOx species. In a separate EPR and Raman/Infra red operando spectroscopic study of methanol oxidation over 20 wt% $MoO_3/\gamma–Al_2O_3$ at 250 ^oC, reported by Brandhorst et al [90], revealed diminishing intensity of M=O vibration 992 cm^{-1} band with increasing 840 cm^{-1} band and increase in DME formation in the absence of oxygen. The catalyst revealed 93 % methanol conversion at 52 % formaldehyde selectivity due to reoxidation of Mo^{5+} - Mo^{6+} in the presence of oxygen. The authors attributed DME

formation to interaction of methoxy species with Mo – O – Al support, while formaldehyde emanated from redox sites on polymolybdate species.

Despite the vast literature on supported MoO_3 based catalysts, little attention has been paid on the use of nanodiamond as support for selective oxidation catalyst. Methanol oxidation on MoO_3/Al_2O_3 is widely reported, but thermal pre-treatment of the support before impregnation and use of chelating agent (citrate) during catalyst (MoO_3/Al_2O_3) synthesis is seldom reported. This has a profound effect on the activity as well as dispersion of MoOx species on the support.

Model Mo – oxide based catalyst

The use of Mo – oxide based model catalyst in selective oxidation catalysis is a new emerging area in heterogeneous catalysis; geared towards bridging the gap between surface science and catalysis, to derive a better understanding of catalytic active sites and reactivity at atomic scale during the reaction. Bowker's group [91] and Freund's [92] had reported few articles on the fabrication of iron molybdate model catalysts. However, no work has been carried out on the fabrication of MoO_3 and $Fe_2(MoO_4)_3$ film on $\alpha - Al_2O_3$ (0001) single crystal as model catalysts.

1.6 Previous work carried out in the group

Researchers from Bowker's group had worked on selective oxidation of methanol to formaldehyde, which is an important industrial reaction for the production valuable product of high demand. House [93] investigated aerobic and anaerobic oxidation of methanol on iron molybdate, and also investigated the effect of varying cationic ratio on activity and selectivity of methanol to formaldehyde. In addition, Yaseneva [94] worked on methanol oxidation on mixed oxide catalysts, while Alshehri [95] had studied selective oxidation of methanol on transition metal oxides.

1.7 Research Objectives

The focus of this study is to investigate selective oxidation of methanol over molybdenum oxides based catalysts ranging from unsupported single oxides, mixed oxides catalysts, to supported oxide catalysts. This will include:

Preparation of high surface area MoO_3 catalysts and probing catalytic active and selective sites for methanol oxidation reaction

Investigating effect of K doping on activity and selective of methanol oxidation on prepared MoO_3 catalysts

Studying catalytic active sites on iron molybdates catalyst of varying Mo : Fe ratios

Making MoOx supported on nanodiamond and γ-Al_2O_3 supports prepared by incipient impregnation, and their effect in methanol oxidation reaction

Fabrication and characterization of MoO_3 and $Fe_2(MoO_4)_3$ films on an Al_2O_3 (0001) single crystal using a novel wet chemical deposition method, meant for use as model catalysts for investigation of reaction kinetics and catalytic active sites during methanol oxidation. This is aimed at study of selective oxidation reaction at atomic level, as such bridging the gap between surface science and catalysis.

References

1. Ross JRH. Heterogeneous catalysis. Amsterdam, The Netherlands: Elsevier; 2012. Available from: www.elsevier.com.

2. Green S, editor. Industrial catalysis. New York: Macmillan Company; 1928.

3. Davy H. Some New Experiments and observation on the combustion of gaseous mixtures, with an account of a method of preserving a continued light in mixture of inflammable gases in air without flame. Phil Trans 1817; 107:77-85.

4. Davy E. On some combination of platinum. Phil Trans. 1820;110:108-25.

5. Bowker M. The Basis and application of heterogeneous catalysis. Oxford: Oxford University Press; 1998.

6. Schulz H. Short history and present trends of fischer - tropsch synthesis. Appl. Catal A. 1999;186(1):3-12.

7. Partington JR, editor. A history of chemistry. London: Macmillan; 1964.

8. Reddy BM. Redox properties of metal oxides. in: Fierro JLG, editor. Metal oxides; chemistry and application. New York: CRC Taylor and Francis; 2006. p. 215-36.

9. Bielanski A, Haber J. Oxygen in catalysis on transition metal oxides. J Catal Rev-Sci Eng. 1979;19(1):1–41.

10. Grasselli RK, Burrington JD. Selective oxidation and ammoxidation of propylene by heterogeneous catalysis. Adv Catal. 1981;30:133–63.

11. Gellings PJ, Bouwmeester HJM. Solid state aspects of oxidation catalysts. Catal Today 2000;58:1-53.

12. Mars P, Van krevelen DW. Oxidation carried out by means of vanadium oxide Catalyst. Chem Eng Sci. 1954;3:41-59.

13. Papakondylis AA, Sautet P. Ab Inizio study of the a- MoO_3 solid and study of the adsorption of H_2O and CO molecules on its (100) surface. J Phys Chem. 1996;100:10681-8.

14. Busca G, Ramis G, Lorenzelli V. FTIR study of the surface prperties of polycrystalline vanadia and reduced metal centre. Journal of molecular catalysis 1989;50:231-40.

15. Cavani F, Trifiro F. Selective oxidation of light alkanes; interaction between the catalyst and the gas phase on different classes of catalytic materials. Catal. Today. 1999;51:561-80.

16. Smith MR, Ozkan US. The partial oxidation of methane to formaldehyde: Role of different crystal planes of MoO_3. J Catal. 1993;141:124 – 39.

17. Smith MR, Zhang L, Driscoll SA, Ozkan US. Effect of surface species on activity and selectivity of MoO_3/SiO_2 catalysts in partial oxidation of methane to formaldehyde. Catalysis Letters. 1993;19:1-15.

18. Spencer ND, Pereira CJ. V_2O_5/SiO_2 - catalyzed methane partial oxidation with molecular oxygen. Journal of Catalysis. 1989;116:399-406.

19. Banares MA, Fierro JLG. Selective oxidation of methane to formaldehyde on supported molybdate catalyst. Catalysis Letters. 1993;17:205-11.

20. Suzuki K, Hayakawa T, Shimizu M, Takehira K. Partial oxidation of methane over silica-supported molybdenum oxide catalyts. Catalysis Letters. 1995;30:159-69.

21. Banares MA, Rodriguez I, Guerrero A, Fierro JLG. Mechanistic aspects of the selective oxidation of methane to C_1 oxygenate over MoO_3/SiO_2 catalyst. In: Guczi L, Solymosi F, Tenenyi P, editor. In Proceeding of the 10th International Congress on Catalysis; Budapest: Akademiai Kiado Budepest; 1993. p. 1131.

22. Gai-Boyes PL. Defect in oxide catalysts: Fundamental studies of catalysis in action Catal Rev Sci Eng. 1992; 34(1):1-54.

23. Chen NF, Oshihara K, Ueda W. Selective oxidation of ethane over hydrothermally synthesized Mo-V-Al-Ti oxide catalysts Catal Today. 2001;64:121.

24. Botella P, Lopez Nieto JM, Dejoz A, Vazquez MI, Martinez-Arias A. Mo-V-Nb mixed oxides as catalysts in selective oxidation of ethane. Catal Today. 2003;78:507.

25. Osawa T, Ruiz P, Delmon B. New results on the oxidative dehydrogenation of ethane to ethylene: promoting catalytic performance of Mo-V- and Ni-V- oxide by alpha-Sb_2O_4. Catal Today. 2000;61:309.

26. Vella OJ, Anderson A, Jens KJ. The oxidative dehydrogenation of ethane by perovskite type catalysts containing oxides of strontium, cerium and ytterbium. Catal Today. 1990;6:567.

27. Hargreaves JSJ, Hutchings GJ, Joyner RW, Taylor SH. Methane partial oxidation to methanol over Ga_2O_3 based catalysts: use of the CH_4/D_2 -exchange reaction as design tool. Chem Commun. 1996:532-3.

28. Taylor SH, Hargreaves, JSJ, Hutchings GJ, Joyner RW, Lembacher CW. The partial oxidation of methane to methanol: An approach to catalyst design. Catal Today. 1998;42(3):217-24.

29. Boyle R. Boyle discusses the distillation of liquid from the wood of box shrub. In: Cadwell J, editor. *The Sceptical Chymist*. London, England1661. p. 192 - 5.

30. Bernhard S, Zeikus JG. Microbial methanol fprmation; A major end product of pectin metabolism. Curr Microbiol. 1980;4(6):387-9.

31. Hansen JB, Nielsen PEH. Methanol synthesis In Ertl G, Knozinger H, Schuth F, Weitkamp J, editors. Handbook of heterogeneous catalysis. Weinheim, Germany: Wiley-VCH Verlag GmbH& Co. KGaA; 2008 p. 2920-96.

32. Liu X-M LG, Yan Z-F, Beltramini J. Recent advances in catalysts for methanol synthesis via hydrogenation of CO and CO_2. Ind Eng Chem Res 2003;42 6518-30.

33. Pontzen F LW, Gronemann V, Rothaemel M, Ahlers B. CO_2-based methanol and DME – efficient technologies for industrial scale production. Catal Today. 2011;171 242–50.

34. Methanol toxicity [Internet]. Medscape. 2015 [cited 9/03/15]. Available from: htpp://emedicine.medscape.com/article/1174890-overview.

35. Formaldehyde [Internet]. 2015 [cited 2/03/2015]. Available from: http://en.m.wikipedia.org/wiki/formaldehyde.

36. Butlerov A. Ueber einige des Jodmethylens (On some derivatives of methylene iodide). Annalen der Chemie und Pharmacie. 1859;III:242-52.

37. Hiofmann AW. Zur Kenntnis des Methyl aldehyds. Annalen der Chemie und Pharmacie. 1869;145(3):357-61.

38. Formaldehyde and 1-tert-butoxy propan-2-ol. 88 Lyon, France: International Agency for Research on Cancer, 2006.

39. Fair JR, Kmetz RC. Formaldehyde. In: Mc Ketta JJ, and Cunningham W A, editor. Encyclopaedia of Chemical Processing and Design. 23. U S A: Marcel Dekker Inc.; 1985. p. 350.

40. Reuss G, Disteldorf W, Gamer AO, Hilt A. Formaldehyde. Ullmann's Encyclopedia of Industrail Chemistry. A11. 6th ed. Weinheim: VCH; 2001. p. 619.

41. Formaldehyde plant project description [Internet]. Dynea Canada Ltd. 2006 [cited 23/03/2012]. Available from: www.dynea.com.

42. Qian M, Liauw MA, Emig G. Formaldehyde synthesis from methanol over silver catalysts Appl Catal A: General. 2003;238:211-22.

43. Johnson Matthey. [cited 23/05/2013]. Available from: http://www.formox.com.

44. Bowker M, Holroyd R, Elliott A, Morrall P, Alouche A, Entwistle E, et al. The selective oxidation of methanol to formaldehyde on iron molybdate catalysts and one component oxides. Catalysis letters 2002; 83(3-4):165-76.

45. Bowker M, Holroyd R, House M, Bracey R, Bamroongwongdee C, Shannon M, et al. The Selective oxidation of methanol on iron molybdate catalysts. Top Catal. 2008;48:158–65.

46. Hsu C-S, Chan C -C, Huang H -T, Peng C -H, Hsu W -C. Electrochromic properties of nanocrystalline MoO_3 thin films. Thin Solid Films 2008;516:4839–44.

47. Farneth WE, Ohuchi F, Staley RH, Chowdhry U, Sleight AW. Mechanism of partial oxidation of methanol over MoO_3 ss studied by temperature-programmed desorption. J Phys Chem 1985;89 2493-7.

48. Soares APV, Farinha Portela M. Methanol selective oxidation to formaldehyde over iron-molybdate catalysts. Catal Rev. 2004;47:125-74.

49. Routray K, Zhou W, Kiely CJ, Grünert W, Wachs IE. Origin of the synergistic interaction between MoO_3 and iron molybdate for the selective oxidation of methanol to formaldehyde. J Catal. 2010;275(1):84-98.

50. Tatibouet JM, Germain JE. A structure-sensitive oxidation reaction: Methanol on molybdenum trioxide catalysts. J Catal. 1981;72(2):375-8.

51. Abon M, Massardier J, Mingot B, Volta JC, Floquet N, Bertrand O. New unsupported [100]-oriented MoO_3 catalysts II. Catalytic properties in propylene oxidation. J Catal 1992;134(2):542 – 8.

52. Vedrine JC. Revisiting active sites in heterogeneous catalysis: Their structureand their dynamic behaviour. Appl Catal A Gen. 2014;474 40–50.

53. Machiels CJ, Cheng WH, Chowdhry U, Farneth WE, Hong F, Mc Carron EM, et al. The effect of structure of molybdenum oxides on the selective oxidation of methanol. Appl Catal 1986;15(1-2):249 – 56

54. Farneth WE, McCarron III EM, Sleight AW, Staley RH. Comparison of the surface chemistry of two polymorphic forms of molybdenum trioxide. Langmuir. 1987;3(2):217-23.

55. Chung JS, Miranda R, Bennett CO. Mechanism of partial oxidation of methanol over MoO_3. J Catal. 1988;114(2):398 – 410.

56. Allison JN, Goddard III, WA. Oxidative dehydrogenation of methanol to formaldehyde. J Catal. 1985;92(1):127 – 35.

57. Cheng W. Methanol and formaldehyde oxidation over molybdenum oxide. J Catal. 1996; 158(2):477 – 85.

58. Bowker M, Carley AF, and House M . Contrasting the behaviour of MoO_3 and MoO_2 for the oxidation of methanol. Catalysis Letters 2008; 120: 34 – 9.

59. Vedrine JC, Coudurier G, Millet MJ. Molecular design of active sites in partial oxidation reactions on metallic oxides Catal Today. 1997;33:3-13.

60. Mestl G, Ruiz P, Delmon B, Knozinger H. Oxygen-exchange properties of MoO_3: An in-situ Raman spectroscopy study. J Phys Chem 1994;98 11269-75.

61. Driscoll AD, Ozkan US. Transient isotropic labelling using $^{16}O_2/^{18}O_2$ over alkaline-metal-promoted molybdate catalyst in oxidation coupling of methane. J Phys Chem. 1993;97:11524-9.

62. Driscoll AD, Gardner DK, Ozkan US. Characterization, activity, and adsorption/desorption behaviour of alkali-promoted molybdate catalysts for the oxidative coupling of methane. J Catal. 1994;147:379-92.

63. Adkins H, Peterson WR. The oxidation of methanol with air over iron, molybdenum, and iron-molybdenum oxides. J Am Chem Soc. 1931;53 1512 – 20.

64. Sun-Kou MR, Mendioroz S, Fierro JLG, Palacios J M, Guerrero-Ruiz A. Influence of the preparation method on the behaviour of Fe-Mo catalysts for the oxidation of methanol. J Mater Sci. 1995;30(496-503).

65. Soares APV, Farinha Portela M, Kiennemann A, Hilaire L, Millet JMM. Iron molybdate catalysts for methanol to formaldehyde oxidation: effects of Mo excess on catalytic behaviour. Applied Catalysis A: General 2001;206: 221–9.

66. House MP, Carley AF, Echeverria-Valda R, Bowker M. Effect of varying the cation ratio within iron molybdate catalysts for the selective oxidation of methanol. J Phys Chem C 2008;112: 4333-41.

67. Li J-L, Zhang Y-X, Liu C-W, Zhu Q-M. Improvement in reactivity, reproducibility and stability of Fe-Mo catalysts by wet mixing. Catal Today 1999;51:195-9.

68. Soares APV, Portela M F, Kiennemann A, Hilaire L. Mechanism of deactivation of iron-molybdate catalysts prepared by coprecipitation and sol–gel techniques in methanol to formaldehyde oxidation. Chem Eng Sci 2003;58:1315-22.

69. Yan Huang Y, Cong L, Yu J, Eloy P, Ruiz P. The surface evolution of a catalyst jointly influenced by thermal spreading and solid-state reaction: A case study with an Fe_2O_3–MoO_3 system. J Mol Catal A: Chem 2009;302:48–53.

70. Beale AM, Jacques SDM, Sacaliuc-Parvalescu E, O'Brien MG, Barnes P, Weckhuysen BM. An iron molybdate catalyst for methanol to formaldehyde conversion prepared by a hydrothermal method and its characterization. Appl Catal A: Gen 2009;363:143–52.

71. Bowker M, Brookes C, Carley AF, House MP, Kosif M, Sankar G, et al. Evolution of active catalysts for the selective oxidative dehydrogenation of methanol on Fe_2O_3 surface doped with Mo oxide. Phys Chem Chem Phys. 2013;15:12056-67.

72. Brookes C, Wells PP, Cibin G, Dimitratos N, Jones W, Morgan DJ, et al. Molybdenum Oxide on Fe_2O_3 Core−Shell Catalysts: Probing the Nature of the Structural Motifs Responsible for Methanol Oxidation Catalysis. ACS Catal. 2014;4:243−50

73. Okamoto Y, Morikawa F, OH-Hiraki K, Imanaka T, Teranishi S. Role of Excess of MOO, in Fe,O,-Moo, Methanol Oxidation Catalysts Studied by X-Ray Photoelectron Spectroscopy. J Chem Soc Chem Commun. 1981:1018-9.

74. Soderhjelm E, House MP, Cruise N, Holmberg J, Bowker M, Bovin J, Andersson A. On the synergy effect in MoO_3–$Fe_2(MoO_4)_3$ catalysts for methanol oxidation to formaldehyde. Top Catal. 2008.

75. Wachs IE, Routray K. Catalysis science of bulk mixed oxides. ACS Catal. 2012;2:1235-46.

76. House PM, Carley AF, Bowker M. Selective oxidation of methanol on iron molybdate catalysts and the effects of surface reduction. J Catal. 2007;252:88–96.

77. Deshmukh SARK, Annaland M, Kuipers JAM. Kinetics of the partial oxidation of methanol over a Fe-Mo catalyst. Appl Catal A: Gen. 2005;289(2):240-55.

78. Andersson A, Hernelind M, Augustsson O. A study of the ageing and deactivation phenomena occurring during operation of an iron molybdate catalyst in formaldehyde production. Catal Today 2006;112: 40–4.

79. Mitov I, Asenov S, Tomov T, Klissurski D. In situ Mossbauer study of the interaction of methanol with An iron-molybdenum oxide Catalyst. J Phys Chem C. 2007;111: 5389-93.

80. Jacques SDM, Leynaud O, Strusevich D, Beale AM, Sankar G, Martin C M, et al. Redox behavior of Fe-Mo-O catalysts studied by ultrarapid In situ diffraction. Angew Chem Int Ed 2006; 45:445 –8.

81. Jacques SMD, Leynaud O, Strusevich D, Stukas P, Barnes P, Sankar G, et al. Recent progress in the use of in situ X-ray methods for the study of heterogeneous catalysts in packed-bed capillary reactors. Catal Today. 2009;145:204–12.

82. Pradhan S, Bartley JK, Bethell D, Carley AF, Conte M, Golunski S, et al. Non-lattice surface oxygen species implicated in the catalytic partial oxidation of decane to oxygenated aromatics. Nat Chem. 2012;4:134-9.

83. Tatibouet JM, Germain JE, Volta JC. Structure-sensitive catalytic oxidation: alcohols on graphite-supported molybdenum trioxide. J Catal. 1983;82:245-51.

84. Tatibouet JM. Methanol oxidation as a catalytic surface probe. Appl Catal A: Gen 1997;148:213-52.

85. Castillo R, Dewaele K, Ruiz R, Delmon B. Mechanical mixtures of alpha-Sb_20_4 and MoO_3 as highly selective catalysts for the oxidation of methanol to formaldehyde. Appl Catal A : Gen. 1997;153:1-8.

86. Briand LE, Farneth WE, Wachs IE. Quantitative determination of the number of active surface sites and the turnover frequencies for methanol oxidation over metal oxide catalysts I. Fundamentals of the methanol chemisorption technique and application to monolayer supported molybdenum oxide catalysts. Catal Today. 2000;62:219–29.

87. Chen Y, Wachs IE. Tantalum oxide-supported metal oxide (Re_2O_7, CrO_3, MoO3, WO_3, V_2O_5, and Nb_2O_5) catalysts: synthesis, Raman characterization and chemically probed by methanol oxidation. J Catal 2003;217 468–77.

88. Matsuoka Y, Niwa M, Murakami Y. Morphology of molybdena supported on various oxides and its activity for methanol oxidation J Phys Chem. 1990;94(4):1477-82.

89. Hu H, Wachs IE. Catalytic properties of supported molybdenum oxide catalysts: in situ Raman and methanol oxidation studies. J Phys Chem. 1995;99:10911-22.

90. Brandhorst M, Cristol S, Capron M, Dujardin C, Vezin H, Le bourdon G, et al. Catalytic oxodation of methanol on Mo/Al_2O_3 catalyst: An EPR and Raman/infrared operando spectroscopies study. Catal Today. 2006;113(1-2):34-9.

91. Bamroongwongdee C, Bowker M , Carley AF, Davies PR, Davies RJ, Edwards D. Fabrication of complex model oxide catalysts: Mo oxide supported on Fe_3O_4(111). Faraday Discussion. 2012;162:12-7.

92. Uhlrich JJ, Sainio J, Lei Y, Edwards D, Davies R, Bowker M, et al. Preparation and characterization of iron–molybdate thin films. Surf Sci. 2011;605 1550–5.

93. House PM. Selective oxidation of methanol over iron molybdate catalyst [PhD Thesis]. Cardiff: Cardiff University; 2007.

94. Yaseneva P. Selective Oxidation of Methanol on mixed oxide catalysts. Cardiff: Cardiff University; 2011.

95. Al Shehri A. Methanol oxidation on transition elements oxides. Cardiff: Cardiff University; 2013.

Chapter 2 Experimental

Contents

2.1 Introduction

This chapter focuses on materials and techniques used throughout this research work. The first section describes the various methods used in the preparation of catalysts tested for activity and selectivity of methanol oxidation in a CATLAB micro Pulsed flow reactor. Characterization of the catalytic materials were conducted using nitrogen adsorption BET surface analysis, Raman Spectroscopy, X-Ray Diffraction (XRD), Scanning Electron Microscopy-Energy Dispersive X-ray (SEM-EDX), X-ray Photoelectron Spectroscopy (XPS), and Atomic Force Microscopy (AFM) techniques .

2.2 Catalyst synthesis

The catalysts studied in this research were synthesized by variety of methods discussed in the next paragraph. Single oxide commercial molybdenum trioxide (MoO_3, 99.5 % BDH) and iron (III) oxide (Fe_2O_3 99 % Sigma Aldrich) were also used for comparison. The powder catalysts were pressed at 10 tonnes in a pellet die, before sieving to a grain size between 850 – 600 microns. The sieved catalysts were stored in an air tight glass vial before testing in the CATLAB micro reactor.

Co precipitation Method

Unsupported single-component and multi-component metal oxides catalysts studied were synthesized using this technique. This involved precipitation of active metal oxide species or co-precipitation of mixed oxide species in solution using acids or bases, via nucleation and growth into single or mixed phases. The evaporation of the solvent was carried out before activation into catalyst [1].

Molybdenum oxide (MoO_3) and iron (III) oxide (Fe_2O_3) were synthesised by drop-wise addition of 50 ml each of 0.072 M ammonium heptamolybdate tetrahydrate ($(NH_4)_6\ Mo_7\ O_{24}.4H_2O$) and 0.34 M iron (III) nitrate nanohydrate ($Fe(NO_3)_3.9H_2O$) solution, into separate beakers containing 100 ml deionised water acidified to a pH 2 with HNO_3. The solutions were evaporated to near dryness at 90 ^oC, heated overnight at 120 ^oC before calcination at 500 ^oC for 48 hours. However, MoO_3 samples were prepared at various pH using the above method by adjusting the pH of the solution using dilute HNO_3 and ammonia solution.

Iron molybdate $Fe_2(MoO_4)_3$ of varying molybdenum ratio of 1.5 and 2.2, corresponding to 0.036 M and 0.053 M (4.476 g and 6.565 g of ammonium

heptamolybdate tetrahydrate $(NH_4)_6\ Mo_7\ O_{24}.4H_2O$ (Sigma Aldrich) in 100 ml of deionised water respectively), was acidified to a pH 2 using dilute HNO_3 acid. The solution was co-precipitated via drop wise addition of iron (III) nitrate nanohydrate ($Fe(NO_3)_3.9H_2O$ Sigma Aldrich) solution (containing 6.83 g in 50 ml of deionised water) with stirring at 60 ^oC, while the pH was maintained at 2 by drop wise addition of dilute ammonia solution. The canary yellow precipitate formed was aged for 2 hours at 60 ^oC before evaporation to near dryness at 90 ^oC. The slurry was dried overnight at 120 ^oC in air oven prior to Calcinations at 500 ^oC for 48 hours.

The choice of iron (III) nitrate as precursor, is due to its good solubility in water and ease in removal of NO_3^- ion species during calcination above 250 ^oC [2, 3].

Incipient Wetness Impregnation

The incipient-wetness impregnation method, involves the use of a certain volume of solution containing active precursor that is sufficient to fill the pores of the support, accompanied by stirring before drying [1]. The mechanism of this preparative technique involves transport of the precursor to the pore body of the support, diffusion within its pore, and finally uptake into the pore wall [4].

The methods used in the preparation of both promoted and supported catalysts are outlined in Table 2. 1 below:

a. K-promoted MoO_3 was prepared by dissolving a measured amount of KNO_3 based on percentage monolayer coverage into a sufficient volume of deionised water to fill the pores of the synthesized MoO_3. The material was mixed using a pestle and mortar until a paste was obtained. The paste was dried at 120 ^oC for 2 hours before calcination at 500 ^oC.
b. The supports were annealed at different temperatures before use for impregnation. Nanodiamond (ND) supports of 5 nm size were purchased from Microdiamant and Syndea Company in Switzerland. The support was annealed from 200-500 ^oC in an air oven for 5 hours to oxidise and remove amorphous carbon from its surface. Nanodiamond support annealed at 500 $^o C$ was used for catalysts preparation using incipient wetness impregnation method.

Gamma aluminium oxide (γ-Al_2O_3 Alfar Aesar 99 % metal basis) was calcined in an oven between 400-900 ^oC for 12 hours; samples annealed at 500 ^oC and 700 ^oC were used as supports for impregnation.

The molybdenum loading on the supports was calculated based on % monolayer coverage of the support surface as well as % weight loading.

Nanodiamond supported MoO_3 was prepared by dissolving the correct amount of ammonium heptamolybdate tetrahydrate ($(NH_4)_6Mo_7O_{24}\cdot 4H_2O$), into a volume of deionised water required to fill the pores of the support. The sample was mixed with a pestle until a paste is obtained, and then dried in an oven at 120 ^oC for 2 hours before calcination in flowing air at 410 ^oC for 3 hours.

γ- alumina supported MoO_3 was prepared via two routes:

i. Citrate method; γ-Al_2O_3 supports annealed at 500 ^oC and 700 ^oC were used for this preparation. The required amount of AHM was dissolved into desired volume of deionised water required to fill the pore of the support, and 0.1 g of citric acid was added to this solution and swirled to dissolve. The pH was increased to 6 by addition of 2-3 drops of dilute ammonia solution, and then sonicated for 20 min. The solution was loaded onto the support and mixed until paste was obtained using a pestle and mortar. The paste was dried over night at 120 ^oC, before calcination at 500 ^oC for 5 hours.
ii. Water method: this was used for γ-Al_2O_3 supports annealed at 500 ^oC. The preparative method was similar to the citrate method above, except that neither citric acid nor dilute ammonium solution was utilised.

The catalysts were cooled and stored in an airtight glass container for further characterization.

Table 2. 1 ***Support and precursor used for incipient wetness impregnated catalyst***

Support/Catalyst (2g)	Active precursor	Deionised water used (ml)
Prepared MoO_3	KNO_3	0.6
Nanodiamond (ND)	$(NH_4)_6Mo_7O_{24}\cdot 4H_2O$	7.0
γ-Al_2O_3	$(NH_4)_6Mo_7O_{24}\cdot 4H_2O$	2.8

2.3 Thin film preparation method

The single crystal alumina (α-Al_2O_3 (0001)) of two different sizes 1 cm^2 and 5 mm^2 , were supplied by Prof. Bowker and Alineason Materials Technology GmbH, Frankfurt, Germany respectively. The crystals were cleaned with ultra pure water and 2-propanol after treating with a solution of 4:1 H_2SO_4 : H_2O_2 for 20 min, before drying with nitrogen gas.

MoO_3/ α-Al_2O_3 (0001)

The precursor loading was calculated based on the surface area of the crystals. The required weight of AHM was dissolved in 3 ml of deionised water, and then mixed with 35 ml of ethanol forming a white colloid. This colloidal solution was acidified with 2-3 drops of Nitric acid (0.2M) or citric acid, which gave a clear light yellowish solution before sonication for 20 min. A drop of this solution was placed on clean α-Al_2O_3 (0001) single crystal using a pipette, and dried in a closed vial. The crystal was annealed in an air oven at different temperature between the range 100-500 ^oC for an hour. The model catalysts were then cooled and stored in a closed glass vial (airtight).

$Fe_2(MoO_4)_3$/ α-Al_2O_3 (0001)

The required amount of ammonium heptamolybdate in 3 ml of deionised water was mixed with 35 ml of ethanol to form a white colloidal solution. Addition of 2-3 drops of dilute nitric acid and sonication for 15 minutes dissolved the white colloids to give a clear light yellowish solution. The required amount of iron nitrate in 3 ml of deionised water was added drop wise into the acidified solution under stirring for 5 minutes, and then made up to 50 ml with ethanol. The mixture was stirred again until a homogenous clear canary yellow solution was obtained. A drop of this solution was placed on a cleaned crystal and allowed to dry in a closed vial, before calcinations between 100 ^oC – 500 ^oC for an hour. The crystal was cooled and stored in a glass vial for further characterization.

2.4 CATLAB Micro Pulsed Flow Reactor

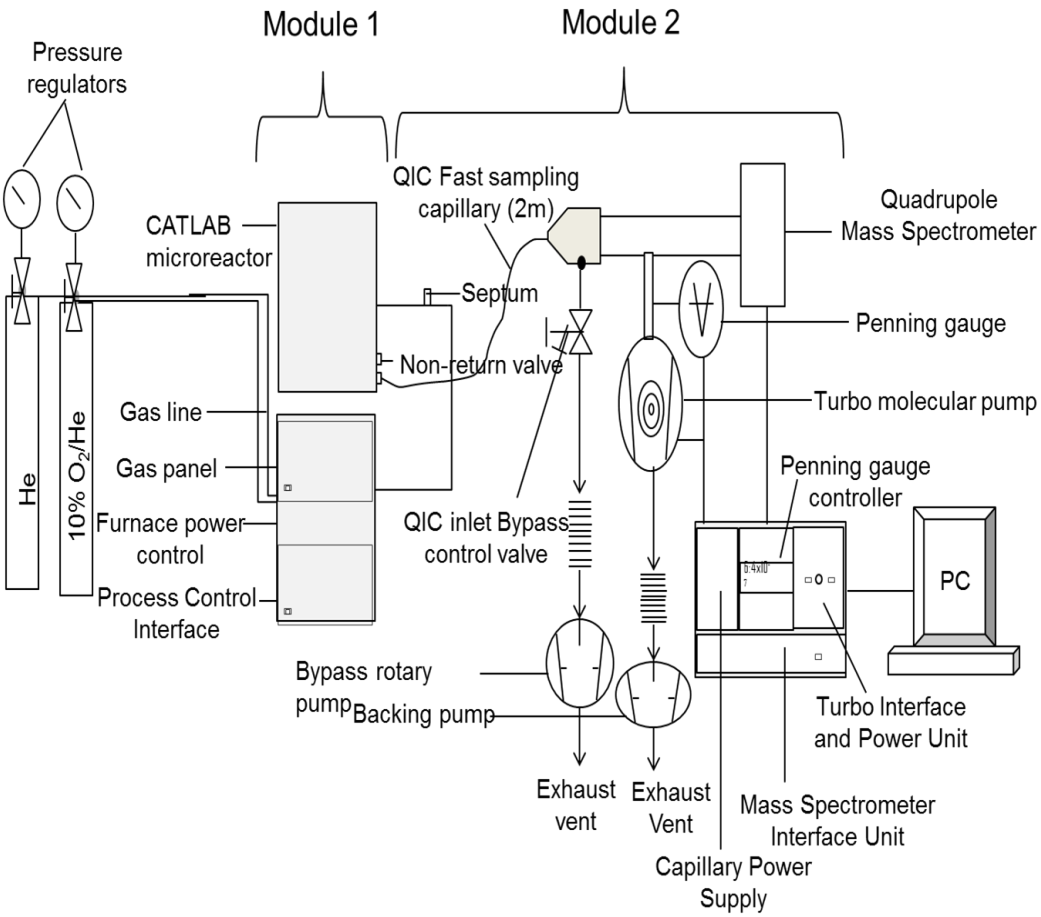

Fig. 2. 1 ***Overview of CATLAB micro pulsed flow reactor system***

Fig. 2. 1 above gives a general overview of the CATLAB pulsed flow microreactor setup, which comprises of two basic modules. The first module consists of a gas panel, furnace power control, process control interface, and The CATLAB microreactor. The second module is made up of the QIC -20, which consists of the quartz inlet gas sampler, quadrupole mass spectrometer, ultrahigh vacuum (UHV) turbo molecular pump attached to two rotary pumps, penning gauge, mass spectrometer interface unit (MSIU), and capillary power supply (CPS).

The gas panel is connected to two gas cylinders containing pure helium and 10 % oxygen in helium obtained from BOC Ltd. The gases are allowed to flow from the

cylinder via a valve at a pressure of 2 bar into 1/8 inch plastic line connected to the gas panel at one end and flow into the microreactor via a 1/8 inch stainless steel line with an injection port (septum) heated at 60 ^{o}C by heating tape. The flow rate is controlled by a flow meter integrated within the process control unit, which allows 30 ml and 15 ml of gas to flow through the reactor and bypass during analysis or at standby mode respectively.

About 1µL of methanol was injected through the septum into a stream of carrier gas (He or 10 % O_2/ He), which flows either to the catalyst bed during analysis or to the bypass to measure the mass spectrometer sensitivity signal. During analysis, the injected methanol flows into the quartz reactor tube containing catalyst sample (about 0.1-1 g) held between quartz wool, which was heated by an oven from ambient temperature to 400 ^{o}C at programmed heating rate.

The product species from the reactor flow into the 2 m long fast quartz inlet capillary (QIC) sampling unit connected to the vacuum system. The QIC is designed to sample about 16 ml/min of the gas product species at 160 ^{o}C to prevent condensation of reactive species or water vapour during standard analysis, which is controlled by the capillary power supply unit [5]. The bypass rotary pump is attached to the vacuum system via QIC bypass control valve, which functions as first stage pressure reduction and evacuation of the gas species to about the millibar region. This allows high velocity and low-pressure effluent gas into the turbo inter-stage port via a platinum molecular orifice, which serves as a second stage pressure reduction by impinging the flow of the effluent gas species. The turbo molecular pump is attached to a backing rotary pump and a penning gauge controlled by turbo interface and power unit (TIPU) and penning gauge controller respectively. These provide an oil-free and acceptable pressure environment for operation of the quadrupole mass spectrometer ion source for detection, identification, and quantification of product species.

Mass Spectrometer Interface Unit (MSIU) connected to the personal computer through RS 232 communication cable, controls the quadrupole mass spectrometer via MASsoft and CATLAB software on the computer. The software enables analysis and data acquisition under a Windows Operating System.

CATLAB Microreactor

The microreactor in Fig. 2. 2 consists of a manifold assembly containing an in-bed thermocouple inserted into quartz micro reactor tube with an opening at one end, which contains the catalyst sample held between quartz wools. The reactor tube was placed into a double-coated glass with 2 mm opening within, which allows the gas species to flow from the reactor tube into the Mass Spectrometer inlet. The entire setting is enclosed in a radiant furnace consisting of an external furnace and sentry thermocouples that measure reactor temperature. The furnace operates to a maximum temperature of 1000 ^{o}C, at a variable heating rate of 0.1 – 20 ^{o}C/ min. However, this setup integrates with an auto-switching air-cooling system housed in a bench top cabinet.

About 1µl of the injected sample in a stream of carrier gas, flowing at a constant rate (30 ml/min) in a heated line, flows into the catalyst bed or bypass via a three-way switching valve. However, the QIC fast inlet sampler samples only about 16 ml/min of the product species, while the excess gas species are vented through Vent 1 and Vent 2 during analysis or bypass operational mode respectively.

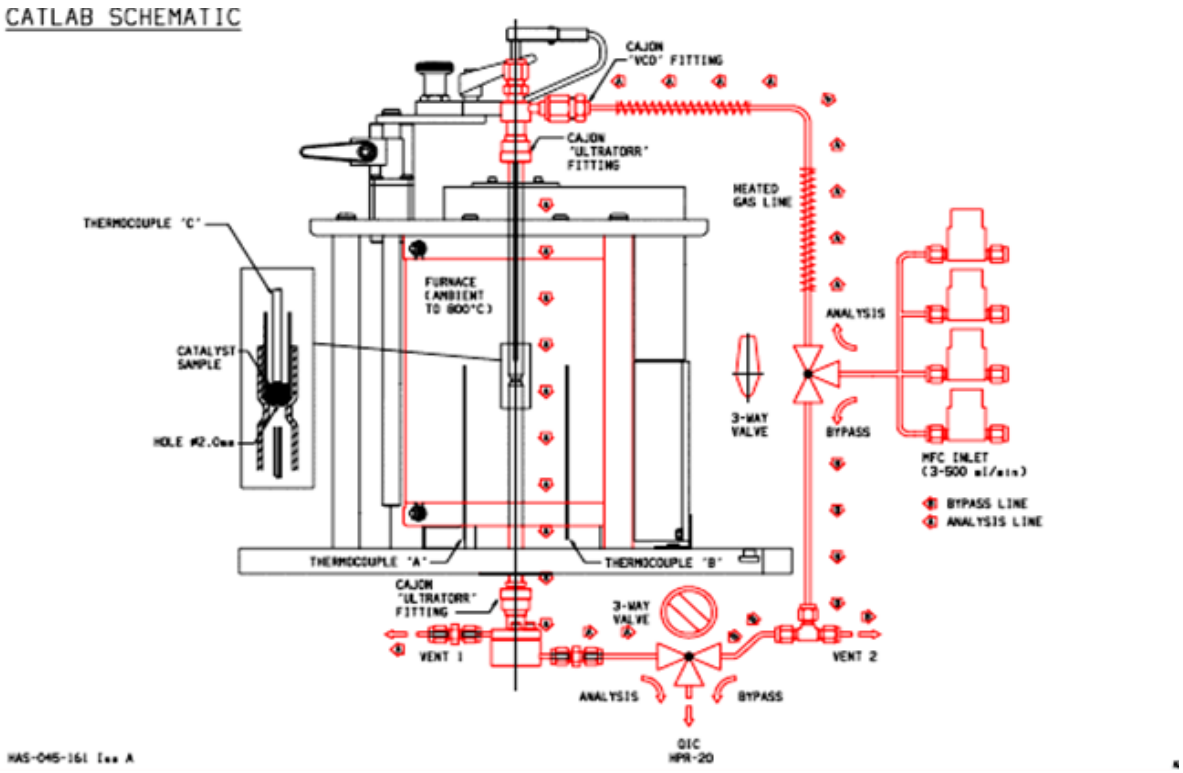

Fig. 2. 2 ***Schematic diagram of the CATLAB micro reactor setup [6]***

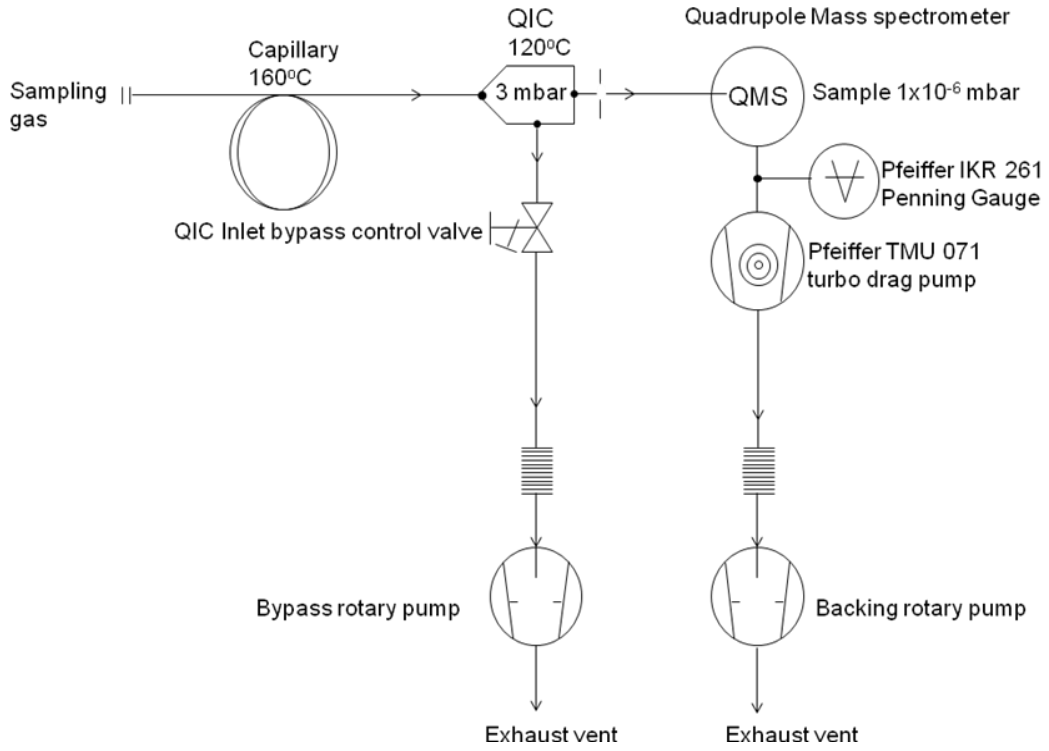

Fig. 2. 3 ***Schematic diagram of the QIC-20 vacuum setup [7]***

QIC-20

The QIC-20 vacuum as depicted in Fig. 2. 3 comprises of an inlet system, ultrahigh vacuum (UHV) chamber, and electronic control unit designed around a quadrupole mass spectrometer assembled in a bench top cabinet. The QIC-20 is connected to a personal computer via a RS 232 serial communication cable, which enables analysis and data acquisition by a MASsoft application operating under Windows (operating system).

UHV System

The ultrahigh vacuum (UHV) system consists of a Pfeiffer TMU 071 drag turbo molecular pump connected to bypass and backing rotary pumps via a QIC inlet bypass control valve and a UHV chamber respectively. The former reduces the pressure of sample gas, while the latter provides an oil-free pumping system by expelling exhaust pressure from UHV system. The turbo pump control by turbo interface and power unit (TIPU) creates a high vacuum by evacuating the UHV chamber at a pumping rate of 70 litres per second. The total pressure of the UHV system is monitored by an IKR 261 penning gauge attached to the chamber. However, an automated vent valve fitted to the turbo pump vents the UHV chamber during system shutdown.

Inlet System

The QIC-20 system consists of a QIC (Quartz Inert Capillary) fast sampling capillary inlet. The QIC provides a dynamic system of sampling reactive or condensable gases by a mass spectrometer. The inlet uses a two-stage pressure reduction system, which provides acceptable pressure limit for proper functioning of the mass spectrometer ion source [5].

Sample gas is sucked into the quartz capillary by the bypass pumping effect, which acts as the first stage pressure reduction step, allowing gas to exit the capillary at high velocity. The platinum orifice further reduces the pressure of flowing gas in the second stage before entry into mass spectrometer ion source. The capillary exit is 4 mm from the orifice, while the orifice is 12 mm to the ion source. This distance gives optimum and free transmission of gas species to ion source with minimum surface contact or memory effect [5].

However, vapour condensation or adsorption of reactive gas species is limited by continuous heating of the inlet capillary (160 ^{o}C), orifice, and the bypass region (120 ^{o}C) by a capillary temperature controller [5].

Quadrupole Mass Spectrometer

Mass spectrometry is the most extensive and versatile analytical technique that measures the molecular mass of atoms and compounds utilizing their mass-to-charge ratio. The QIC-20 system has a standard quadrupole mass spectrometer probe mounted inside a high vacuum system consisting of a quadrupole mass analyzer coupled to an ion source which generate ions, and a detector which measures the mass of the resolved ion. The probe scan range is usually between 2-200 atomic mass unit (amu) [8].

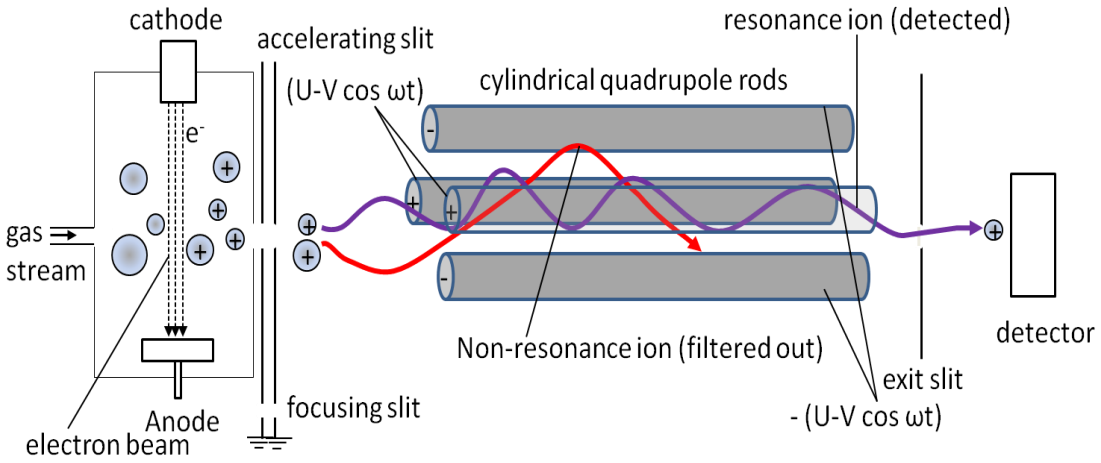

Fig. 2. 4 ***Schematic diagram of a quadrupole mass analyzer***

The quadrupole consists of four cylindrical rods (electrodes; 125 mm long and 6 mm in diameter) assembled asymmetrically to each other, or ideally arranged in a hyperbolic geometry to give a molecule trajectory path (z-axis) as shown in Fig. 2. 4, in which, applying a combination of direct current (DC) and radio frequency (RF) voltages, U and Vcos (ωt) respectively, forms a complex electric field region that is time-dependent.

The electron-impact ionization source consists of oxide-coated iridium filament (cathode) producing a beam of high-energy moving electron, which knock-off electrons from the stream of neutral gas molecules on collision to form unstable, positively charged molecular ions. These ions fragment into smaller ions, as they exit the ionization chamber via a series of accelerating and focusing slits, which direct them into the quadrupole mass filter. The anode electrode traps the excess electrons in the chamber. However, ions entering the quadrupole are filtered based on their mass-charge ratio due to an alternating DC and RF electric field. Eventually this process allows only small mass-charge resonance ion at stable trajectory to reach the detector, while the electrodes filter out the large non-resonance ions colliding with the electrodes.

Mode of Analysis

There are two major operating modes of the CATLAB pulse flow microreactor:

i Temperature Programmed Desorption ii Temperature Programmed Reaction

i. Temperature Programmed Desorption (TPD)

This technique is vital in the field of surface science and catalysis. It is a tool for understanding kinetics as well as energetics of surface desorption, enthalpy of adsorption/desorption, and determination of active sites on catalyst surface using methanol adsorption as expressed in equation 2.2 – 2.5. This mode of analysis involves saturation of the catalyst by adsorption of methanol on its surface, following pre-treatment in 10 % O_2/He at 400 ^oC for 30 minutes. The temperature is then ramped from room temperature to 400 ^oC at a heating rate of 12 ^oC/minute, while the quadrupole mass spectrometer detects and analyses component of desorbed effluent gas species. Fig. 2. 5 A and B below depict a typical plot of the TPD profile.

The peak maximum temperature (T_m) of desorption of a given spectrum is used in the determination of its activation energy (Ea) using the Redhead equation in Equation 2.1. However, the methanol desorption on catalyst surface obeys the first order kinetics, which is independent of the surface coverage

$$\frac{Ea}{RT_m^2} = \frac{v_1}{\beta} \times e^{-Ea/RT_m} \qquad \text{Equation 2.1}$$

where; Ea - Activation energy (kJ/mol)

R - Gas constant (J /K mol)

T_m- Peak maximum temperature (K)

v_1 - Pre-exponential factor (10^{13}/s)

β - Heating rate (K/s)

More so, the amount of chemisorbed methanol on the catalyst surface during pulsing can be used to determining specific active site area based on the following analysis steps:

The volume CH_3OH is determined by relating the peak integral area of chemisorbed CH_3OH on the surface to that physisorbed CH_3OH after saturation, from which the mass of CH_3OH can be determined.

$$\text{Mass of } CH_3OH(g) = \rho \times V \qquad \text{Equation 2.2}$$

Where ρ - Density of CH_3OH (0.7918g/cm^3 at STP)

V - Volume of CH_3OH (cm^3)

$$\text{Number of moles of } CH_3OH = \frac{mass\ of\ CH_3OH}{RMM\ of\ CH_3OH} \quad \text{Equation 2.3}$$

Where RMM is the relative molecular mass of CH_3OH (32.04g/mol)

$$\text{Number of atoms of } CH_3OH = \text{Number of mole of } CH_3OH \times \text{Avogadro's number}$$

Equation 2.4

$$\text{Avogadro's Number} = 6.022 \times 10^{23}/mol$$

The amount of atoms in $1m^2$ area of a surface is assumed to contain 10^{19} atoms

$$\text{Area of active sites} = \frac{\text{Number of } CH_3OH \text{ adsorbed on active sites (atoms)}}{10^{19} \text{ atoms (sites) on surface}} \times 1\ m^2$$

Equation 2.5

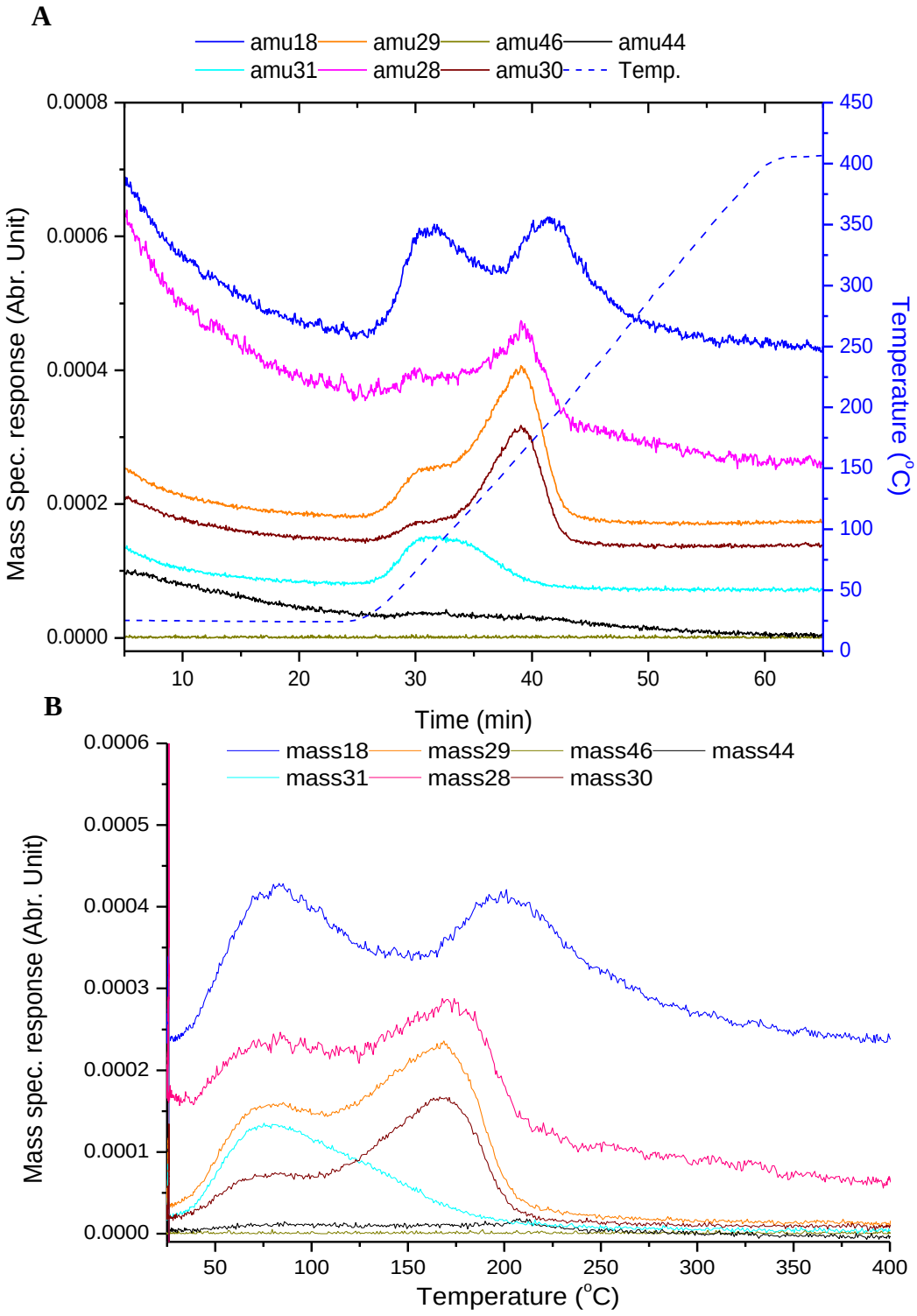

Fig. 2. 5 ***A and B depicts the TPD profile of methanol over $Fe_2(MoO_4)_3$ catalyst***

Fig 2.5 A and B revealed plot of mass spectrometer response and temperature against time, and mass spectrometer response against temperature respectively.

ii. Temperature Programmed Reaction (TPR)

This transient mode of analysis provides pulsed flow reaction data for measuring selectivity and reactivity of selective oxidation reaction as shown in Fig. 2. 6. About 1microlitre (µL) of methanol is injected on the pre-treated catalyst every 2 minutes at room temperature (usually about five injections), before the catalyst is heated at 8 ^{o}C/minute from room temperature to 400 ^{o}C. As the reaction progresses with time, the methanol peak (mass 31) intensity decreases with increasing temperature, which evidenced conversion of methanol to other products as shown in Fig. 2.6.The data obtained from the pulses were treated and calculated for reactivity and selectivity based on the formula below:

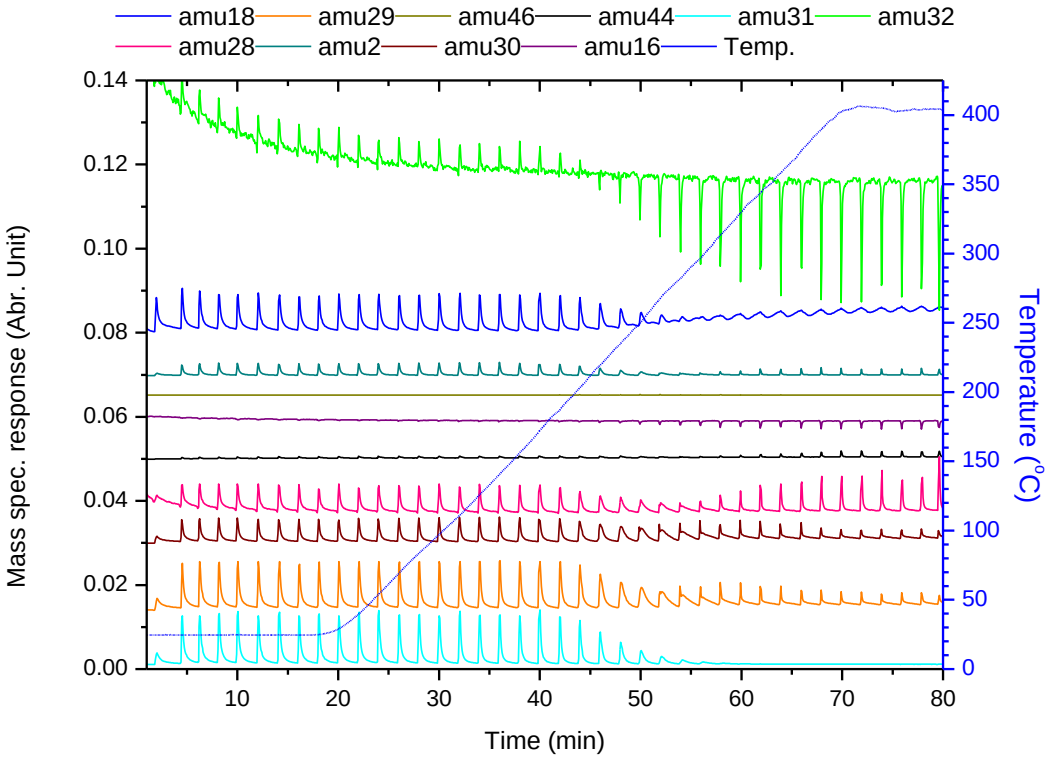

Fig. 2. 6 ***TPR raw data of methanol oxidation over $Fe_2(MoO_4)_3$ catalyst***

$$Methanol\ Conversion\ (\%) = \left(\frac{Reacted\ Methanol}{Total\ Methanol}\right) \times\ 100 \quad \text{Equation 2.6}$$

$$Selectivity\ (\%) = \left(\frac{[Formaldehyde]}{Total\ Products}\right) \times\ 100 \quad \text{Equation 2.7}$$

The mass spectrometer was calibrated by injecting five pulses of reagent or products into the carrier gas stream (He or 10% O_2/He) ranging from 0.2 to 1µl before

experiment and after a period of operation (every 6 months) or after reactor shutdown: for repair or maintenance, to check its sensitivity and reliability of the data.

Table 2. 2 depicts cracking pattern of compound investigated during selective oxidation reaction of methanol to formaldehyde. Each compound has a specific fragmentation pattern in the mass spectrometer, as such the masses to be selected and analysed for interpretation of cracking pattern but be treated with care.

Table 2. 2 ***Mass spectrometer cracking pattern of compounds of interest***

Compound	Cracking fraction
Hydrogen	2(1000), 1(21)
Water	18(1000), 17(211), 16(09), 19(05), 20(03)
Carbon monoxide	28(1000), 12(47), 16(17), 29(12), 14(08), 30(02), 13(01)
Formaldehyde	29(1000), 30(885), 28(309), 14(44), 13(43), 12(33), 31(19), 16(17)
Methanol	31(1000), 32(717), 29(421), 28(90), 30(78), 33(11), 27(05)
Carbon dioxide	44(1000), 16(94), 28(82), 12(67), 29(01), 13(09)
Dimethyl ether	45(1000), 29(788), 15(573), 46(456), 14(125), 31(70), 13(54), 30(36)

The masses analysed for compound of interest in this study are as follows: methanol (mass 31), formaldehyde (mass 30), water (mass 18), dimethyl ether (mass 45), carbon dioxide (mass 44), and carbon monoxide (mass 28).

The methanol mass (mass 31) has a trace contribution from masses of other compounds like formaldehyde (1.9 %) and dimethyl ether (7.0 %) as shown in Fig. 2.6, which can be removed to obtain the correct response of methanol in the mass spectrometer. This is achieved by subtracting integral of average methanol peak area (obtain from five injection over bypass) from the integral of peak area of other masses, and then multiplying by mass spectrometer calibration coefficient of each mass. The subtraction of formaldehyde and dimethyl ether contribution to mass 31 gives the true methanol response in the mass spectrometer. Subsequently, the subtracted integrals are adjusted for sensitivity of the masses of other compound in the mass spectrometer.

Similarly, contribution of other masses to formaldehyde, dimethyl ether, carbon dioxide and carbon monoxide can be subtracted using same method.

2.5 BET Surface Area Measurement

The surface area is a significant physical parameter in surface science and catalysis. It is used in measuring activity of a catalyst. The BET Theory was first established in 1938 by Stephen Brunauer, Paul Hugh Emmett, and Edward Teller. This theory proposed a technique for determination of specific surface area based on multi-layer physisorption of gas molecules to establish a monolayer volume on solid surfaces at different pressure. This theory extends beyond a monolayer adsorption proposed by Langmuir as depicted in Fig. 2. 7. It hypothesized that gas molecules adsorbed non-selectively onto a solid surface at lower pressure than their vapour pressure by a weak force of interaction (van der Waals force) forming a multilayer. These adsorbed multilayer are believed to not interact amongst themselves [9].

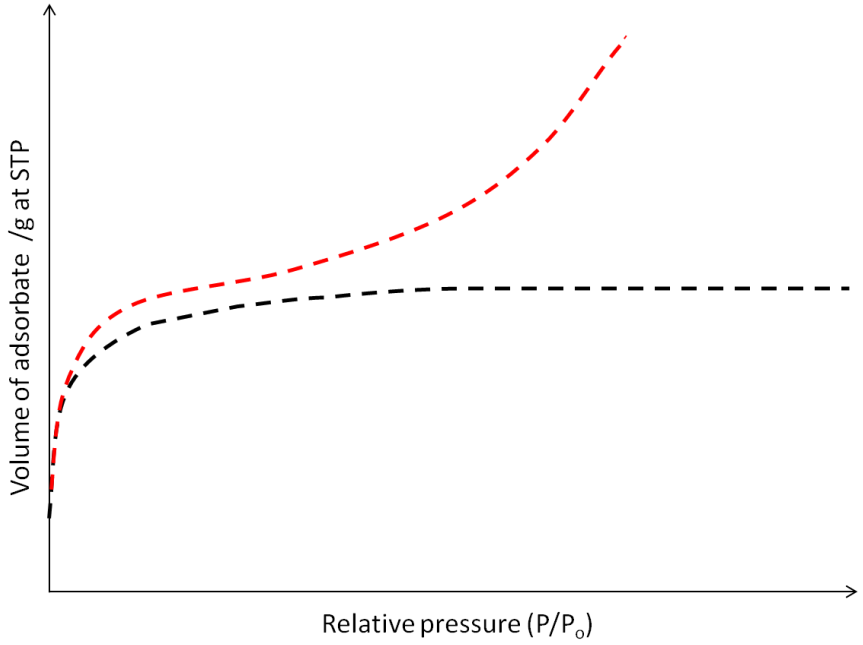

Fig. 2. 7 ***Isotherm profile (--- Langmuir isotherm, --- BET Isotherm)***

Fig 2.7 depicts Langmuir and BET adsorption isotherm, with the latter indicating multilayer absorption on catalyst surface. However, the BET equation expressed in equation 2.8 below indicates the relationship between pressure and volume of adsorbed molecules:

$$\frac{P}{V(Po-P)} = \frac{1}{VmC} + \ C - \frac{1}{VmC}\ \left(\frac{P}{Po}\right) \qquad \text{Equation 2.8}$$

Where P and Po are equilibrium and saturation pressure of the absorbate at different adsorption temperature respectively, V is the volume of adsorbate at standard temperature and pressure, Vm is the volume of adsorbate required to form a monolayer coverage, and C is the BET constant.

$$C = \ e^{(\Delta Hads - \Delta Hl)}/RT \qquad \text{Equation 2.9}$$

Where $\Delta Hads$ and ΔHl are heat of adsorption on the first layer and heat of adsorption (liquefaction) on the second or multi-layers respectively, R is the gas constant, and T is temperature in kelvin.

The plot of the $\frac{P}{V(Po-P)}$, against $\frac{P}{Po}$ gives a linear graph as seen in Fig. 2. 8 with a slope $C - \frac{1}{VmC}$ and intercept $\frac{1}{VmC}$.

The linearity of this plot is usually valid in the range of $\frac{P}{Po}$ value between 0.05 – 0.3

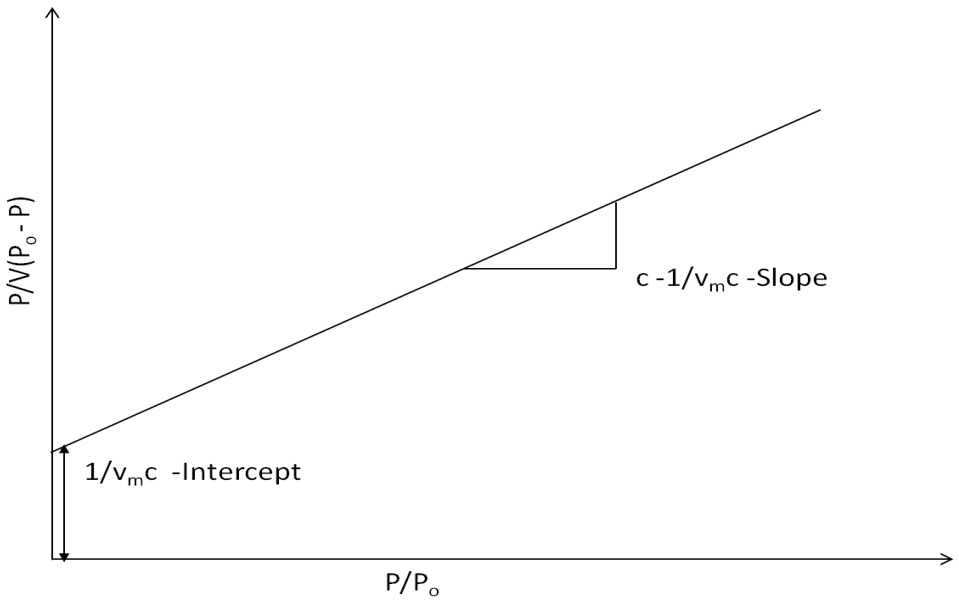

Fig. 2. 8 ***Diagram of a typical BET plot***

The value of Vm and C can be calculated from the value of the slope and intercept from the above plot using relationship in Equation 2.10 and 2.11.

$$Vm = \frac{1}{slope+intercept}$$ Equation 2.10

$$C = 1 + \frac{slope}{intercept}$$ Equation 2.11

Therefore, the Surface Area (SA) and Specific Surface Area (SSA) can be determined from equation 2.12 and 2.13 respectively:

$$\text{SA } (m^2) = Vm(m^3) \times \frac{N}{V} (\text{molecules}/m^3) \times A$$ Equation 2.12

$$\text{SSA}(m^2/g) = \frac{SA}{W}$$ Equation 2.13

Where N is the Avogadro's number, V and A are the molar volume and cross sectional area of adsorping gas species (usually nitrogen with A= 0.162 nm^2) respectively, while W is the weight of catalyst used [10].

The Micromeritics Gemini 2360 BET machine consists of two reservoirs filled with equal volume of adsorbate (usually nitrogen). The equipment was calibrated by metering the gas from the reservoir into an empty quartz sample and a balance tubes via a servo valve. The sample in the sample tube is weighed and degassed at 120 ^oC under a nitrogen flow for an hour to remove adsorbed moisture and impurities on its surface, then re-weighed after cooling to ascertain the actual weight of sample. The servo valve allows the flow of gas into the sample, and maintains a constant pressure equilibration during adsorption at liquid nitrogen temperature (77 K). A transducer placed between the tubes and the reservoirs measures the pressure difference between the sample and the balance tubes, which indicates the amount of adsorbed gas in the sample. These parameters are used in the determination of the surface area of the sample.

2.6 Raman Spectroscopy

Raman spectroscopy is a non-destructive and significant tool for studying molecular vibrations based on inelastic scattering of electromagnetic radiation.

Theory

This technique is based on the inelastic scattering of electromagnetic radiation due to its interaction with molecules, resulting in molecular vibration or rotational changes (Polarization). However, the excitation vibration of these molecules gives characteristic bands at specific frequencies range and intensities, which provides information on the molecular structure of materials [11]. The interaction of electromagnetic radiation of specific wavelength $h\upsilon_o$ within the ultraviolet, visible or near-infrared region with molecules, results in elastic and inelastic scattering. The former type of scattering is referred to as Rayleigh scattering, where there is no change in vibrational energy during the interaction of exciting radiation with the molecules, while the latter involves change in vibrational energy from Eo – E and is called Raman scattering. However, the Raman scattering further classified as stokes and anti – stokes. The Raman scattering is said to be stokes, when molecule gains energy and causes it to vibrate (υ_o - υ_{vib}), or anti-Stokes when it loses energy as it vibrates on same phase as the interacting photon (υ_o + υ_{vib}), as illustrated in Fig. 2. 9. The peak intensity of the Stokes signal is quite intense compared to the anti-Stokes [12].

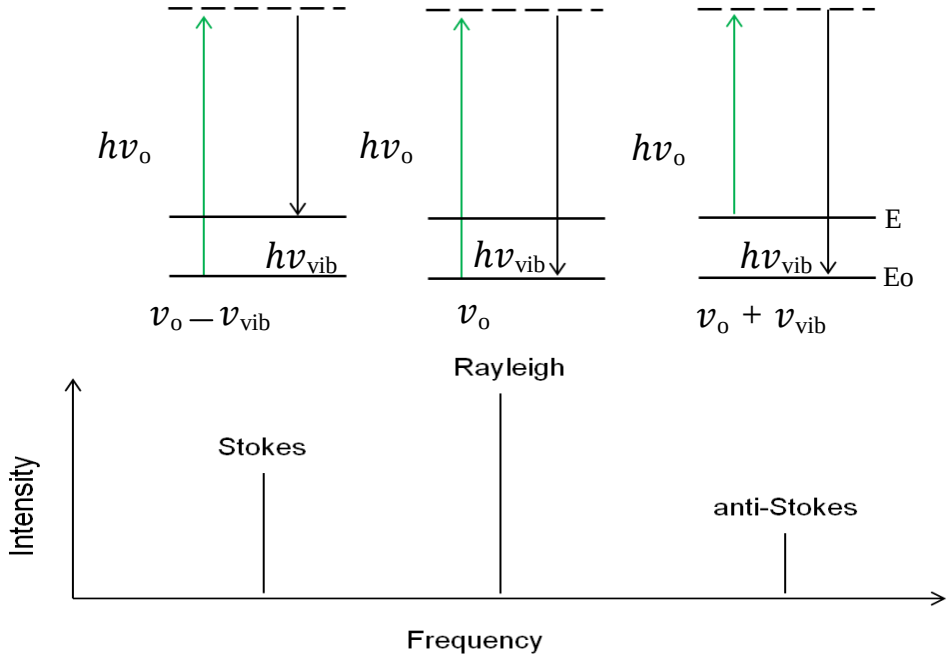

Fig. 2. 9 ***Diagram of elastic and inelastic scattering of light and energy changes***

Experimental

The phase determination was carried out using a RE 04 Via a Raman spectrometer produced by Renishaw, with an Ar^+ ion laser (λ-514 nm) and 785 nm laser source operating with the following parameters:

Laser average power of 25 mW , beam diameter - 0.65 mm, beam divergence - 0.95 mrad, beam point stability of < 30 μrad, and peak power of 50 mW.

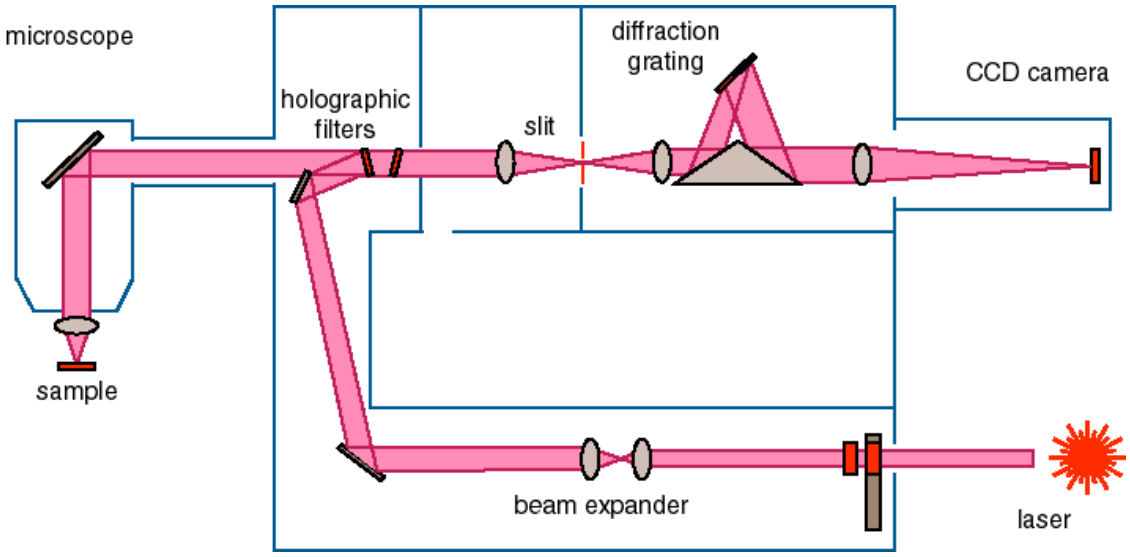

Fig. 2. 10 ***Diagram of a typical Raman spectrometer [13]***

The spectrometer was calibrated daily using a 514 nm or 785 nm silicon reference standard, which gives a single silicon peak at 520 cm^{-1}.

About 0.2 g of the sample was placed on aluminium slide, before loading onto the sample stage. The sample was brought to focus using the 20 – 50 x magnification lenses. The laser radiation passes through beam expander before focusing monochromatic beam on the sample with the help of lenses and diffracting gratings. The scattered light is collected by a lens, which is then passed through a holographic filter and diffracting grating before reaching a charge-coupled device (CCD) camera, which records the signal as shown in Fig. 2. 10. These signals are displayed as spectrum plots of intensity against wavelength displayed on a computer connected to the equipment. The spectral acquisitions were replicates from different points to give a true representation of the sample.

2.7 X-Ray Diffraction (XRD)

X-ray radiation was first discovered by a German Physicist Wilhelm Conrad Rontgen in 1894 [14], but its application as diffraction techniques by William Henry Bragg and his son William Lawrence Bragg in 1913, had led to a profound success in characterization of crystalline and amorphous structure of solid materials on atomic scale. It provides information on the dimension and phase, as well as crystallite size/strain from diffraction peak position, peak intensity, and peak broadening respectively [15].

Theory

The X-ray diffractometer consists of three basic components: X-ray tube, sample holder, and a detector. An X-ray is generated from the X-ray tube, where high-energy electrons from a tungsten filament (cathode) with high negative potential, hits an anode at ground state. This generates a lot of heat, and as such is constantly cooled by flowing water. This beam of rays from the anode is allowed to pass through a filter (nickel), which screens out the Kβ radiation from the Kα radiation. The Kα radiation (monochromatic beam) is focused on the sample by series of slits (divergent and anti-scatter). The incident photons diffract from the sample (Diffraction) and hit the detector placed at an angle from the incident radiation in a typical Bragg-Brentano geometry as in Fig. 2. 11. The signal from the detector translates into a defined diffraction pattern, which is usually a plot of intensity/count against diffraction angle (2 θ).

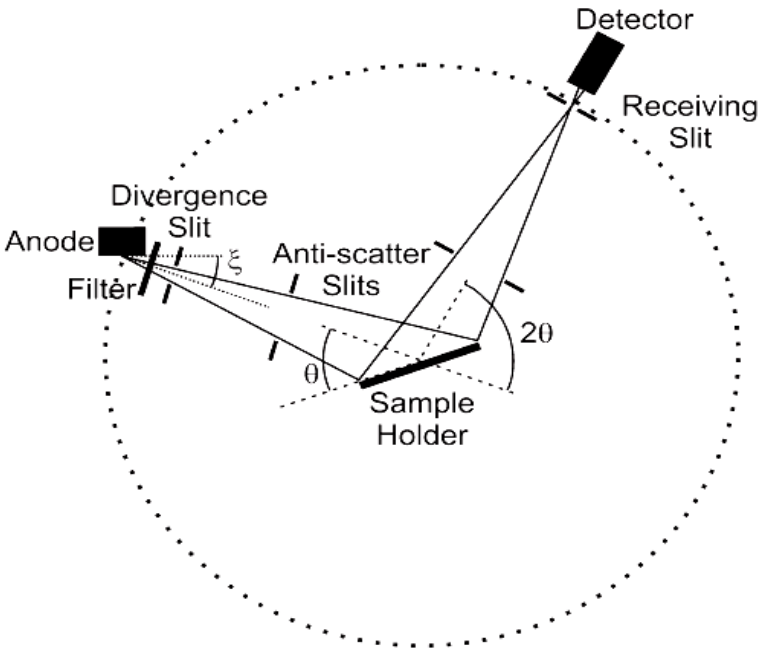

Fig. 2. 11 ***Bragg-Brentano geometry of an X-ray diffractometer [16]***

Experimental

The sample was ground to a fine powder of about ~50 μm particle size and homogenized by physical mixing to represent the entire catalyst bulk. About 0.2 g of the specimen was pressed and flattened on a sample holder. The analysis was conducted using an X'pert PRO diffractometer (Model: DY2759) manufactured by PAN analytical, using the following parameters and conditions: source slit- 0.04 mm, Ni filter (to separate Kα radiation from Kβ radiation), Cu Kα radiation source with λ = 1.5406 Å, current = 40 mA, and voltage = 40 kV. The analysis was conducted using the Batch sample method, with a run time of 45 minutes per sample.

Bragg developed the relation for scattering angle for diffraction called Bragg equation as illustrated in *Fig. 2. 12* and Equation 2.14

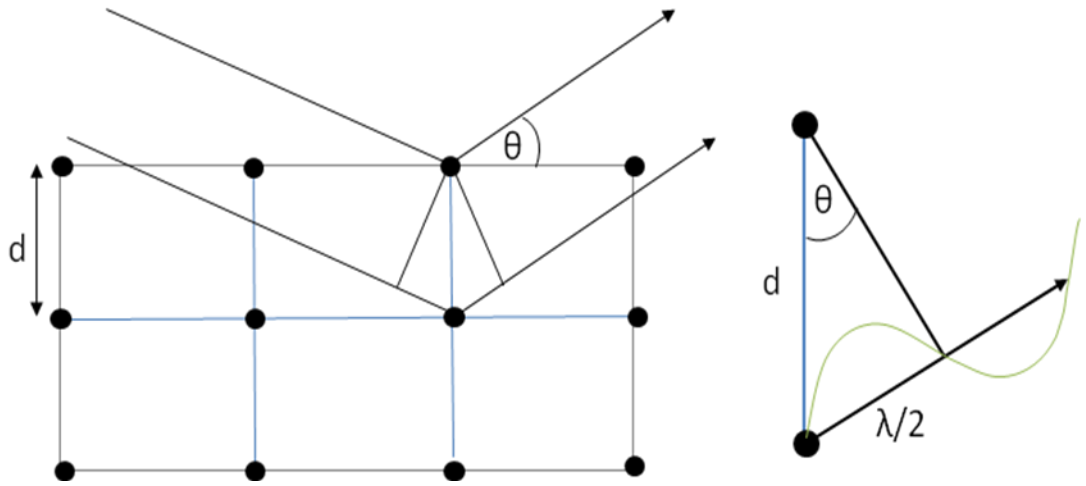

Fig. 2. 12 Simplified diagram for Bragg diffraction

$$n\lambda = 2d\sin\theta \qquad \text{Equation 2.14}$$

where d is the distance between the crystal planes, n is the number of diffraction layers, θ is the diffraction angle, while λ is the wavelength of the radiation. The distance between the crystal planes (d) in powder diffraction can be calculated using Bragg equation.

Peak position, phase identification, and d-spacing is determined by searching and matching acquired data with Powder Diffraction File (PDF) incorporated in International Centre for Diffraction Data (ICDD) software and literatures.

2.8 X-ray Photoelectron Spectroscopy (XPS)

It is also known as Electron Spectroscopy for Chemical Analysis (ESCA). This surface sensitive spectroscopic technique is used in quantitative analysis of elemental composition, valence, and chemical states of atoms on surfaces of materials.

Theory

The XPS consists of an X-ray source, electron transfer lens, electron energy analyser, and a detector enveloped in an ultrahigh vacuum system as depicted in Fig. 2. 13. A monochromatic X-ray source illuminates a specific area volume of the sample, which leads to emission of photoelectrons of define kinetic energy by a photoemission process. The resulting photoelectron passes through a series of electron transfer lenses,

which act as virtual probes that select an area of analysis. However, an objective lens collects and passes emitted photoelectrons into the retarding projector lens via an aperture. Electrons leaving a retarding lens are introduced into a hemispherical Sector analyser (HSA) consisting of outer and inner concentric hemispheres, which allows photoelectrons sorted based on their energies to reach the detector by varying the voltage between the hemispheres. The intensity of photoelectrons is plotted against their binding energies.

$$BE = h\upsilon - (K.E + \Phi) \qquad \text{Equation 2.15}$$

where BE is the binding energy in eV, $h\upsilon$ is the photon energy, KE the kinetic energy of the emitted photoelectron, and Φ is a combined spectrometer and sample work function that is instrument dependent.

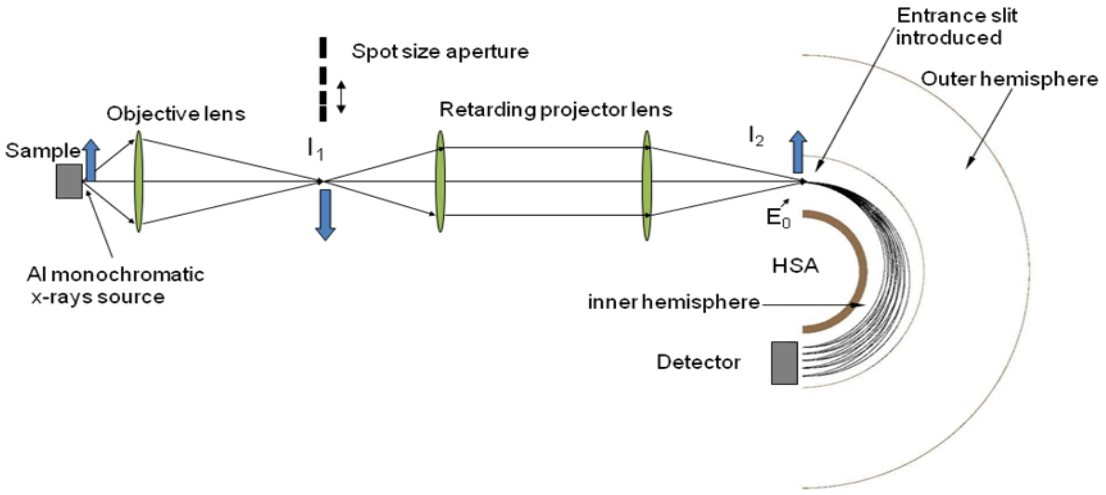

Fig. 2. 13 ***Schematic of a typical KRATOS XPS set up [17]***

Experimental

A Kratos Axis Ultra DLD system was used to collect XPS spectra using a monochromatic Al $K\alpha$ X-ray source, operating at 120 W. Data were collected in the Hybrid mode of operation, using a combination of magnetic and electrostatic lenses, and at pass energies of 40 and 160 eV for high resolution and survey spectra respectively. All spectra were taken at 90 ^{o} take off angle, while the base pressure was maintained at ~1×10^{-9} Torr. Magnetically confined charge compensation was used to minimize sample charging and the resulting spectra were calibrated to the C(1s) line at 284.5 eV.

The analysis was conducted by Dr. David Morgan XPS at Cardiff University.

2.9 Scanning Electron Microscopy – Energy Dispersive X-rays (SEM–EDX)

The SEM is used to study the surfaces of heterogeneous material of both organic and inorganic origin. Its capability of obtaining three-dimension-like images at nano meter (10^{-9} μ) size (up to 50 nm for the model used), has made it gain application in the wide field of research.

Theory

The SEM consists of two basic components: an electronic console and an electron column.

The electronic console comprises of two computers and a control panel connected to the detector, while the electron column consists of an electron gun, condenser lenses, scanning coil, sample stage and detector, which connect to a vacuum pump that evacuates the column to a pressure of $<10^{-6}$ torr for proper functioning of the electron gun. The electron gun emits a beam of high-energy (1-30 KV) electrons, which travel down the electron column via series of magnetic lenses designed to focus the electrons to a very fine spot. The scanning coil sweeps the beam back and forth across the surface of the specimen scanning in raster. The interaction of the electron beam with specific volume of specimen surface generates secondary electrons, backscattered electrons, characteristic X-ray, and photons of different energies, which hit the detector as depicted in Fig. 2. 14. The detector counts these electrons and sends the signal to an amplifier, which displays the resulting image on a computer screen [18].

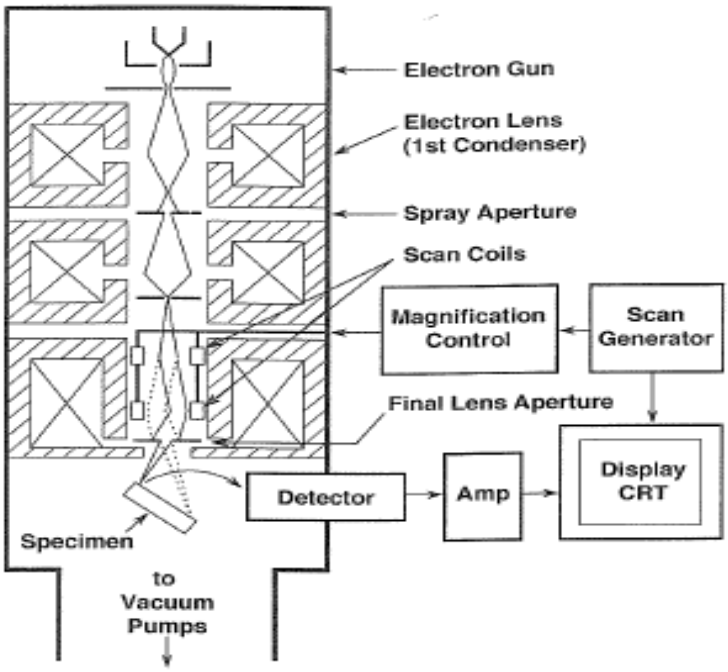

Fig. 2. 14 ***Typical set up of a Scanning electron microscope [18]***

The secondary and backscattered electrons provided information of surface topography, while the information from the energy dispersive X-ray is used for qualitative and quantitative determination of elemental composition.

Experimental

The analysis was conducted using an EVO40VP model Carl Zeiss scanning electron microscope. About 0.2 g of ground and homogenised sample was sprinkled over a carbon disc stuck onto an aluminium stub to achieve maximum surface coverage. The excess sample was tapped off the disc prior to attaching to the sample holder. However, the entire column is pumped down to attain a good vacuum ($<10^{-6}$ Torr) required for proper functioning of the SEM. The sample stage was placed at a working distance of about 8-10 mm. The electron gun emits an electron beam within a voltage range of 5-25 KV at an I-probe current of 1000 pA (1.0 nA), generating secondary and backscattered electrons for topographic analysis.

Meanwhile, the sample EDX analysis was carried out following calibration of the equipment using a cobalt standard via the INCA software installed on the operating system. This operates at an EHT voltage of 25 KeV and I-probe value of 10,000 to generate sufficient X-rays for a good statistical count to achieve quantitative elemental analysis.

2.10 Atomic Force Microscopy (AFM)

This is a non-destructive technique used to measure structure with high resolution, of the order of nanometre scale and accuracy by probing the sample surface using a sharp tip. Atomic force microscope (AFM) instrument was first developed in 1986 by Binnig, Quate, and Gerber [19].

Theory

The AFM comprises of three basic components: the microscope stage, control electronics, and computer. The microscope stage, which is the essential part of the AFM, is usually mounted on a vibration isolation stage to minimize noise. It consists of piezoelectric scanner/transducer, sample holder, optical lever sensor/transducer and a feedback control. The laser beam is focused onto the back of the cantilever, which reflects onto the photo detector. The piezoelectric scanner/ transducer moves the cantilever tip over the sample surface. The interaction between the tip and the surface causes a small displacement of the laser path, which is amplified by the optical lever sensor to create a large displacement (as a measure of force) on the photo detector as shown in Fig. 2. 15. The electronic control receives the signal via the feedback control, which is then displayed as an image on the computer.

Modes of operation

AFM has three basic operational modes: contact, non – contact, and tapping modes [20].

Contact mode: this mode measures topography of sample by sliding the cantilever probe tip across the surface. The interaction between forces (electrostatic, magnetic or friction) on the surface and the tip causes the tip to snap, which leads to deflection of the laser beam. The deflected laser beam falls onto a photo detector, which converts it into electric signals (measured in volts); these signals are then translated as image. The major drawback of the mode is damage caused to either the sample or the tip.

Non – contact mode: this mode measures surface topography by sensing interaction between attractive surface van der waals forces and probe tip, which causes deflection of the laser beam on to a photodetector. However, this operational mode provides less resolution compared to the other two modes.

Tapping mode: this operational mode uses a vibrational cantilever tip, which oscillates vertically to measure surface topography of sample. The interaction between the tip and the surface causes change in the initial laser deflection pattern by the tip. The deflected laser beam falls onto a photo detector, converting sinusoidal electric signal to voltage.

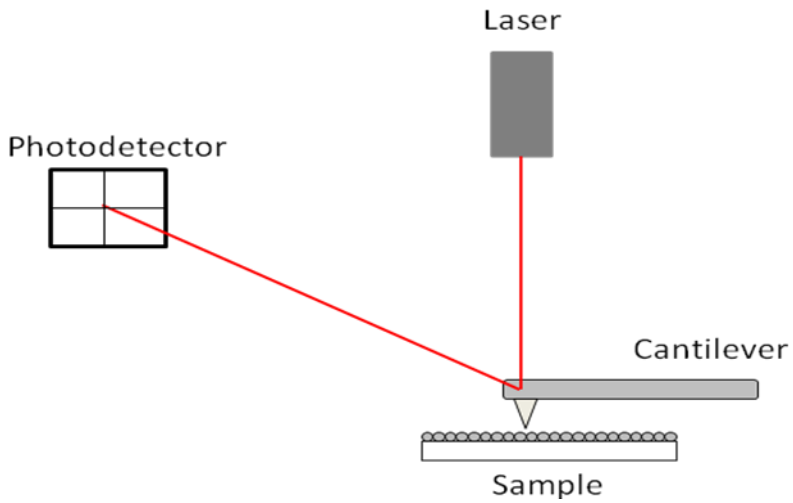

Fig. 2. 15 ***Schematic of an optical lever sensor of AFM***

Experimental

The sample was placed on a metal disk using a double-sided sticky dot before mounting on the scanner stage of Multimode TM AFM 2026EX series manufactured by Veeco Ltd. The metal disk is held tightly onto the stage by a magnetic force. The mounting probe fitted with a cantilever was placed and tightened on the stage, with the cantilever tip brought close to the sample surface (about 2 mm) using a toggle switch located below the scanner tube. The optical and laser light were focused on the sample with laser beam aligned on the cantilever to obtain maximum signal on the liquid crystal display (LCD) meter, which signifies the laser reflection onto the photodiode cavity. The photo detector signal was aligned by adjusting the vertical and horizontal difference to about zero (between -0.5 – 0.5 V), prior to auto-tuning of the cantilever, to achieve a good resonance peak on the amplitude graph displayed on the screen. The analysis was conducted using tapping mode with the following parameters: Scan size – 1 µm, Scan rate – 2Hz, Sample/line resolution 256 pixels, Drive amplitude – 50 mV at a slow scan rate. Integral/Proportional gain are varied between 0.4 – 4.

2.11 Light Microscopy

Theory

A light (optical) microscopy operates using series of lenses. Firstly, an objective lens close to the object collects light, which focuses the actual image of the object inside the microscope. The image is then magnified by a series or group of magnifying lenses called the eyepiece, which gives an enlarged virtual image of the object. However, the use of Charge-couple device (CCD) camera allows image to be captured and stored in a computer.

Experimental

The model catalyst comprising of MoO_3 or $Fe_2(MoO_4)_3$ thin film on an alumina (0001) single crystal were viewed under Olympus BX50 light microscope using 20 x magnification lenses.

References

1. Schwarz JA, Contescu C, Contescu A. Methods for preparation of catalytic materials. Chem Rev. 1995;95(3):477-510.
2. Hill Jr CG, Wilson III J H. Raman spectroscopy of iron molybdate catalyst systems: Part I. Preparation of unsupported catalysts. Journal of molecular catalysis. 1990;63(1):65-94.
3. House PM. Selective oxidation of methanol over iron molybdate catalyst [PhD Thesis]. Cardiff: Cardiff University; 2007.
4. Mul G, Moulijn JA. Preparation of supported metal catalysts. Catal Sci Series. 2005;5:1-32.
5. Isochema-HidenAnalytical. QIC fast sampling capillary inlet user manual. England: 2004 Contract No.: HA-085-027.
6. CATLAB. An integrated microreactor– mass spectrometer for catalyst characterisation and Evaluation [Internet]. [cited 20/04/12]. Available from: http://www.iestechsales.com/Portals/63951/docs/pp700_catlab.pdf.
7. Isochema-HidenAnalytical. QIC-20 Gas analysis system user manual. England: 2005 Contract No.: HA-085-073.
8. Isochema-HidenAnalytical. CATLAB user manual. England: 2005 Contract No.: HA-085-083.
9. Condon JB. Surface area and porosity determinations by physisorption: measurements and theory. Netherlands: Elsevier; 2006.
10. Bowker M. The basis and application of heterogeneous catalysis. Oxford: Oxford University Press; 1998.
11. Schrader B, editor. Infrared and Raman spectroscopy; methods and applications. Weinheim, Germany: Wiley-VCH Verlag GmbH; 1995.
12. Davydov A. Molecular spectroscopy of oxide catalyst surfaces. England: John Wiley & Sons Ltd; 2003. 690 p.
13. Appl_of_Raman_Spectroscopy [Internet]. [cited 20/04/2012]. Available from: www.ccmr.cornell.edu/igert/modular/.../Appl_of_Raman_Spectroscopy..
14. Novelline R. Squires's Fundamentals of Radiology. 5th ed: Harvard University Press; 1997. 638 p.
15. Suryanarayana C, Grant Norton M. X-Ray Diffraction: A practical approach. 1st ed. New York: Springer Science+Business Media; 1998. 3-18 p.
16. Jeremy KC, Andrew N F. Experimentl Setup. In: Robert ED, and Simon JL B, editor. Powder Diffraction Theory and Practice. United Kingdom: RSC Publishing; 2008. p. 34.
17. New AXIS Ultra DLD; Small spot, parallel imaging multi-technicque photoelectron spectrometer [Internet]. 2010 [cited 29/03/2014]. Available from: http://www.docstoc.com/docs/56805521/AXIS-Instruments.
18. Goldstein JI, New bury D, Joy DC, Lyman C E, Echlin P, Lifshin E. Scanning electron microscopy and X-ray microanalysis. 3rd ed. New York: Kluwer Academic/Plenum Publishers; 2003. 675 p.
19. Eaton P, West P. Atomic force microscopy. New York: Oxford University Press; 2010.
20. Veeco. Multimode SPM instrument manual. 2004 Contract No.: 004-210-000 and 004-210-100.

Chapter 3 Methanol oxidation on unsupported molybdenum oxide based Catalysts

Contents

3.1 Introduction and Literature Review:

This first result chapter is aimed at studying specific unsupported molybdenum oxide based catalysts; single oxides, promoted catalysts, as well as mixed oxides catalysts used in selective oxidation of methanol to formaldehyde.

The chapter covers characterization and reaction measurements on iron oxide (Fe_2O_3), and various molybdenum oxide based catalysts ranging from unsupported molybdenum trioxides (MoO_3) to potassium (K) promoted molybdenum oxides and ferric molybdates ($Fe_2(MoO_4)_3$). This will focus particular interest in understanding structural sensitivity, effects of promoter and synergic effects between multiphases in mixed oxide catalysts with respect to activity, selectivity, and mechanism during methanol oxidation to formaldehyde.

Iron (III) oxides (Fe_2O_3)

This is one of the readily available compounds of iron on earth, formed naturally from weathering of magmatic rocks or synthesised from iron hydroxide (FeOOH) precursors [1]. It exists in four different structural forms as haematite (α-Fe_2O_3), maghemite (γ-Fe_2O_3), β-Fe_2O_3 and ε-Fe_2O_3, the last two compounds being rare can be obtained through synthetic routes in the laboratory [1].

Haematite (α-Fe_2O_3) is the most thermodynamically stable form of iron (III) oxide with a structure similar to corundum (α-Al_2O_3) and chromia (α-Cr_2O_3). It comprises of hexagonal unit cell belonging to R-3c group with lattice parameter of a = 5.034 Å, and b = 13.75 Å. It consists of hexagonal close packing (hcp) oxygen atoms arranged along (001) plane, with about two- third of these sites occupied by iron in Fe^{3+} state. The structural arrangement involves two iron atoms stacked in regular pattern preceding a vacant site along (001) plane forming six-fold rings. The cation arrangement results in formation of FeO_6 octahedral structure, with each octahedron involved in edge sharing with three neighbouring octahedra on (001) plane and a face sharing with an octahedron adjacent to (001) plane as in Fig. 3. 1below [1].

However, maghemite (γ-Fe_2O_3) is isostructural with magnetite (Fe_3O_4). It has a cubic unit cell with a = 8.34 Å, consisting of thirty two anion (O^{2-}) sites, eight cations occupying the tetrahedral sites with the remaining sixteen cations randomly distributed into the octahedral sites having two vacant sites, indexed as F_{d3m} space group. It

differs from magnetite by possessing iron only in the Fe^{3+} state and lattice vacancies, which are responsible for its ferromagnetic property [1]. Amongst the different forms of Fe_2O_3, promoted haematite (α-Fe_2O_3/K_2O, α-$Fe_2O_3/SiO_2/K_2O$) has found wide application in catalysis: as catalysts in selective dehydrogenation of ethyl benzene to styrene, Fischer–Tropsch synthesis (reduced to magnetite) or used as starting material in catalyst synthesis such as iron molybdates ($Fe_2(MoO_4)_3$) and iron vanadates ($FeVO_4$) for selective oxidation of methanol to formaldehyde [1]. γ-Fe_2O_3 has recently attracted attention as both a sorbent and photo catalyst in waste water treatment [2].

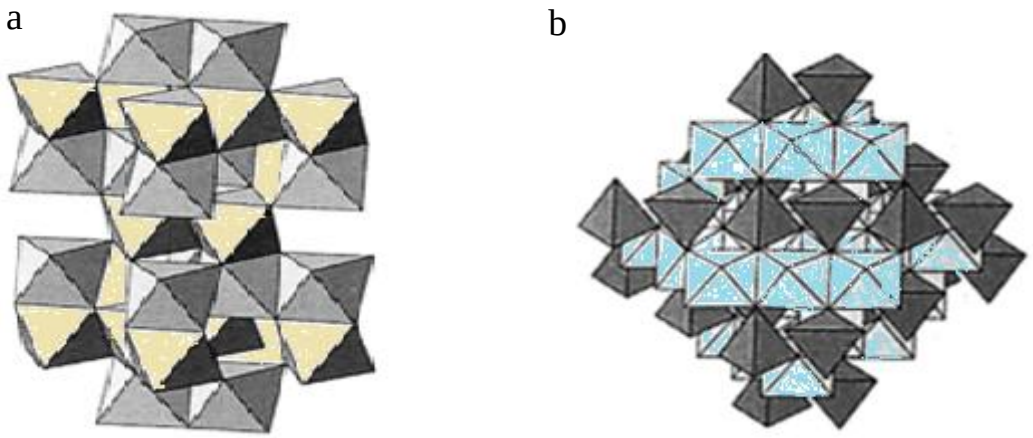

Fig. 3. 1 ***Structure of (a) Haematite, (b) and Maghemite [1]***

Molybdenum oxides

Molybdenum oxide catalysts play versatile roles as metal oxide catalysts in selective oxidation catalysis of alkenes, alkanes, and alcohols to aldehydes and other organic intermediates of immense industrial importance. Their varying oxidation state, structure-sensitivity and chemical environment is widely explored in catalysing different acid-base processes which includes: redox, addition or decomposition, and isomerisation reactions reported by Vedrine et al [3], Harber and Lalik [4], and Grasselli [5] respectively.

Molybdenum trioxide (MoO_3)

Molybdenum trioxide (MoO_3) belongs to the space group P_{bmn} with lattice parameter of a = 3.628 Å, b = 13.855 Å, and c = 3.6964 Å. It exists in two basic forms; an alpha (α) and beta (β) molybdenum trioxide (MoO_3). The α-MoO_3 is the most thermodynamically stable phase, whereas the β-MoO_3 phase is metastable. The α-MoO_3 consists of MoO_6 octahedral unit stacked in bi-layers sharing corners and edges along a, b, c axis; each MoO_6 unit has molybdenum (Mo) bonded to six oxygen atoms forming a distorted octahedral structure as shown in Fig. 3. 2 below. The α-MoO_3 bulk consists of three basic oxygen-bonding types. These include terminal oxygen (O_t) bonding with one Mo atom at 1.67 Å, bridging asymmetric oxygen (O_a) bonded to two Mo atoms at 1.73 Å and 2.25 Å. The third bridging symmetric oxygen (O_s) bonding involving O_s bonded to two Mo atoms on the same layer at 1.94 Å and a third Mo from a second layer beneath at 2.33 Å [6] as shown in Fig. 3. 3.

However, oxygen defects in the bulk α-MoO_3 structure results in a slight change in its structure as compared to perfect α-MoO_3 depicted in Fig. 3. 3 b. The introduction of terminal oxygen vacancies shorten the asymmetric oxygen bond lengths to 1.70 Å and 1.81 Å, with the former taking the place of the terminal oxygen by shifting from an angle of 94.8 ^{o} to 37.4 ^{o} as observed using a DFT+U calculation by Coquet and Willock [7]. The β-MoO_3 has a ReO_3 – like structure consisting mainly of MoO_6 octahedral units involved in corner sharing.

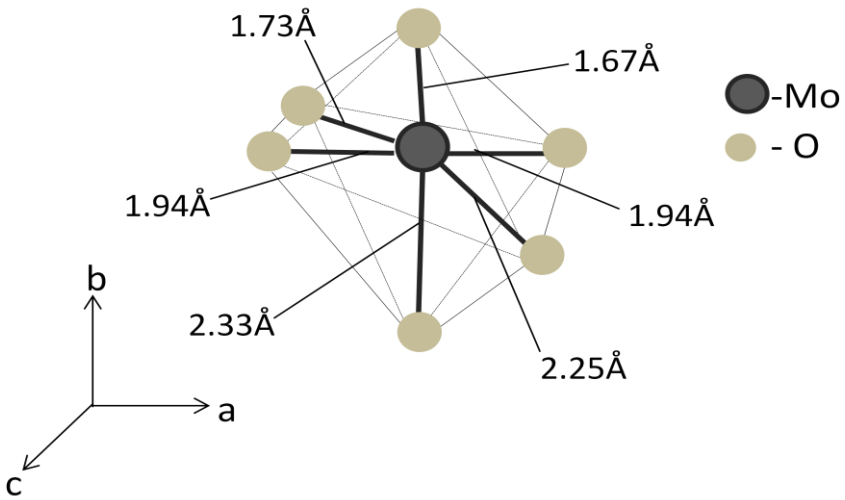

Fig. 3. 2 ***Structure of MoO_6 distorted octahedral unit***

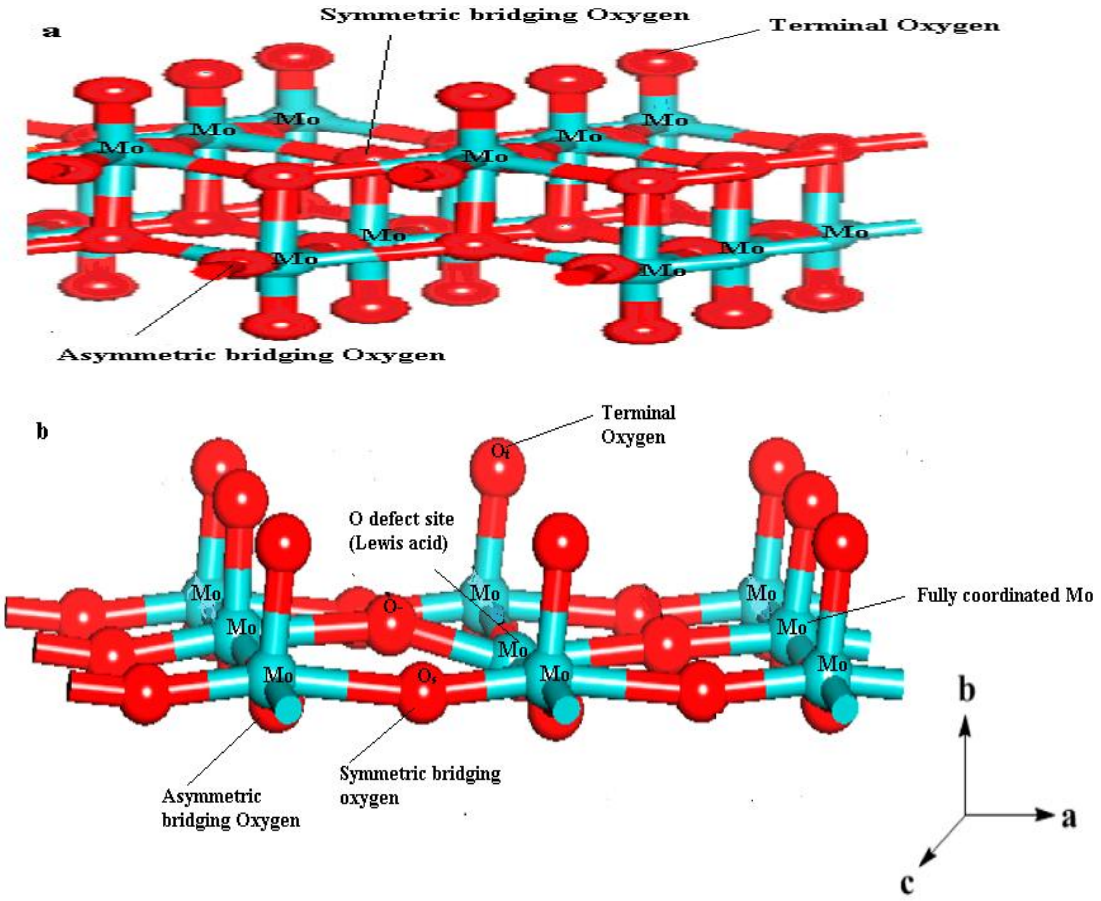

Fig. 3. 3 ***Structure of (a) α-MoO_3 (b) and oxygen defect in α-MoO_3 [8]***

A methanol oxidation study over molybdenum trioxide (MoO_3) conducted by Tatibouet and Germain revealed the structure – sensitivity of the catalyst, with the orthorhombic being selective (formaldehyde) but less active while the hexagonal phase being less selective but active, but only selective to dehydration product (dimethyl ether) at low temperature [9]. They inferred that the percentage of different exposed crystal planes: base (010), side (100), and apical surface (001 and 110) led to formation of formaldehyde and dimethyl ether respectively. Abon et al [10], held a slightly different view, that the active phase (100) is actually truncated to a more stable (012) phase (step atomic structure), which is juxtaposed between (100) and (010) phases. They conclude that the (012) faces of MoO_3 consist of mild acidic sites with molybdenum (Mo^{6+}, Mo^{5+}) sites at the Mo=O terminal oxygen. A recent review by Vedrine [11] infers that (101) and (001) plane on MoO_3 also bare both redox and

Lewis acid sites, which expose oxygen ions that act as both Lewis base and electron donor enhancing molecular adsorption and dissociation of oxygen.

However, isotopic labelling [12], in-situ infra-red [13], temperature programmed desorption (TPD), temperature programmed reaction, and reduction/microbalance reactor studies [12-14] of methanol oxidation to formaldehyde over MoO_3, is accepted to occur via dissociative chemisorption of the methoxy group on a partially oxidized molybdenum site (oxygen vacancies) and hydroxyl group (from α-hydrogen abstraction by the Mo=O site). The existence of the methoxy group as the main intermediate species for formaldehyde production is established, with further abstraction of a β-hydrogen from the surface methoxy group reported by Chung et al [15], Sleight et al [12], and Machiels et al [13], to be the rate-limiting step in formaldehyde production. Ab-initio quantum chemical calculations conducted by Allison and Goddard [16] suggested the presence of dual adjacent surface di-oxo sites are responsible for the activation and abstraction of H from methanol. Although Sleight et al [12] accepted the function of di-oxo site for hydrogen abstraction, Sleight et al [12] and Gai-Boyes [17] argued that the unsaturated molybdenum (under-coordinated) sites are the possible sites for methanol activation and selective oxidation on the MoO_3 catalyst [17].

Furthermore, X-ray diffraction analysis (XRD) and atomic force microscopic (AFM) studies of MoO_3 reported by Smith and Rohrer [18], indicated the occurrence of pits due to formation and sublimation of molybdenum oxy-hydroxides ($MoO_2(OH)_2$). This happens at the catalyst surface during calcinations (in the presence of water vapour), or reaction with alcohols between 300 – 400 ^oC. The pit formation is aided by an elastic strain along a defect, which increases the amount of side plane (h0l), as such bringing the side and basal planes into close proximity. This effect leads to formation of oxygen vacancies and crystallographic shear planes along (001) axis, which intersect the surface to form steps [18]. The step defect formation is believed to increase catalytic activity of MoO_3 by creating a new atomic co-ordination environment (leading to MoO_6 corner sharing), enhancing oxygen ion diffusivity, and increases electronic conductivity [18-20] . More so, Smith and Rohrer [21] argue that the lack of pit formation in MoO_3 basal plane (010) at temperature below 300 ^oC could relate to its catalytic inactivity during methanol oxidation.

An infra red/reactor study conducted by Cheng [22], unravelled competitive adsorption of water, methanol and formaldehyde on the same catalytic site on MoO_3 during the methanol oxidation reaction. The authors inferred that high selectivity to formaldehyde during methanol selective oxidation was due to water, a reaction product, which retards further oxidation of the formaldehyde to carbon oxides.

TPD study of methanol oxidation on MoO_3 indicated that it proceeds via the Mars-van Krevelen mechanism, which involves lattice oxygen exchange between bulk catalyst and its surface that is replenished by gaseous oxygen [3, 12]. The significance of the lattice oxygen: Mo=O terminal and Mo-O-Mo bridge vacancies in directing product selectivity to varying products during methanol oxidation was reported in a mechanistic in-situ infra red study conducted by Chung et al [15]. They revealed that Mo=O terminal vacancy sites are responsible for formaldehyde and carbon oxide production, while high-order products, dimethoxymethane (DMM) and dimethyl ether (DME), are produced on Mo-O-Mo bridge vacancy. They highlighted the effect of the electronic and geometric properties of MoO_3 catalyst on product distribution. Hence, oxidised vacancy sites result in weak carbon-oxygen (C-O-) bond interaction (electrophilic) between chemisorbed methoxy group and Mo^{6+} sites, but strong carbon-hydrogen (nucleophilic) bonding ($C\text{-}H_3$), while reduced vacancy Mo^{4+} sites foster strong carbon-oxygen (C-O-) bonding but weak carbon-hydrogen bonding ($C\text{-}H_3$). A temperature programmed reduction study on MoO_3 using methanol reported by Chung et al [15], and on hydrogen reported by Smith and Ozkan [23], indicated that Mo-O-Mo are more easily reduced as well as oxidised compared to Mo=O, as such resulting in shear plane formation as well as reduction of the molybdenum surface from +6 to +4 states. Haber and Ressler et al [4, 24, 25], reported that this change in oxidation state of MoO_3 from Mo^{6+} to MoO^{4+} occurs on the surface of the catalyst, at about 320 ^oC. However, an in-situ neutron powder diffraction (NPD) analysis conducted by Lalik et al [26] revealed that the mechanism of MoO_3 reduction to MoO_2 at 550 ^oC occurs via formation of an oxygen defect Mo_4O_{11}.

A contrasting behaviour of the molybdenum oxides Mo^{6+} and Mo^{4+} valence states in methanol oxidation conducted by Bowker et al [27] revealed that the Mo^{6+} state of the catalyst is highly selective to formaldehyde, while the reduced Mo^{4+} is the active site for CO production in aerobic condition and vice versa in anaerobic condition. They

demonstrated a complete independence between molybdenum oxidation state and methanol conversion, and attributed high activity of Mo^{4+} over Mo^{6+} to a surface area effect [27]. However, an in-situ Raman spectroscopic study of MoO_3 conducted by Mestl [28] explains the significant role played by MoO_3 defects (oxygen vacancy) in promoting oxygen exchange between gas phase and catalyst bulk.

Recently, Mizushima et al [29, 30] reported a comparative study of methanol oxidation over α- MoO_3 and β-MoO_3. They revealed that β-MoO_3 showed a higher catalytic conversion of methanol compared to α- MoO_3, with a drastic decline in methanol conversion at 623 K. They attributed this effect to the phase transition of β-MoO_3 to α-MoO_3, which enhances heat generation during methanol oxidation. Infra red (IR) study of chemisorbed pyridine on both catalysts indicates that the high catalytic activity of β-MoO_3 is due to the presence of a large number of Lewis acid sites.

However, oxygen defects on a bulk α-MoO_3 structure have recently been a focus point for density functional theory (DFT) simulation study. A recent DFT and DFT+U modelling studies conducted by Hermann et al [31], Tokarz-Sobieraj et al [32], Chen et al [33], and Coquet and Willock [7], proposed that the oxygen vacancy occurred on terminal oxygen. An X-ray spectroscopic and DFT + U study by Cavalleri et al [34] and Coquet and Willock [7] proposed that the creation of terminal oxygen vacancies results in a decrease in bond length, due to the orientation of the asymmetric oxygen to 45 ^{o} and 37.4 ^{o} from the 94.8 ^{o} position of the terminal oxygen. Furthermore, Coquet and Willock [7] suggest the adsorption of molecular oxygen on the terminal vacancy in a parallel configuration aligned along the asymmetric and symmetric oxygen site, resulting in formation of weakly adsorbed electrophilic oxygen species (O_2^- and O_2^{2-}) coordinated to Mo^{5+} and Mo^{6+}. The implication of such electrophilic-like oxygen species (O^-) have continuously been invoked by Bielanski and Haber [35], Panov et al [36], Zhao and Wachs [37], Wachs and Roberts [38], and Carley et al [39] to be the catalytic active species, which partakes in selective oxidation on metal oxides surfaces at low temperature. However, there were no reports investigating the participation of such oxygen species during selective oxidation of methanol on defective MoO_3.

K- Promoted MoO_3

Doping of bulk MoO_3 surface with alkali metal or metal promoters of less cationic charge than Mo^{6+} has profound effects on the physico-chemical properties of the catalyst. The application of promoter results in major modifications of structural and electronic properties of metal oxide, which was considered to be concentration dependent by Bowker [40]. However, a survey on the effect of alkali promoters on metal oxides by Grzybowska-Swierkosz [41] revealed that lower concentration of promoters (< 0.01 atomic %) modifies chiefly the electronic property of the catalyst by reducing surface acidity, substituting cationic/anionic vacancies, enhancing electron and oxygen transfer on interstitial or sub lattice of metal oxide. At higher alkali concentration, it results in formation of a new phase, which stabilizes the bulk or enhances synergic effect between the different phases.

Oxidative dehydrogenation of propene over alkaline promoted MoO_3/ZrO_2 reported by Chen et al [42] revealed a relationship between alkaline basicity and activity/selectivity, with activity decreasing/selectivity increasing with strength of alkaline basicity. However, Klinsin'ka et al [43] reported an increase in propene selectivity due to K promotion on V_2O_5/SiO_2 catalyst in comparison to transition metal promoters, used in oxidative dehydrogenation of propane. They reported a decline in activity, which they ascribed to blockage of active site by K. More so, the authors conclude that CO is a main by product of consecutive oxidation of propane. Similarly, enhancement in selectivity to acrylic acid during oxidation of propane over K-promoted Mo-V-Sb mixed oxides was reported by Botella et al [44], with maximum selectivity observed for 0.005 atomic weight % K loading, which declined with increasing K concentration.

Moreover, despite neutralizing acidic sites, decreasing reducibility of cationic sites and enhancement of electron transfer on metal oxide surface, K doping mediates the adsorption and dissociation of gas phase oxygen on the catalyst surface. A TPD and steady state reaction study of transient isotopic labelling oxygen for methane coupling over alkali promoted molybdates ($MnMoO_4$) reported by Driscoll et al [45, 46] revealed easy pathway for dissociative adsorption of gas phase oxygen on $MnMoO_4$, which is influenced by K-promotion. This indicates that K controls mobility and exchange of gas phase oxygen with the catalyst surface or sub surface lattice. A similar

observation was reported by Zhoa et al [47] to promote complete oxidation of diesel soot over V_2O_5/SiO_2. Despite many studies on K-promotion on molybdates and other supported oxides, little attention has been paid on the effect of K doping on oxygen vacancies on bulk MoO_3 surface.

Ferric molybdates ($Fe_2(MoO_4)_3$) catalysts

Monoclinic $Fe_2(MoO_4)_3$ crystal is indexed in the P_{21} space group with lattice parameters of: a = 15.693 Å, b = 9.235 Å, c = 18.218 Å, β = 125.21 ^{o}. It consists of eight crystalloghraphically distinct Fe atoms, each coordinated by six oxygen atoms with an average distance of 1.756 Å; each of the twelve Mo atoms form distorted tetrahedral bonding with oxygen at an average Mo – O distance of 1.756 Å. Each FeO_6 octahedron is linked to a MoO_4 tetrahedron via an oxygen bond, forming an open structure with the closest Fe-Fe distance of 5.03 Å [48]. The structure of $Fe_2(MoO_4)_3$ is depicted in Fig. 3. 4 below:

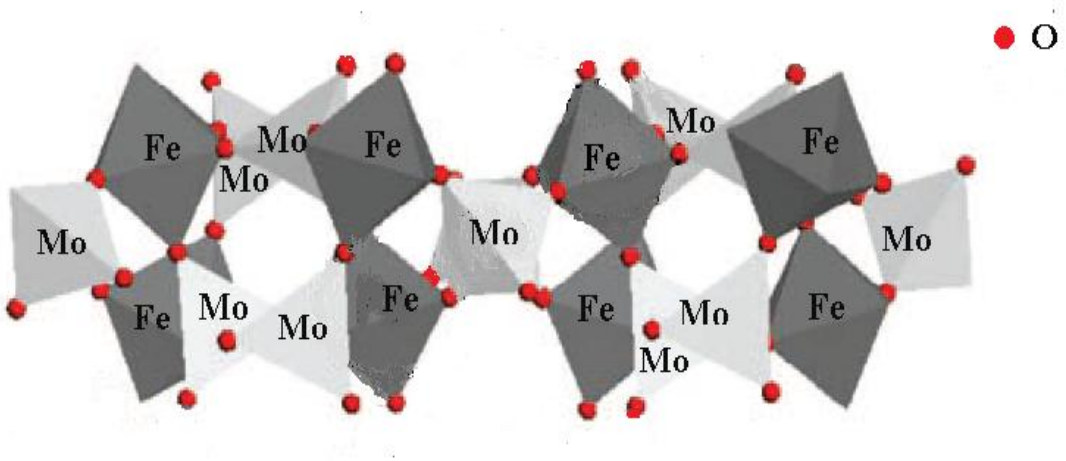

Fig. 3. 4 ***Structural representation of iron molybdate ($Fe_2(MoO_4)_3$) [49]***

Ferric molybdate mixed oxide catalysts and silver are the two major industrial routes for formaldehyde synthesis from methanol. The former is based on oxidative dehydrogenation of methanol over $Fe_2(MoO_4)_3$ Hader et al [50], while the latter is based on dehydrogenation of methanol-rich air mixture using silver catalyst as reported by Qiam et al [51].

A pioneering study of methanol oxidation over $Fe_2(MoO_4)_3$ and MoO_3 in 1931 by Adkins and Peterson [52] attracted much attention towards investigating preparatory

techniques and activity of the mixed metal oxide catalyst. Ferric molybdates are prepared using different techniques which include: co precipitation as reported by Adkins and Peterson [52], Sou-Kou et al [53], Soares et al [54], and House et al [55]; thermal spreading as reported by Haung et al [56] and wet-mixing as reported by Li et al [57]. Other techniques include: sol-gel preparation as reported by Soares et al [58], hydrothermal synthesis as reported by Beale et al [59], and incipient wetness impregnation as reported by Bowker et al [60] and Brookes et al [61], with iron and molybdenum observed in their highest oxidation state of Fe^{3+} and Mo^{6+} respectively. The evolution of the $Fe_2(MoO_4)_3$ phase begins between 250 – 400 ^oC, with segregation of MoO_3 over bulk $Fe_2(MoO_4)_3$ recorded above 400 ^oC, usually influenced by increasing Mo loading. Moreover, wet-mixing and sol-gel catalysts synthesized by Li et al [57] and Soares et al [58] respectively, exhibit better thermal stability with good reaction reproducibility than co-precipitation and thermal spreading catalysts. However, the co-precipitation and incipient wetness impregnation catalysts reveals higher activity and selectivity to formaldehyde as observed by Bowker's group [55, 61].

The nature of active phase in $Fe_2(MoO_4)_3$ catalyst remains a long-standing debate in the field of catalysis, material science and surface sciences, with an early XPS (X-ray photoemission spectroscopy) study conducted by Okamoto et al [62] revealing bulk $Fe_2(MoO_4)_3$ with excess Mo (1.7 ratio) as the active phase. They proposed that the excess Mo dispersed on defective Fe – O – Mo sites, which promotes electron transfer and enhances activity. Although the concept was accepted by Sun-Kou et al [53], they proposed that the active phase consists of > 1.7 Mo ratio . A comprehensive review reported by Soares and Farinha-Portela [63], concluded the active phase to be stoichiometric phase (1.5) with excess Mo required to prevent exposure of Fe-rich site during volatilization of Mo throughout the reaction. However, a scanning transmission electron microscopy (STEM) study reported by House et al [64] revealed that the $Fe_2(MoO_4)_3$ surface was dominated by Mo, while ultra-violet (UV) Raman, scanning electron microscopy (SEM) and XPS study reported by Xu et al [49] indicated the coordinative nature of the surface Mo species. The authors proposed that at ≤ 1.5 Mo ratios, Mo are in tetrahedral coordination; at ≥ 1.5, they remain in octahedral coordination on the surface. A recent high resolution transmission electron

microscopy (HRTEM) study reported by Soderhjelm et al [65] revealed the amorphous MoOx on bulk $Fe_2(MoO_4)_3$ as the active phase. They proposed a synergic effect between excess Mo and $Fe_2(MoO_4)_3$ phase, with the excess Mo required to maintain both activity and formaldehyde selectivity during methanol oxidation. In a HRTEM, low-energy ion scattering (LEIS) and methanol-temperature programmed surface reaction (CH_3OH-TPSR) study reported by Routray et al [66], and Wachs and Routray [67] , the authors disputed the existence of a synergic effect between crystalline MoO_3 and bulk $Fe_2(MoO_4)_3$, since both stoichiometric and Mo excess $Fe_2(MoO_4)_3$ reveal similar catalytic activity. However, they confirmed the amorphous MoOx monolayer on crystalline $Fe_2(MoO_4)_3$ bulk as the active phase, and concluded that the crystalline excess MoO_3 phase on the bulk $Fe_2(MoO_4)_3$ serves as a reservoir, which furnishes the FeOx with amorphous MoOx to maintain the activity and replenish the volatile Mo species during reaction.

Furthermore, temperature programmed reaction study in a pulsed flow reactor by Bowker's group [55, 60, 61, 68] revealed correlation between increasing formaldehyde selectivity with increasing Mo loading in both co precipitated and impregnated catalysts, with maximum selectivity > 90 % at 90 % conversion recorded for 2.2 Mo ratio. However, they attributed the decline in formaldehyde selectivity to CO formation from surface exposed isolated Mo and Fe sites. A steady-state kinetic study of methanol oxidation over industrial $Fe_2(MoO_4)_3$ between 230 ^oC – 360 ^oC using a differential reactor reported by Deshmukh et al [69] revealed that the reaction is first order at low methanol concentration, but independent at higher concentration showing Langmuir-Hinshelwood type dependency on oxygen due to saturation of active sites by methanol. They attributed CO formation to secondary oxidation of formaldehyde. Moreover, methanol oxidation over $Fe_2(MoO_4)_3$ using an adiabatic layer reactor conducted by Ivano and Dimitrov [70], revealed that formaldehyde selectivity is significantly affected by methanol concentration and feed velocity. They reported optimum formaldehyde selectivity of 92 – 95 % at 100 % conversion between 200 – 350 ^oC, using < 0.5 wt% methanol and attributed CO formation to secondary oxidation of formaldehyde. In a separate comparative study of $Fe_2(MoO_3)_4$ catalysts obtained from an industrial plant and a pseudo-thermal reactor (mimicking the industrial plant) they [71] confirmed no significant change or reduction in phase

and composition of spent catalysts obtained at bed temperatures below 300 ^{o}C characterized by XRD and Mossbauer spectroscopy. Catalysts obtained from the intense process zone (above 300 ^{o}C) of the reactor in the industrial plant indicated an increase in iron composition at the expense of Mo due to sublimation of MoO_3 at the reactor hot spot zone over a period of 12 months. They concluded that catalyst deactivation to Fe_2O_3 and $FeMoO_4$ is not the significant factor affecting its catalytic properties at low temperature (below 300 ^{o}C).

A previous deactivation study of co precipitation and sol-gel $Fe_2(MoO_4)_3$ catalysts by Soares et al [58] evidenced that water produced during reaction facilitates catalyst deactivation via formation of volatile $MoO_2(OH)_2$ species, which thus hindering surface re-oxidation. They attribute surface reduction (deactivation) of stoichiometric and sol-gel $Fe_2(MoO_4)_3$ catalysts to lack of excess Mo reservoir to replenish the lost Mo species and irreversible reduction due to loss of surface lattice oxygen during calcinations respectively. However, Andersson et al [72] argued that volatilization of excess Mo is caused by methanol, and proposed the mechanism below for deactivation of the active phase:

Reaction resulting in volatilization of surface MoO_3 species:

$$CH_3OH + Fe_2(MoO_4)_3 \rightarrow CH_2O + H_2O + 2FeMoO_4 + MoO_3 \quad \text{Equation 3.1}$$

Reoxidation in excess MoO_3:

$$2FeMoO_4 + MoO_3 + \tfrac{1}{2}\, O_2 \rightarrow Fe_2(MoO_4)_3 \quad \text{Equation 3.2}$$

Reoxidation in scarcity of MoO_3:

$$3FeMoO_4 + \tfrac{3}{4}\, O_2 \rightarrow Fe_2(MoO_4)_3 + \tfrac{1}{2}\, Fe_2O_3 \quad \text{Equation 3.3}$$

An in-situ Mossbauer study of methanol interaction on $Fe_2(MoO_4)_3$ reported by Mitov et al [73], they found that reduction proceeded via formation of anion vacancies during steady state reaction, resulting in disruption of sub surface crystal layer at 300 ^{o}C, which increases at higher temperature. Moreover, they confirmed no phase reduction of α-$Fe_2(MoO_4)_3$ to β-$FeMoO_4$ is observable during reaction in air, but this became appreciable when conducted in Ar. An in-situ rapid powder diffraction study of $Fe_2(MoO_4)_3$ deactivation in H_2 and O_2 reported by Jacques et al [74], revealed that the kinetics for re-oxidation of β-$FeMoO_4$ to α-$Fe_2(MoO_4)_3$ is faster than its reverse

kinetic of reduction at 472 ^{o}C. They contested the concept of anion mobility due to rapid reoxidation kinetics, and inferred that H_2O formed during reaction blocks the active site for H abstraction on $Fe_2(MoO_4)_3$. However, in a separate in-situ multi-technique study reported by Jacques et al [75] using wide-angle-X-ray scattering (WAXS)/extended-X-ray absorption fine structure (XAFS)/ UV-visible and mass spectrometry, surface reduction of $Fe_2(MoO_4)_3$ in methanol proceeded via the disappearance of MoO_3 and $Fe_2(MoO_4)_3$ and appearance of MoO_2, amorphous material and MoC at 350 ^{o}C. They observed that the rate of reduction in methanol and oxidation in O_2 were faster for the catalyst with excess Mo, which was ascribed to either surface area effect, or promotion effect, or possible substitution of Fe^{3+} by Mo^{6+} ion. However, they maintain the view that excess Mo is essential for maintaining both structural stability and selectivity during reaction.

Recently, partial oxidation of decane on $Fe_2(MoO_4)_3$ reported by Pradhan et al [76], revealed the involvement of non-lattice oxygen in formation of oxygenated aromatics at lower temperature, which attained maximum selectivity at 350 ^{o}C. These findings indicated the possible implication of non lattice surface oxygen in selective oxidation on $Fe_2(MoO_4)_3$ catalyst at lower temperature.

This section is aimed at studying the effect of acidic sites and K doping on high surface area MoO_3 (small particles size) prepared by hydrothermal method as it relates to activity and selectivity of methanol oxidation reaction. In addition, it investigates the active and selective phase in methanol oxidation over $Fe_2(MoO_4)_3$ catalysts.

3.2 Results and Discussion

Iron (III) Oxide (Fe_2O_3)

The characterization study of the Fe_2O_3 Aldrich sample was limited to BET surface area determination for comparison purpose only, since previous methanol oxidation studies on the catalyst in a pulsed flow reactor conducted by Bowker's group indicates high selectivity for CO_2 [77].

Table 3. 1 BET surface area of iron (III) oxide

Catalyst	BET Surface area (m^2/g)
Fe_2O_3 (Aldrich)	2.6
Fe_2O_3 (Prepared)	11

Table 3. *1* above, compares the BET surface area of two iron oxides (Fe_2O_3) with surface areas of 2.6 and 11 m^2/g for the commercial (Aldrich) Fe_2O_3 and prepared Fe_2O_3 catalyst respectively. The data reveals that the prepared Fe_2O_3 has a larger surface area compared to the commercial Aldrich sample. This could be an effect of the starting precursor as well synthetic route involved in their preparation. The synthesis of prepared Fe_2O_3 involved formation of acidified (using nitric acid) solution of $Fe(OH)_2$ species, in which slow evaporation results in the formation of high surface area catalyst.

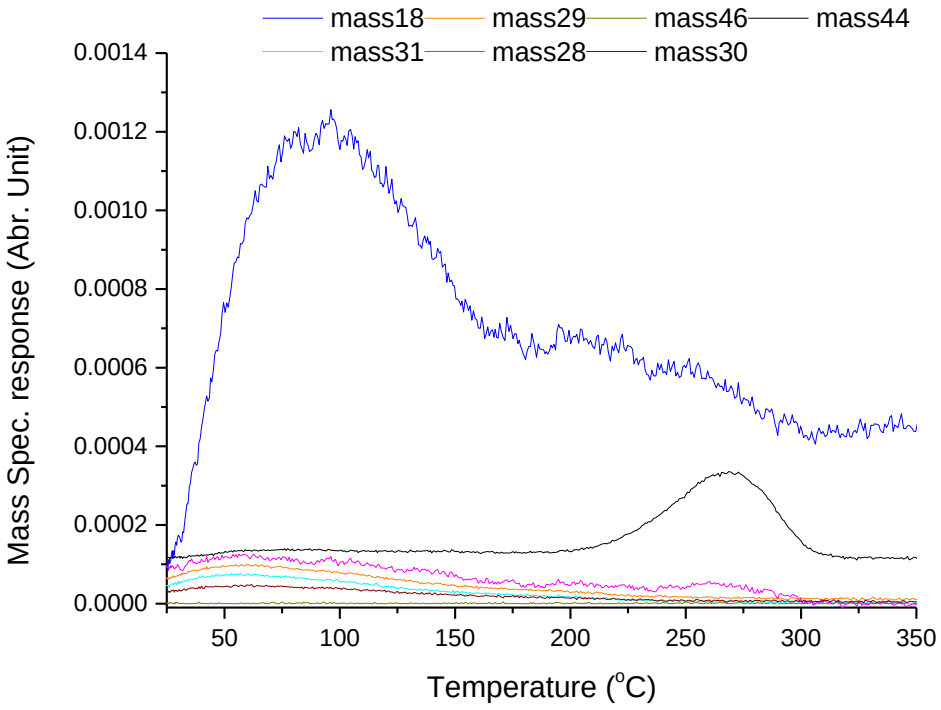

Fig. 3. 5 ***TPD desorption profile for methanol over iron oxide (Fe_2O_3): water (mass 18), CO_2 (mass 44), methanol (mass 31), CO (mass 28), formaldehyde (mass 30), and DME (mass 46)***

TPD profile for the prepared Fe_2O_3 in Fig. 3. 5 illustrates small but broad desorption peak of methanol at 50 ^oC before large and broad water peak at 96 ^oC, with a later CO_2 desorption peak observed at 270 ^oC.

The methanol peak is associated with molecular physisorbed methanol on Fe_2O_3, while broad water peak could be associated with recombination of surface hydroxyl groups resulting from chemisorbed methanol [14]. The TPD profile indicates high selectivity for CO_2 with desorption peak at 270 ^oC. The strong chemisorption of the methoxy species on the Fe vacant site (acidic site) results in abstraction of hydrogen. In addition, this leads to oxidation of the methoxy species by oxygen in the Fe_2O_3 network into formate species. The recombination of the hydroxyl species results in the production of a large water peak at 96 ^oC. Further, oxidation to CO and CO_2 at high temperature was evidenced by Bowker et al [77] to occur via formation of bidentate formate species, which is quite stable below 200 ^oC . This stable species blocks the active sites and prevent further reaction of methanol at low temperature (< 200 ^oC), but

decompose at high temperature (> 200 ^{o}C) to CO_2 making Fe_2O_3 a complete combustor of methanol.

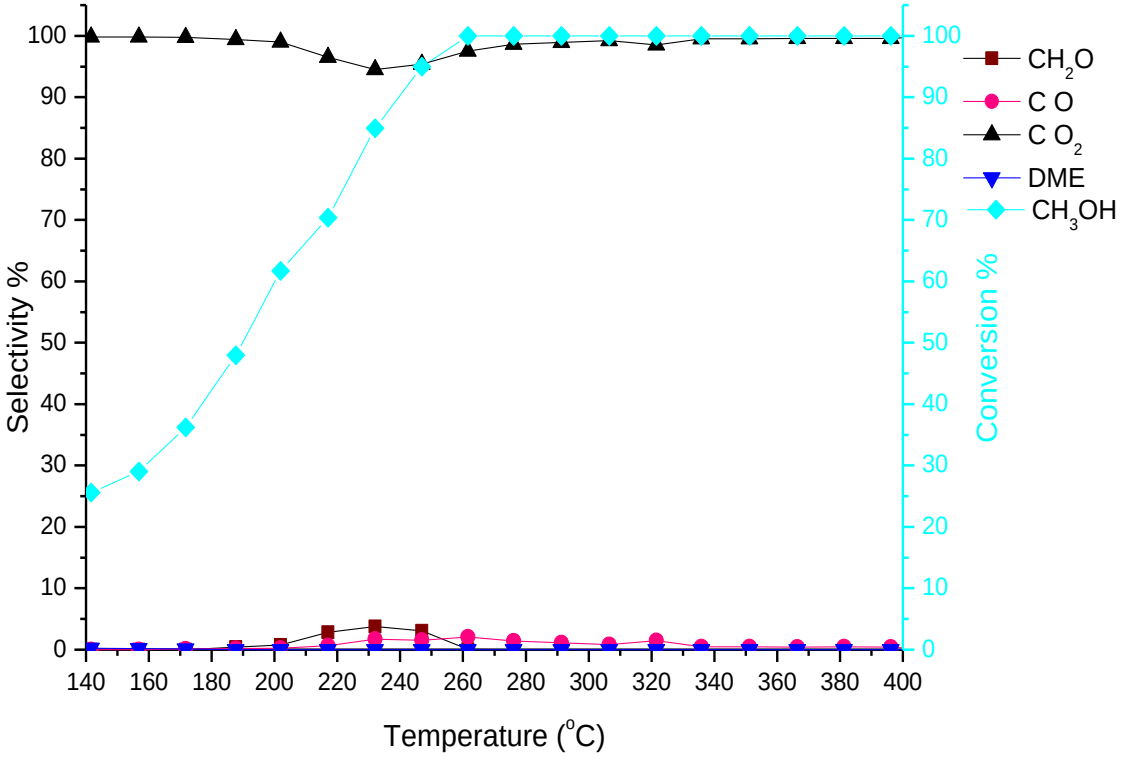

Fig. 3. 6 ***Selectivity and conversion of methanol over Fe_2O_3***

The pulsed flow reaction study of methanol over Fe_2O_3 in Fig. 3. 6 reveals high selectivity to CO_2, with selectivity being ~100 % by140 ^{o}C and 25 % at 262 ^{o}C and ~ 100 % methanol conversion respectively. Methanol conversion reaches 85 % by 232 ^{o}C with slight selectivity to formaldehyde (~ 4 %) as CO_2 drops in selectivity to 95 %. CO formation begins at 189 ^{o}C which reaches ~2 % by 261 ^{o}C. The CO_2 selectivity is ~100 % above 300 ^{o}C at ~100 % methanol conversion. The above result indicates Fe_2O_3 as a very active catalyst, but unfortunately a combustor of methanol.

Molybdenum trioxide (MoO_3)

Table 3. 2 BET surface area of molybdenum trioxide (MoO_3)

Catalyst	BET Surface area (m^2/g)
MoO_3 (BDH)	0.6
MoO_3 (Prepared)	4.9

The data in Table 3. *2* shows a surface area of 4.9 m^2/g and 0.6 m^2/g for the MoO_3 samples prepared by precipitation method and the commercial BDH sample respectively. The lower surface area observed in the commercial BDH samples could be attributed to a well aligned MoO_6 orthorhombic structure with edge and corner sharing of bridge molybdenum- oxygen-molybdenum bond along (0k0) and (h00 or 00l) plane form layer structure as reported by Smith and Ozkan [23]. This layer structure leads to formation of a large crystalline MoO_3 structure. The MoO_6 octahedral structure consists of layer structure held together by a weak van der waals interaction. The distortion of the orthorhombic structure results in formation of a crystallographic shear plane and edge sharing of the bridge oxygen in the prepared MoO_3 sample as well as amorphous MoOx layer, leading to different morphological and crystallites structure. Since the BET surface area measurement depends upon multilayer adsorption of gas molecules on solid surface, exposure of the sides plane (h00, h0k + 00l) and increasing density of the active sites by amorphous MoOx (smaller particle size) in the prepared MoO_3; this could be possible reason of its higher surface area as observed by Bruckman et al [78] and Vedrine [11]. The layer structure of the commercial MoO_3 (BDH) sample (large particle size) consisting of side and corner sharing, exhibit a geometric effect that limits gas adsorption. This could probably account for its low surface area as shown in Table 3. 2.

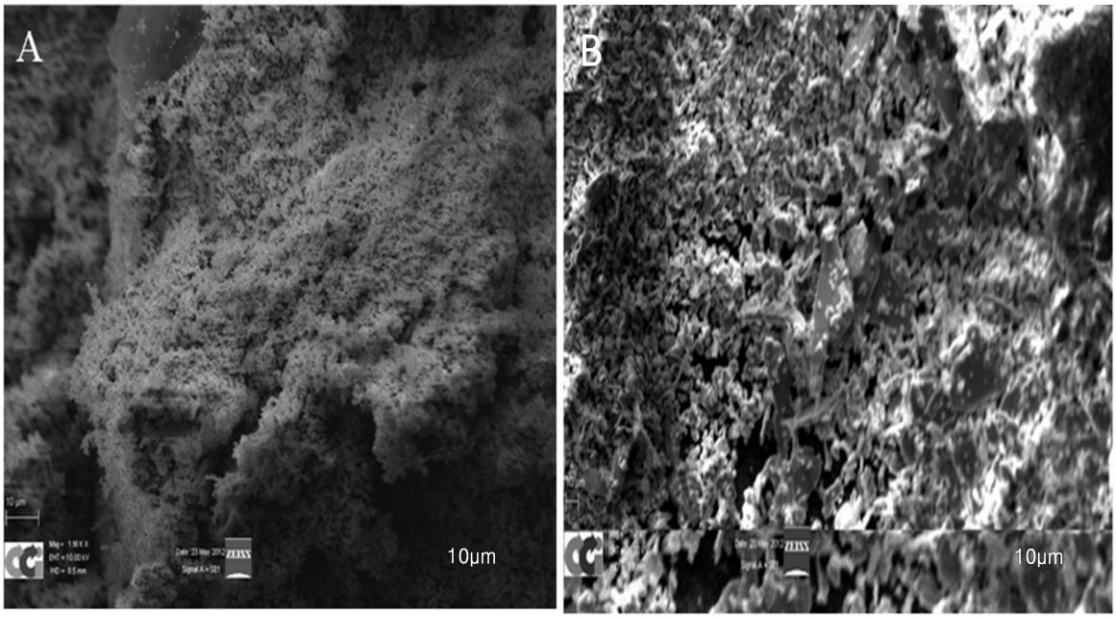

Fig. 3. 7 ***SEM micrograph of different molydenium trioxide samples: A- prepared MoO_3 and B- commercial MoO_3 (BDH) sample (scale 180 x 120 µ)***

The SEM micrograph of the different MoO_3 samples in Fig. 3. 7 reveals small crystallites or ribbon-like structure for the prepared MoO_3 sample A, while the as-received commercial (BDH) sample in B displays a large plate-like and amorphous crystallite structure. The amorphous MoOx on the platy structure depicts a bright white region due to charging effect of the MoO_3 surface.

The plate-like structure observed in sample B, is attributed to (010) basal plane of orthorhombic MoO_3 as previously reported by Bruckman et al and Smith and Ozkan [23, 78]. The small spherical or ribbon like structure of the sample A was close to mechanically-ground MoO_3 sample observed by Bruckman et al. This implies that hydrothermal and mechanical treatment of MoO_3 or precursors has a morphological effect on MoO_3, which leads to small particle size.

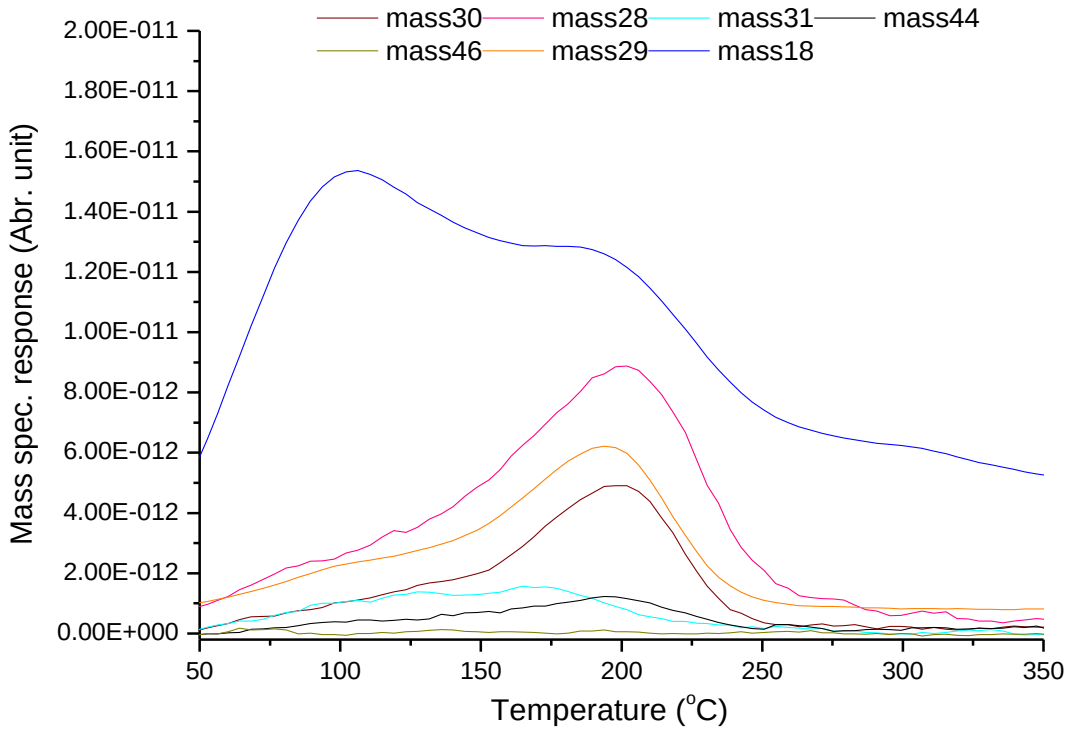

Fig. 3. 8 ***TPD desorption profile for methanol over 1g MoO_3 BDH sample: water (mass 18), CO_2 (mass 44), methanol (mass 31), CO (mass 28), formaldehyde (mass 30), and DME (mass 46)***

The TPD profile of methanol on BDH MoO_3 in Fig. 3. 8 above reveals a broad methanol desorption peak beginning at 65 ^oC, which tails until ~225 ^oC, with two broad water peaks at 100 ^oC and 186 ^oC preceding formaldehyde peak at 198 ^oC.

However, the tailing of methanol peak until about 225 ^oC indicates desorption of molecular adsorbed methanol species as they diffuses on the catalyst surface. This observation supports the findings reported by Sleight et al [12], and Farneth [14]. The low chemisorption of methanol over the BDH MoO_3 sample could be attributable to the presence of saturated Mo sites and geometric effect, which could limit accessibility to active sites. The water desorption peaks at 100 ^oC and 186 ^oC result from recombination of surface hydroxyl species abstracted from both α and β hydrogen of methanol. The lower temperature desorption of the second water peak reveals a typical characteristic of fully coordinated Mo sites, as evidenced in a comparative study of methanol desorption on different MoO_3 reported by Farneth [14].

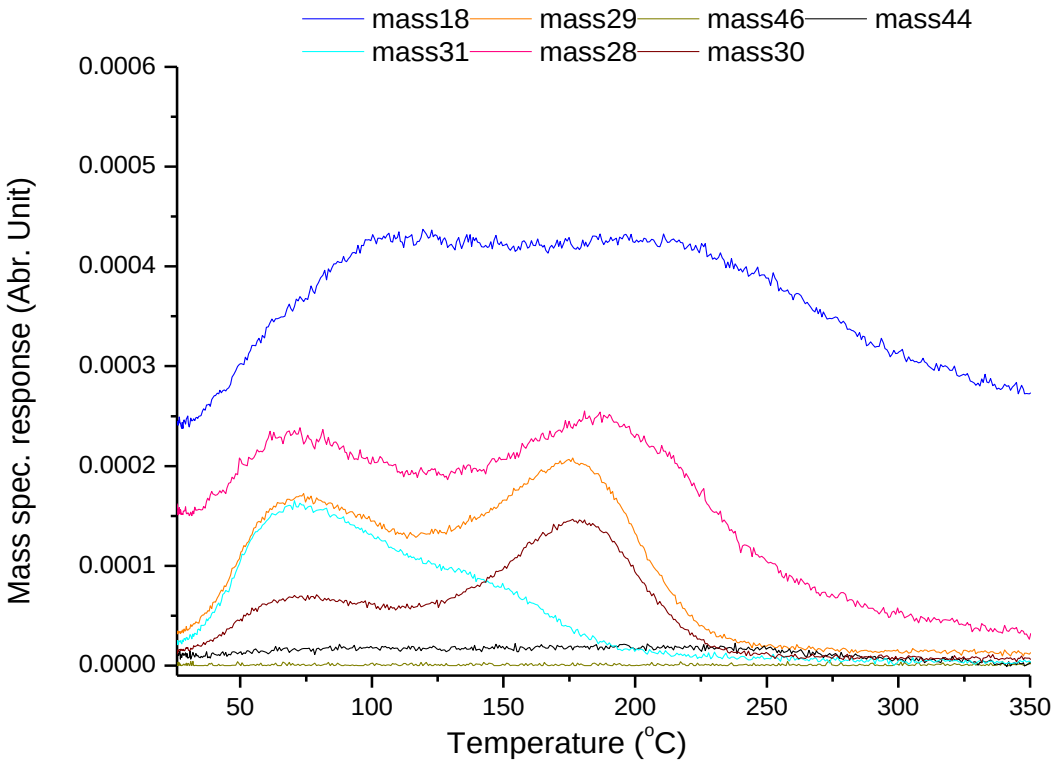

Fig. 3. 9 ***TPD desorption profile for methanol over 1g Prepared MoO_3: water (mass 18), CO_2 (mass 44), methanol (mass 31), CO (mass 28), formaldehyde (mass 30), and DME (mass 46)***

The TPD profile of methanol over prepared MoO_3 in Fig. 3. 9 indicates methanol desorption peak at 71 ^oC, with a slightly lower shoulder peak at 140 ^oC which tails until 200 ^oC. A broad water peak appears at 110 ^oC. Formaldehyde peak was observed at 178 ^oC, with CO at 188 ^oC (broadening of the mass 28 signal above 220 ^oC) preceding second broad water peak at 210 ^oC.

The methanol desorption peak at 71 ^oC is associated with molecularly physisorbed methanol, while the shoulder peak could possibly result from recombination of chemically absorbed methoxy (CH_3O) and hydroxyl (OH) species as suggested by Farneth [14]. The TPD profile is in agreement with previous findings reported by Sleight et al [12], Farneth et al [14] and Bowker et al [79]. Interestingly, the formaldehyde desorption at lower temperature (178 ^oC) could be attributed to electrophilic-like (O^{*-}) oxygen species, which is coordinated to Mo on the oxygen vacancy sites of defective MoO_3, responsible for activation of methanol (by abstraction

of hydrogen) as such creating a lesser energetic pathway for formaldehyde formation. The broadening of the water desorption peaks indicates possible diffusion, re-adsorption and combination of loosely bonded surface hydroxyl species. These species were reported by Lei and Chen [8] to diffuse along asymmetric bridging oxygen on defect MoO_3 surface during reaction. These findings are in conformity with density DFT+U studies of adsorbed hydrogen and methyl species on oxygen defective MoO_3 conducted by Hermann [31], Friend [33], Lei and Chen [8], and on α-MoO_3 by Sha et al [80] . The CO shoulder peak observed at 188 ^oC preceding a higher temperature second water peak at 210 ^oC indicates further abstraction of hydrogen from formaldehyde by possible reactive adsorbed transient (O^{*-}) oxygen species on the catalyst surface, which has been invoked by some researchers [4, 7, 36, 67] to participate in oxidation of surface chemisorbed species.

We propose a possible mechanism of the methanol reaction on MoO_3 surface as in the following equations below:

$CH_3OH + a \rightarrow CH_3OHa$ Equation 3.4

$CH_3OHa + Oa \rightarrow CH_3Oa + OHa$ Equation 3.5

$CH_3Oa + Oa \rightarrow CH_2O + OHa$ (nucleophilic O) Equation 3.6

$CH_3OHa + O^{*-} \rightarrow CH_2O + H_2O + a$ (electrophilic-like O) Equation 3.7

$CH_3Oa + O^{*-} \rightarrow CH_2O + HO^{*-}$ (electrophilic-like O) Equation 3.8

$CH_2Oa + O^{*-} \rightarrow CO + H_2O + a$ (electrophilic-like O) Equation 3.9

$CH_3Oa + OHa \rightarrow CH_3OH(g) + Oa + a$ Equation 3.10

$OHa + OHa \rightarrow H_2O(g) + Oa$ Equation 3.11

$2a + O_{2(g)} \rightarrow 2Oa$ (lattice O formation) Equation 3.12

$2^{*-} + O_2 \rightarrow O_2^{*-}$ (electrophilic-like O formation) Equation 3.13

Where O^{*-}, a, Xa and g are electrophilic oxygen, surface, adsorbed molecule and gas phase species respectively.

Table 3. 3 Comparison of activation energy of CH_2O for MoO_3 samples

MoO_3 Sample	Peak Maximum Temperature (Tm) ^oC	Activation Energy of CH_2O (kJ/mol)
BDH	198	122
Prepared	178	116

Table 3. 3 above shows the desorption energy (activation energy) of formaldehyde on MoO_3 calculated using the Redhead equation. The table reveals lower desorption energy of 116 kJ/mol for prepared MoO_3 in comparison to 122 kJ/mol for BDH commercial sample, which could be due to the defect (vacancies) sites on the prepared MoO_3 sample which leads to formation of step as reported by Abon et al [10].

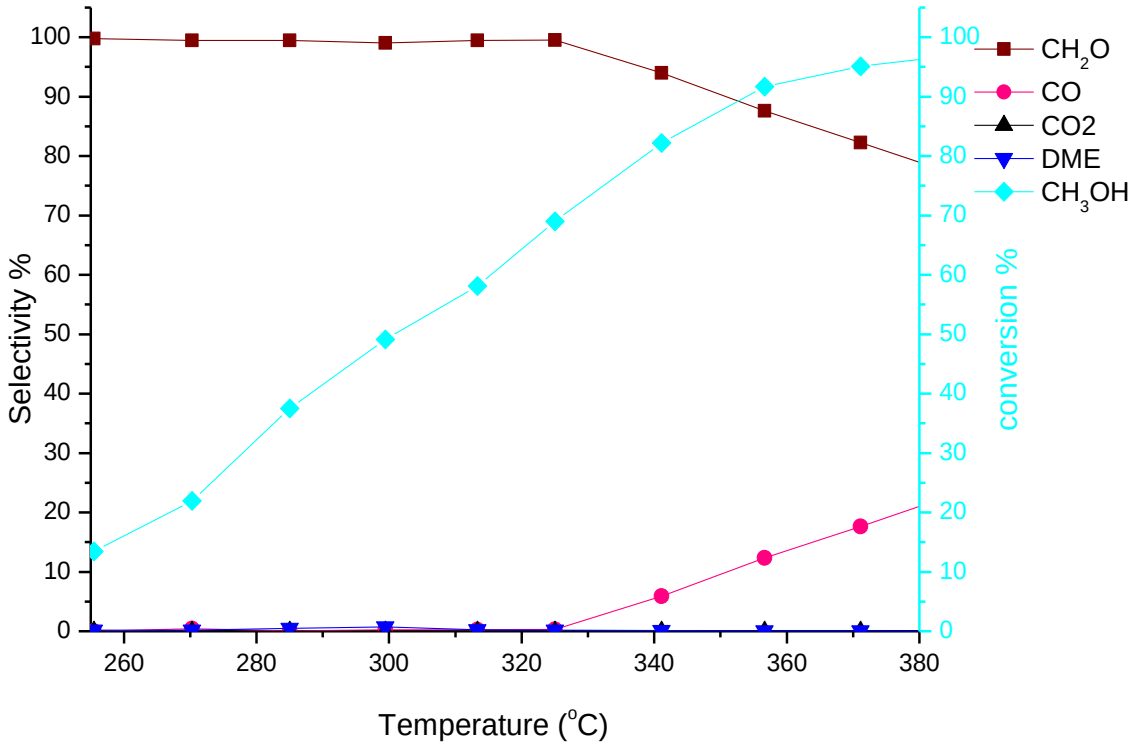

Fig. 3. 10 ***Selectivity and conversion of methanol over1g MoO_3 BDH sample***

Methanol oxidation over the commercial BDH MoO_3 sample in Fig. 3. 10 above indicates ~100 % selectivity to formaldehyde at 13 % methanol conversion at 255 ^oC; with slight drop in formaldehyde selectivity to 93 % at ~ 82% methanol conversion by 341 ^oC. However, methanol reaches a maximum conversion of 96 % at 380 ^oC with a steady decline in formaldehyde selectivity to 79 % due to an in increase in CO selectivity to 21 %.

The low activity of the BDH sample is due to low surface area. However, fully coordinated Mo=O is reported by Smith and Rhorer [21] not to be active at low reaction temperature (< 300 ^oC), whereas the (010) basal plane form a thermally stable methoxy species, which is highly selective to formaldehyde as established by Tatibouet and Germain [9], and Allison and Goddard [16]. Furthermore, the steady increase in CO selectivity above 320 ^oC could result from surface reduction of Mo oxidation state from +6 to +4 as reported by Bowker et al [27] and Ressler et al [24]. The reduction of the oxidation state of Mo at higher temperature enhances the concentration and mobility of labile oxygen on the surface, and diffusion into the bulk as observed by Mestl [28], which could result in further oxidation of formaldehyde to CO and CO_2 at higher temperature. However, it is important to note that above 320 ^oC the reduced Mo site was not re oxidised during reaction under oxygen flow. The plausible explanation for this could be that the rate of lattice oxygen diffusion to re oxidize the reduced Mo site was slower than the rate of its reduction by methanol, resulting in formation of CO. The implication of this is the possibility that the MoO_3 (BDH) sample does not strictly obey the Mars-van Krevelen mechanism at such reaction temperatures (< 300 ^oC). The observation on MoO_3 catalyst was recently reported by Routray et al [81].

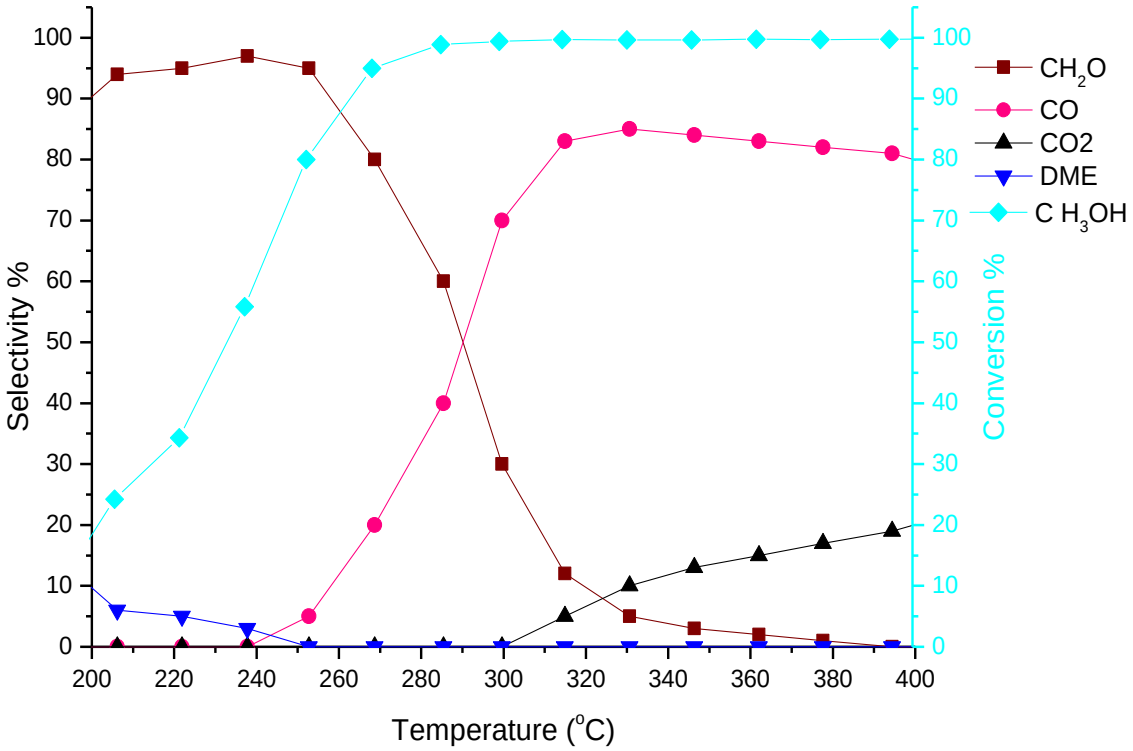

Fig. 3. 11 ***Selectivity and conversion of methanol over 1g MoO_3***

The reaction profile of methanol oxidation over the prepared MoO_3 catalyst in Fig. 3. 11 illustrates high activity at lower temperature, with formaldehyde and dimethyl ether selectivity reaching 90 % and 10 % respectively at ~20 % methanol conversion by 200 ^oC. Meanwhile, formaldehyde selectivity reaches a maximum of 95 % at 80 % methanol conversion by 253 ^oC, which declines to 80 % at 95 % methanol conversion by 269 ^oC. CO and CO_2 selectivity reaches 85 % and 10 % respectively by 331 ^oC, and the former declined steadily as the temperature increase up to 400 ^oC.

Dimethyl ether formation at low temperature indicates presence of mild acidic sites, which is a characteristic of oxygen defect site located on (100) site of MoO_3. Such sites result in coordinative unsaturated Mo cations (Lewis acid) capable of activating and dehydrating methanol, as observed by Abon et al [10], Tatibouet and Germain [9] and Tatibouet [82]. The decrease in formaldehyde selectivity at higher temperature (~300 ^oC) could be attributed to rapid reduction of molybdenum surface (to lower oxidation

state of 4+) by methanol, as was previously observed by Chung et al [15] and Bowker et al [27]. However, the increase in CO selectivity at low temperature below 300 ^{o}C could result from further abstraction of hydrogen from formaldehyde by surface non-lattice transient oxygen (O*$^{-}$) species, which was reported by Bielanski and Haber [35], Zhao and Wachs [37] and Pradhan et al [76] to participate in selective oxidation reactions.

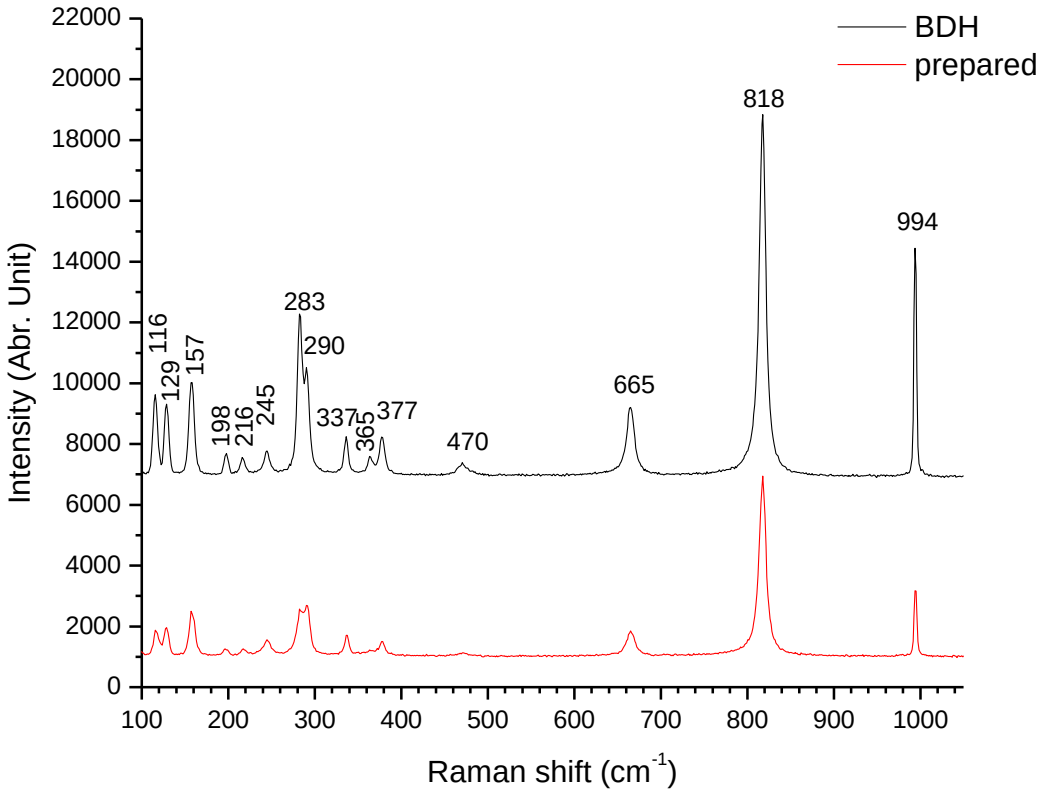

Fig. 3. 12 ***Raman spectra of MoO_3 samples: black line (commercial (BDH), red line (prepared)***

Table 3. 4 Raman bands of MoO_3 samples in comparison to reported values [83, 84]

Reported band cm^{-1}	BDH band cm^{-1}	Prepared band cm^{-1}	Assignment
995	994	994	Mo=O asymmetric stretching
819	818	818	Mo-O-Mo symmetric stretching
666	665	665	Mo-O-Mo asymmetric vibration
473	470	470	Mo-O-Mo bending vibration
379	377	379	Mo-O-Mo scissoring vibration
365	365	363	Mo-O-Mo scissoring vibration
337	337	338	Mo-O-Mo bending vibration
291-283	290-283	290-283	O=Mo=O wagging vibration
246	245	245	O=Mo=O twisting vibration
217	216	217	Rotational rigid MoO_4 chain mode
198	198	196	O=Mo=O twisting vibration
158	157	157	Translational rigid MoO_4 chain mode
129-116	129-116	129-116	Translational rigid MoO_4 chain mode

The Raman spectra of the different MoO_3 samples shown in Fig. 3. 12 depict Raman bands, which are in close conformity with data obtained by Py and Maschke [83] and Seguin et al [84] for single crystal and synthesised MoO_3 respectively, as illustrated in Table 3. 4. These Raman bands at 996, 818, 665 and 470 cm^{-1} are attributed to υ_{as} Mo=O stretch, υ_s O-Mo-O stretch of bridge O, υ_{as} O-Mo-O and υ_{as} O-Mo-O stretch and bend respectively. The lower vibration mode at 377, 365, 337, 290, 283, 246, and 216 cm^{-1} correspond to (B_{1g}) scissoring, A_{1g} scissoring, $B_{1g,}$ δ O-Mo-O bend, $B_{3g,}$ δ O=Mo=O wagging, $B_{2g,}$ δ O=Mo=O wagging, $B_{3g,}$ τ O=Mo=O twist, and A_g rotational rigid MoO_4 chain mode (RCM) respectively. Meanwhile, the bands at 197, 159, 129 and 116 cm^{-1} are ascribed to B_2 τ δ O=Mo=O twist vibration, A_g/B_{1g}, translational rigid MoO_4 chain mode, $B_{3g,}$ translational rigid MoO_4 chain mode, and B_{2g}, translational rigid MoO_4 chain mode respectively.

The slight reverse in intensity of the 129 cm^{-1} peak with respect to 116 cm^{-1} of the prepared MoO_3 in comparison to the BDH commercial sample, indicates microcrystalline (change in crystallite size) nature of the prepared MoO_3 due to perturbation of the layer structure in the prepared MoO_3 as reported by Mestl [28]. This effect implies formation of oxygen vacancies usually induced by mechanical or thermal treatment at higher temperature. More so, the decrease in peak intensity and broadening of the bending, scissoring and rotational (RCM) vibration at 470 cm^{-1}, 365 cm^{-1} and 216 cm^{-1} observed in the prepared sample could result from distortion of the bond distance due to oxygen defect. Meanwhile, the decrease in peak intensity of 283 cm^{-1} with respect to 290 cm^{-1} associated with polarised B_{2g} and B_{3g}, δ O=Mo=O wagging vibration parallel to the c-axis respectively, reveals symmetry change due to distortion in direction of the c-axis induced by oxygen deficiency in the prepared samples. A diffuse reflectance UV/VS and Raman spectroscopic study of the I_{283}/I_{290} band intensity ratio conducted by Dieterle [85], indicates that this ratio decreases with increasing oxygen vacancy concentration in $MoO_{3\ S}$amples.

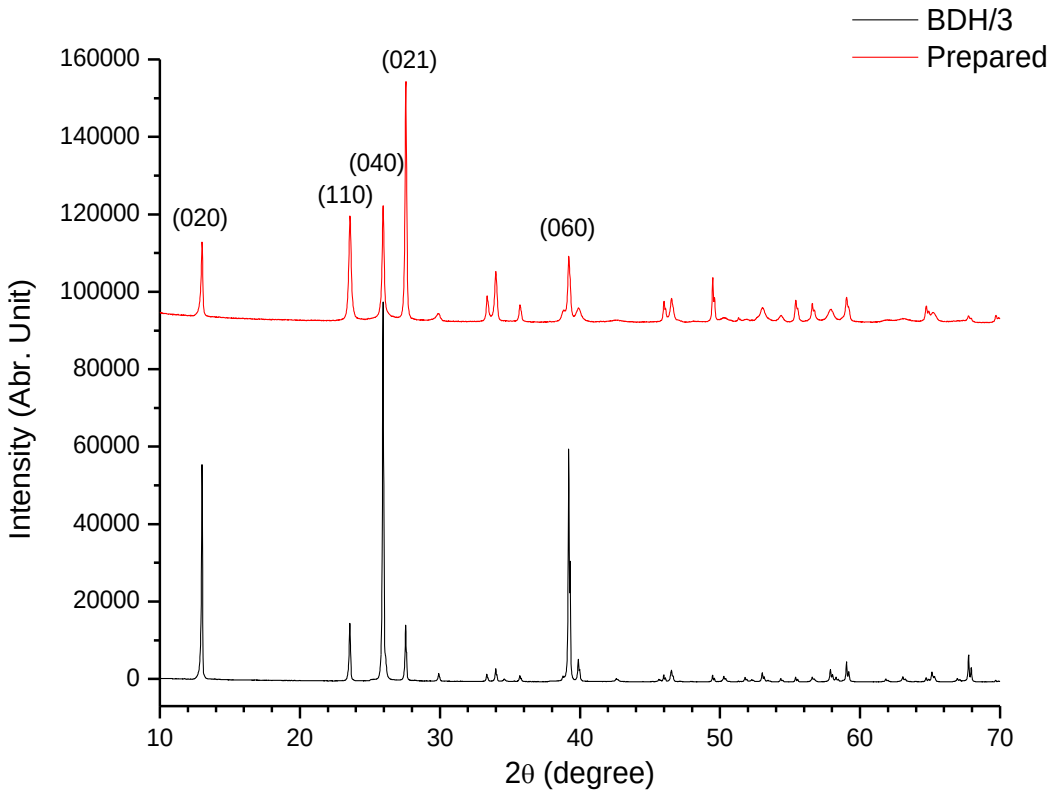

Fig. 3.13 D*iffractogram of MoO_3 sample: black solid line (commercial MoO_3 (BDH)) sample, red solid line (prepared MoO_3 sample)*

The diffractogram in Fig. 3.13 reveals peaks at 2θ value of 12.5 ^{o}, 23.4 ^{o}, 25.7 ^{o} and 27.4 ^{o} for the BDH sample, and values of 12.7 ^{o}, 23.6 ^{o}, 25.9 ^{o}, and 27.6 ^{o} for the prepared sample, which are in close conformity with assignment for (020), (110), (040) and (021) planes in single crystal MoO_3 respectively. The prepared sample indicates 2θ value shift of 0.2 ^{o} compared to the BDH sample, due to instrumental alignment.

However, these peaks indicate diffraction pattern for orthorhombic MoO_3 as indexed in JCPD No.01-076-1003 [86]. Apparently, the increase in (040) peak intensity associated with basal plane in comparison to (110) and (120) peaks of the BDH sample reveals high exposure of this plane on the BDH MoO_3 sample. The prepared sample indicates an increase in the peak intensity of (021) plane compared to (011) and (040), attributed to exposure of truncated (100 + 010) facets leading to formation of stepped planes due to oxygen vacancies as reported by Abon et al [10]. More so, the peak broadening of the prepared MoO_3 indicates the nanocrystalline nature of the sample.

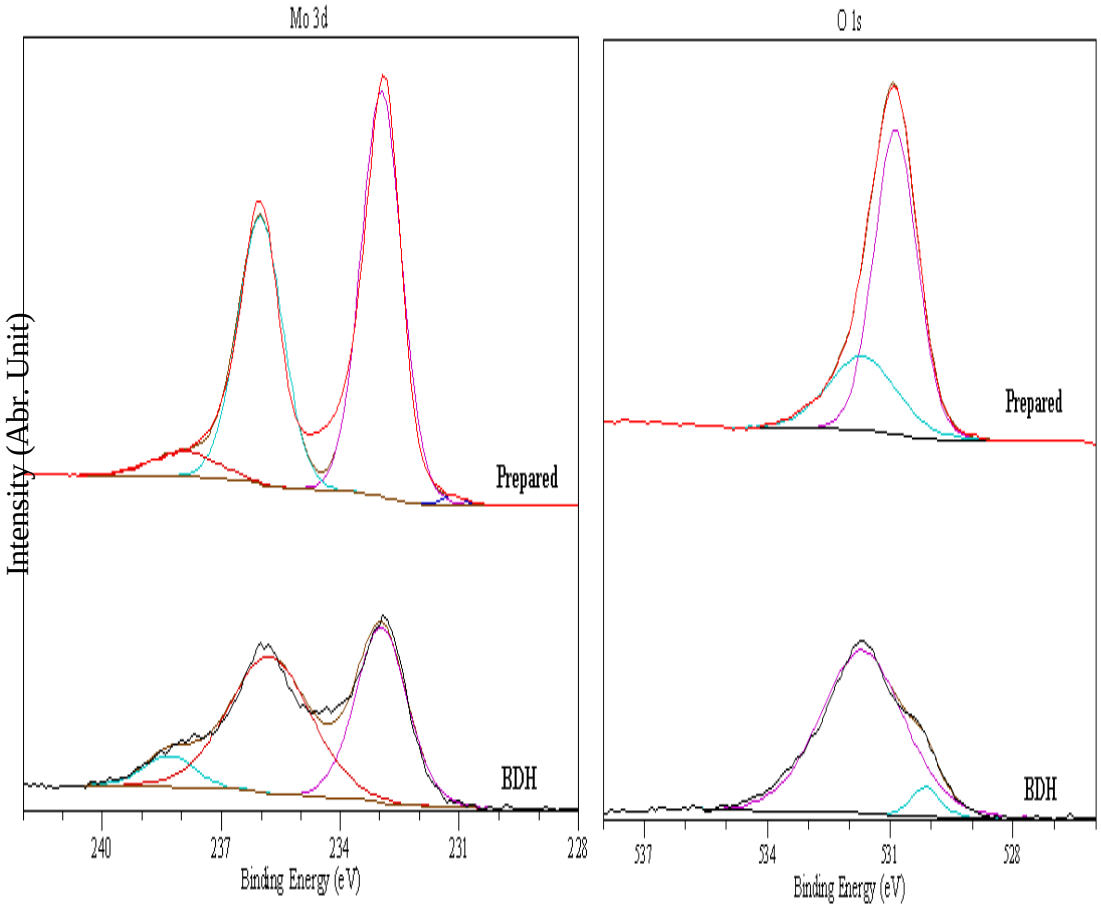

Fig. 3. 14 Comparison of XPS of prepared and BDH MoO_3 samples

The XPS analysis in Fig. 3. 14 indicates Mo 3d doublet spectra with binding energies at 232.9 ± 0.2 and 235.8 ± 0.2 eV assigned to $3d_{5/2}$ and $3d_{3/2}$ respectively, with an extra peak at 238.3 ± 0.2 eV on BDH MoO_3 sample. The prepared sample indicates a slight increase in the Mo binding energy at 233 ± 0.2 and 236 ± 0.2 eV assigned to $3d_{5/2}$ and $3d_{3/2}$ respectively in comparison with BDH sample, with an extra peak at 237.9 ± 0.2 eV and 231.2 ± 0.2 eV. Moreover, the figure depicts O1s binding energy of 530.9 ± 0.2 eV and 531.7± 0.2 eV, and a double peak at 530.1 ± 0.2 and 531.7± 0.2 eV for the prepared and BDH samples respectively.

The Mo 3d binding energies for both samples indicate the highest oxidation state of Mo^{6+} with an extra peak at 231.2 ± 0.2 eV in prepared sample that could be associated to Mo^{+5} of defective MoO_3, which are in agreement with observations made by Choi and Thompson [87], Smith and Ozkan [23], and Massa et al [88] for perfect and partially reduced MoO_3 samples. The extra peak in the BDH sample at 238.3 ± 0.2 eV

reveals possible charging effect; while the extra peak at 237.9 ± 0.2 eV in the prepared could be to due amorphous MoO_x phase as observed by Morgan [89].

The Mo 3d spectra did not reveal any peak at lower binding energy associated with Mo^{4+} oxidation states. However, O1s binding energy of 531.1 ± 0.2 eV of the prepared sample concurs with binding energy associated with (O^- ion) oxygen vacancies in metal oxide lattice as reported by Dupin et al [90], Mao et al [91], and Chen et al [92] . The O1s peaks in the BDH sample at 530.2 ± 0.2 , and 531.7 ± 0.2 eV for both samples agrees with values assigned to terminal (O^{2-}) and bridging oxygen in MoO_3 lattice respectively as reported by Cavalleri et al [34]. Although the O1s peak at 531.7 ± 0.2 eV observed is often associated to adsorbed hydroxyl species or moisture from atmosphere, it is unlikely due the following reasons:

a. Both samples treated in same environment and conditions, yet vary in the intensity and area of O1s peak.

b. The surface area of the prepared sample exposes about 8 times higher the surface area of the BDH sample, but reveals lower O1s peak intensity and area.

K-promoted MoO_3

The doping of the prepared MoO_3 surface with varying % coverage of K, is aimed at neutralizing the acidity of the surface using its basic property.

Table 3. 5 BET surface area of K-promoted MoO_3 in comparison to prepared sample

MoO_3 sample	BET Surface area (m^2/g)
Prepared	4.9
25% K	4.5
100% K	4.6

The BET analysis of the K-promoted catalyst in comparison to the prepared sample as shown in Table 3. 5 illustrates a surface area value of 4.9, 4.5, and 4.6 m^2/g for the prepared MoO_3, 25 % K, and 100 % K promoted samples respectively. This indicates no significant influence in the surface area of the catalysts due to K-promotion.

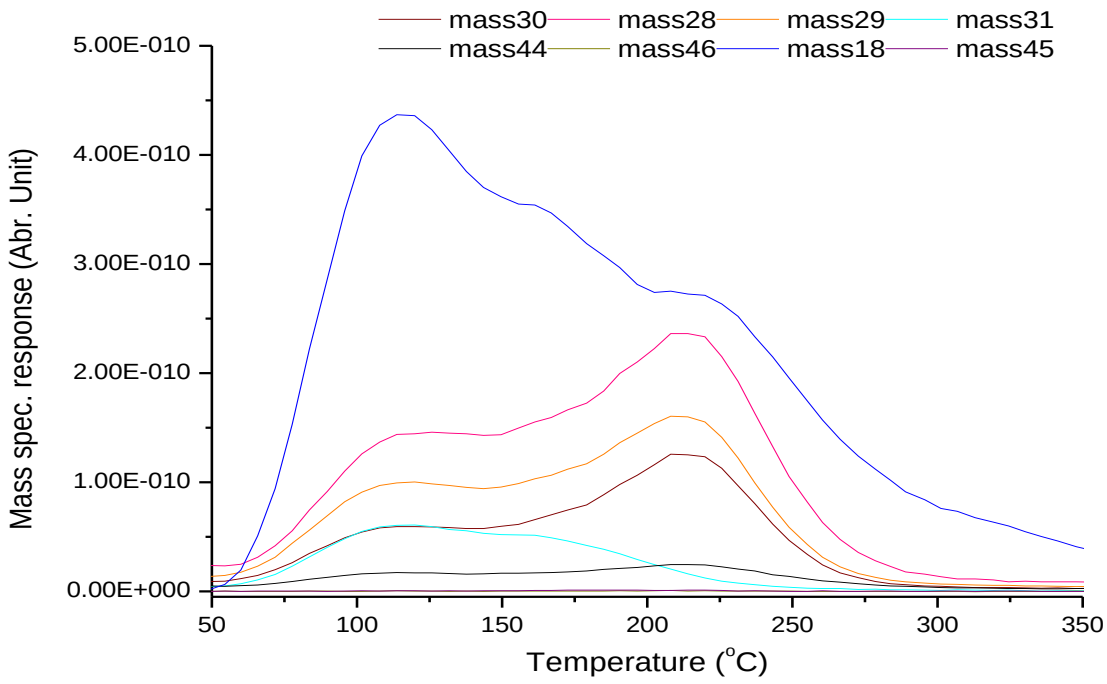

Fig. 3. 15 ***TPD desorption profile for methanol over 1g 25 % K-MoO_3: water (mass 18), CO_2 (mass 44), methanol (mass 31), CO (mass 28), formaldehyde (mass 30), and DME (mass 45 and 46)***

The TPD profile in the Fig. 3. 15 above depicts a methanol desorption peak at 110 ^{o}C with a shoulder peak at 160 ^{o}C, which tails until 225 ^{o}C. A water desorption peak was observed at 115 ^{o}C with two shoulder peaks at 160 ^{o}C and 212 ^{o}C, which coincides with methanol shoulder peak and formaldehyde desorption peak respectively. The desorption of methanol is mostly associated with molecular adsorbed species, but the shoulder peak could possibly result from recombination of chemisorbed methoxy and hydroxyl species as evident by a kinetics study conducted by Holstein and Machiels [93], while the second water shoulder peak is a likely product of surface recombination of hydroxyl species. The delay in formaldehyde desorption peak until 212 ^{o}C could be attributed to K addition, which neutralizes the active Lewis acids sites, and as such stabilizing the surface methoxy species. However, reaction between surface hydroxyl and methoxy species results in desorption of the methanol shoulder peak. This supports previous findings reported by Cheng [22], which evidenced competitive adsorption between water, methanol, and formaldehyde on same site. The adsorption of hydroxyl group on these sites could reduce the concentration of methoxy species on catalyst surface as reported previously by Holstein and Machiels [93].

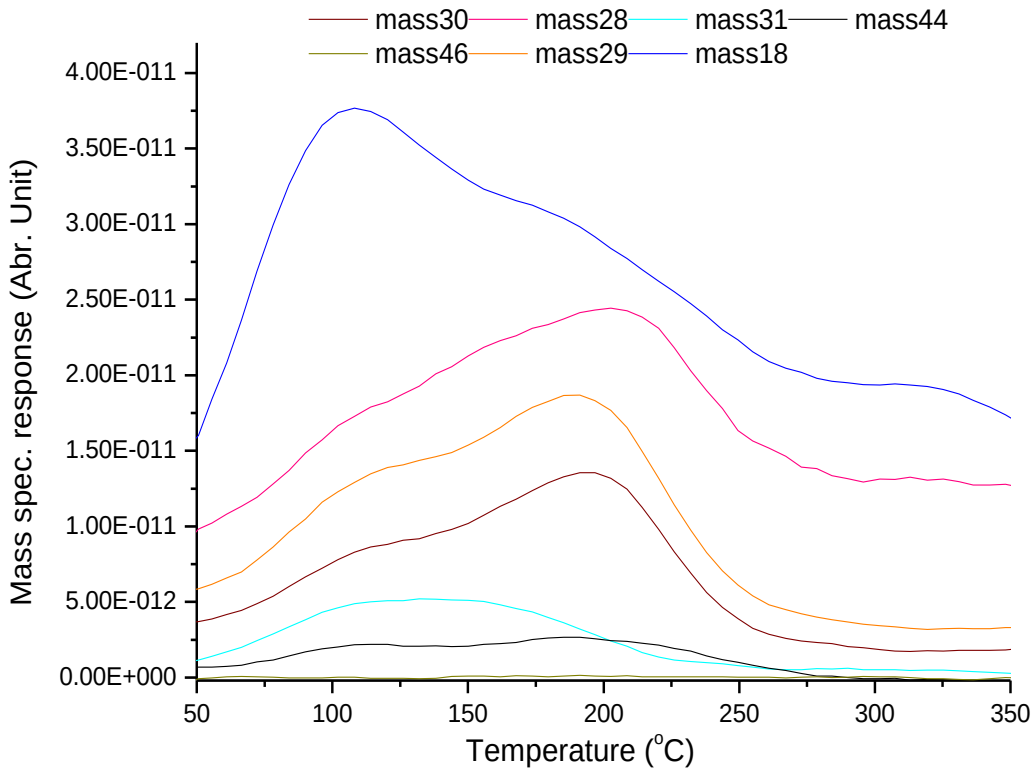

Fig. 3. 16 ***TPD desorption profile for methanol over 1g 100% K-MoO_3: water (mass 18), CO_2 (mass 44), methanol (mass 31), CO (mass 28), formaldehyde (mass 30), and DME (mass 45 and 46)***

The TPD desorption of methanol over 100 % K-MoO_3 in Fig. 3. 16 above indicates formaldehyde peak at 197 ^oC, preceding water desorption peaks, which coincides with methanol peak at 107 ^oC. Furthermore, the decline in methanol desorption peak is accompanied by a water shoulder peak at about 160 ^oC. Meanwhile, the profile reveals CO shoulder peak at slightly higher temperature of 210 ^oC after the formaldehyde peak.

The water shoulder peak indicates possible recombination of surface hydroxyl species, which desorbed at about 160 ^oC before the formaldehyde peak. The CO peak at 210 ^oC could indicate further oxidation of formaldehyde by adsorbed oxygen species on K-promoted MoO_3. The K seems to provide an alternative path for molecular oxygen adsorption on MoO_3, as well as increasing the residence time of methoxy adsorption on

the surface, thus facilitating further abstraction of hydrogen. This effect was previously observed by Driscoll, Gardner and Ozkan [46].

The mechanism of methanol reaction on K-promoted MoO_3 is similar to MoO_3, although K doping neutralizes surface acidity, and modifies the electronic structure and binding energy of surface adsorbed oxygen species. The 25 % K-MoO_3 reveals delay in formaldehyde desorption due blockage of Lewis acids sites, which is responsible for further abstraction of β – H to form formaldehyde, leading to stabilization of surface methoxy species. Furthermore, diffusion and reaction between surface methoxy and hydroxyl, as well as recombination of hydroxyl species could result in methanol and water desorption as expressed in Equation 3.10 and 3.11.

Table 3. 6 Comparison of activation energy of CH_2O for K-promoted and prepared MoO_3 samples

MoO_3 Sample	**Peak Maximum Temperature (Tm) ^oC**	**Activation Energy of CH_2O (kJ/mol)**
Prepared	178	116
25 % K	212	127
100 % K	197	121

The activation energy levels for formaldehyde desorption are given in Table 3. 6 showing values of 116, 127 and 121 kJ/mol for prepared MoO_3, 25 % K, and 100 % K promoted MoO_3 samples respectively.

These values reveal higher activation energy for K promoted MoO_3 catalyst in comparison to the prepared MoO_3 sample, which is attributable to neutralization of Lewis acid sites, electronic modification and difference in binding energy of K-promoted surface. The 25 % K promoted catalyst display the highest activation energy, which could result from stabilization of surface methoxy species due to K basic property, as well as competitive adsorption on the surface.

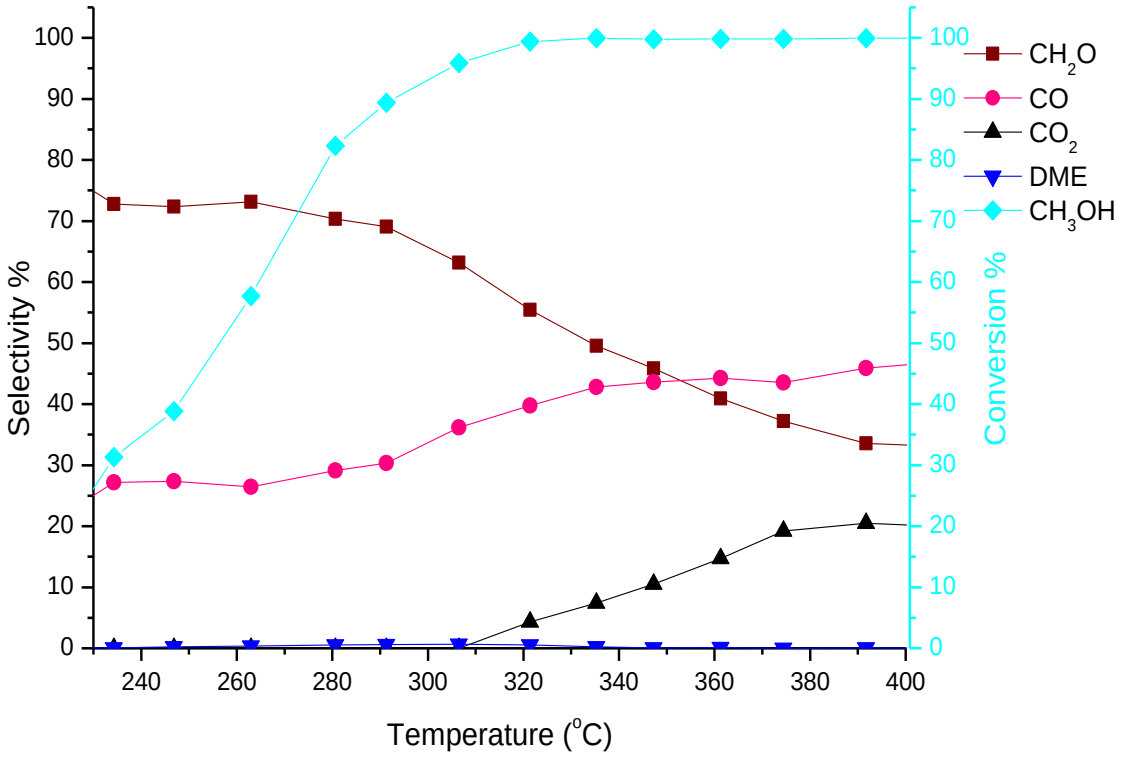

Fig. 3. 17 ***Selectivity and conversion of methanol over 25 % K- MoO_3***

Fig. 3. 17 depicts methanol oxidation over 25 % K promoted MoO_3 indicates ~75 % and 25 % selectivity to formaldehyde and CO respectively at 26 % methanol conversion by 230 ^{o}C. However, at maximum methanol conversion of ~99 %, formaldehyde selectivity diminishes to 57% with CO and CO_2 formation reaching 40 % and 5 % respectively by 320 ^{o}C.

The reaction profile for 25 % K-MoO_3 reveals a decline in catalyst activity resulting from blockage of one-eighth (1/8th) of the surface active sites by K, which results in decrease in both formaldehyde selective and methanol conversion at 230 ^{o}C to 75 % and 26 % respectively in comparison to the prepared MoO_3. The increase in CO selectivity to about 25 % at 230 ^{o}C could result from longer residence time of methoxy species or formaldehyde on the surface leading to partial oxidation to CO. Interestingly, formation of formaldehyde, CO and CO_2 at 320 ^{o}C indicates competitive reaction pathways occurring on the catalyst surface which includes preventing the

reduction of Mo^{6+} by K and activation of electrophilic oxygen on defect sites, which promotes selective and complete oxidation respectively.

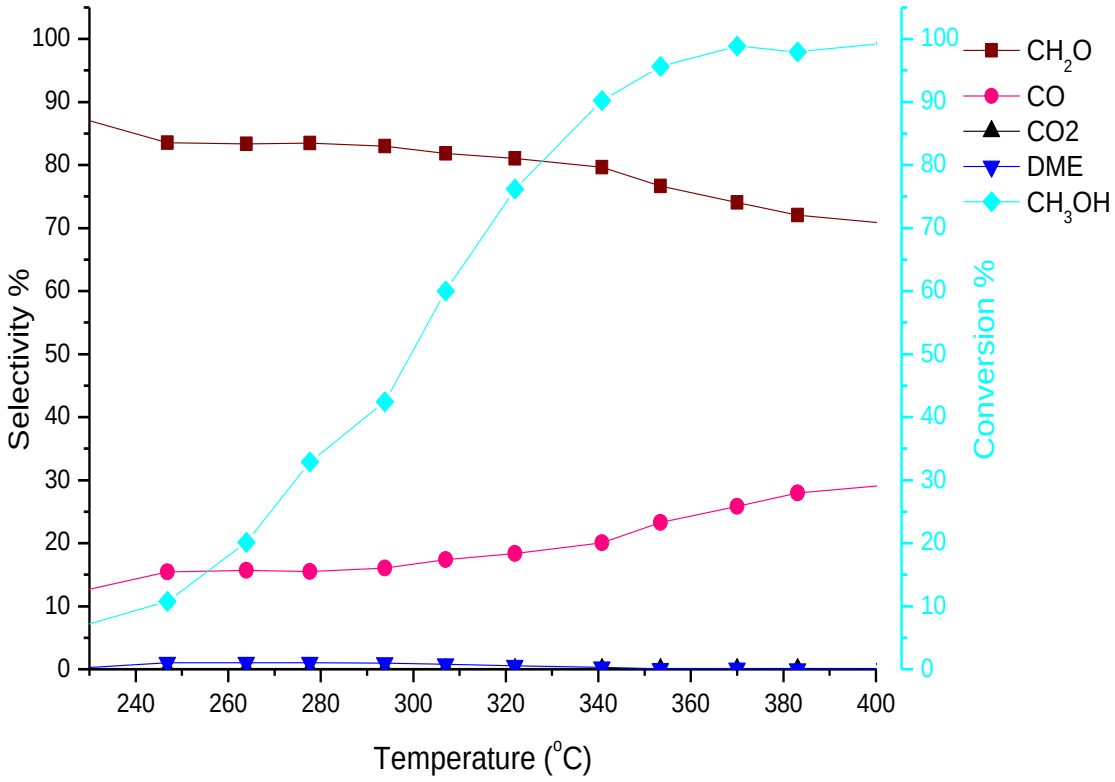

Fig. 3. 18 ***Selectivity and conversion of methanol over 100 % K- MoO_3***

Reaction measurement of methanol oxidation over 100 % K promoted MoO_3 catalyst in Fig. 3. 18 above depicts 85 % selectivity to formaldehyde at ~10 % methanol conversion, with CO selectivity reaching 15 % by 240 ^{o}C. Furthermore, the stability of formaldehyde selectivity (~85 %) extends until 340 ^{o}C, which decline to ~71 % with CO selectivity reaching ~29 % by 380 ^{o}C at about ~98 % methanol conversion.

Potassium doping neutralizes the surface acidity of the prepared MoO_3, by lowering the binding energy of Mo sites essential for dissociative chemisorptions of methanol, resulting in less activity. It also seems to influence surface interaction with molecular oxygen by providing an easier path for dissociative adsorption of gas phase oxygen on the catalyst surface, but blocks the vacant oxygen sites which enhances oxygen

mobility and diffusion within the bulk, as reported by Ozkan and Watson [94]. However, this oxygen species shows similar reactivity as the lattice, inhibiting complete oxidation of formaldehyde to CO_2 at higher temperature.

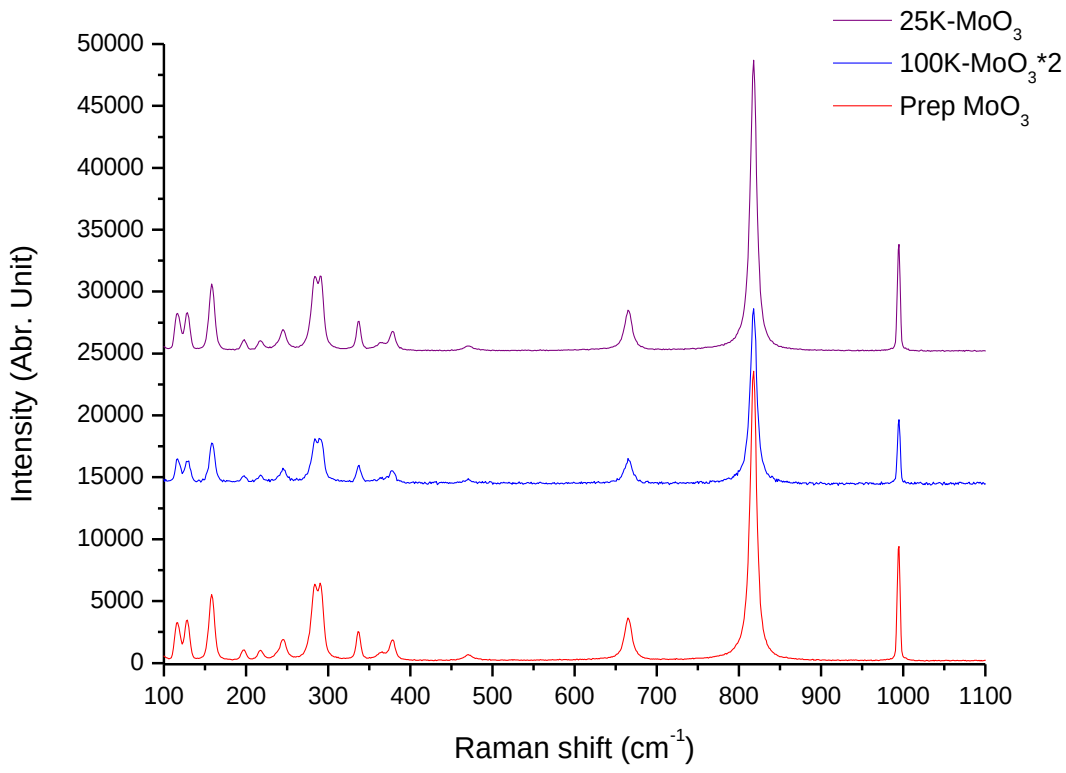

Fig. 3. 19 ***Raman spectra of potassium MoO_3 samples in comparison to prepared sample: red line (prepared), blue (100 % K-MoO_3), and purple (25 % K-MoO_3)***

The Raman spectra in Fig. 3. 19 reveals similar bands at 995, 818, 665, and 470 corresponding to υ_{as} Mo=O stretch, υ_s O-Mo-O stretch of bridge O, υ_{as} O-Mo-O and υ_{as} O-Mo-O stretch and bend vibration mode respectively. Other lower vibration modes ascribed to scissoring, bending, wagging, and twisting were observed at 377-365, 337, 290- 283, and 246 cm^{-1} respectively, with other bands at 216, 197, 159, 129 and 116 cm^{-1} vibration assigned to rotational, twist vibration, and translational rigid MoO_4 chain mode respectively.

The Raman spectra reveal no evidence of additional Raman bands ascribable to $KMoO_4$, even at 100 % K coverage, indicating that the K could remain on the surface of the promoted MoO_3 catalyst or it exists in minute quantity (beyond detection limit by Raman spectroscopy) that was not involved in the formation of a new phase. The 100 % K-MoO_3 sample indicates increase in Raman band intensity of 116 cm^{-1} peak compared to 129 cm^{-1} assigned to translational rigid MoO_4 chain mode. However, there is an observable decrease in Raman band intensity and noise in background of the 100 % K-MoO_3 sample in comparison to prepared and 25 % K-MoO_3 catalyst, which could likely be an electronic effect induced by K at high % monolayer coverage.

Table 3. 7 Analysis of terminal, bridging and wagging Raman bands intensity ratio

MoO_3 sample	**995 cm^{-1} Mo=O (FWHM)**	**818 cm^{-1} Mo-O-Mo (FWHM)**	**I_{995}/I_{818} (Mo=O/Mo-O-Mo)**	**I_{283}/I_{290} (Mo=O wagging)**
Prepared	4.10	9.48	0.12	1.22
25 % K	4.09	9.21	0.13	1.20
100 % K	4.01	9.25	0.13	1.07

The analysis of the Raman bands at 995 and 818cm^{-1} associated with M=O (terminal) and Mo-O-Mo (bridging) oxygens respectively in Table 3. 7 above indicates a decrease in full width half maximum (FWHM) of the spectra with increasing % K coverage. Such band broadening indicates partial reduction in MoO_3, as reported by Smith and Ozkan [23]. However, there is no observable change in I_{995}/I_{818} intensity ratio with K coverage amongst the promoted catalyst, but the wagging mode intensity ratio I_{283}/I_{290} decreases significantly with increasing K coverage. This reveals that the K^+ ion possibly binds on the O^- anion of defect MoO_3 sites as such, decreasing the intensity ratio of the I_{283}/I_{290} wagging vibration, with no observable effect on the I_{995}/I_{818} intensity ratio of the terminal/bridging mode.

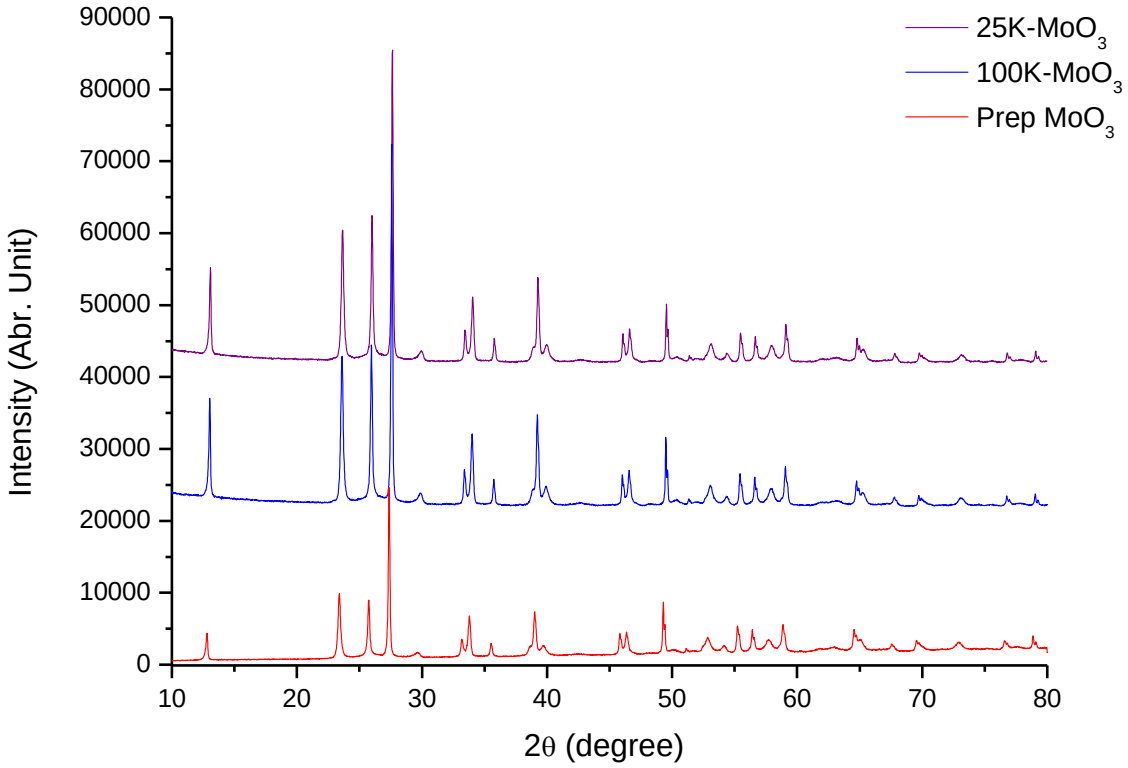

Fig. 3. 20 D*iffractogram of K-promoted MoO_3*

Fig. 3. 20 depicts the diffraction pattern for orthorhombic MoO_3 as indexed in JCPD No.01-076-1003 [86]. It reveals peaks at 2θ value of 12.7 ^{o}, 23.6 ^{o}, 25.9 ^{o}, and 27.6 ^{o} for both K-promoted and the prepared sample, without detection of additional peak

corresponding to a new K_2MoO_4 phase. However, K- doped catalysts exhibit increasing peak intensity in comparison to prepared MoO_3, which increases with K-loading. This increase in peak intensity was previously reported by Driscoll, Gardner, and Ozkan [46] .

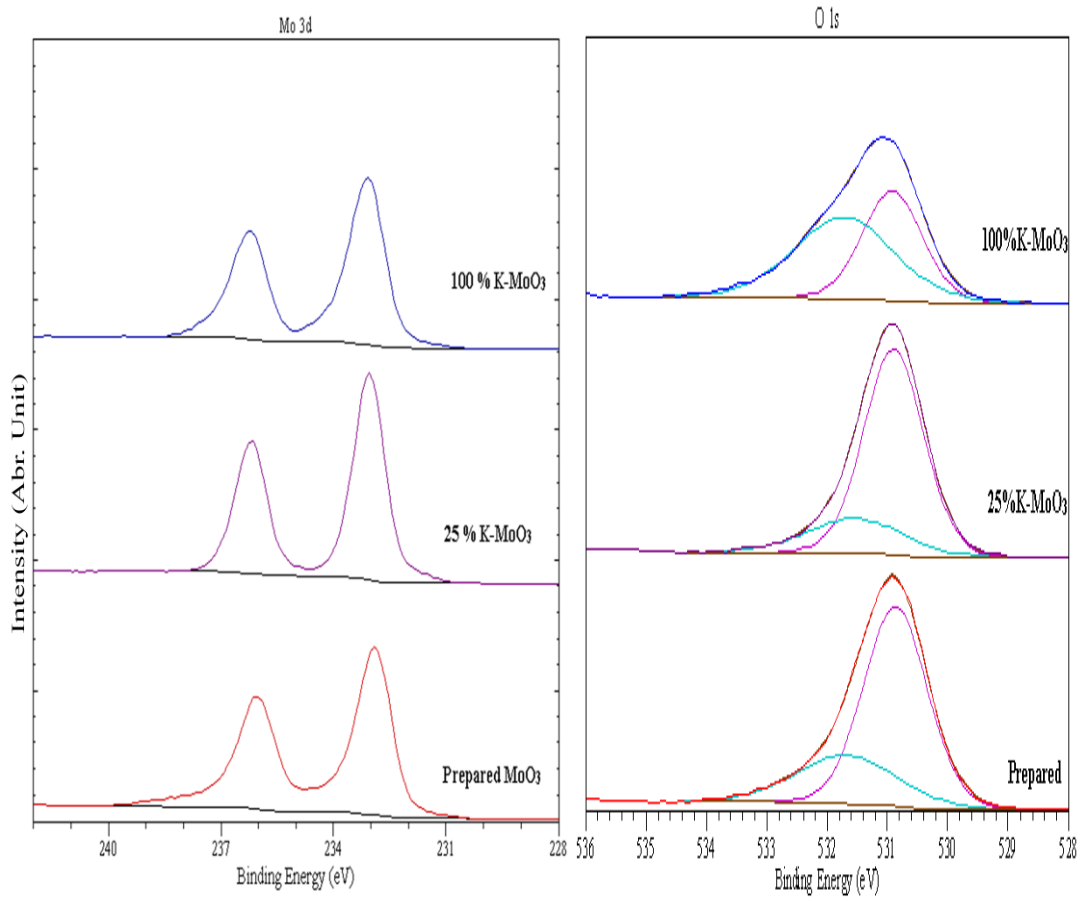

Fig. 3. 21 ***Comparison of XPS of prepared and K-MoO₃ samples***

The Mo doublet in Fig. 3. 21 reveals a binding energies of 233 ± 0.2 eV and 236 ± 0.2 eV attributed to $Mo3d_{5/2}$ and $3d_{3/2}$ components respectively for both the prepared sample, and the K doped sample. Moreover, the prepared samples exhibit a high binding energy peak at 238 ± 0.2 eV. The O1s deconvoluted peak depicts a main peak at a binding energy of 530.9 ± 0.2 eV for all samples, with a slightly higher binding energy at 531.7± 0.2 eV, which is maximised for the 100 % K-MoO_3 sample.

The Mo 3d binding energies of 233 – 233.1± 0.2eV and 236 – 236.2± 0.2eV indicate high oxidation state of Mo^{6+} for all samples, which are in good conformity with results

reported by Smith and Ozkan [23], and Diaz-Droguett et al [95]. The peak at 238 ± 0.2 eV for prepared sample could be attributable to amorphous MoOx species or possible surface charging effect. However, O1s binding energy at 530.9 ± 0.2 eV in all samples reveals a characteristic peak attributed to terminal oxygen (O^{2-}) in a crystalline MoO_3 network, but the high binding energy between 531.5 – 531.7 ± 0.2 eV for the samples could be ascribed to ionized oxygen (O^-) species in the sub lattice of MoO_3, which compensate for its deficiency (net electronic charge balance). The oxygen species exhibit low electron density in comparison to O^{2-} species as previously observed by Dupin et al [90]. The increase in intensity of O1s deconvoluted peak at 231.7 ± 0.2 eV for 100 % K-MoO_3 relative to the prepared sample indicates increasing population of O^- species coordinated onto the subsurface influenced by increasing K loading. K doping on molybdates has previously been reported by Driscoll and Ozkan [45] to promote adsorption and exchange between surface and gas phase oxygen species.

Ferric Molybdate Catalysts

Table 3. 8 BET surface area of varying Fe:Mo ratio in $Fe_2(MoO_4)_3$

Catalyst	BET Surface area (m^2/g)
$Fe_2(MoO_4)_3$ 1.5	**3.4**
$Fe_2(MoO_4)_3$ 2.2	**4.5**

Table 3. *8* shows BET surface area of varying Fe: Mo ratios of $Fe_2(MoO_4)_3$ catalysts, with 1.5 and 2.2 ratios corresponding to surface area of 3.4 and 4.5 m^2/g respectively. The surface area obtained for 2.2 Fe:Mo ratio is greater than 1.5, which is consistent with those reported by Andersson et al [72] for industrial $Fe_2(MoO_4)_3$ catalysts with a stoichiometric (1.5) ratio, which had the lowest surface area than other ratios. This indicates possible well ordered morphology of single phase $Fe_2(MoO_4)_3$. However, the surface area of 2.2 ratio catalyst increases to 4.5 m^2/g, which is attributable segregation of MoOx and formation of excess crystalline MoO_3 phase on the iron molybdates. The increase in surface areas due to increasing Mo ratio for the co precipitated $Fe_2(MoO_4)_3$ are consistent with previous findings reported by House et al [55] and Soares et al [54].

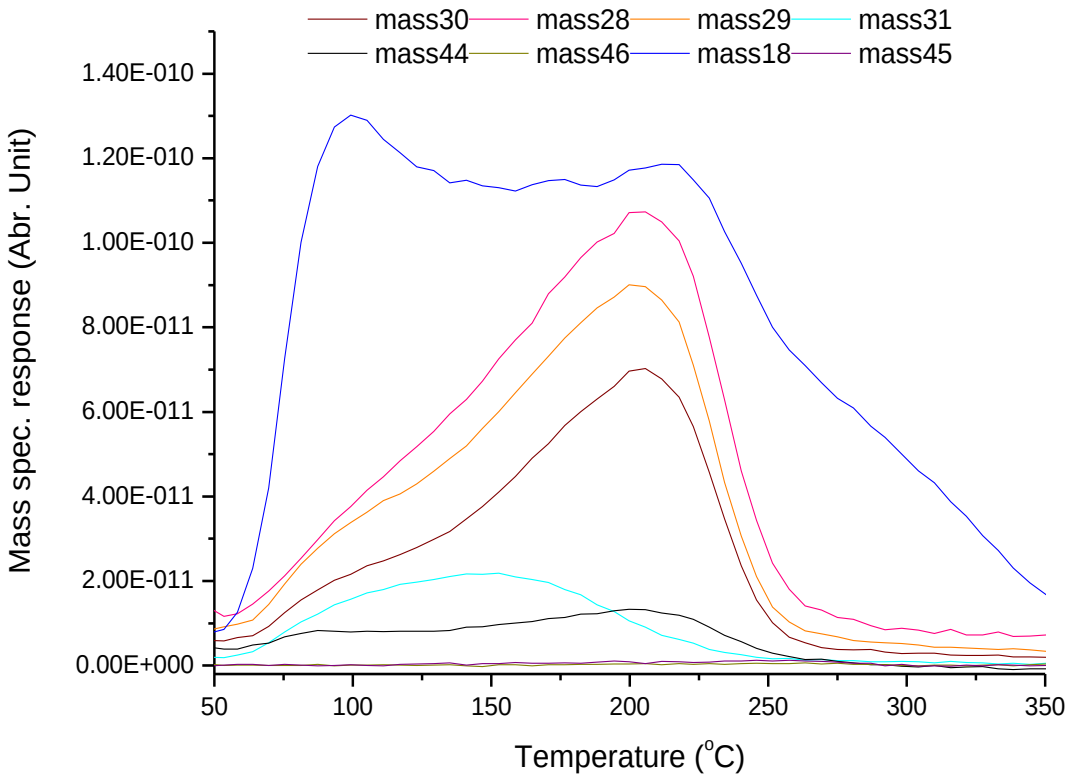

Fig. 3. 22 ***TPD desorption profile for methanol over 1.5 $Fe_2(MoO_4)_3$: water (mass 18), CO_2 (mass 44), methanol (mass 31), CO (mass 28), formaldehyde (mass 30), and DME (mass 45 and 46)***

Fig. 3. 22 illustrates the TPD desorption profile for 1.5 $Fe_2(MoO_4)_3$, with first water desorption peak at ~100 ^oC preceding a methanol desorption peak, which is centred at 150 ^oC. Formaldehyde desorption peak is the only carbon product observed at 204 ^oC between two broad water peaks, with the former at 177 ^oC and latter at 212 ^oC.

The broad methanol desorption peak beginning from 60 – 250 ^oC is associated with molecular adsorbed methanol species, while first water desorption peak at ~100 ^oC could result from recombination of surface hydroxyl species. However, the desorption of the broad water shoulder peak at 177 ^oC after the methanol peak, indicates possible diffusion and recombination of hydroxyl species formed from hydrogen abstracted from molecular adsorbed methanol by surface oxygen species. These species seem to be stable up to 220 ^oC. The formaldehyde desorption peak at 204 ^oC is attributed to

decomposition of surface methoxy species, which agrees with observation made by House et al [55] and Routray et al [81]. The second water peak at 215 ^{o}C, results from recombination of hydroxyl species after abstraction of β-hydrogen.

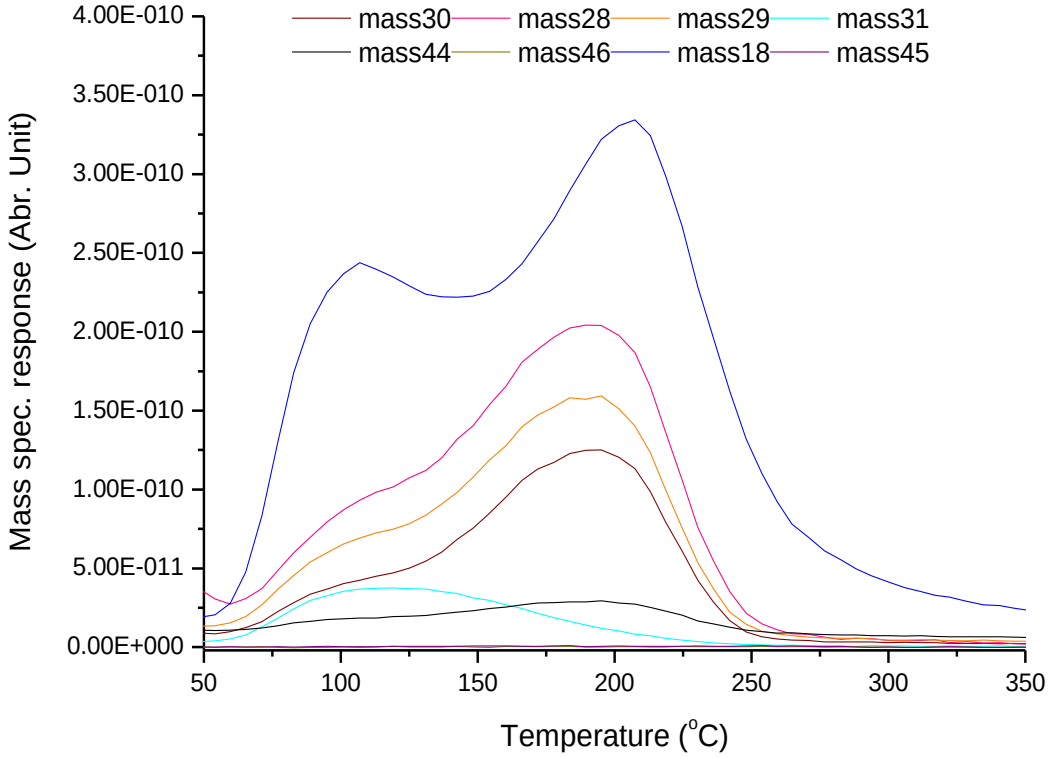

Fig. 3. 23 ***TPD desorption profile for methanol over 2.2 $Fe_2(MoO_4)_3$: water (mass 18), CO_2 (mass 44), methanol (mass 31), CO (mass 28), formaldehyde (mass 30), and DME (mass 45 and 46)***

A TPD profile of 2.2 $Fe_2(MoO_3)_4$ catalyst in Fig. 3. 23 depicts a methanol desorption peak at 100^{o}C, preceding first water desorption peak at 107 ^{o}C. Formaldehyde desorption peak was observed at 190 ^{o}C, prior to second water peak at 207 ^{o}C.

The TPD desorption profile for 2.2 $Fe_2(MoO_3)_4$ reveals a characteristic of redox active sites, producing mainly water and formaldehyde, with the former due to recombination of surface hydroxyl species and the latter resulting from decomposition of surface methoxy species. Formaldehyde desorption peak at 190 ^{o}C is consistent with value obtained for an industrial Perstorp $Fe_2(MoO_3)_4$ catalyst previously reported by Bowker

et al [96], which is known to possess excess Mo phase to replenish lost MoO_3 due to volatilization of polymeric Mo ($MoOx(OCH_3)$ species during reaction.

Table 3. 9 Comparison of activation energy of CH_2O for $Fe_2(MoO_4)_3$ samples

$Fe_2(MoO_4)_3$ Sample	Peak Maximum Temperature (Tm) ^oC	Activation Energy of CH_2O (kJ/mol)
1.5	204	123
2.2	190	120

The activation energies for formaldehyde desorption in Table 3. 9 indicates a value of 123 and 120 kJ/mol for prepared 1.5 and 2.2 ratios $Fe_2(MoO_4)_3$ catalysts respectively.

The above table reveals similar desorption energy of 123 and 120 kJ/mol for stoichiometric and 2.2 $Fe_2(MoO_4)_3$ catalysts.

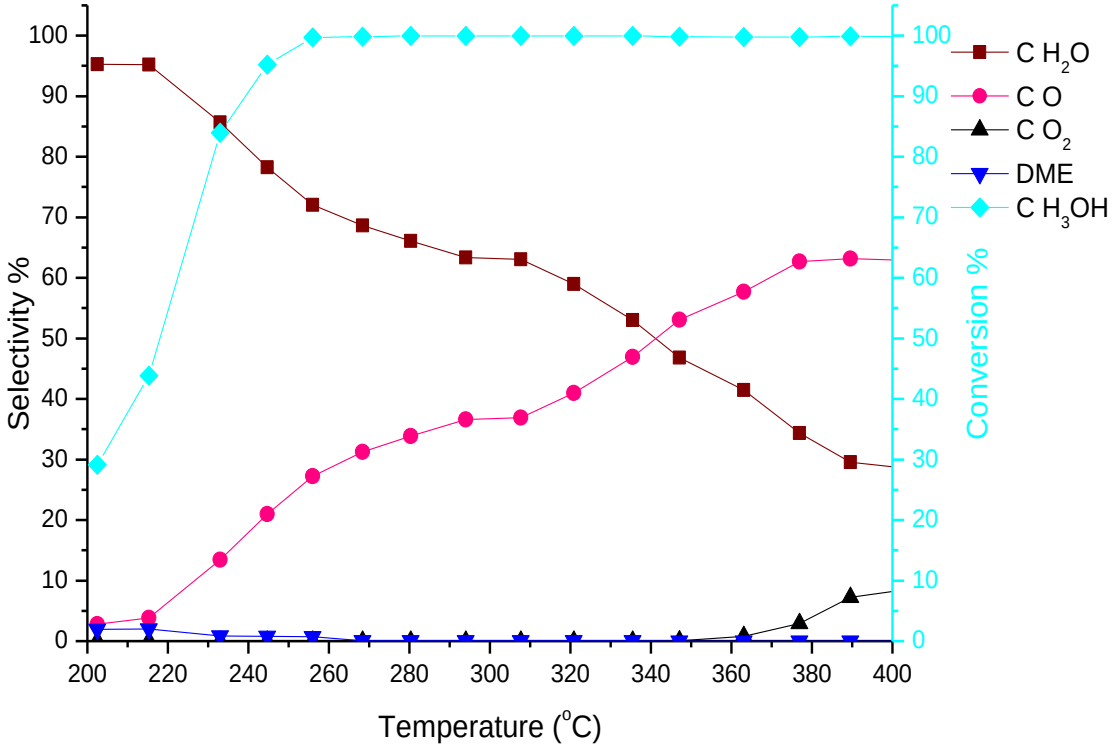

Fig. 3. 24 ***Selectivity and conversion of methanol over 1.5 ratio $Fe_2(MoO_4)_3$***

The reaction profile for methanol oxidation over stoichiometric $Fe_2(MoO_4)_3$ (1.5 ratio) in Fig. 3. 24 above shows 95 % formaldehyde selectivity at ~30 % methanol conversion by 200 ^oC, which declines to 85 % at ~85 % conversion by 230 ^oC. Methanol conversion reaches ~100 % resulting in CO selectivity reaching 35 % by 300 ^oC, with consequential decline in formaldehyde selectivity to 65 %. Decline in formaldehyde selectivity was previously attributed to deactivation of the 1.5 ratio $Fe_2(MoO_4)_3$ by methanol or water, as such aiding formation of $\beta FeMoO_4$ or Fe_2O_3 phase on the catalyst surface as reported by House et al [68] and Soares et al [58]. However, most deactivation studies of $Fe_2(MoO_4)_3$ using CH_3OH or H_2 by Bowker's group [97], Mitov et al [73] and Jacques et al [74] were conducted in the absence of oxygen. Recent in situ studies revealed that reduction of $Fe_2(MoO_4)_3$ to $FeMoO_4$ is much slower than its reverse oxidation process in the presence of oxygen, which is much quicker, as such could not be the possible reason for decline in formaldehyde selective. The plausible explanation could be secondary oxidation of formaldehyde to CO at higher temperature by surface oxygen species (electrophilic in nature) as observed by Routray et al [81] and Pradhan et al [76].

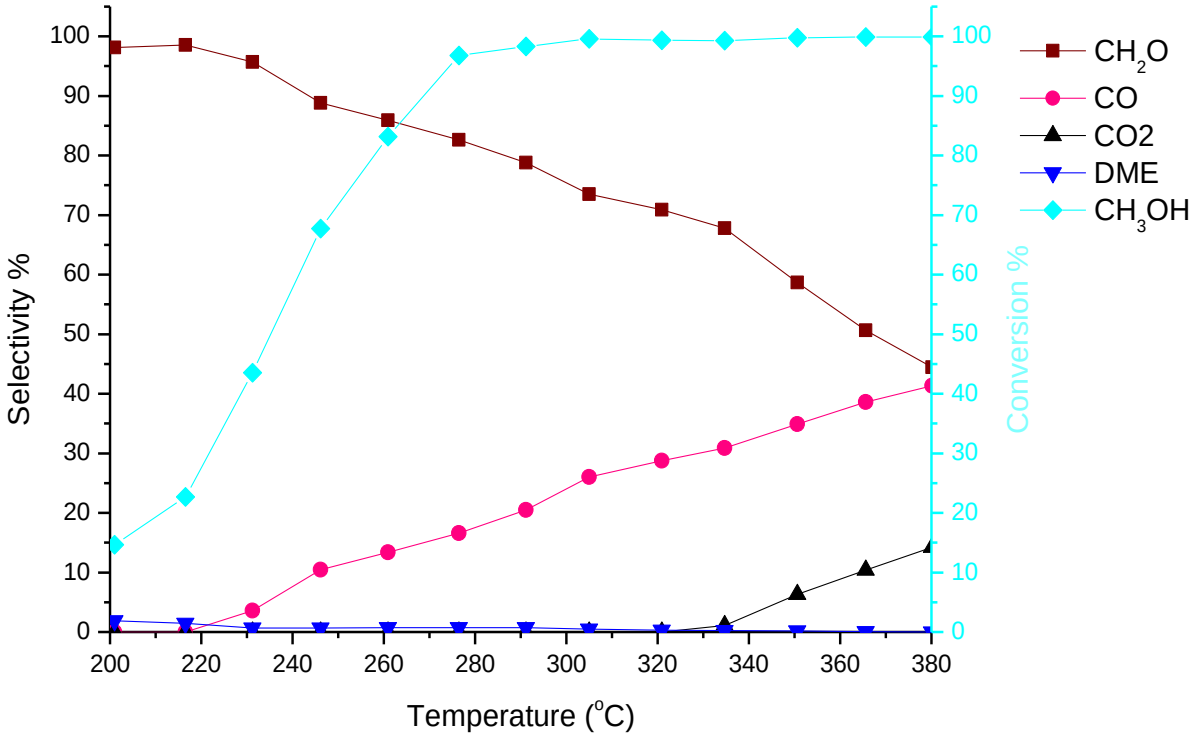

Fig. 3. 25 ***Selectivity and conversion of methanol over 2.2 $Fe_2(MoO_4)_3$***

The reaction profile for 2.2 Mo: Fe ratio catalyst as shown in Fig. 3. **25** depicts 15 % methanol conversion, with formaldehyde and DME selectivity reaching 98 % and 2 % respectively by 200 ^{o}C. Formaldehyde selectivity reaches 86 % at 83 % methanol conversion by 261 ^{o}C, while CO selectivity reaches 13 %. However, at maximum methanol conversion of ~100 %, formaldehyde selectivity declines steadily to 74 % with CO reaching 26 % by 305 ^{o}C, while at 365 ^{o}C CO and CO selectivity increases to 39 % and 11 % respectively as the formaldehyde selectivity drops to 51 %.

The reaction profile for 2.2 ratio reveals enhancement of formaldehyde selectivity by increased Mo loading at the expense of reactivity, which is a characteristic of an excess crystalline MoO_3 phase on bulk $Fe_2(MoO_4)_3$. However, decline in formaldehyde selectivity with alternating increase in CO selectivity could result from possible secondary oxidation of formaldehyde by surface non lattice (electrophilic) oxygen at lower temperature (< 300 ^{o}C), as reported by Routray et al and Deshmukh et al [69]. Since the surface of 2.2 ratio $Fe_2(MoO_4)_3$ is dominated by excess MoO_3, the possibility

of exposure of free Fe sites due to volatilization of Mo is very unlikely, because it will require repeated runs to expose the Fe free site. Moreover, methanol oxidation in O_2 limits the possibility of formation of $FeMoO_4$ phase, since the rate of re oxidation of $FeMoO_4$ to $Fe_2(MoO_4)_3$ in oxygen is faster than its reduction kinetics as confirmed in an in-situ study by Jacques et al [75].

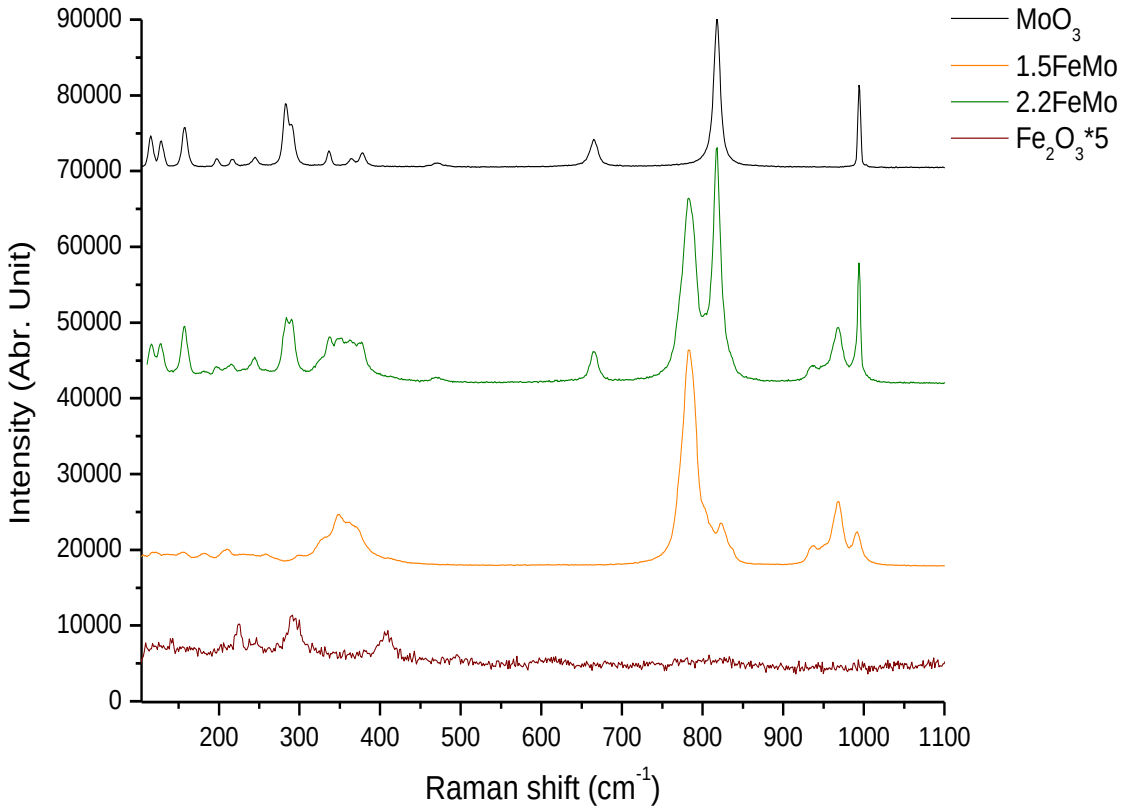

Fig. 3. 26 ***Raman spectra of iron molybdates and component oxides***

Table 3. 10 Raman bands assignment for iron molybdates and molybdenum oxide

Raman band (cm^{-1}) of $Fe_2(MoO_4)_3$		
Fe-Mo 1.5	**Fe-Mo 2.2**	**Assignment**
992	-	υ_s terminal Mo=O stretching in MoO_4
968	968	υ_s terminal Mo=O stretching in MoO_4
938	938	υ_s Mo=O stretching in MoO_4
823	-	υ_{as} O-Mo-O stretch in MoO_4
783	783	υ_{as} O-Mo-O stretch in MoO_4
350	352	terminal Mo=O bending in MoO_4
Raman band (cm^{-1}) of MoO_3 phase in $Fe_2(MoO_4)_3$		
MoO_3	**Fe-Mo 2.2**	**Assignment**
995	994	υ_s terminal Mo=O stretching
818	818	υ_s O-Mo-O stretch
666	664	O=Mo=O wagging vibration
472	473	O=Mo=O twisting vibration
365	363	Mo-O-Mo scissoring
336	338	δ O-Mo-O bend
290-283	290-283	δ O=Mo=O wagging
245	245	τ O=Mo=O twist
156-116	156-116	Translational rigid MoO_4 chain mode

The Raman spectra in Fig. 3. 26 depict Raman bands at 992, 968, and 938 cm^{-1} assigned to Mo=O terminal symmetric vibration of MoO_4 unit in $Fe_2(MoO_4)_3$ as indicated in Table 3. *10* above. Moreover, the bands at 823, 723, and between 348-352 cm^{-1} are ascribed to υ_{as} O-Mo-O stretch in MoO_4 and terminal Mo=O bending in MoO_4 respectively. The $Fe_2(MoO_4)_3$ bands concur with values reported by Hill and Wilson [98], Xu et al [49], and Beale et al [59], with bands at 992 and 823 cm^{-1} recently assigned to Mo=O terminal and υ_{as} O-Mo-O stretch of MoO_4 in $Fe_2(MoO_4)_3$ by Tian et al [99] .

Moreover, bands attributed to the MoO_3 phase were discerned between 994 – 995, 818, 664 – 665, and 469 – 473 cm^{-1}, which are assigned to υ_s terminal Mo=O stretching, υ_s O-Mo-O stretching, υ_{as} O-Mo-O stretching, and O=Mo=O twisting vibration respectively. Other lower MoO_3 Raman bands revealed at 362 – 365, 336 – 338, 290 – 283, and 245 cm^{-1}, are ascribable to Mo-O-Mo scissoring, δ O-Mo-O bend, O=Mo=O wagging, and τ O=Mo=O twisting vibration respectively, which are in conformity with those reported by Routray et al [81] and Py and Maschke [83] for MoO_3. In addition, lower bands between 156 – 116 cm^{-1} are attributed to translational rigid MoO_4 chain mode. These bands were also observed in stoichiometric (1.5 ratio) $Fe_2(MoO_4)_3$ at a slightly higher frequency of 132 and 119 cm^{-1}. However, the bands at 225, 291, and 410 cm^{-1} are consistent with bands reported for Fe_2O_3 by de Faria et al [100].

The Raman spectra of varying Fe:Mo ratios from 1.5 – 2.2 in Fig. 3. 26 and table 3.10 reveal no band associated with free Fe_2O_3, although Fe_2O_3 has a poor Raman scattering effect. The stoichiometric ratios (1.5) iron molybdate catalyst Raman spectra indicates pure $Fe_2(MoO_4)_3$ phase with no band associated with excess MoO_3 phase, although the band at 823 cm^{-1} is not associated with excess MoO_3 phase since the Raman spectra reveals no band at 665, 473, 290-283 cm^{-1} distinct to crystalline MoO_3 phase as reported by Tian et al [99].

However, the 2.2 ratio catalyst reveals an increasing intensity and sharpness of peaks associated with excess crystalline MoO_3 phase, which results in the appearance of extra peaks at 338 and 245 cm^{-1} ascribable to O-Mo-O bending and twisting O=Mo=O vibration respectively. The increase in the intensity ratio of the MoO_3 peak at 818 cm^{-1} in 2.2 ratio in comparison to $Fe_2(MoO_4)_3$ peak at 783 cm^{-1}, evidence segregation of excess crystalline MoO_3 phase over bulk $Fe_2(MoO_4)_3$. The high intensity of the 818 cm^{-1} band in comparison to the 783 cm^{-1}, is typical characteristic of $Fe_2(MoO_4)_3$ catalysts prepared by maintaining the pH at 2 as previously observed by Hills and Wilson [98].

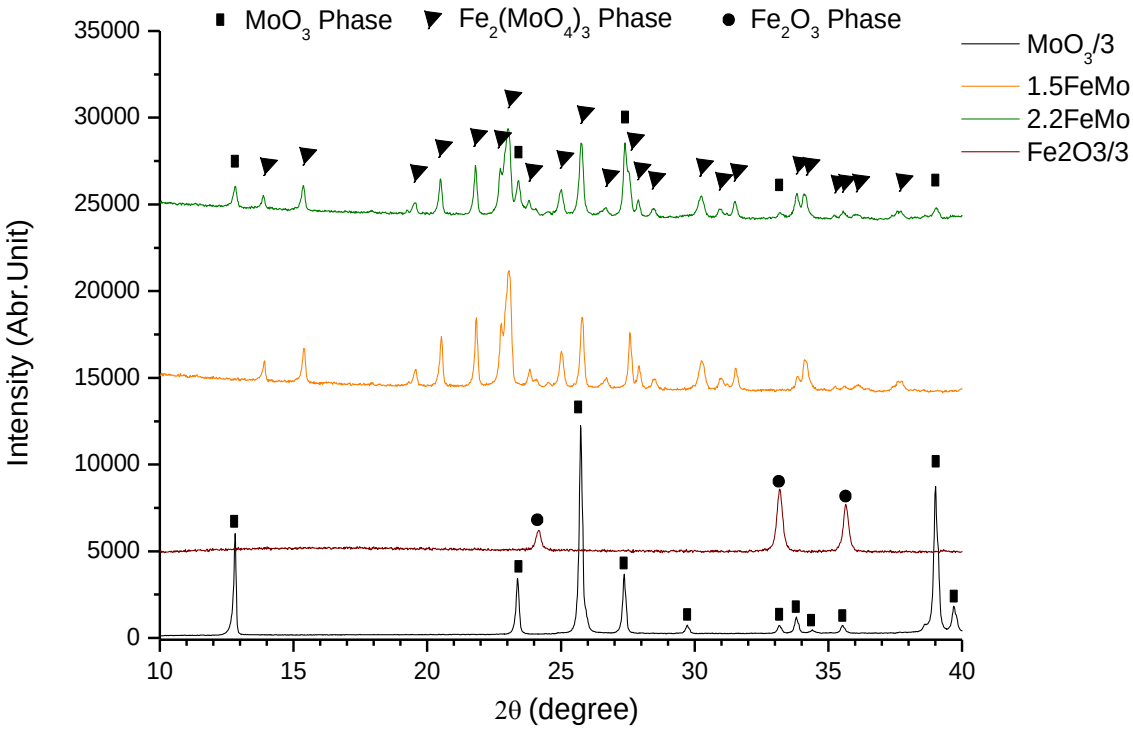

Fig. 3. 27 ***Comparison of X-ray powder diffraction of Fe_2O_3, $Fe_2(MoO_4)_3$ and MoO_3 phases***

The X-ray powder diffractogram in Fig. 3. 27 shows 2θ peaks at 13.91 °, 15.39 °, 19.58 °, 20.53 °, 21.84 °, and 22.77 ° attributed to monoclinic $Fe_2(MoO_4)_3$ phase as indexed in JCPDS no. 00-035-0183 [101] for 1.5 $Fe_2(MoO_4)_3$ (stoichiometric ratio) catalysts. However, the 2.2 ratio reveal peaks at 2θ value of 12.83 °, 30.98 °, with additional

peaks observed at 23.84 °, 33.84 °, and 39.04 °, which corresponds to MoO_3 phase as indexed in JCPDS no. 01-076-1003 [86].

The 1.5 ratio indicates formation of pure bulk $Fe_2(MoO_4)_3$, with no peaks corresponding to free iron oxides phase. Meanwhile, the appearance of additional peaks 12.83°, 30.98°, 23.84°, 33.84°, and 39.04° in 2.2 ratio, evidence the presence of excess crystalline MoO_3 phase on the bulk $Fe_2(MoO_4)_3$, which is agreement with previous phase observed by House et al [55] and Pradhan et al [76] for powder diffraction $Fe_2(MoO_4)_3$ samples.

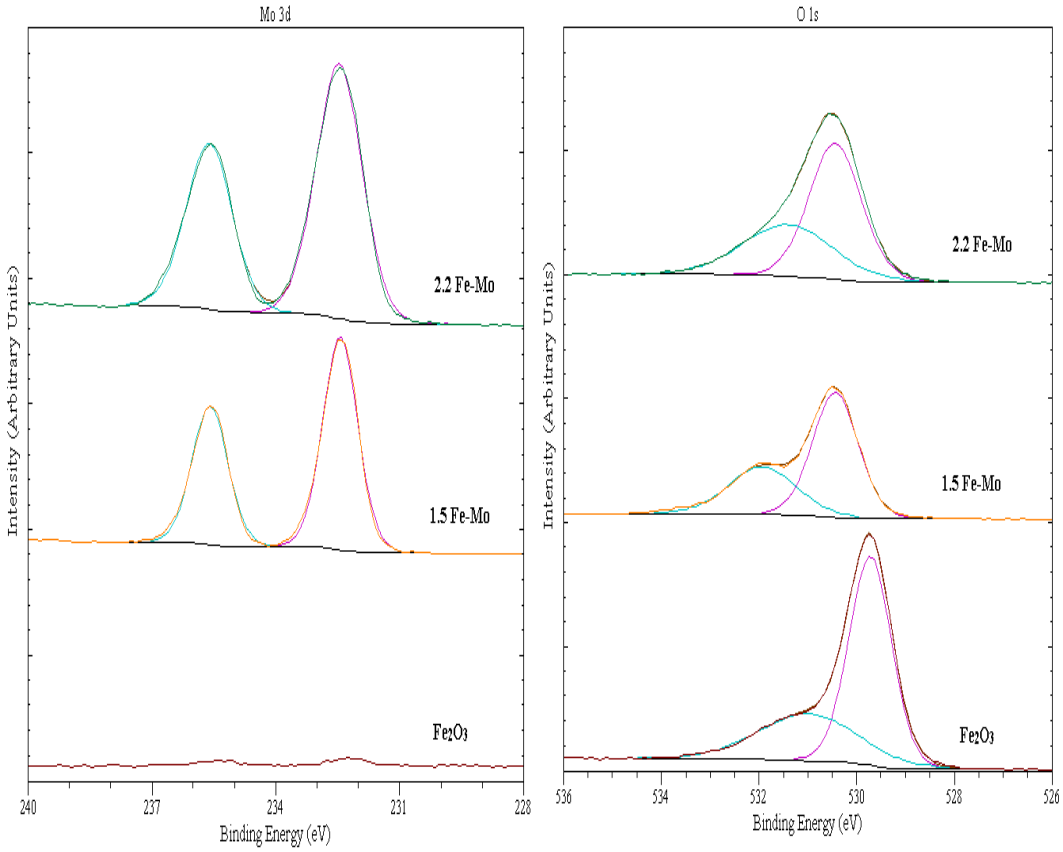

Fig. 3. 28 ***XPS spectra for Mo 3d and O1s in iron molybdates and iron oxide***

Table 3. 11 Binding energies of Mo 3d, O1s and Fe 2p in iron molybdates and iron oxide

Sample	Binding Energy (eV)				
	Mo $3d_{5/2}$	**FWHM**	**Mo $3d_{3/2}$**	**O1s**	**Fe $2p_{2/3}$**
2.2 Fe-Mo	232.5 ± 0.1	1.3	235.6 ± 0.1	531.4, 530.4 ± 0.1	711.6
1.5 Fe-Mo	232.4 ± 0.1	0.9	235.6 ± 0.1	531.9, 530.4 ± 0.1	711.4
Fe_2O_3	-	-	-	529.7, 530.9	710.9

XPS spectra in Fig. 3.28 and data in Table 3.11 reveal Mo 3d binding energies for iron molybdates at 232.4 ± 0.1eV and 235.6 ± 0.1eV for $3d_{5/2}$ and $3d_{3/2}$ components respectively, with Fe $2p_{2/3}$ binding energies ranging between 711.4 – 711.6eV. Moreover, the peak fitting of O1s reveals binding energies ranging between 530.4 – 531.9± 0.1eV.

The Mo 3d and Fe 2p binding energy reveal high oxidation state of Mo^{6+} and Fe^{3+} for both Mo and Fe respectively in all ratios of $Fe_2(MoO_4)_3$ catalysts, which are in agreement with those previous reported by House et al [55] and Xu et al [49] . However, the increase in $Mo3d_{5/2}$ full width half maximum (FWHM) from 0.9 – 1.3 signifies increase in Mo segregation on bulk $Fe_2(MoO_4)_3$ due to an increase in Mo loading. This results in slightly different Mo 3d binding energy of the $Fe_2(MoO_4)_3$ catalysts. Moreover, The O1s binding energy of 530.4 ± 0.1 eV could be assigned to terminal oxygen (O^{2-}) in $Fe_2(MoO_4)_3$ network, while the binding energy at 531.4 eV in 2.2 $Fe_2(MoO_4)_3$ ratios could be attributed to oxygen deficiency (O^-) or possibly OH species on excess MoO_3 on bulk $Fe_2(MoO_4)_3$. Interestingly, the stoichiometric $Fe_2(MoO_4)_3$ reveals a higher binding energy of O1s at 531.9 eV, which could be attributed to bridging oxygen binding MoO_4 tetrahedron to FeO_6 octahedron in pure $Fe_2(MoO_4)_3$ phase.

Fe_2O_3 exhibits Fe^{3+} oxidation state with $2p_{2/3}$ and O1s BE of 710 eV and 529.7 eV with shoulder peak at 530.9 eV, which is consistent with values reported by McIntyre and Zetaruk [102], and Grosvenor et al [103] for α-Fe_2O_3. The O1s binding at 529.7 and 530.9 could be ascribable to O^{2-} in Fe network and O^- in oxygen deficient site or adsorbed OH species in Fe_2O_3 respectively.

3.3 Summary

In summary, the results in this chapter indicate:

The prepared MoO_3 sample reveals oxygen defect sites (Lewis acid) as well as amorphous MoOx phase, which are catalytic active sites for methanol chemisorptions and formation of electrophilic-like (O^{*-}) surface oxygen from molecular oxygen at lower temperature(< 300 ^oC).

The defect sites on prepared MoO_3 catalyst provide a lower energy pathway for formaldehyde desorption at 178 ^oC and higher selectivity of 95 % at 80 % methanol conversion at 253 ^oC.

The commercial MoO_3 (BDH) sample although highly selective to formaldehyde (~100 %), is less active due to low surface area and plate-like morphology with completely saturated Mo^{6+} coordinated to a nucleophilic oxygen (O^{2-}) species.

Lattice oxygen diffusion from bulk to surface of MoO_3 is rather slow, but only appreciable above 300 ^oC, which increases with formation of defect sites on MoO_3 surface.

Potassium (K) doping of the prepared MoO_3 decrease reducibility of the Mo^{6+} site by neutralizing the Lewis acid sites, as well as controlling gas phase oxygen adsorption and diffusion within the bulk.

It also exhibits significant influence on intensity ratio of the I_{283}/I_{290} wagging vibrations with increasing coverage, but does not reveal any observable influence on the in I_{995}/I_{818} intensity ratio ascribable to terminal (M=O) and bridging (Mo-O-Mo) Raman vibration mode.

The 100 % K doping of the defect MoO_3 enhances formaldehyde selectivity at higher temperature and prevents deeper oxidation of formaldehyde to CO_2, but adversely affects the activity of the catalyst.

K doping below complete surface coverage (25 %) promotes formation of stable methoxy species which increases formaldehyde desorption temperature, and enhances diffusion and reaction between adsorbed methoxy species and hydroxyl species on the surface.

Amorphous MoOx on bulk on $Fe_2(MoO_3)_4$ is the active phase as evident from reactor study of stoichiometric ratios.

The control and maintenance of pH at 2 during co precipitation of precursors is essential in achieving $Fe_2(MoO_3)_4$ catalyst with greater dispersion of MoO_3 on its surface as evidenced by Raman, XRD, and XPS characterization.

The excess crystalline MoO_3 phase on 2.2 ratio $Fe_2(MoO_4)_3$ enhances formaldehyde selectivity at higher reaction temperature compared to 1.5 ratio, and acts as Mo reservior for replenishment of lost Mo and a source for MoOx species necessary to maintain catalytic activity.

The CO formation on MoO_3 excess $Fe_2(MoO_4)_3$ could possibly result from secondary oxidation of formaldehyde by surface adsorbed oxygen (O^{*-}) species at low temperature ($< 300^oC$).

3.4 Conclusion

The study of methanol oxidation over molybdenum oxides, K-doped molybdenum oxide and ferric molybdates, and characterization studies by BET, Raman, XRD, SEM and XPS aimed at understanding behaviour of unsupported molybdenum oxides and molybdenum based oxides catalyst in this chapter has shown that: MoO_3 demonstrates structural sensitivity during methanol oxidation to formaldehyde. It reveals high selectivity to formaldehyde on fully coordinated Mo^{6+} in BDH sample. However, the oxygen defect sites on the prepared MoO_3 promote higher activity and selectivity to formaldehyde during methanol oxidation at low temperature, creating a less energetic pathway for formaldehyde production. CO formation could result from secondary oxidation of formaldehyde by non-lattice surface electrophilic oxygen (O^{*-}) species generated from the defect sites, which need to be accounted for in considering reaction mechanism of methanol oxidation on MoO_3. The regeneration of redox sites on MoO_3 is rather slow, which implies lack of adherence to Mars-van Krevelen mechanism at low temperature (< 300 ^{o}C).

However, potassium doping on defective MoO_3 modifies the surface electronic structure, by knocking off Lewis acids sites, as such decreasing the reducibility of Mo^{6+}.This profoundly increases the formaldehyde selectivity at high temperature for the 100 % K-MoO_3 catalyst, with adverse effect on activity. The K promoter also controls adsorption and diffusion of gas phase oxygen on to the surface, as such suppressing secondary oxidation of formaldehyde to CO.

In addition, characterization and reaction study confirms that the activity of $Fe_2(MoO_4)_3$ is due to the MoOx phase on bulk $Fe_2(MoO_4)_3$, while the crystalline excess MoO_3 phase serves as a reservoir for maintaining the MoOx phase as well as replenishing lost Mo species. The high formaldehyde selectivity of Mo-rich $Fe_2(MoO_4)_3$ (2.2 ratio) sample is attributed to the crystalline MoO_3 phase as evidenced by Raman , XRD and XPS results. However, decline in formaldehyde selectivity resulting in CO production could be due to secondary oxidation of formaldehyde by electrophilic adsorbed surface oxygen. The findings indicate no synergetic effect between the crystalline MoO_3 and bulk $Fe_2(MoO_4)_3$.

References

1. Cornell RM, Schwertmann U. The iron oxides: Structure, properties, reactions, occurences and uses. 2nd ed. Weinheim, Germany: Wiley-VCH; 2003.

2. Xu P, Zeng GM, Huang DL, Feng CL, Hu S, Zhao MH, et al. Use of iron oxide nanomaterials in wastewater treatment: a review. Science of the Total Environment. 2012;424:1-10.

3. Vedrine JC, Coudurier G, Millet M J. Molecular design of active sites in partial oxidation reactions on metallic oxides Catal Today. 1997;33:3-13.

4. Haber J, Lalik E. Catalytic properties of MoO_3 revisted. Catal Today. 1997;33: 119-37.

5. Grasselli RK. Fundamental principles of selective heterogeneous oxidation catalysis. Top Catal. 2002;21(1-3):79-88.

6. Kihlborg L. The structure of MoO_3. Ark Kemi 1963;21:357–64.

7. Coquet R, Willock D J. The (010) surface of a-MoO_3, a DFT + U study. Phys Chem Chem Phys. 2005; 7 3 8 1 9 – 3 8 2 8.

8. Lei Y-H, Chen, Z-X. DFT+U study of properties of MoO_3 and hydrogen adsorption on MoO_3(010) J Phys Chem C 2012; 116:25757−64.

9. Tatibouet JM, Germain JE. A structure-sensitive oxidation reaction: Methanol on molybdenum trioxide catalysts. J Catal. 1981;72(2):375-8.

10. Abon M, Massardier J, Mingot B, Volta JC, Floquet N, Bertrand O. New unsupported [100]-oriented MoO_3 catalysts II. Catalytic properties in propylene oxidation. J Catal 1992;134(2):542 – 8.

11. Vedrine JC. Revisiting active sites in heterogeneous catalysis: Their structureand their dynamic behaviour. Appl Catal A Gen. 2014;474 40–50.

12. Farneth WE, Ohuchi F, Staley RH, Chowdhry U, Sleight AW. Mechanism of partial oxidation of methanol over MoO_3 as studied by temperature-programmed desorption. J Phys Chem 1985;89 2493-7.

13. Machiels CJ, Cheng WH, Chowdhry U, Farneth WE, Hong F, Mc Carron EM, et al. The effect of structure of molybdenum oxides on the selective oxidation of methanol. Appl Catal 1986;15(1-2):249 – 56

14. Farneth WE, McCarron III EM, Sleight AW, Staley RH. Comparison of the surface chemistry of two polymorphic forms of molybdenum trioxide. Langmuir. 1987;3(2):217-23.

15. Chung JS, Miranda R, Bennett CO. Mechanism of partial oxidation of methanol over MoO_3. J Catal. 1988;114(2):398 – 410.

16. Allison JN, Goddard III, WA. Oxidative dehydrogenation of methanol to formaldehyde. J Catal. 1985;92(1):127 – 35.

17. Gai-Boyes PL. Defect in oxide catalysts: Fundamental studies of catalysis in action. Catal Rev Sci Eng. 1992; 34(1):1-54.

18. Smith RL, Rohrer GS. An atomic force microscopy study of the morphological evolution of the MoO_3 (010) surface during reduction reaction. J Catal. 1996; 163:12 – 7.

19. O'Keeffe M, editor Solid state batteries, and devices proceeding of the NATO advanced study institutes; 1973; North – Holland, Amsterdam.

20. Greenblatt M. Molybdenum oxide bronzes with quasi-low- dimensional properties. Chem Rev. 1988;88(1):31-5.

21. Smith RL, Rohrer GS. The protonation of MoO_3 during the partial oxidation of alcohols. J Catal. 1998;173(1):219 – 28.

22. Cheng W. Methanol and formaldehyde oxidation over molybdenum oxide. J Catal. 1996; 158(2):477 – 85.

23. Smith MR, Ozkan US.The partial oxidation of methane to formaldehyde: Role of different crystal planes of MoO_3. J Catal. 1993;141:124 – 39.

24. Ressler T, Wienold J, Jentoft RE, Neisius T. Bulk structural investigation of the reduction of MoO_3 with propene and the oxidation of MoO_2 with oxygen. J Catal. 2002; 210:67-83.

25. Ressler T, Wienold J, Jentoft R, Girgsdies F. Evolution of defects in the bulk structure of MoO_3 during the catalytic oxidation of propene. Eur J Inorg Chem 2003 (2):301-12.

26. Lalik E, David WIF, Barnes P, Turne JFC. Mechanisms of reduction of MoO_3 to MoO_2 reconciled? J Phys Chem B 2001;105:9153-6.

27. Bowker M, Carley AF, House M . Contrasting the behaviour of MoO_3 and MoO_2 for the oxidation of methanol. Catalysis Letter 2008; 120: 34 – 9.

28. Mestl G, Ruiz P, Delmon B, Knozinger H. Oxygen-exchange properties of MoO_3: An in situ Raman spectroscopy study. J Phys Chem 1994;98 11269-75.

29. Mizushima T, Fukushima K, Ohkita H, Kakuta N . Synthesis of b-MoO_3 through evaporation of HNO_3-added molybdic acid solution and its catalytic performance in partial oxidation of methanol. Appl Catal A Gen. 2007;326:106 – 12.

30. Mizushima T, Moriya Y, Huy Phuc NH, Ohkita H, Kakuta N. Soft chemical transformation of α-MoO_3 to β-MoO_3 as a catalyst for vapor-phase oxidation of methanol. Catal Commun 2011;13 10–3.

31. Hermann K, Witko M, Michalak A. Density functional studies of the electronic structure and adsorption at molybdenum oxide surfaces. Catal Today 1999;50:567-77.

32. Tokarz-Sobieraj R, Hermann K, Witko M, Blume A, Mestl G, Schlogl R. Properties of oxygen sites on at the MoO_3 (010) surface: density functional theory cluster studies and photoemission experiments. Surface Science. 2001;489:107-25.

33. Chen M, Friend CM, Efthimios Kaxiras. The chemical nature of surface point defects on MoO_3(010): Adsorption of hydrogen and methyl. J Am Chem Soc 2001;123:2224-30.

34. Cavalleri M, Hermann K, Guimond S, Romanyshyn Y, Kuhlenbeck H, Freund H-J. X-ray spectroscopic fingerprints of reactive oxygen sites at the MoO_3 (0 1 0) surface. Catal Today 2007;124:21–7.

35. Bielanski A, Haber J. Oxygen in catalysis. New York: Marcel Dekker, Inc.; 1991.

36. Panov GI, Dubkov KA, StaroKon EV. Active oxygen in selective oxidation catalysis. Catal Today. 2006;117:148-55.

37. Zhao C, Wachs IE. An operando Raman, IR, and TPSR spectroscopic investigation of the selective oxidation of propylene to acrolein over a model supported vanadium oxide monolayer catalyst. J Phys Chem C 2008;112:11363–72.

38. Wachs I, Roberts CA. Monitoring surface metal oxide catalytic active sites with Raman spectroscopy. Chem Soc Rev 2010;39:5002-17.

39. Carley AF, Davies PR, Robert MW. Oxygen transient states in catalytic oxidation at metal surfaces. Catal Today 2011;169: 118–24.

40. Bowker M. Effect of sintering on active site distribution on promoted catalysts. Appl Catal 1988;45(1):115-30.

41. Grzybowska-Swierkosz B. Effect of additives on the physicochemical and catalytic properties of oxide catalysts in selective oxidation reactions. Top Catal 2002; 21(1–3):35-46.

42. Chen K, Xie S, Bell AT, Iglesia E. Alkali effects on molybdenum oxide catalysts for the oxidative dehydrogenation of propane. J Catal 2000;195:244–52.

43. Klisin´ska A, Samson K, Gressel I, Grzybowska B. Effect of additives on properties of V_2O_5/SiO_2 and V_2O_5/MgO catalysts I. Oxidative dehydrogenation of propane and ethane. Appl Catal A: Gen 2006; 309:10–6.

44. Botella P, Concepcion P, Lopez Nieto JM, Soisona B. Effect of potassum doping on the catalytic behaviour of Mo-V-Sb mixed oxide catalyst in the oxidation of propene to acrylic acid. Catalysis Letter. 2003;89(3-4):249.

45. Driscoll AD, Ozkan US. Transient isotropic labelling using $^{16}O_2/^{18}O_2$ over alkaline-metal-promoted molybdate catalyst in oxidation coupling of methane. J Phys Chem 1993;97:11524-9.

46. Driscoll AD, Gardner DK, Ozkan US. Characterization, activity, and adsorption/desorption behaviour of alkali-promoted molybdate catalysts for the oxidative coupling of methane J Catal. 1994;147:379-92.

47. Zhaoa Z, Liua J, Duan A, Xu C, Kobayashi T, Wachs IE. Effects of alkali metal cations on the structures, physico-chemical properties and catalytic behaviors of silica-supported vanadium oxide catalysts for the selective oxidation of ethane and the complete oxidationof diesel soot. Top Catal 2006;38(4):309-25.

48. Rapposch MH, Anderson JB, Kostiner E. Crystal structure of ferric molybdate, $Fe_2(MoO_4)_3$. Inorg Chem 1980 19:3531-9.

49. Xu Q, Jia G, Zhang J, Feng F, Li C. Surface phase composition of iron molybdate catalysts studied by UV Raman spectroscopy. J Phys Chem C 2008;112: 9387–93.

50. Hader RN, Wallace RD, McKinney RW. Formaldehyde from Methanol. Ind Eng Chem. 1952;44(7):1508 – 18.

51. Qiam M, Liauw MA, Emig G. Formaldehyde synthesis from methabol over silver catalysts. Appl Catal A: Gen 2003; 238:211 - 22.

52. Adkins H, Peterson WR. The oxidation of methanol with air over iron, molybdenum, and iron-molybdenum oxides. J Am Chem Soc 1931;53 1512 – 20.

53. Sun-Kou MR, Mendioroz S, Fierro JLG, Palacios JM, Guerrero-Ruiz A. Influence of the preparation method on the behaviour of Fe-Mo catalysts for the oxidation of methanol. J Mater Sci. 1995;30(496-503).

54. Soares APV, Farinha Portela M, Kiennemann A, Hilaire L, Millet JMM. Iron molybdate catalysts for methanol to formaldehyde oxidation: effects of Mo excess on catalytic behaviour. Appl Catal A: Gen 2001;206: 221–9.

55. House MP, Carley AF, Echeverria-Valda R, Bowker M. Effect of varying the cation ratio within iron molybdate catalysts for the selective oxidation of methanol. J Phys Chem C 2008;112: 4333-41.

56. Huang Y, Cong L, Yu J, Eloy P, Ruiz P. The surface evolution of a catalyst jointly influenced by thermal spreading and solid-state reaction: A case study with an Fe_2O_3–MoO_3 system. J Mol Catal A: Chem. 2009;302:48–53.

57. Li J-L, Zhang Y-X, Liu C-W, Zhu Q-M. Improvement in reactivity, reproducibility and stability of Fe-Mo catalysts by wet mixing. Catal Today 1999;51:195-9.

58. Soares APV, Portela M F, Kiennemann A, Hilaire L. Mechanism of deactivation of iron-molybdate catalysts prepared by coprecipitation and sol–gel techniques in methanol to formaldehyde oxidation. Chem Eng Sci 2003;58:1315-22.

59. Beale AM, Jacques SDM, Sacaliuc-Parvalescu E, O'Brien MG, Barnes P, Weckhuysen BM. An iron molybdate catalyst for methanol to formaldehyde conversion prepared by a hydrothermal method and its characterization. Appl Catal A: Gen 2009;363:143–52.

60. Bowker M, Brookes C, Carley AF, House MP, Kosif M, Sankar G, et al. Evolution of active catalysts for the selective oxidative dehydrogenation of methanol on Fe_2O_3 surface doped with Mo oxide. Phys Chem Chem Phys. 2013;15:12056-67.

61. Brookes C, Wells PP, Cibin G, Dimitratos N, Jones W, Morgan DJ, et al. Molybdenum oxide on Fe_2O_3 core−shell catalysts: Probing the nature of the structural motifs responsible for methanol oxidation catalysis. ACS Catal. 2014;4:243−50

62. Okamoto Y, Morikawa F, OH-Hiraki K, Imanaka T, Teranishi S. Role of excess of M_OO, in Fe,O,-MoO, methanol oxidation catalysts studied by X-Ray photoelectron spectroscopy. JCS CHEM COMM. 1981:1018-9.

63. Soares APV, Farinha Portela M. Methanol selective oxidation to formaldehyde over iron-molybdate catalysts. Catal Rev. 2004;47:125-74.

64. House MP, Shannon MD, Bowker M. Surface segregation in iron molybdate catalysts. Catalysis Letter. 2008;122:210–3.

65. Soderhjelm E, House MP, Cruise N, Holmberg J, Bowker M, Bovin J, et al. On the Synergy effect in MoO_3–$Fe_2(MoO_4)_3$ catalysts for methanol oxidation to formaldehyde. Top Catal. 2008.

66. Routray K, Zhou W, Kiely CJ, Grünert W, Wachs IE. Origin of the synergistic interaction between MoO_3 and iron molybdate for the selective oxidation of methanol to formaldehyde. J Catal. 2010;275(1):84-98.

67. Wachs IE, Routray K. Catalysis science of bulk mixed oxides. ACS Catal. 2012;2:1235-46.

68. House PM, Carley AF, Bowker M. Selective oxidation of methanol on iron molybdate catalysts and the effects of surface reduction. J Catal. 2007;252:88–96.

69. Deshmukh SARK, Annaland M, Kuipers JAM. Kinetics of the partial oxidation of methanol over a Fe-Mo catalyst. Appl Catal A: Gen. 2005;289(2):240-55.

70. Ivanov KI, Dimitrov DY. Methanol oxidation over iron-molybdate catalysts: optimization of the process. Top Catal. 2009;52:813–22.

71. Ivanov KI, Dimitrov DY. Deactivation of an industrial iron-molybdate catalyst for methanol oxidation. Catal Today 2010;154 250–5.

72. Andersson A, Hernelind M, Augustsson O. A study of the ageing and deactivation phenomena occurring during operation of an iron molybdate catalyst in formaldehyde production. Catal Today 2006;112: 40–4.

73. Mitov I, Asenov S, Tomov T, Klissurski D. In situ mossbauer study of the interaction of methanol with an iron-molybdenum oxide catalyst. J Phys Chem C. 2007;111: 5389-93.

74. Jacques SDM, Leynaud O, Strusevich D, Beale AM, Sankar G, Martin CM, et al. Redox behavior of Fe-Mo-O catalysts studied by ultrarapid in situ diffraction. Angew Chem Int Ed 2006; 45:445 –8.

75. Jacques SMD, Leynaud O, Strusevich D, Stukas P, Barnes P, Sankar G, et al. Recent progress in the use of in situ X-ray methods for the study of heterogeneous catalysts in packed-bed capillary reactors. Catal Today. 2009;145:204–12.

76. Pradhan S, Bartley JK, Bethell D, Carley AF, Conte M, Golunski S, et al. Non-lattice surface oxygen species implicated in the catalytic partial oxidation of decane to oxygenated aromatics. Nat Chem. 2012;4:134-9.

77. Bowker M, Holroyd R, Elliott A, Morrall P, Alouche A, Entwistle E, et al. The selective oxidation of methanol to formaldehyde on iron molybdate catalysts and one component oxides. Catalysis letter 2002; 83(3-4):165-76.

78. Bruckman K, Grabowski R, Haber J, Mazurkiewicz A, Sloczynski J, Wiltowski T . The Role of different MoO_3 crystal faces in elementary steps of propene oxidation. Catal Today. 1987;104: 71 – 9.

79. Bowker M, Carley AF, House MP. Selective oxidation of methanol on iron molybdate catalysts and the effects of surface reduction. J Catal 2007;252:88 – 96.

80. Sha X, Chen L, Cooper AC, Pez GP, Cheng H. Hydrogen absorption and diffusion in bulk alpha-MoO_3. J Phys Chem C. 2009; 113:11399–407.

81. Routray K, Zhou W, Kiely CJ, Grünert W, Wachs IE. Origin of the synergistic interaction between MoO_3 and iron molybdate for the selective oxidation of methanol to formaldehyde. J Catal. 2010;275:84–98.

82. Tatibouet JM. Methanol oxidation as a catalytic surface probe. Appl Catal A: Gen 1997;148:213-52.

83. Py MA, Maschke K. Intra-and interlayer contributions to the lattice vibrations in MoO_3. Physica B+C. 1981;105(1):376.

84. Seguin L, Figlarz M, Cavagnat R, Lasskgues C. Infrared and Raman spectra of MoO_3, molybdenum trioxides and MoO_3, . xH_2O molybdenum trioxide hydrates. Spectrochim Acta A 1995; 51: 1323- 44.

85. Dieterle M. in situ resonance Raman studies of molybdenum oxide based selective oxidation catalysts [PhD Thesis]. Berlin: der Technischen Universitaat Berlin; 2001.

86. JCPDS Card Number 01-076-1003.

87. Choi JG, Thompson LT. XPS study of as-prepared and reduced molybdenum oxides. Appl Surf Sci 1996;93:143-9.

88. Massa M, Häggblad R, Hansen S, Andersson A. Oxidation of methanol to formaldehyde on cation vacant Fe–V–Mo-oxide. Appl Catal A: Gen 2011;408:63– 72.

89. Morgan DJ. Conversation with Dr. David J. Morgan at group meeting. 2014.

90. Dupin J-C, Gonbeau D,Vinatierb P, Levasseur A. Systematic XPS studies of metal oxides, hydroxides and peroxides. Phys Chem Chem Phys. 2000;2:1319-24.

91. Mao Y, Li W, Sun X, Ma Y, Xia J, Zhao Y, et al. Room-temperature ferromagnetism in hierarchically branched MoO_3 nanostructures. CrystEngComm 2012;14:1419-24.

92. Chen M, Wang X, Yu YH, Pei ZL, Bai XD, Sun C, et al. X-ray photoelectron spectroscopy and auger electron spectroscopy studies of Al-doped ZnO films. Appl Surf Sci 2000;158 134–40.

93. Holstein WL, Machiels CJ. Inhibition of methanol oxidation by water vapour-effect on measured kinetics and relevance to the mechanism. J Catal. 1996;162:118-24.

94. Ozkan US, Watson RB. The structure–function relationships in selective oxidation reactions over metal oxides. Catal Today 2005;100:101–14.

95. Diaz-Droguett DE, El-Far R, Fuenzalida VM, Cabrera AL. In situ-Raman studies on thermally induced structural changes of porous MoO_3 prepared in vapor phase under He and H_2. Mater Chem Phys 2012;134:631-8.

96. Bowker M, Holroyd R, Elliott A, Morrall P, Alouche A, Entwistle E, et al. The selective oxidation of methanol to formaldehyde on iron molybdate catalysts and on component oxides. Catalysis Letter. 2002;83(3-4):165-76.

97. Bowker M, Holroyd R, House M, Bracey R, Bamroongwongdee C, Shannon M, et al. The selective oxidation of methanol on iron molybdate catalysts. Top Catal. 2008;48:158–65.

98. Hill Jr CG, Wilson III JH. Raman spectroscopy of iron molybdate catalyst systems: Part I. Preparation of unsupported catalysts. Journal of Molecular Catalysis. 1990;63(1):65-94.

99. Tian H, Wachs IE, Briand LE. Comparison of UV and visible Raman spectroscopy of bulk metal molybdate and vanadate catalysts J Phys Chem B. 2005;109:23491-9.

100. de Faria DLA, Venaü ncio Silva S, de Oliveira MT. Raman microspectroscopy of some iron oxides and oxyhydroxides. J Raman Spectrosc. 1997;28:873-8

101. JCPDS Card Number 00-035-0183

102. McIntyre NS, Zetaruk DG . X-ray photoelectron spectroscopic studies of iron oxides. Anal Chem. 1977;49(11):1521-9.

103. Grosvenor AP, Kobe BA, Biesinger MC, McIntyre NS. Investigation of multiplet splitting of Fe 2p XPS spectra and bonding in iron compounds. Surf Interface Anal 2004;36:1564–74.

Chapter 4 Methanol Oxidation on Supported MoO_3 Catalysts

Contents

4.1 Introduction and Literature Review:

Catalyst supports are generally materials with high surface area normally used to maximize catalytic performance of an active phase. This second results chapter will focus largely on characterization and reaction measurements of Nanodiamond (ND) and γ-Alumina supports and MoO_3 on these supports, aimed at understanding support interaction with MoO_3 phase and their activity and selectivity towards methanol oxidation reaction.

Nanodiamond (ND) and MoO_3/ND

Nanodiamond comprises of a sp^3 diamond core covered by non-diamond carbon (carbon fullerene, carbon onion, graphitic and amorphous carbon). Its surface is usually terminated by various functional groups such as carbonyl, esters, hydroxyl, amide, flouro etc., as well as adsorbed water based on its purification method. It often consists of metal and non-metal impurities encapsulated into its core or lattice, arising from its synthesis or purification techniques. Fig. 4. 1 below depicts a schematic diagram of nanodiamond.

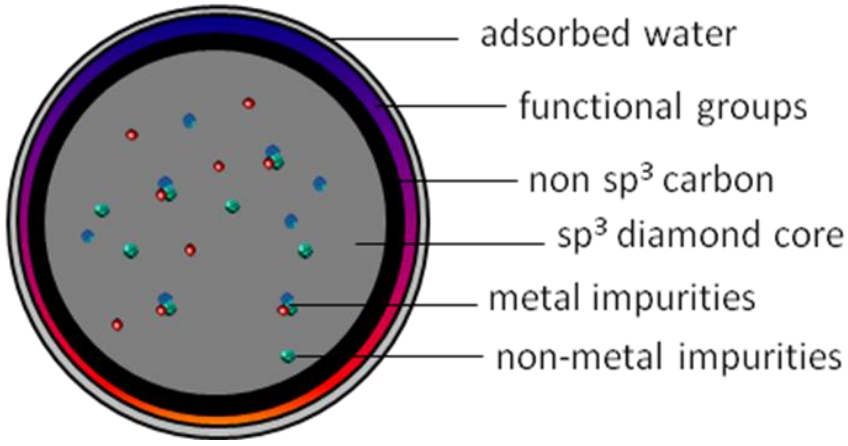

Fig. 4. 1 ***Schematic diagram of Nanodiamond particle***

A pioneering discovery of Nanodiamond was made by Volkov, Danilenko and Elin via detonation synthesis in 1963, using compressed shock wave from explosives with negative oxygen balance (60 wt% trinitrobezene ($C_6H_2(NO_2)_3CH_3$) + 40 wt % hexogen ($C_3H_6N_6O_6$)). It was carried out at high-pressure ≥ 10 Gpa and temperature ≥ 3000 K in an adiabatic reactor vessel to convert graphitic carbon to nanodiamond. Despite its secret discovery, the first commercial scale production of

nanodiamond only began in the USSR in 1992 as reported by Danilenko [1], Dolmatov [2], Vul et al [3], and Mochalin et al [4]. In addition, research and commercial production of nanodiamond was suspended due to lack of application of this super hard material.

However, the breakthrough discovery of single digit (4 – 5 nm size) dispersed nanodiamond by wet-milling techniques using yettrium stabilised zirconia micro-beads after ultrasonication of agglomerates as reported by Osawa [5], rekindled the interest in nanodiamond research once again. This mono dispersed nanodiamond possesses carboxylic acid group which interact with water molecules or a polar solvent by orienting partial positive charge terminal towards a non-freezing hydration shell, enhancing its higher dispersion and stability in water and other polar solvents such as alcohol and dimethyl sulfoxide. Differential scanning calorimetric studies reported by Korobov et al [6], evidenced the existence of a nanophase of water on 5 nm size nanodiamond, due to desorption of two endothermic peaks at 265 K and 273 K attributed to frozen and non-frozen bulk water respectively. Although Osawa [5] contested that only single nanodiamond particles are capable of forming non-freezing water phase.

Currently, other available commercial routes for nanodiamond production besides detonation synthetic route include: high-energy milling of high-pressure high-temperature (HPHT) diamond crystals and Laser ablation techniques reported by Yang et al [7] and Boudou et al [8] respectively.

Synthesized nanodiamond normally consists of metal, non-metal and non-diamond carbon impurities, which are purified using various wet and dry techniques. Dolmatov [2] and Mochalin et al [4] reported the use of liquid oxidant such as HNO_3, H_2SO_4 and HCl to remove amorphous graphitic carbon and metal impurities. However, this method uses hazardous chemicals and requires additional purification methods (washing and ion exchange) to remove admixture introduced during purification, which renders it expensive and raises environmental concerns. Recently, Osswald et al [9] reported a novel purification method of nanodiamond using air, which is cheap, environmentally benign, and effective for removal of sp^2 bonded and amorphous carbon at an optimum temperature between 400 – 430 ^oC

without affecting the sp^3 carbon. More so, this method increases sp^3 carbon content from 23 – 85 %, as well as enhancing surface oxygen functionalities and better dispersion in water. Moreover, air enriched ozone/ozone purification of nanodiamond studied by Petrov et al [10] and Shenderova et al [11] revealed excellent surface properties which include: high density of oxygen functionalities, high acidity (1.6 – 1.8 pH), enrichment of surface radical species, low sp^2 content and outstanding colloidal stability across wide range of pH (2-12). In addition, thermal desorption mass spectrometry (TDMS) studies revealed surface carboxylic anhydrides as the predominant functional group on ozone purified nanodiamond. Petrov et al [10] highlighted the inability of both acid and ozone treatment to completely remove sp^2 carbon. However, Shenderova et al [12] reported that acid treated nanodiamond agglomerates due to presence of surface unsaturation and functional group bonding adjacent particles: they surmised that oxidation of the acid treated nanodiamond, sonication between 100-400 W, and subsequent step wise centrifugation, produces a highly dispersed and stable hydrosol, which could be used in various applications.

Purification and annealing of nanodiamond in different gas environments impact different surface functionalities and properties on nanodiamond. Annealing nanodiamond in oxygen and argon as investigated by Xu et al [13] revealed that surface graphitization of nanodiamond, which begins at 670 ^oC in argon stream, while oxidation occurs at 496 ^oC. They reported higher transition temperature of nanodiamond in comparison to bulk diamond, which they attribute to high surface energy, small particle size, and large surface to bulk ratio. In a separate differential thermal analysis, Xu et al [14] observed surface graphitization and oxidation at 843 K and 863 K respectively. They observed that the surface carboxylic group on nanodiamond increase with increasing calcination temperature from 863 – 900 K in air, resulting in a negatively charged surface, increasing electrostatic repulsion between particles, and shifting of the isoelectric point from 4.4 of the as received sample to < 2. Xu and Yu [15], proposed that the mechanism of nanodiamond oxidation begins with the rupturing of C=C bond, leading to formation of oxo group between adjacent particles, while further oxidation results in complete destruction of the graphitic layer. They highlighted the possibility of metal

carbonate formation at high oxidation temperatures due to reaction of metal or metal oxides in the graphitic layer with carbon. Moreover, Yushin et al [16] and Bogatyreva et al [17] reported sintering effect of ultra-dispersed nanodiamond heated at 1400 ^{o}C and at a pressure range between 4.5 – 7 GPa for three minutes. They revealed decrease in amorphous sp^2 carbon content and surface area, as well as improved average grain size. This property enhances nanodiamond usage in surface polishing as well as sorbent in chromatograph. Xie et al [18], reported a similar graphitization effect during annealing of thin films of nanodiamond supported on singles crystal silicon in nitrogen, with the sp^2/sp^3 ratio of the un annealed sample increasing from 0.44 to 6.08 at 1500 ^{o}C.

The vast amount of nanodiamond literature centre heavily on surface modification and characterization (microscopic and spectroscopic) studies, due to the variety of nanodiamond with different surface properties based on synthesis, purification and end use target. XPS and CKVV Auger spectra study of the surface electronic properties of nanodiamond by Belobrov et al [19], revealed that nanodiamond comprises of a hybridised sp^3 core with distinct sp^2/sp^3 surface carbon. The surface has an electronic structure of δs^1 δp $^2\pi^1$ similar to that in graphite, without overlapping of the π-level due to restriction of nanodiamond curvature. This only allows overlapping of the p_z orbital of the nearest carbon atom as opposed to graphite. The authors reported a shift of 2.5 eV from natural diamond δp level to Fermi level, but observed similar surface state as nanodiamond after hydrogenation of natural diamond surface. A comparative Auger spectra studies of nanodiamond and graphite surface carbon atoms by Dementjev et al [20], supported the same electronic configuration (δs^1 δp $^2\pi^1$), with nanodiamond π-level displaced 1eV below the Fermi level. They conclude that the surface carbon atoms are inactive to atmospheric configuration which made it suitable for use as a molecular sieve and adsorbent. A recent comparative XPS and Auger studies of nanodiamond, nanodiamond soot, fullerene, and high ordered pyrolytic graphite by Dementjev and Maslakov [21] revealed that nanodiamond surface consist of hybridised sp^3 carbon, with its electron at the Fermi level. They proposed that the mechanism of formation and nucleation of nanodiamond inner core during detonation synthesis is similar to the outer surface: therefore, the surface carbon atoms cannot be

specifically assigned to sp^2 or sp^3 hybridised carbon. A separate XPS study of modified nanodiamond surface by oxidation in the temperature range between 200 - 400 ^oC, hydrogenation between 800 – 900 ^oC for five hours, and fluorination at 20 ^oC for 48 hours by Dementjev et al [22], revealed no observable change in the state of carbon on the surface to about 10 monolayers. They attributed the broadening of C1s peak of oxidised nanodiamond to increasing oxygen containing functional group, which deagglomerates the samples, while hydrogenation results in narrowing of the C1s peak due to hydroxyl group formation that enhances surface agglomeration with about 9 % flouro functional group on fluorinated nanodiamond surface. Qualitative and quantitative analysis of surface functional groups on oxidized nanodiamond using FTIR and Boehm titration techniques reported by Schmidin et al [23] revealed that the nanodiamond surface is predominated by carboxylic acid and lactones functional groups, situated on the edges. They recorded carboxylic acid sites of 0.81/nm for their synthesised sample in comparison to 0.15/nm of commercial detonated synthesised sample.

Ultrahigh vacuum scanning tunnelling microscopy/scanning tunnelling spectroscopy studies of hydrothermally treated nanodiamond and nanographite by Enoki et al [24] revealed nanodiamond surface to terminate with tangling unsaturated bonds on the edges, forming a zigzag and armchair configuration attributable to transpolyacetylene and isopolyacetylene respectively. Saturation and hydrogenation of the edges and apices are barely complete due to presence of unstable chemically active dangling bonds region of polyhedral nanodiamond particles. These active bonds result in surface reconstruction to graphitic shell. They observed the conversion of nanodiamond to nanographite in argon at 1600 ^oC. Liu et al [25] reported the fluorination of nanodiamond surface in F_2/H_2 gas at 310 ^oC. These fluorinated nanodiamonds are highly solubility in organic solvent. They indicated that the rich fluorine functional group chemistry could be explored for further functionalization to carboxylic, amino and various groups, which could be used in surface binding for both biomedical and engineering applications. However, modification of carboxylated nanodiamond surface by annealing in H_2 /Ar stream at 650 ^oC and above enhances formation of nanocarbon structure, graphitization and modification of surface defects. Raman spectroscopic analysis

using 532 and 488 nm as reported by Mona et al [26] revealed that graphitization of nanodiamond enhances photoluminescence intensity of the sample, which is pronounced using 488 nm.

The Raman studies of synthetic and natural diamond films deposited on SiO_2 by plasma excitation and hot filament excitation conducted by Knight and White [27] revealed two Raman active mode at 1332 cm^{-1} corresponding to triply degenerate stretching of cubic diamond, while the band at 1357 cm^{-1} and 1580 cm^{-1} are attributed to in-plane C-C stretching of disordered graphitic carbon. However, Wang et al [28] indicated that the band at 1360 cm^{-1} is a mode inherent to a graphitic layer, which is only observable when symmetry is broken by the edges. Yoshikawa et al [29] reported a lower nanodiamond peak at 1322 cm^{-1} in comparison to bulk diamond attributed to sp^3 diamond peak, with the band at 1600 cm^{-1} assigned to sp^2 clusters. Raman studies of sintered ultra-dispersed diamond by Yushin et al [16] attributed Raman band at 1250 cm^{-1} to amorphous diamond carbon. More so, theoretical studies of the D (breathing mode in nanocrystalline or amorphous carbon) and G (sp^2 stretching in chain or ring) bands by Ferarri and Robertson [30], revealed that the intensity, position and band width of these bands could be used to characterize and estimate the ratio of sp^2 and sp^3 carbon clusters. They surmised that the D band in most amorphous carbon appears as a broad lower shoulder peak to the G band peak. The authors attributed the red shifting this band and decreasing intensity to increasing disorder of smaller aromatic cluster of sp^2 dimers and increase in degree of disorderliness of graphitic ring respectively. In addition, they highlighted that the change in sp^2 configuration from ring to olefenic of short chain length is evidenced by shifting of the G band peak position from 1510 – 1570 cm^{-1}. In a separate Raman studies of amorphous and nanocrystalline carbon films by Chu and Li [31], the authors attributed Raman band at 1150 cm^{-1} to nanocrystalline phase of diamond, whereas the bands at 1350, 1500 and 1580 cm^{-1} were assigned to D band (breathing mode in nanocrystalline or amorphous carbon), disordered sp^3 carbon, and G band (sp^2 stretching in chain or ring) respectively. Although the band at 1150 cm^{-1} and its complementary at 1480 cm^{-1} were correctly assigned to transpolyacetylene on nanodiamond surface by Ferrari and Robertson [32], they observed the disappearance of the 1150 band and

shifting of 1480 bands during isotopic analysis using deuterium. However, these peaks reappeared after removal of the deuterium species. Raman analysis of air purification of nanodiamond as reported by Osswald et al [9], revealed that the controlled removal of sp^2 amorphous carbon increases the intensity of the diamond peak at ~1325 cm^{-1} between 400 – 430 ^oC. They attributed the broadening of band signal at 1750 cm^{-1} to C=O stretching due to oxygen functionalities. Chu et al [33], revealed that the C=O stretching band position is dependent on their local environment as well as temperature. They highlighted that the red-shift of C=O band from 1795 – 1817 cm^{-1} for carboxylated nanodiamond annealed from room temperature up to 400 ^oC, is due to breakage in hydrogen bonding linkage between adsorbed water and carboxylic functional groups. The pre annealed sample indicated a blue shift with increasing annealing temperature, which they attributed to competitive surface mechanism leading to more desorption of surface species and formation of thermally stable C=O species. An UV Raman and FTIR studies of annealed nanodiamond from room temperature to 900 ^oC in Ar as reported by Mochalin et al [34], revealed the presence of a peak at 1640 cm^{-1} attributed to OH stretching of surface functionality or absorbed water species. This band shifts to a higher band at 100 ^oC and completely disappears at 300 ^oC, but reappearing after cooling to 50 ^oC. Laser deposited and sputtered nanodiamond on Au and Ag films promotes accessibility of carbon-metal interaction resulting in enhanced Raman signal of sp^2 carbon species. Perevedentseva et al [35] reported that such interaction enables good Raman signal for graphitic and amorphous carbon, although they observed surface graphitization of nanodiamond prepared by laser deposited techniques.

Recently, nanodiamond has attracted the attention of researchers in the field of catalysis for use as both a robust catalyst and support for selective dehydrogenation/oxidative dehydrogenation of alkanes and alcohols. Although nanodiamond possesses distinct properties, it contains similar surface functional groups as other carbon materials. A review of carbon surface functionality by Figueiro and Pereira [36] revealed that the amount and nature of these functional groups are essential for maintaining stability and formation of products. They surmised that quinone groups serve as redox sites with carboxylic acid groups

acting as sites for alcohol dehydration. The pyridine, carbonyl, lactone, and carboxylic acid groups act as basic sites essential for environmental catalysis (NO and CO oxidation). However, methanol dehydration to DME catalysed by activated carbon using H_2O_2, HNO_3 and $(NH_4)_2S_2O_8$ as reported by Moreno-Castilla et al [37] indicated high activity for $(NH_4)_2S_2O_8$ oxidised activated carbon, due to the presence of a small amounts of strong carboxylic acid groups. Tveritinova et al [38], confirmed the presence of acid groups on nanodiamond, which are responsible for the dehydration of ethanol, 1-propanol, and 2-propanol to ethylene, dipropyl ether, and propylene respectively. In addition, the presence of bridging carbonyl groups due to oxidation of nanodiamond surface, increases the activity and selectivity of 1-propanol and 2-propanol dehydrogenation to propanal and acetone respectively. The application of nanodiamond as catalyst for oxidative dehydrogenation of ethylbezene to styrene was reported by Zhang et al [39] : they recorded high selectivity (>70%) and greater steady-state stability, which surpasses that of commercial K-promoted Fe_2O_3 catalyst. The authors revealed that dissociative chemisorption occurs on C=O sites forming both styrene and hydroxyl, with hydrogen stabilization of graphitic π bond resulting in desorption of styrene, whereas C-OH decomposition regenerates the active sites. However, increasing surface hydroxyl species result in loss in activity of the catalyst, which is reversible via oxidation in air. Recently, oxidative dehydrogenation of n-butane over nanodiamond reported by Liu et al [40], revealed high selectivity to butadiene and alkenes with superior stability due to reconstruction of active sites to more stable quinone and lactone group on disordered sp^2-sp^3 region. They attributed electrophilic oxygen to carboxylic acid and acid anhydrides sites, while the quinone and lactone sites are sources of nucleophilic oxygen. However, Frank et al [41] observed molecular activation of substrate on nucleophilic oxygen at the edges, but proposed that mobile epoxide species from sp^2 carbon at defective graphite (0001) plane are responsible for oxygen insertion into acrolein during oxidation to acrylic acid. The defective site on (0001) basal plane enhances adsorption of molecular oxygen and sequential transition to more stable nucleophilic oxygen at the edges. Modification of the graphite edges by doping with B_2O_3 and P_2O_5 results in significant decline in activity of the catalyst.

A recent review reported by Chen et al [42]: the authors highlighted the significance of defect and edges sites in oxidative dehydrogenation reaction on carbon materials. The oxygen adsorption on defect sites results in formation of lactone groups that are highly reactive (electrophilic): the edges form carbonyl group (nucleophilic), which are only reactive at higher temperature. Nakagawa et al [43], reported selective dehydrogenation of ethane to ethene over Cr_2O_3 supported on nanodiamond using CO_2 as oxidant. The authors recorded high selectivity of 87.7 % for ethene which increases with CO_2 partial pressure. They highlighted the significance of surface oxygen on nanodiamond and CO_2 in enhancing dehydrogenation and eliminating deposited carbon to maintain high oxidation state of Cr respectively. In a separate studies, Okumura et al [44] reported high activity for V_2O_3 supported over nanodiamond used in oxidative dehydrogenation of C_2H_6 to CH_3CHO in the presence of CO_2. They proposed that the major by products; CH_2O and C_2H_4, result from decomposition of CH_3CHO. However, the use of nanodiamond as support for Fischer-Tropsch synthesis was reported by Suzuki [45], the author recorded high conversion over 5 wt % Co supported catalyst, which increases to 70% on promotion with 0.3 % Mn. The promoted catalyst revealed better activity which surpasses that of Co supported on SiO_2, due to weak support interaction and better dispersion (small crystallite size) preventing reduction of Co. Vershinin et al [46] reported the use of Pt support catalyst for room temperature oxidation of CO to CO_2.

γ-Al_2O_3 and MoO_3/ γ-Al_2O_3

Gamma alumina (γ-Al_2O_3) is one of the most-used metal oxides in heterogeneous catalysis. The nature of its structure remains debatable but is commonly considered to have cubic structure with a tetrahedral spinel defect belonging to F_{d3m} space group. It consists of 32 oxygen ions in a closed pack arrangement, with 23 Al ions occupying octahedral (16d) and tetrahedral (8a) sites. It has 8/3 defects or vacancies randomly distributed within the tetrahedral sites as reported by Levin and Brandon [47], and Trueba and Trasatti [48]. Most commercially synthesised γ-Al_2O_3 are produced from decomposition of amorphous alumina, gibbsite ($Al(OH)_3$) or boehmite (AlOOH) precursor. Despite wide acceptability of the spinel γ-Al_2O_3

structure, a non-spinel γ-Al_2O_3 structural model based on studies of evolution γ-Al_2O_3 from crystalline boehmite parent structure is gaining acceptance, due to the consistency of the model with DFT calculation and most experimental data. The non-spinel γ-Al_2O_3 structure as shown in Fig. 4. 2 below indicates a pseudo-morphs of boehmite with its (100) surface yielded from same basal (010) and edge (100) of boehmite, while its (110) and (111) surfaces correspond to lateral (001) and (101) structure of boehmite respectively. The transition of boehmite to γ-Al_2O_3 leads to strong contraction (about 29 %) in (010) plane, which causes the collapse of the hydrogen-bonded layer of the boehmite giving rise to predominantly stable (100) and (110) surfaces [49]. The (100) surface consists of about 25% unsaturated pentacoordinated Al atom (Al_V) bonded to triple coordinated oxygen atom, while (110) surface comprises of 75 % unsaturated Al_{III} and Al_{IV} atom inherited from bulk octahedral Al atoms bonded to oxygen atom. The Al_{IV} atom relaxed inward with outward projection of its bonded oxygen to form pseudo tetrahedral structure, while the Al_{III} forms a planar structure as reported by Digne et al [50].

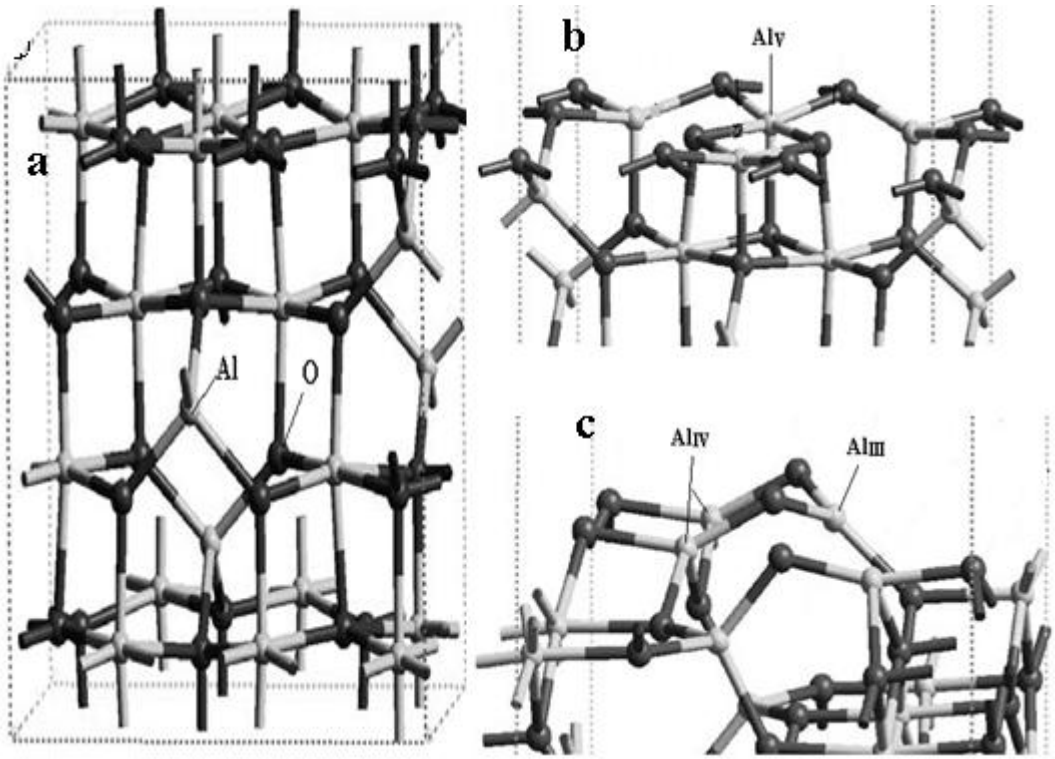

Fig. 4. 2 ***Structure of γ –Al_2O_3 and surfaces (a) dehydrated γ –Al_2O_3 (b) (100) surface and (c) (110) surface [49-51]***

An in situ neutron diffraction study by Paglia et al [52] of crystalline boehmite calcined from room temperature – 900 ^oC, revealed formation of distorted tetragonal γ –Al_2O_3 between 450 – 750^oC, with no evidence of a cubic γ –Al_2O_3 phase above 750 ^oC. Instead, the authors detected a new prime alumina phase (γ'–Al_2O_3) assigned to P_{4m2} space group. In a separate NMR and theoretical XRD simulation studies conducted by Krokidis et al [51], the authors proposed a mechanism for boehmite dehydration to γ –Al_2O_3 which begins with transfer of H within the inter layer of octahedral boehmite structure at 320 ^oC, with water desorption and eventual collapse of the boehmite structure to monoclinic structure observed between 253 – 425 ^oC. This result in migration of Al atoms from octahedral to tetrahedral sites, with complete surface dehydroxylation achieved at 700 ^oC. Furthermore, NMR studies of the γ –Al_2O_3 confirmed existence of 25 – 31 % tetrahedrally coordinated Al atoms. A DFT study of surface hydroxyl group on γ –Al_2O_3 by Digne et al [50] indicated that the (100) surface of γ –Al_2O_3 is fully dehydroxylated at 320 ^oC, whereas dehydroxylation of (110) surface is incomplete at high temperature. The authors revealed that adsorption and molecular chemisorption occurs on hydroxyl bonded to Al_{IV} and Alv sites, and indicated a correlation between surface acidity and increase in surface energy with degree of reduction of surface hydroxyl group bonded to Al atom on (100) and (110) surfaces. In a separate DFT and IR studies of CO adsorption on γ –Al_2O_3 the authors [49] proposed that surface acidity of γ –Al_2O_3 increases with degree of unsaturated Al sites (i.e Al_{III} > Al_{IV} > Alv), but indicates almost similar energy of adsorption for Alv (100) (- 43 kJ/mol) and Al_{IV} (110) (- 40 kJ/mol) surfaces. However, they concluded that the reactivity and acid-base properties do not only depend on acidity of the surface but also on concentration of OH group bonded on the surface and temperature of operation. Since the Al_{III} centre is the most reactive site but usually hydroxylated during reaction condition. A clearer explanation of the reactivity of these sites is highlighted in a DFT study of N_2, CO adsorption and methane reactivity on γ–Al_2O_3 as reported by Wischert et al [53, 54]. The authors attributed the reactivity of Al_{III} sites during reaction condition to adsorption of water molecules on $Al_{IV,}$ as such bridging two Al_{IV} sites at lower water coverage; 3 OH nm^{-2}. This lead to reconstruction of the truncated Al_{IV} octahedral structure to

a tetrahedral structure as such leaving the metastable Al_{III} sites free, and slightly modified the structure from a planar to pyramidal structure, via formation of weak bonding to a second layer oxygen atom. The low water coverage of 3 OH nm^{-2} increases the acidity of the Al_{III} sites and basicity of the non-adjacent oxygen atom facing these sites, forming highly reactive Al_{III}-O acid-base pairs. These acid-base pairs are more reactive than completely dehydrated (110) surface. However, these sites (Al_{III}-O) indicate lower energy barrier of 45 kJ/mol for CH_4 dissociation, with limitless barrier for H_2 dissociation. In addition, the increase in surface hydroxylation, increases the energy barrier and decreases surface acidity. However, the authors [54] indicated similar reactivity of Al_{IV} sites (as Al_{III}) during high temperature reaction with H_2 on a partially hydroxylated (110) surface (3 OH nm^{-2}) forming stable Al-H tetrahedral species. The authors also attributed the decline in reactivity of γ–Al_2O_3 calcined above 700 ^oC to high mobility of surface O of Al_2O_3 and exposure of inactive Al_{IV} sites due to bulk transition to θ and α Al_2O_3 phase. More so, micro calorimetric study of water adsorption on anhydrous nanostructure γ–Al_2O_3 surface by Castro and Quach [55] revealed that dissociative adsorption water to form a monolayer coverage with ~ 3.6 OH nm^{-2}, while further adsorption resulting in transition from gas-liquid water film on γ–Al_2O_3 with constant adsorption energy of – 44 kJ/mol. The surface energy decreases with increasing water adsorption.

Moreover, these reactive Lewis acids sites (Al_{III} and Al_{IV}) account for the high activity of γ–Al_2O_3 in ethylene dehydrogenation as reported by Hindwin and Weller [56]. The H_2-D_2 exchange and transfer between CH_4 and CD_4 reported by Weller and Hindwin [57], and van Cuawelert and Hall [58], as well as increase in surface acidity reported by Maciver et al [59] and Peri [60] were observed for γ–Al_2O_3 calcined between 450 – 700 ^oC. In addition, ESR studies of γ–Al_2O_3 calcined at different temperature reported by Flock hart et al [61] revealed oxidation of pyrlene from yellow to lavender colour on γ–Al_2O_3 calcined up to 900 ^oC in the presence of oxygen, with no effect observed for sample calcined at 300 ^oC and 1100 ^oC. The authors attributed this to Al^{3+} site capable of producing O^{2-} (Lewis base) electron transfer with molecular oxygen, which reacted with pyrelene. A study of heterolytic splitting of H_2 and CH_4 on unsaturated Al defect sites (Al_{IV}

and Al_{III}) by Joubert et al [62] revealed low temperature (25 ^oC) dissociation of H_2 to form Al_{IV}-H and Alv-H on sites of about 0.069 nm^{-2} (~4 OH nm^{-2}), while CH_4 dissociates selectively on Al_{III} sites around 100-150 ^oC to form Al_{IV}-CH_3. They surmised that dehydration of γ–Al_2O_3 at 500 ^oC expose a small fraction of Al_{III} sites, while water plays a crucial role in stabilization of γ–Al_2O_3 structure.

In addition, bulk and surface investigation of γ–Al_2O_3 transition to θ- Al_2O_3 using XRD and ethanol TPD reported by Kwak et al [63] indicated similar desorption temperature for ethylene at 225 ^oC and 250 ^oC on γ–Al_2O_3 surface calcined at 200 ^oC and 500 ^oC. The authors attributed low ethylene desorption temperature to occur from a bronsted acid OH group bonded to Al_V, and the higher desorption temperature from Alv sites on (100) surface. However, both calcined γ–Al_2O_3 at 800 ^oC and θ-Al_2O_3 indicate similar ethylene desorption temperature, which revealed that the phase transition of γ–Al_2O_3 to θ- Al_2O_3 occurs on the surface forming a thin layer that could not be detected by bulk XRD technique for sample calcined below 800 ^oC. More so, IR studies of pyridine adsorption over γ–Al_2O_3 reported by Roy et al [64] revealed the existence of only Lewis acid sites on γ–Al_2O_3 due to band at 1451 cm^{-1} with no band at 1541 cm^{-1} attributable to bronsted acid (due to pyridinium ions). In addition, TPD-TGA measurement of 2-propanamine over γ–Al_2O_3 evacuated at 773 K evidenced desorption of intact amine with no trace of ammonia or propene between 575 and 650 K due to protonation of amine by Bronsted acid sites. Roy et al [65], surmised that alcohol dehydration mechanism over γ–Al_2O_3 proceeds via a transition state involving formation of stable carbenium-ion, which determines desorption of dehydration products, whereas water molecules block the reactive Al sites during reaction. In a separate kinetic and mechanistic studies of ethanol dehydration on γ–Al_2O_3 reported by Dewilde et al [66], the authors revealed two different reaction mechanisms, with ethylene formation involving C-H cleavage and subsequent desorption of water molecule. Furthermore, they attributed diethyl ether (DEE) formation to dehydration of ethanol from Lewis acid sites that is limited by either C – O or Al – O bond cleavage. The authors reported a rate dependency of DEE formation at low ethanol and water pressure whereas the rate of both DEE and ethylene formation are independent at high ethanol and water pressure: they

proposed that formation of bimolecular (dimer) surface species is responsible for the inhibition of ethylene and DEE formation. Moreover, Greenler [67] revealed that both methanol and ethanol chemisorbed on γ–Al_2O_3 forming methoxy and ethoxy species respectively, with formation of formate and acetate species corresponding to IR bands at 1377 cm^{-1} and 1575 and 1416 cm^{-1}. Schiffino and Merrill [68] reported two routes for methanol dehydration to DME over γ–Al_2O_3 at different reaction temperatures involving both methoxy and adsorbed methanol species:

Reaction between adsorbed methanol and methoxy species below 280 ^oC

$$CH_3OH_a + CH_3O_a \rightarrow CH_3OCH_{3\,(g)} + OH_a \qquad \text{Equation 4.1}$$

Reaction between methoxy species above 280 ^oC

$$CH_3O_{\,a} + CH_3O_a \rightarrow CH_3OCH_{3\,(g)} + O_a \qquad \text{Equation 4.2}$$

where (a) refers to adsorbed species and (g) stand for gas phase species

The OH groups recombine to form water, which adsorbed strongly on active sites even at high reaction temperatures inhibiting methanol adsorption which resulting in the decline in DME selectivity. Moreso, Zuo et al [69] reported that DME synthesis over γ–Al_2O_3 and boehmite (AlOOH) in gas phase reaction occurs via chemisorbed methoxy species (with activation barrier of 1.58 eV), and adsorbed methanol species or between methoxy, and adsorbed methanol species (low activation barrier of 0.68 eV) respectively. Water or hydroxyl groups above 200 ^oC, cause the deactivation of the sites responsible for DME formation.

MoO_3 supported on γ–Al_2O_3 is reported to be a widely used as catalyst for the methanation reaction by Wang et al [70], oxidative dehydrogenation (ODH) of alkane by Abello et al [71] and Christodoulakis et al [72], and selective oxidation of methanol to formaldehyde by Hu and Wachs [73], Matsuoka et al [74], and Brandhorst et al [75]. A Raman and UV – Visible diffuse reflectance spectroscopic studies of MoO_3 supported over Al_2O_3 reported by Zingg et al [76] and Tian et al [77] indicated the presence of tetrahedral MoOx species at low Mo

loading of ~ 4 wt %, with both tetrahedral and octahedral coordinated MoOx evidenced at monolayer coverage on the support. Matsuoka et al [74] reported that the formation of bulk molybdate species on Al_2O_3, unlike multilayer vanadates species observed for V_2O_5 supported on Al_2O_3. The authors concluded that prolong calcination at 500 ^oC and calcination at 700 ^oC of higher Mo loading resulted in formation of $Al_2(MoO_4)_3$. In addition, Tian et al [77] inferred that $[MoO_4]^{-2}$ species are the predominant species on hydrated Al_2O_3 and ZrO_2 support at lower Mo coverage.

An XPS and EPR studies of surface MoOx species on γ–Al_2O_3 and physical mixture of MoO_3 and γ–Al_2O_3 reported by Zingg et al and Mestle et al indicated the presence of octahedral Mo^{6+} and distorted octahedral Mo^{5+} species on γ–Al_2O_3 support, with Mo^{5+} species being very stable against reoxidation in the presence of O_2. In addition, reduction study (TPR in H_2) of supported MoO_3/ γ–Al_2O_3 reported by der Arco et al and Abello et al revealed two distinct reduction temperatures for MoOx species supported over γ–Al_2O_3. They revealed a lower reduction temperature of < 970 K and a higher reduction temperature of ≥ 970 K for octahedral MoOx and dispersed tetrahedral MoOx species respectively.

A study of ODH of propane reported by Abello et al revealed dependence of activity of the reaction over MoO_3/γ–Al_2O_3 to increasing Mo loading up to monolayer coverage, with slight increase in propene selectivity. The authors inferred that Bronsted acid sites on the supported catalyst are essential for C – H cleavage as well as sites for formation of electrophilic species which oxidises propene to COx. An operando Raman spectroscopic study of ODH of methane over MoO_3/γ–Al_2O_3 catalyst reported by Christodoulakis et al [72] indicated a good correlation between methane reactivity/conversion and Mo – O – Al bond, which increases to monolayer coverage and then decreases with increase in formation of polymeric MoOx species. Wang et al [70] reported that tetrahedral coordinated MoOx species are catalytically active than octahedral species in synthetic gas methanation reaction.

However, methanol oxidation over MoO_3/γ–Al_2O_3 reported by Matsouka et al [74] indicated an increase in turn over frequency (TOF) of methanol with increasing Mo

loading, which shows strong dependence on MoO_3 support interaction. In addition, in-situ Raman study of methanol oxidation in presence and absence of oxygen reported by Hu and Wachs [73] revealed reduction of Mo=O vibration band from 1004 – 995 cm^{-1} for 20 wt% in the absence of oxygen, which was re-oxidized in O_2 with about 70 % of the band recovered at 530 K. The authors surmised that structural morphology of MoO_3 on γ–Al_2O_3 does not affect formaldehyde selectivity. However, they observed marked increase in activity of polymeric tetrahedral/octahedral MoOx species at a factor of 2 – 4 in comparison to isolated tetrahedral MoOx species. Moreover, Briand et al [78] indicated that TOF of methanol oxidation on a monolayer of MoO_3 over different supports; including γ–Al_2O_3, decreases with increasing electronegativity of the metal cation-support interaction. However, an EPR and Raman/infra-red operando spectroscopic studies of methanol oxidation over 20 wt% MoO_3/γ–Al_2O_3 at 250 ^oC revealed diminishing intensity of M=O vibration 992 cm^{-1} band with increasing 840 cm^{-1} band, and increase in DME formation in the absence of oxygen. The catalyst revealed 93 % methanol conversion at 52 % formaldehyde selectivity due to reoxidation of Mo^{5+} - Mo^{6+} in the presence of oxygen. The authors surmised that DME formation resulted from interaction of methoxy species with Mo – O – Al support while formaldehyde emanated from redox sites on polymolybdate species.

Despite the previous literatures and researches on supported MoO_3 catalysts, the use of MoO_3 supported over nanodiamond and pre-treated γ–Al_2O_3 supports for selective oxidation of methanol to formaldehyde is new. This study will investigate nanodiamond and γ–Al_2O_3 support calcined at different temperatures, exploring their high surface area, surface inertness, and electron density (for nanodiamond graphitic layer). In addition, characterization of MoOx species on these supports will be determined using BET surface area, microscopic and electronic techniques, and the effect MoO_3 species and support interaction on methanol oxidation reaction will be measured by TPD and TPR method using CATLAB micro pulsed flow reactor.

4.2 Results and Discussion

Nanodiamond (ND) Characterization and Reactivity

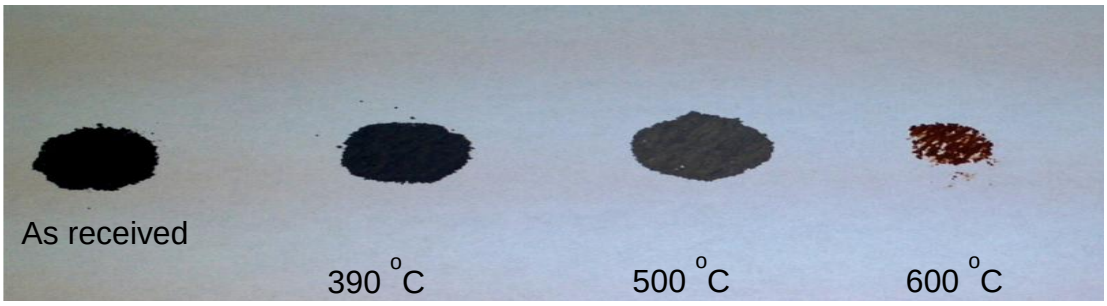

Fig. 4. 3 ***Sample of as received and calcined nanodiamond at different temperatures in air for five hours***

Oxidation of the nanodiamond support for five hours in ambient air as seen in Fig. 4.3 shows a significant colour change from black (as received) to grey (390 ^{o}C), light grey (500 ^{o}C), and dark brown (600 ^{o}C) with increasing calcination temperature. Oxidation of the as-received sample is evident from the 390 ^{o}C sample which begins at 375 ^{o}C as reported by Osswald et al [9], due to removal of sp^2 graphitic ribbon and amorphous carbon, carbon onion, and fullerenic shell bonded to its surface. The light grey appearance of the sample oxidized at 500 ^{o}C evidenced purification of the surface from amorphous carbon and graphitic ribbon species, which is consistent with observation reported by Osswald et al [9] and Xu and Yu [15] for oxidized detonation nanodiamond sample at same duration and temperature for 6 hours respectively. Interestingly, complete burning of the support at 600 ^{o}C resulted in dark brownish residue. Metal impurities encapsulated within its matrix could be catalysing the burning of ND sample at 600 ^{o}C, due to their reactive behaviour with molecular oxygen.

Table 4. 1 ***BET surface area and % weight loss of nanodiamond sample calcined at different temperature in air***

Catalyst	BET Surface area (m^2/g)	% wt loss (after 5 hrs)
ND As-received	135	-
ND 390^{o}C	154	6.28
ND 470^{o}C	147	13.67
ND 500^{o}C	149	31.88
ND 600^{o}C	NA	89.59

The as-received nanodiamond sample reveals a surface area of 135 m^2/g as shown in Table 4. 1. The oxidation of the sample in static air resulted in an increase in the surface areas to 154 m^2/g with a corresponding weight loss of 6.28 % at 390 ^{o}C that decreases to 147 m^2/g with 13.67% weight loss at 470 ^{o}C. However, the surface area increases slightly to 149 m^2/g at 500^{o}C with a corresponding weight loss of 31.88 %.

The oxidation of nanodiamond in air results in an increase in the surface area and weight loss of the samples. The increase in surface area of the sample oxidized at 390 ^{o}C corresponding to a weight loss of 6.28 %: however, the weight loss at this temperature is higher in comparison to that reported by Xu and Yu [15] for similar oxidation conditions, at much longer period. Sintering of the support from 154 – 147 m^2/g at 470 ^{o}C with subsequent weight loss of 13.67 %, could result from reconstruction or functionalization surface via dehydration of possible neighbouring hydroxyl and hydrogen species, as well as oxidation of amorphous graphitic carbon species. Further increase in oxygen functionalities and possible surface modification to carboxylic anhydride or more stable ketonic/diketonic carbonyl species at 500 ^{o}C could result in slight increase of the surface area to 149 m^2/g and 31.88 % weight loss respectively. The variation in surface area and increasing weight loss with respect to increasing calcinations are in conformity with burning of amorphous carbon species, functionalization, and modification of nanodiamond surface revealed by FTIR and TGA study reported by Xu and Yu [15] and Osswald et al [9].

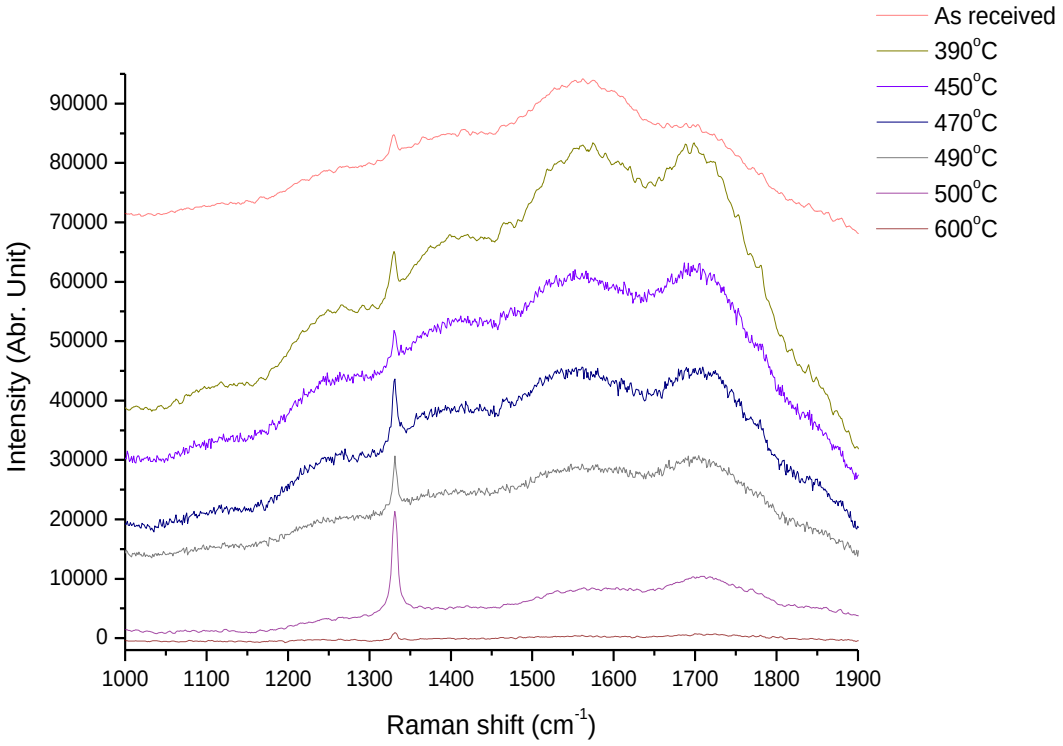

Fig. 4. 4 ***Raman spectra of nanodiamond samples calcined at different temperatures***

Table 4. 2 ***Raman band assignment of as received and oxidized ND samples***

Band or band range (cm^{-1})	**Assignment**
1150 and 1470	Trans-polyacetylene [32]
1248	Amorphous diamond [16]
1331	T_{2g} symmetry sp3 carbon bonding (Diamond band) [29, 33]
1350-1450 1500-1600	D-band (A_{1g} sp2 breathing Mode) G-band (E_{2g} sp2 in-plane bond stretching mode)
1600-1630	O-H bending vibration [34]
1700 – 1800	C=O stretching vibration (Carbonyl group) [9]

Raman spectra in Fig. 4. 4 and Table 4. 2 depict weak peak at 1120 cm^{-1} with a complementary peak at 1450 cm^{-1} associated to vibration trans-polyacetylene on the diamond surface, while the broad band at 1248 cm^{-1} is attributable to

amorphous diamond. The diamond sp^3 peak was observed at 1331 cm^{-1}, with broad band centred at 1399 cm^{-1} and 1562 cm^{-1} assigned to D disorder (amorphous) sp^2 A_{1g} breathing vibration and graphitic sp^2 in-plane bond stretching (G – band) mode respectively. The D – band indicates a weak shoulder peak at 1606-1610 cm^{-1} assignable to OH-bending vibration, with the broad band that centred at 1705 cm^{-1} with weak shoulder at 1780 cm^{-1} for sample heated above 390 ^oC attributed to C=O stretching mode.

The Raman spectra in Fig. 4.4 are in close agreement with those reported by Osswald et al [9] and Mochalin et al [34] for oxidised nanodiamond surface. Oxidation in ambient air at 390 ^oC reveals the weak trans-polyacetylene peak and OH- bending vibration band, with reverse increase and narrowing of the C=O stretching band in comparison to the G-band. This indicates increasing oxygen functionalities (carbonyl and most carboxylic groups), due to surface oxidation of ND as reported by Osswald et al [9]. Increasing calcination to 490 - 500 ^oC results in decrease in OH-bending, trans-polyacetylene and amorphous diamond bands intensity, as well as shifting of broad shoulder peak from 1778 cm^{-1} to 1774 cm^{-1}, with corresponding increase in intensity and shifting of diamond peak from 1330 to 1331 cm^{-1}. These indicates surface reconstruction via removal of surface hydroxyl as well as transformation of carboxylic group to possibly more thermally stable carbonyl functionalities (acid anhydride, lactone, or ketone/diketone). These findings are in conformity with observation reported by Chu et al [33] for temperature dependence of the C=O group on annealed ND and oxidised nanodiamond surface reported by Tveritinova et al [38]. However, the removal of amorphous graphitic carbon which exhibits a shielding effect on the Raman signal of the diamond sp^3 peak, as well as broadening of the D and G bands, indicates degree of disorderliness of the graphitic ring resulting from softening of its valence density of state. Moreover, the absence of the D-band and broadening of the G-band after heating at 500 ^oC, signifies change of the sp^2 graphitic ring structure to olefenic groups of medium or short chain length, with high sp^3 diamond content which agrees with proposed model by Ferrari and Robertson [30] for estimation of sp^3 content of diamond like carbon using visible Raman spectra. Surprisingly, the

intensity of the diamond peak decreases drastically at 600 ^{o}C, indicating almost complete burning of the support.

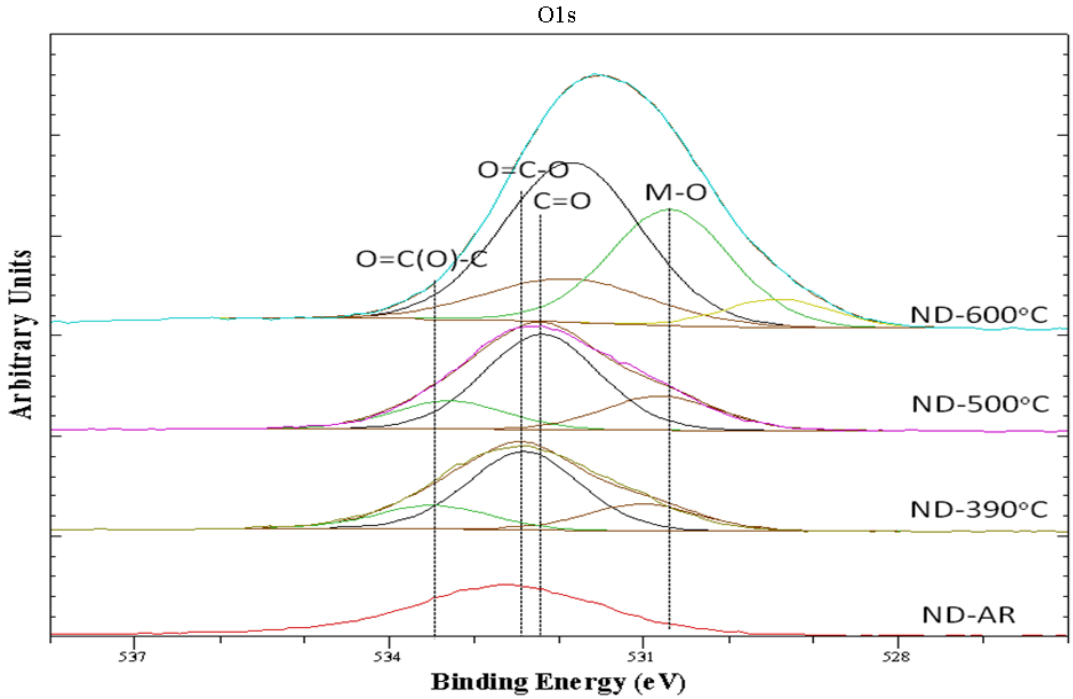

Fig. 4. 5 ***XPS O1s spectra of ND support***

The XPS O1s spectra in Fig. 4. 5 depict binding energies at 529.6 eV and 530.7 eV assigned to oxygen bonded on transition and alkali earth metals respectively in accordance with assignment reported by Dupin et al [79]. The oxygen binding energy at 532.2 eV, 532.5 eV, and 533.5 eV correlates with O1s assignment for carboxylic, alcohol/ester and anhydride functional group respectively as reported by Dementjev et al [22], Lopaz et al [80] and Rosenthal et al [81]. The broadening of ND-600 ^{o}C and shifting of the O1s peak to lower binding energy indicates possible contribution of weakly bonded O on metal surface after complete burning of the support.

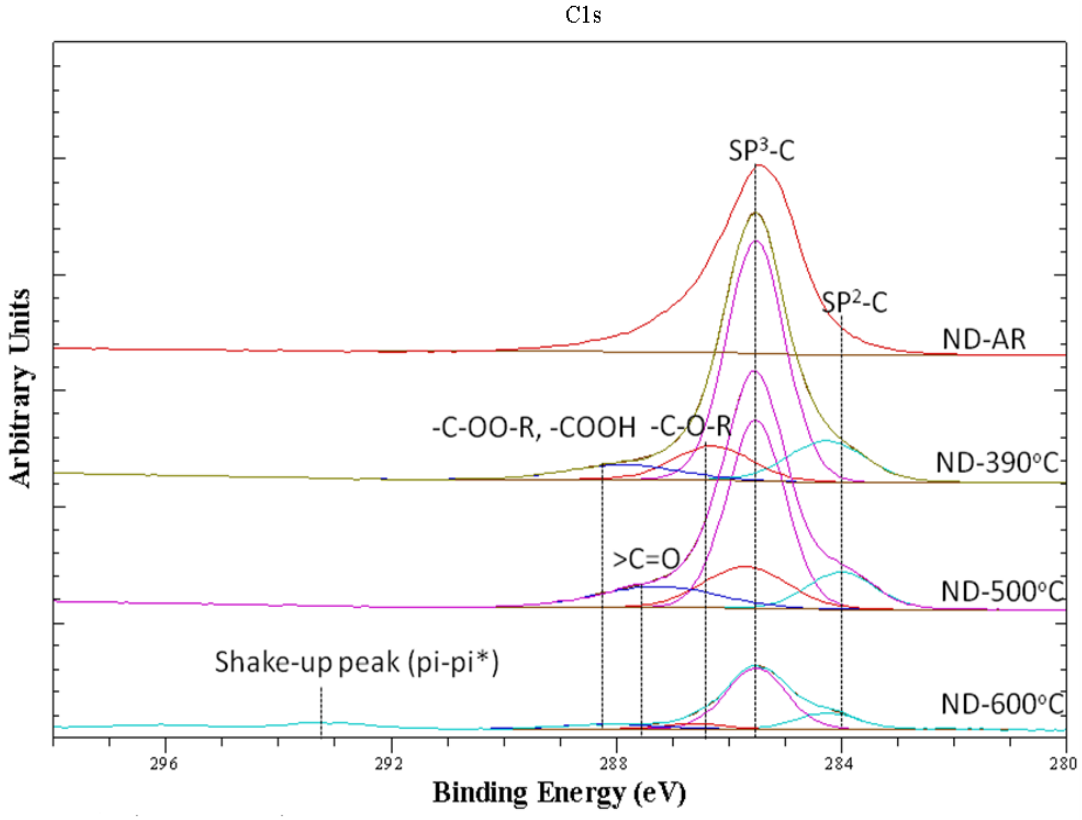

Fig. 4. 6 ***XPS C1s spectra of ND support***

The C1s binding energies of 284 – 284.2 eV and 285.5 eV Fig. 4. 6 is attributed to sp^2 and sp^3 carbon respectively, which are in agreement with value reported by Xie et al [18] for sp^2 and sp^3 carbon. The high C1s binding energies at 285.7 eV, 286.3 – 286.6 eV, 287.2 – 287.9 eV and 288.1 eV are in line with values assigned by Lopez et al [80] , Figueiredo et al [82] and Shenderova et al [11] to ether/alcohol, carbonyl, and carboxylic C1s functional groups respectively. The data indicates a shake-up satellite peak at 293.3 eV, which could be assigned to pi-pi* in graphitic carbon. The broadening of the ND-600 ^{o}C C1s peak results from destruction of the ordered graphitic layer and sp3 carbon network catalysed by transition metal entrapped in its core.

Table 4. 3 ***XPS analysis atomic wt% of element on nanodiamond support surface***

Element Temp (^oC)	C	O	N	Na	Fe	W	P	Si	Al	Ca	Mn
	(Atomic weight %)										
As received	91.4	8.3	0.3	-	-	-	-	-	-	-	-
390	89.3	10.6	-	0.03	-	-	-	0.1	-	-	-
500	85.2	13.8	-	0.23	0.5	-	-	0.5	0.3	-	-
600	29.0	49.4	0.6	3.8	0.5	0.27	1.5	8.1	6.1	0.5	0.3

Table 4. 3 shows the atomic weight percentage and elemental composition of nanodiamond calcined at different temperatures, with the as received sample comprising of major synthetic composition of nanodiamond; 91.44 % C, 8.28 % O and 0.28 % N. The sample calcined at 390 ^oC indicates a decrease in C content to 89.31 % with an increase in O content to 10.56 %, with additional 0.03% Na and 0.1% Si. However, the sample calcined at 500 ^oC indicates a decrease in C content to 85.23% with corresponding increase in O, Na, and Si content to 13.73 %, 0.23% and 0.45% respectively. In addition, the sample also revealed 0.53% Fe and 0.31% Al. Complete burning of the support at 600 ^oC indicates presence of C, O, N, and P, alongside arrays of incombustible metal such Na, Fe, W, Si, Al, Ca and Mn.

The elemental composition of the as received nanodiamond (C, O and N) in Table 4.3 indicates uniqueness of the surface and core basic composition, which conforms with mechanism of nanodiamond formation proposed by Dementjev and Maslakov [21]. Oxidation of the support increases the O content from 8.28 to 13.78 % upon increasing calcination temperature to 500 ^oC, indicating enrichment of the surface with oxygen containing functionalities. The elemental composition of the oxidised nanodiamond at 600 ^oC are in agreement with those reported by Petrov et al [10], except for the absence of Ti and Cr. The oxidation of the nanodiamond surface results in etching of the support from disorder or defect region, leading to

exposure of metal and non- metal impurities encapsulated in the core during commercial synthesis and purification of the original sample.

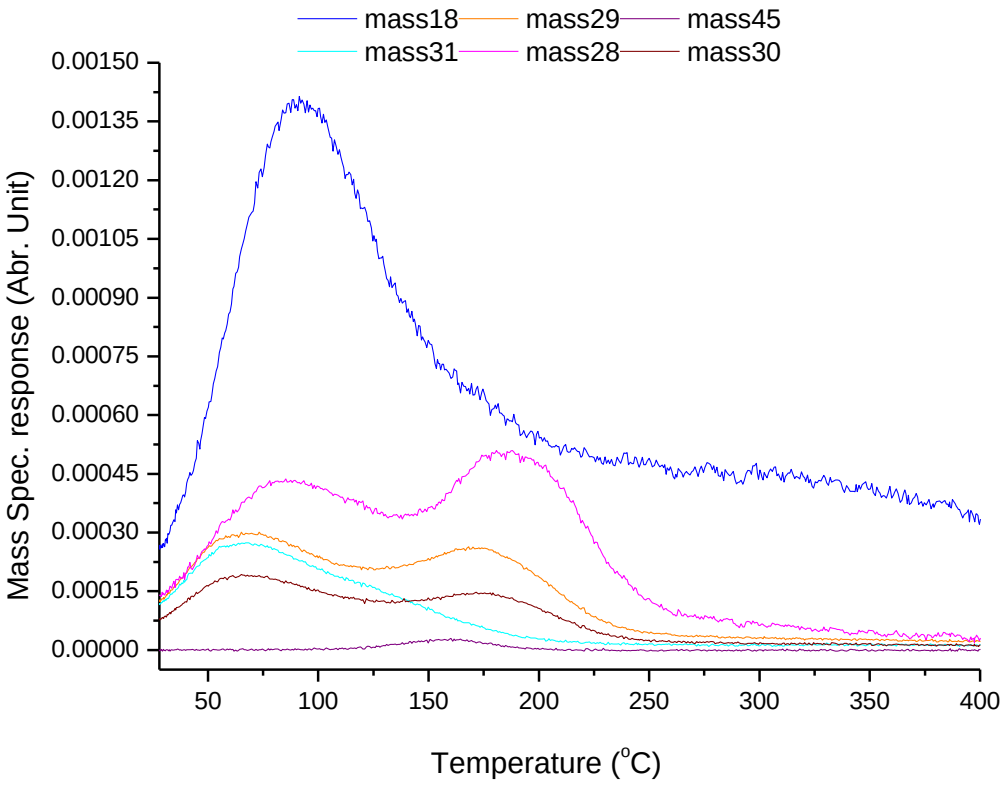

Fig. 4. 7 ***TPD profile of methanol over as- received nanodiamond***

TPD profile in Fig. 4. 7 depicts a methanol desorption peak at 65 ^{o}C, preceding a broad water peak that centred at 91 ^{o}C. A DME desorption peak was evidenced at 161 ^{o}C prior to formaldehyde desorption peak at 173 ^{o}C. The support reveals two CO desorption peaks at 85 ^{o}C and 190 ^{o}C, the former is due to a cracking fragment of methanol, as is the initial part of the peak at 190 ^{o}C. However, some real CO produced, is evident by the broadened profile for after the formaldehyde has diminished.

The as-received nanodiamond (ND) sample reveals heterogeneity of its surface, with methanol desorption which tails till 180 ^{o}C attributed to both chemisorbed and molecular adsorbed methanol species. The first CO peak at 85 ^{o}C results from possible reaction between hydroxyl species with bulk defects in the (0001) plane

of graphitic carbon shell, which conforms with the mechanism for CO desorption on defective graphene as reported by Xu et al [83].

However, DME desorption at 161 ^{o}C could result from intermolecular reaction of methoxy, while formaldehyde peak at 173 ^{o}C could be the product of methoxy dehydrogenation by carbonyl or lactone sites at the edges. The dehydrating effect is similar to those observed by Tveritinova et al [38] for conversion of 1-propanol to dipropyl ether. The later CO peak signifies further dehydrogenation of formaldehyde by unsaturated sp^2 carbon (basic site) or lactone.

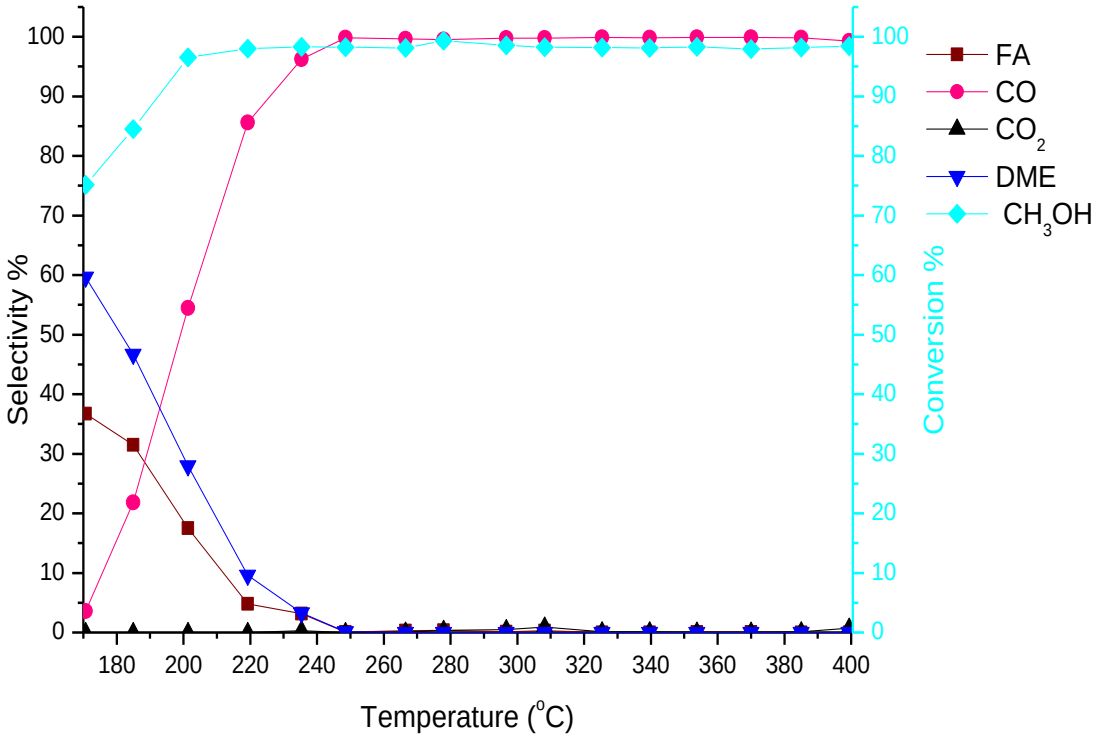

Fig. 4. 8 ***TPR profile of methanol oxidation over as-received ND***

The reaction profile of methanol over as-received nanodiamond in Fig. 4. 8 reveals high activity with 75 % methanol conversion at 170 ^{o}C which reaches ~98 % by 200 ^{o}C. DME and formaldehyde selectivity has a maximum of 60 % and 36 % respectively at 170 ^{o}C which declined steadily by 220 ^{o}C, as such resulting in a steady inclination of CO selectivity to 85 %. Afterward, the selectivity of CO

reaches ~100 % at 98 % methanol conversion throughout the reaction above 220 ^oC.

The reaction profile reveals high activity of the nanodiamond catalyst with high selectivity to CO above 220 ^oC, resulting from further oxidation of formaldehyde and DME. Water produced during the reaction converts surface Lewis acid sites to Bronsted acid, which inhibits complete combustion of substrates to CO_2. The high activity of the nanodiamond support is associated to carbonyl oxygen functionality on the edges with high electron density, capable of activating methanol via hydrogen abstraction. However, it indicates high selectivity to DME (60 %) with 36 % formaldehyde at 75 % methanol conversion at low temperature of 170 ^oC, indicating presences of sp^2 defect or acidic site and carbonyl functionality on the surface. The graphitization of sp^3 to sp^2 during reaction at high temperature suppresses formation of electrophilic oxygen species that promotes complete oxidation, as such controlling oxygen dissociative adsorption diffusion on the surface as reported by Liu et al [40]. Moreover, the surface reveals dehydrogenation effect, which was similar to those observed by Tveritinova et al [38] during reaction of ethanol and 1-propanol on oxidized nanodiamond surface .

MoO_3 Supported on Nanodiamond

BET surface area of MoO_3/ND

Table 4. 4 ***BET surface area of MoO_3 loading on nanodiamond***

Catalyst	BET Surface area (m^2/g)
90 % MoO_3/ND	55
100 % MoO_3/ND	47
400 % MoO_3/ND	37

The BET analysis of MoO_3 supported on nanodiamond in Table 4. 4 presents surface area value of 55, 47 and 37 m^2/g for 90, 100 and 400 % MoO_3 monolayer coverage, respectively: clearly much lower than the original ND itself.

The surface area of the supported MoO_3 reveals decrease in the surface area of the catalysts with increasing MoO_3 loading on the support, which evidences good coverage of the active MoO_3 phase on the support. The 400 % monolayer MoO_3 coverage gives the lowest surface area, which indicates higher coverage of the support.

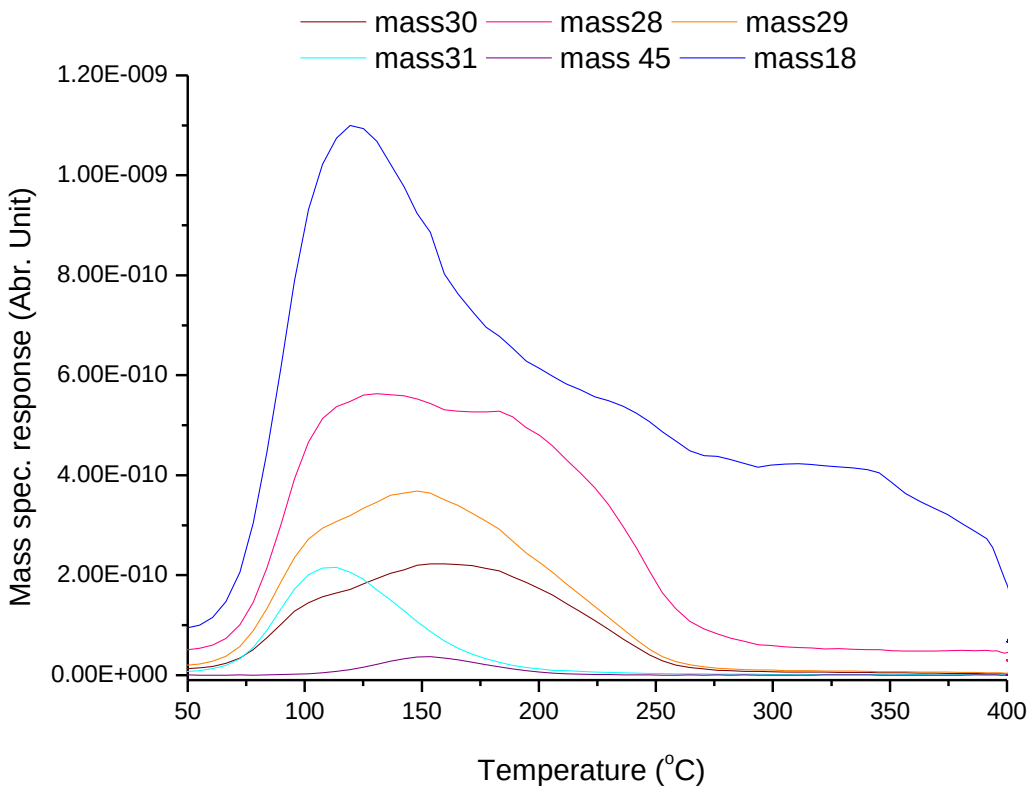

Fig. 4.9 ***TPD profile of methanol over 90 % monolayer coverage of MoO_3/ND***

Methanol desorption profile for 90 % MoO_3 coverage over oxidized ND support in Fig. 4.9 depicting desorption of methanol peak at 114 ^oC, with the preceding first water desorption peak at 120 ^oC. A coincidental desorption of broad formaldehyde and DME peaks appears at 154 ^oC, prior to a CO desorption observed at 183 ^oC alongside a broad second water shoulder peak at 240 ^oC, which lasted until 400 ^oC.

The TPD desorption profile in Fig. 4.9 indicates desorption of molecular adsorbed methanol at 114 ^oC, with coincidental desorption of formaldehyde and DME at 154 ^oC revealing existence of both redox and acid sites on the basal and apical faces

(010 + 101) and apical side face (001) respectively. The formation of DME involves interaction between chemisorbed methoxy on acidic site and surface adsorbed methanol species, which results in formation of water as evident by a slight water shoulder peak at the same temperature, but formaldehyde formation emanates from redox sites on MoOx. However, decomposition of DME resulted in formaldehyde and CO due to the broadening of the formaldehyde peak, while subsequent dehydrogenation of formaldehyde results in CO formation at 183 ^{o}C, usually accompanied by later water desorption peak at 240 ^{o}C. The low desorption of the second water peak could imply that the hydrogen abstracted from formaldehyde molecules are involved in possible bonding with nucleophilic oxygen on functional group or surface defect sites leading to lesser hydroxyl recombination on MoOx surface to produce water. Furthermore, the 90 % monolayer coverage MoO_3 over ND reveals lower formaldehyde desorption temperature of 154 ^{o}C in comparison to 173 ^{o}C of the ND support, which is due to the increasing density of redox sites provided by MoOx species dosed on the support. This species are responsible for dissociative adsorption of methanol as well as abstraction of H from surface methoxy, as such providing lesser energy path for formaldehyde desorption.

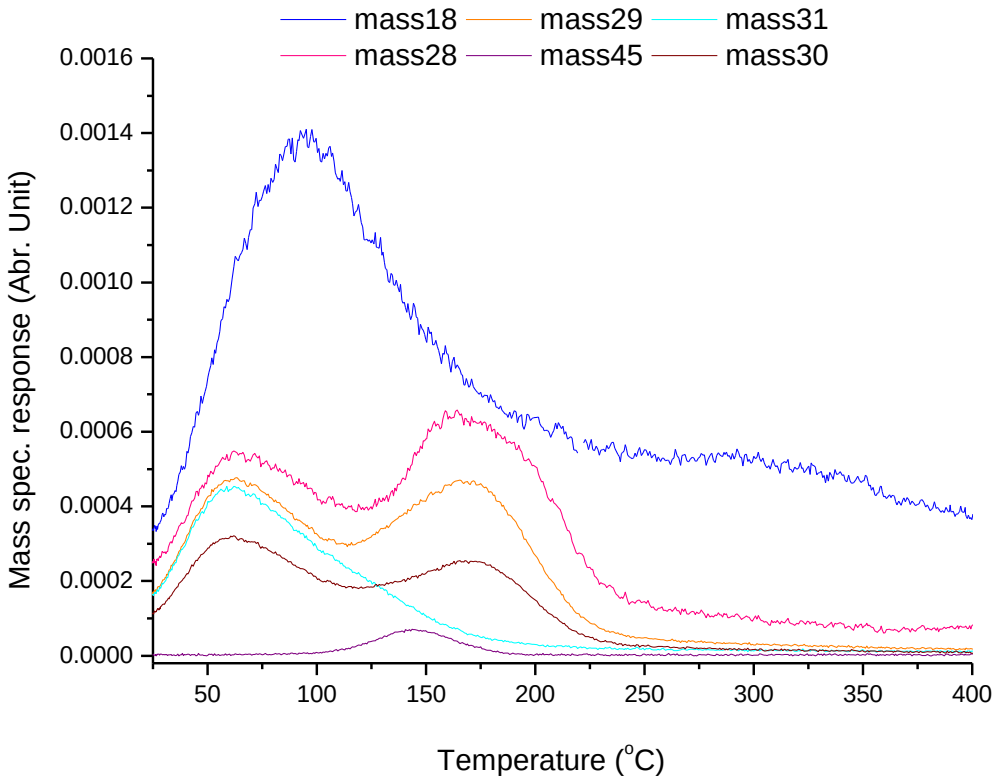

Fig. 4.10 ***TPD profile methanol over 100 % monolayer coverage of MoO_3/ND***

The 100 % MoO_3/ND catalyst in Fig. 4.10 reveals a low temperature methanol desorption peak at 59 ^oC, preceding broad water desorption at 95 ^oC. DME desorption was observed at 145 ^oC, with formaldehyde peak centred at 170 ^oC accompanied by CO desorption peak at 190 ^oC.

The low methanol desorption peak at 59 ^oC results from molecular adsorbed species. However, chemisorbed methoxy species yield DME at 145 ^oC and formaldehyde at 170 ^oC, with the former occurring on acid site (apical side faces) via reaction with adsorbed methanol species and the later on redox sites (basal faces) due to abstraction of hydrogen. The decomposition of DME results in formation of formaldehyde as evidenced by a decline in DME desorption peak at 164 ^oC, with subsequent oxidation of formaldehyde to CO resulting in CO shoulder peak by 190 ^oC.

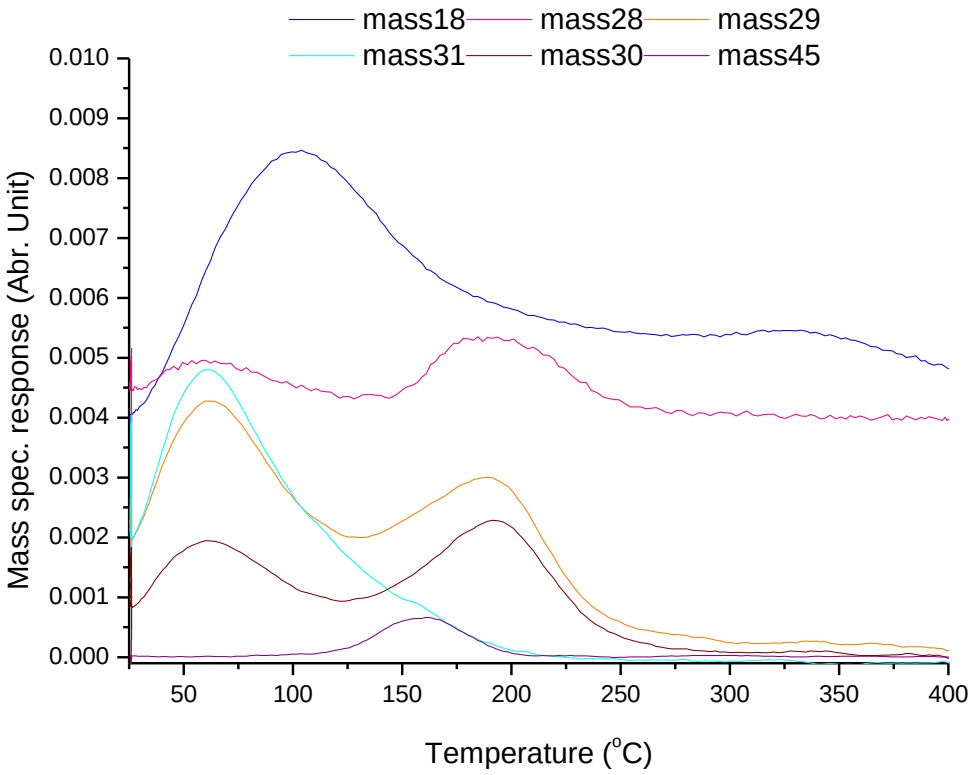

Fig. 4. 11 ***TPD profile of methanol over 400 % MoO_3/ND***

TPD desorption profile in Fig. 4. 11 depict molecular desorption of methanol at 62 °C prior to a broad water peak at 95 °C. Formaldehyde desorption peak was observed at 194 °C, with DME peak at 161 °C. However, a post-edge CO peak was observed at 201 °C.

The desorption profile of methanol over 400 % MoO_3/ND shows similar desorption trend and products as 100 % MoO_3/ND catalyst, but with higher desorption temperature of 194 °C and 161 °C for formaldehyde and DME respectively. This revealed the stability of surface chemisorbed methoxy species, with desorption temperature of formaldehyde similar to those reported by Farneth et al [84] on unsupported MoO_3 catalyst. However, the supported MoO_3 surface exhibit structure sensitivity, with acidic (apical faces) and redox (basal faces) sites producing DME and formaldehyde respectively, with such structure sensitivity of MoO_3 during methanol reaction observed by Tatibouet et al [85], Tatibouet and Germain [86], and Machiels et al [87] on methanol oxidation over MoO_3 supported on graphite and unsupported MoO_3.

Table 4. 5 ***Activation energy of CH_2O desorption on Nanodiamond and MoO_3/ND catalysts***

Catalyst	CH_2O desorption peak temperature (Tm)		Activation Energy
	^oC	K	(kJ/mol)
Nanodiamond (ND) support	173	446	115
90 % MoO_3/ND	154	427	110
100 % MoO_3/ND	170	443	114
400 % MoO_3/ND	194	467	121

The activation energy for formaldehyde desorption in Table 4. 5 indicate energy barrier of 115, 110, and 114 kJ/mol for nanodiamond support, 90 and 100 % MoO_3 coverage over nanodiamond support respectively. The 400 % MoO_3/ND catalyst reveals a higher activation barrier of 121 kJ/mol.

The results presented in Table 4.5, reveal similar desorption energies for nanodiamond support and 90 -100 % MoO_3 monolayer coverage.

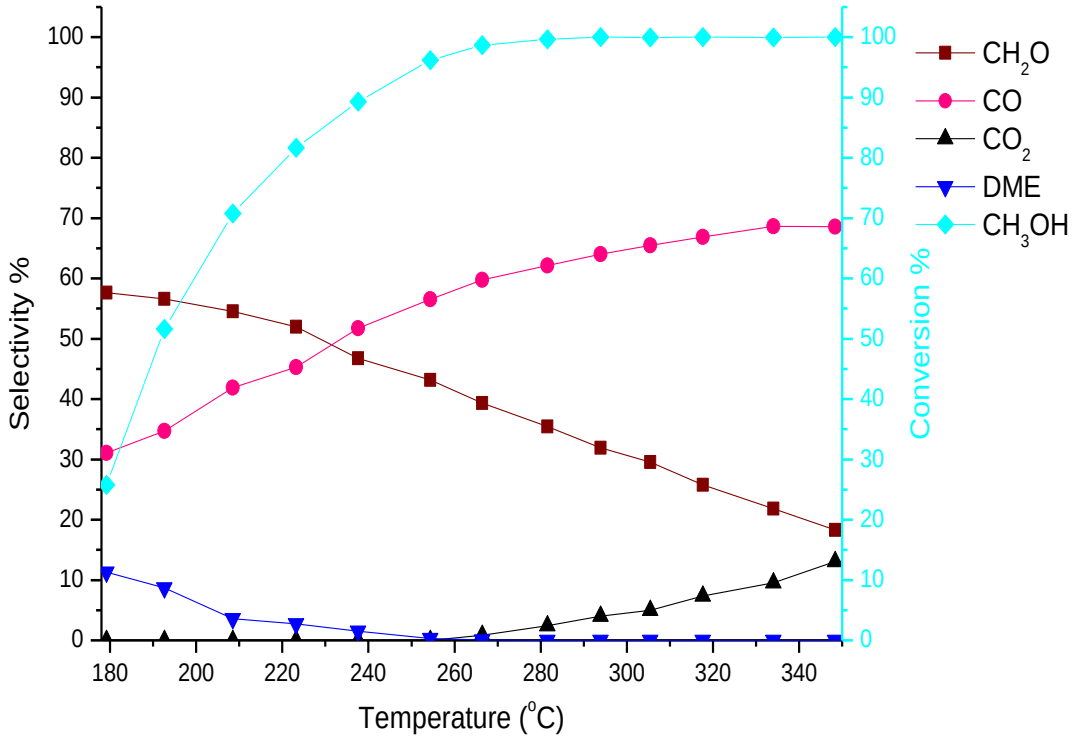

Fig. 4.12 ***Reaction profile of methanol oxidation over 90 % monolayer coverage MoO_3/ND***

The reaction profile in Fig. 4.12 indicates 57 % and 9 % selectivity for DME and formaldehyde respectively at 52 % methanol conversion by 193 ^oC, which declines steadily to 45 % with DME diminishing at 253 ^oC. CO selectivity increases to 60 %, with CO_2 selectivity reaching 3 % by ~100 % methanol conversion by 282 ^oC, and rises progressively at higher temperature.

The reaction profile reveal low activity of the catalyst at about 180 ^oC with low selectivity to formaldehyde and DME. This implies possible metal oxide-support interaction effect. With the MoO_3 binding on the graphitic edges, which are the active sites of the ND support, similar effect was reported on graphite using Ba_2O_3 and P_2O_5 by Frank et al [41]. However, the steady decline in formaldehyde selectivity indicates likely synergic effect between the support and MoO_3, via possible electron buffering and oxygen spill over effect from the graphitic plane, which oxidized the reduced Mo sites. The nanodiamond support could be

controlling the adsorption and diffusion of gas phase oxygen on to the reduced Mo site, similar to effect reported by Castillo et al on MoO_3 supported over α-Sb_2O_4.

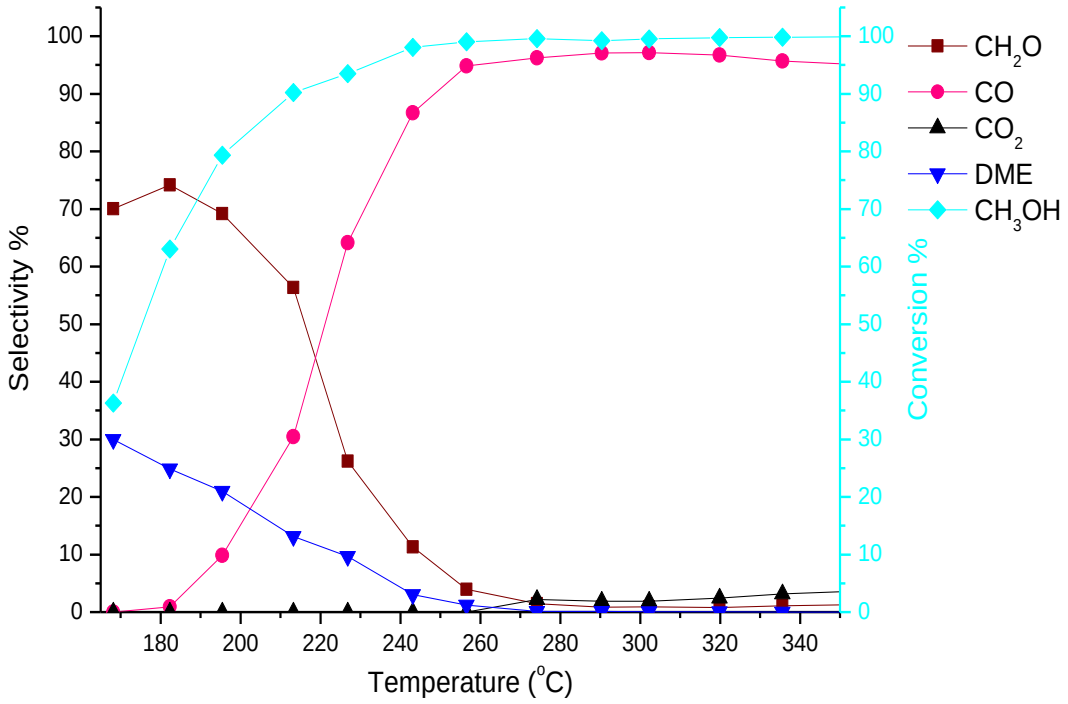

Fig. 4. 13 ***Reaction profile of methanol oxidation over 100 % monolayer coverage MoO_3/ND***

The reaction profile in Fig. 4. 13 reveals 70 % and 30 % selectivity to formaldehyde and DME sequentially at 36 % methanol conversion by 168 ^oC, with maximum formaldehyde selectivity reaching 74 % at 63 % methanol conversion by 182 ^oC. However, the decline in formaldehyde and DME selectivity to 4 % and 1 % respectively at 99 % methanol conversion by 257 ^oC results in increasing CO selectivity to 95 % , and formation of CO_2.

Methanol oxidation over 100 % MoO_3/ND reveals higher selectivity to CO at higher temperature above 250 ^oC. At lower temperature of 168 ^oC it displays higher activity, with methanol conversion reaching 36 % at 70 % formaldehyde selectivity. However, the catalyst exhibits structure sensitivity, with formaldehyde and DME produced on redox and acid sites respectively. The rapid decline in formaldehyde selectivity could result from secondary oxidation of formaldehyde to

CO by surface oxygen species. Although the reaction condition was aerobic, the rate of reduction of the MoO_3 sites exceeds the rate of it reoxidation by lattice oxygen: since diffusion of lattice oxygen from the bulk to the surface sites is less or barely significant at such low temperature (< 300 ^oC). This findings supports previous observation made by Ressler et al [88] . The lack of synergy between the active MoOx phase and the support is possibly due to coverage or large crystallite formation on the support, which limits the adsorption of gas phase oxygen on the support and possible reoxidation of the reduced Mo sites.

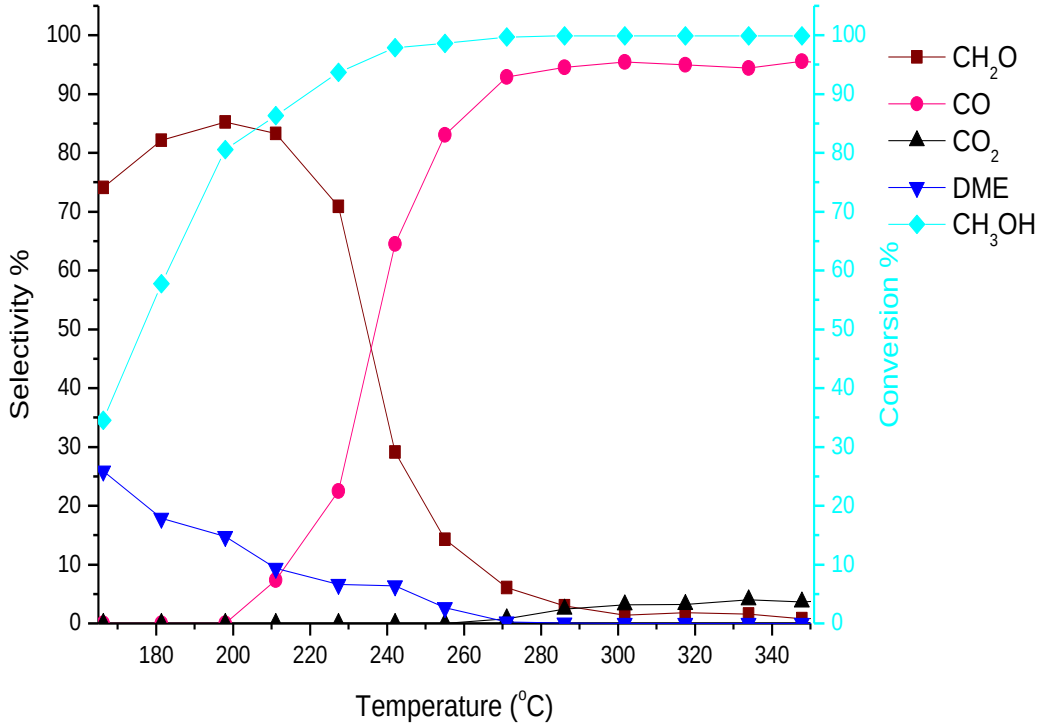

Fig. 4.14 ***Reaction profile of methanol oxidation over 400 % MoO_3/ND***

The reaction profile of methanol over 400 % MoO_3/ND in Fig. 4.14, reveals maximum formaldehyde selectivity of 85 % at 81 % methanol conversion, with DME selectivity reaching 15 % by 198 ^oC. Formaldehyde and DME selectivity decline steadily to 6 % and 1 % respectively at ~100 % conversion, resulting in consequential increases in CO selectivity to 93 %, which reaches 95 % above 300 ^oC.

The reaction profile of 400 % MoO_3/ND indicates similar reaction pathway as 100 % MoO_3/ND, but with higher formaldehyde selectivity of 85 % at high methanol conversion of 81 %, due to increasing MoO_3 loading and coverage on the support. However, above 230 ^oC, the formaldehyde selectivity declines steadily due to reduction of Mo site by methanol and subsequent oxidation of formaldehyde to CO by surface oxygen species. The rate of diffusion of lattice oxygen from the bulk to re oxidised the reduced surface Mo sites is slow at low temperature (< 300 ^oC), as such the rate of Mo site reduction surpasses its re oxidation. More so, DME formation at low temperature indicates presence of acid sites on the exposed MoO_3 (100) faces, which consists of oxygen vacancies and uncoordinated Mo as reported by Tatibouet and Germain [86], and Abon et al [89].

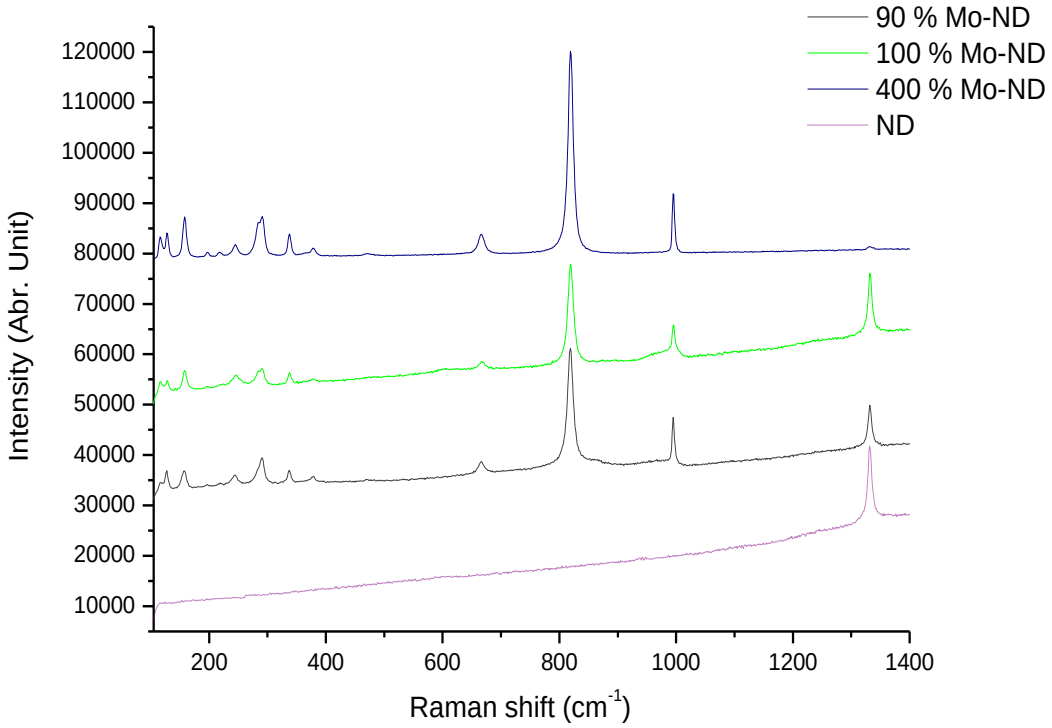

Fig. 4.15 ***Comparison of Raman spectra of MoO_3 /ND calcined at 500 ^oC***

Raman spectra of MoO_3 supported on nanodiamond in Fig. 4.15 depicts Raman bands at 1332, 995, 819, 666 cm^{-1}, assigned to diamond sp^3 C symmetric, asymmetric Mo=O, O-Mo-O symmetric, and asymmetric vibration modes

respectively. However, both 90 and 100% MoO_3 monolayer coverage reveals a broad shoulder peak at 967 cm^{-1} and 970 cm^{-1} respectively attributable to symmetric stretching of dioxo $(=O)_2MoO_2$ species. However, the additional shoulder peak observed at 860 cm^{-1} on 90 % MoO_3/ND sample and the weak broad band at 605 cm^{-1} on the 100 % MoO_3/ND are assignable to Mo-O-ND bond bridging vibration and symmetric stretching of distorted MoO_6 units. The additional lower bands at 470, 379, 337, 291, 245, 219, 197 and 158-117 cm^{-1} are assigned to Mo-O bending, scissoring, δ-bending, wagging, twisting, rotational rigid MoO_4 chain mode, Mo=O twisting and translational rigid chain MoO_4 vibration mode respectively.

The Raman spectra indicates existence of crystalline and MoOx monomeric species forming Mo-O-ND bonding as evident by the band at 860 cm^{-1} for 90 % MoO_3/ND, as well as 967 cm^{-1} for dioxo $(=O)_2MoO_2$ species. The dioxo species band shifted to 970 cm^{-1} in 100 % MoO_3/ND with emergence of the band at 605 cm^{-1} indicating presence of polymeric distorted MoO_6 or MoO_5 species, which are consistent to those reported by Tian et al [77] for MoO_3 supported catalyst at low coverage. More so, the nearly ansent diamond peak at 1332 cm^{-1} and presence of O-Mo-O bending vibration band at 470 cm^{-1} and well defined lower Raman bands on the 400 % MoO_3/ND, indicates complete coverage of the support with crystalline MoO_3.

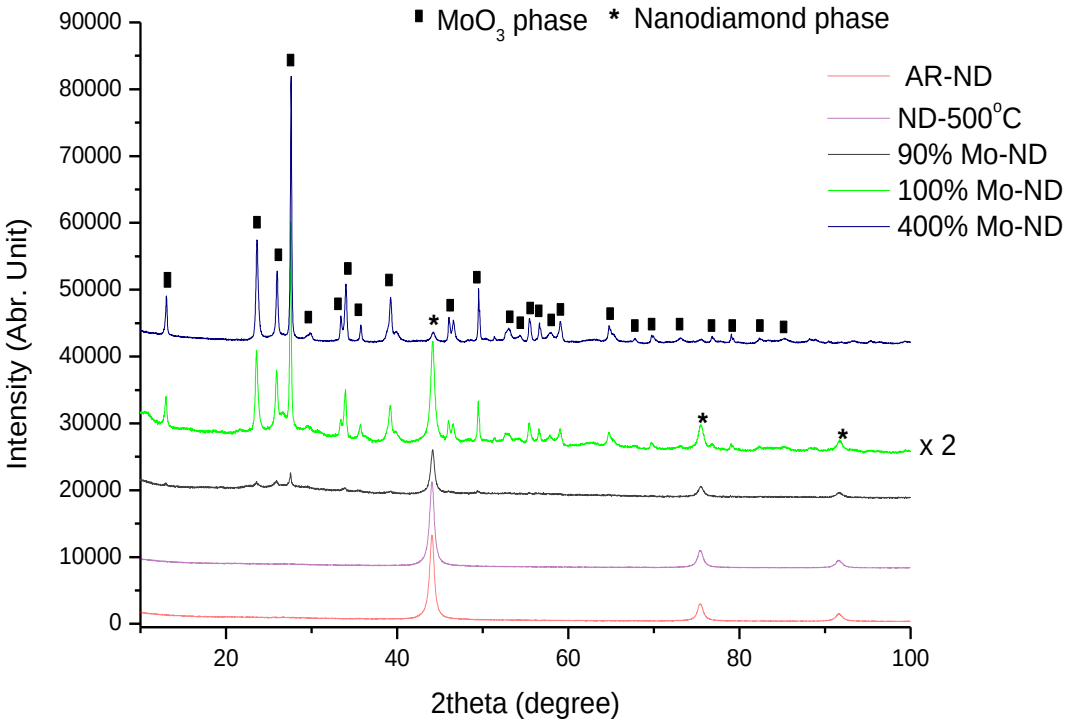

Fig. 4.16 ***Diffractogram of nanodiamond and MoO_3/ND***

A powder X-ray diffractogram of ND and MoO_3 supported on nanodiamond in Fig. 4.16 above depicts peaks at 2θ angle of 13.0 °, 23.6 °, 25.9 °, 27.6 ° and 29.6 ° (corrected to a deviation of ± 0.2) for MoO_3/ND attributed to crystalline α - MoO_3 phase as indexed in JCPDS card no 00-005-0508 [90]. The slant shoulder peak at 26.6 ° in 100 % MoO_3/ND is assigned to crystalline tetragonal Mo_5O_{14} phase as indexed in JCPDS card no. 01-074-1415 [91]. The 2θ angles at 44.1 °, 75.5 ° and 91.6 ° are ascribable to (111), (220) and (311) cubic diamond reflection for both as-received and oxidized nanodiamond calcined at 500 °C based on assignment of JCPDS Card no.03- 065-6329 [92] with no peak at 2θ value of 26 ° attributable to graphite.

The powder diffractogram of MoO_3/ND catalysts reveals crystalline phase of MoO_3. The broadening of the peaks attributed to MoO_3 phase in 90 % monolayer MoO_3 coverage catalyst signifies formation of amorphous MoO_3 phase. However, the 100 % coverage MoO_3/ND catalyst evidences the existence of tetragonal Mo_5O_{14} phase due to additional peak at 26.6 °. The marked decrease in the intensity

of the 44.1 ^{o} (111) nanodiamond reflection peak and increase in the MoO_3 peaks intensity in the 400 % MoO_3/ND catalyst indicates complete coverage of the support by crystalline MoO_3 phase. The broad base of the nanodiamond peaks is associated with grain boundary of crystallites attributed to disordered sp^3 carbon as reported by Mochalin, et al [4]. However, calcination of the support at 500 ^{o}C indicates no observable changes in the structure or phase in comparison to the as received nanodiamond support, contrary to the observation reported by Xu et al [13] for oxidized nanodiamond support at 500 ^{o}C.

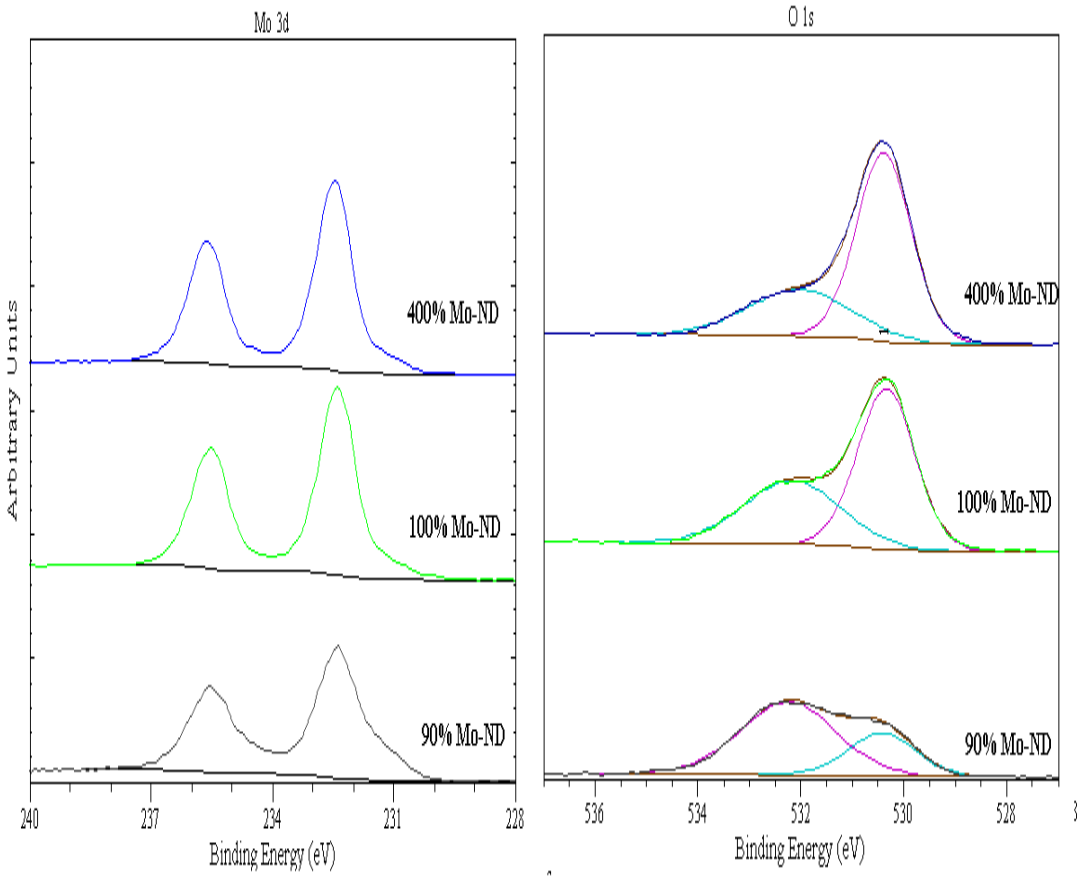

Fig. 4.17 ***XPS Mo 3d and O1s spectra of supported MoO_3/ND catalysts***

The XPS spectra Mo 3d doublet for MoO_3/ND catalysts in Fig. 4.17 indicates Mo binding energy at 235.5 ± 0.2 eV and 232.5 ± 0.2 eV associated with $3d_{3/2}$ and $3d_{5/2}$ splitting respectively for Mo^{6+}, with lower binding energy at 231.1 ± 0.2 eV assigned to Mo^{5+}. The deconvoluted O1s peak of the supported MoO_3 catalysts reveal two distinct peaks at binding energy of 530.4 ± 0.2 eV and 532.1 ± 0.2 eV ascribed to MoO_3 and nanodiamond surface oxygen species respectively.

The Mo 3d binding energies indicate Mo in its highest oxidation state 6+, while the binding energy at 231.1 ± 0.2 eV indicates the presence of under coordinated Mo^{5+} species. However, the deconvoluted O1s peaks assigned to oxygen bounded to molybdenum (O-Mo) and carbon in nanodiamond (C-O) as evidenced by the binding energies at 530.4 ± 0.2 eV and 532.1 ± 0.2 eV respectively reveals increase in intensity of the O-Mo peak in comparison to the C-O peak with increasing Mo loading on the support. This implies increasing surface coverage of MoO_3 on the support as well as titration of the oxidize nanodiamond surface via bond formation with MoOx species, with monolayer coverage achieved by 100 % MoO_3 coverage.

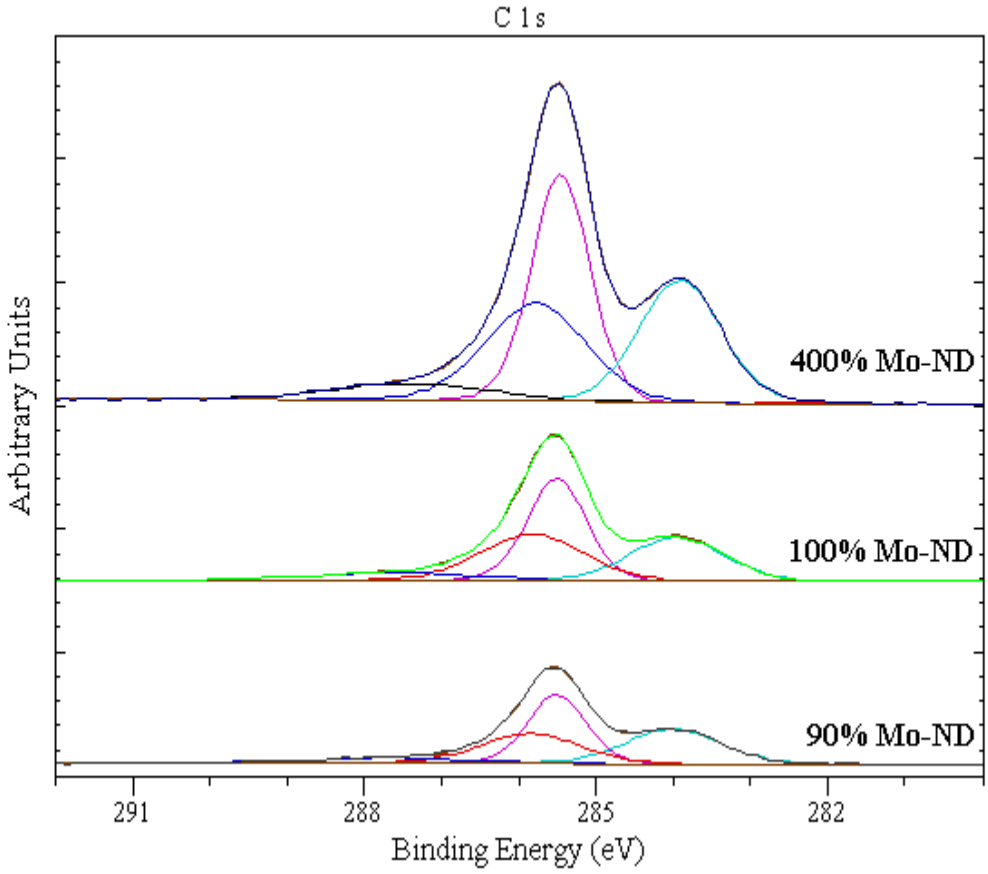

Fig. 4.18 ***XPS C1s spectra of support MoO_3/ND catalysts***

The C1s spectra in Fig. 4.18 reveals the presence of four distinct carbon species with binding energies at 283.9-284, 285.5, 285.8-285.9 and 287.4 – 287.7 eV assigned to sp^2, sp^3, C-C(O)-O, C=O species respectively.

The XPS spectra indicate the presence of sp^2 graphitic carbon, which usually covers the surface of the sp^3 diamond core. The existence of sp^2 graphitic carbon after heating the support at 500 ^oC in ambient air is evident by the C1s peak at 284 eV. These sp^2 carbon species are still present even after oxidation, and does not seem to be involved in bonding with MoOx phase. However, the spectra reveal the presence of small amount of surface carbonyl group (C=O) at 287.7 eV, which could be attributed to ketonic or acid anhydride located at the edges of the nanodiamond surface that are inaccessible to MoO_x.

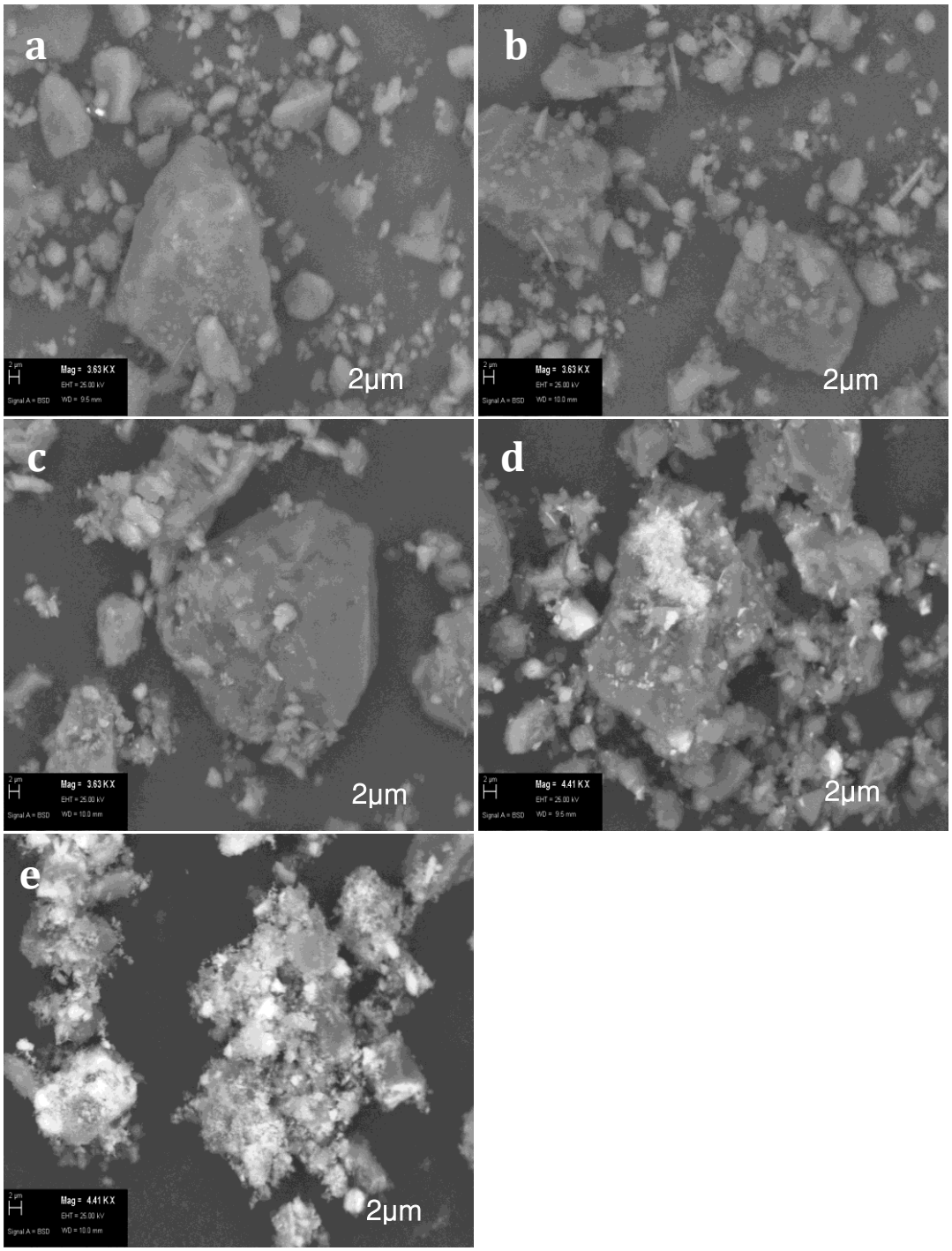

Fig. 4.19 ***SEM micrographs of nanodiamond and MoO_3/ND; (a) As-received ND, (b) Oxidized ND at 500 ^oC, (c) 90 % MoO_3/ND, (d) 100 % MoO_3/ND, (e) 400 % MoO_3/ND, scale; 42 x 48µ***

The SEM micrographs in Fig. 4.19 depict large and small aggregates of nanodiamond for the as received sample in (a), with small grain size observed on the surface of large crystallite in the nanodiamond calcined at 500 ^oC (b). The 90 %

MoO_3/ND in (c) reveals a grey region with disperse patches of white crystallite particles, which increases in brightness and coverage on 100 % MoO_3/ND catalyst as shown in (d), with emergence of highly dense region of spongy-like and isolated island of larger white crystallites structure formed on the edges of the support. More so, the 400 % MoO_3/ND indicates complete coverage of the support by white sponge-like structure, and intense white larger crystallites particles sparingly distributed on the surface.

The micrograph of the as received nanodiamond indicates formation of both small and large aggregates, while the large aggregates disintegrate into small particles due to calcination. This evidence of better dispersion of the particles as in the case of nanodiamond calcined at 500 ^oC. The formation of amorphous white disperse structure in 90 % MoO_3/ND indicates formation of amorphous MoOx on the support, with the large crystallite structure resulting from crystalline MoO_3. However, the dense region of white spongy structure and isolated patches of crystallites on the 100 % MoO_3/ND catalyst could be attributable to both amorphous and crystalline MoO_3 respectively. The formation of dense white crystalline MoO_3 at the edges of the support implies high oxygen density on this region for anchoring of MoOx species. A complete coverage of the support surface at 400 % MoO_3/ND sample is evidence by increased dispersion and density of the white spongy-like crystalline MoOx structure.

Table 4. 6 ***Comparison of Mo content on nanodiamond supported catalysts***

Catalyst	SEM – EDX of Mo content (wt%)
100 % MoO_3/ND	10.7
400 % MoO_3/ND	21.2

The estimates of Mo content of MoO_3/ND catalysts in Table 4. 6 presents 10.7 wt % for 100 % monolayer coverage, with the 400 % MoO_3/ND revealing similar Mo content.

The data indicates MoO_3 is highly segregated on the surface at 100 % coverage, with 400 % MoO_3 loading estimated to have twice the amount of Mo content

required to form 100 % coverage on nanodiamond support. The EDX data is in good agreement with SEM images revealed for 100 % coverage and 400 % MoO_3 loading, which indicates formation of bulk crystalline MoO_3 species on the support.

γ-Al_2O_3 support

Table 4. 7 ***BET surface area of γ-Al_2O_3 calcined at different temperatures***

Catalyst	BET Surface area (m^2/g)
As-received	61
400 ^oC	72
500 ^oC	69
600 ^oC	58
700 ^oC	53
800 ^oC	49
900 ^oC	45

Table 4. *7* above present changes in surface area of the as-received γ-Al_2O_3 with increasing calcinations temperature. The as-received γ-Al_2O_3 support reveals surface area of 61 m^2/g, which increases to 72 m^2/g at 400 ^oC. The surface area reduces steadily from 69 – 45 m^2/g from 500 – 900 ^oC.

The increase in surface area of as-received γ-Al_2O_3 catalyst after calcination at 400 ^oC is attributable to removal of adsorbed water or surface hydroxyl group, which are typical of the boehmite (AlOOH) structure. The slight decrease in the surface area to 69 m^2/g at 500 ^oC might be due to phase transition of boehmite to γ-Al_2O_3, while steady sintering (crystallization) of the support from 53 – 45 m^2/g indicates structural phase transition of γ – δ-Al_2O_3 due to dehydroxylation of surface hydroxyl group. The decreasing in surface area with increasing calcinations temperature above 500 ^oC indicates similar sintering trend observed by Hindin and Weller [56] and Maciver et al [93] for γ-Al_2O_3 calcined between 400 – 900 ^oC.

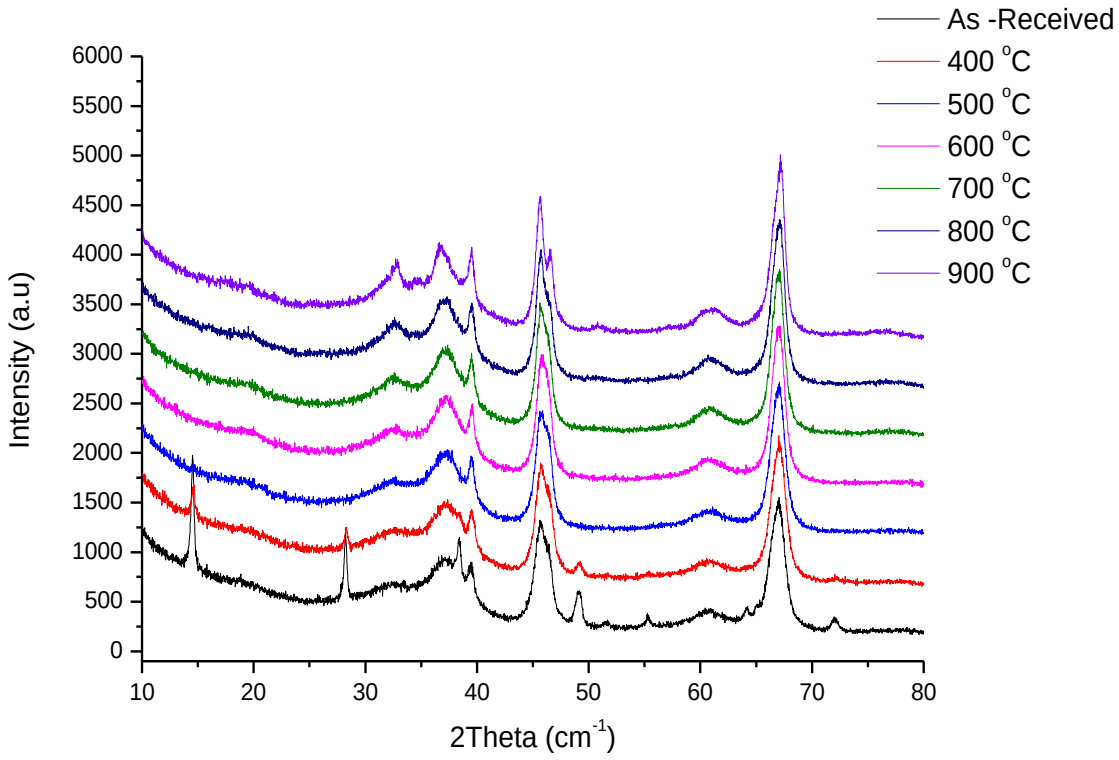

Fig. 4.20 ***Diffractogram of phase evolution and transition of γ-Al_2O_3 sample at various calcination temperatures***

A powder diffractogram in Fig. 4.20 depicts 2θ value at 32.2, 36.8, 39.5, 45.6, 60.4 and 67.1 ^{o} attributed to γ-Al_2O_3 phase in accordance with JPCDS indexed in card no.01-080-0956, with additional peaks at 14.5, 28.3, 38.4, 49.2, 55.3, 64.2 and 72 ^{o} observed on the as-received γ-Al_2O_3 sample assigned to boehmite phase as indexed in JCPDS card no. 01-083-2384. Furthermore, increasing calcination temperatures of the as-received sample to 400 ^{o}C decreases the intensity of the additional peaks, which is completely absent at 500 ^{o}C with slight shift in the peak position of 32.4 ^{o} and 60.6 ^{o} peaks to 34.6 ^{o} and 60.7 ^{o} respectively. These peaks become narrower between 600 – 800 ^{o}C, with corresponding slanting of the 45.6 ^{o} peak shoulder at 800 ^{o}C. The splitting of the 45.6 ^{o} peak results in evolution of side peak at 46.5 ^{o} and appearance of additional peaks observed at 34.6 ^{o}, 46.5 ^{o} and 50.8 ^{o} for support calcined at 900 ^{o}C, which is assigned to δ- Al_2O_3 phase as indexed in JCPDS card no 00-46-1215.

The diffractogram depicts the as received sample as crystalline boehmite with hydroxylated surface, which is orthorhombic bipyramidal in nature. Calcination at

400 ^{o}C reveals a decrease in intensity of the peaks at 14.5 ^{o}, 28.3 ^{o}, 38.4 ^{o}, 49.2 ^{o}, 55.3 ^{o}, 64.2 ^{o} and 72 ^{o} due to gradual transition of the orthorhombic structure of boehmite to γ-Al_2O_3 via dehydroxylation of the hydroxyl layer, which is only complete at 500 ^{o}C. The splitting of 46.5 ^{o} peak for sample calcined at 500 ^{o}C reveals the tetragonal nature of the γ-Al_2O_3 structure. The tetragonal structure reduces at 600 ^{o}C due to collapse of the boehmite structure along a – axis leading to shearing along b – axis. This results in ordering of oxygen atoms in the sublattice (into fcc structure) and migration of both tetrahedral and octahedral Al cation within the interstices framework, which stabilizes around 700 ^{o}C. The splitting of 45.6 ^{o} peak became notable again at 800 ^{o}C, before appearance of the 46.5 ^{o} peak, indicating an increase in tetragonal distortion of γ-Al_2O_3 structure with increasing calcination temperature to 900 ^{o}C. This results from migration of octahedral cation to tetrahedral site within the unit cell. This findings are in agreement with similar transition trend reported by Paglia et al [52] for boehmite derived γ-Al_2O_3: although, the additional peaks at 34.6 ^{o}, 46.5 ^{o} and 50.8 ^{o} for support calcined at 900 ^{o}C indexed to δ- Al_2O_3 phase were appropriately designated as a new gamma alumina prime (γ'-Al_2O_3) phase by Paglia et al [52]. Moreover, this phase may be a transition phase consisting of a mixture of both γ and δ- Al_2O_3 phases.

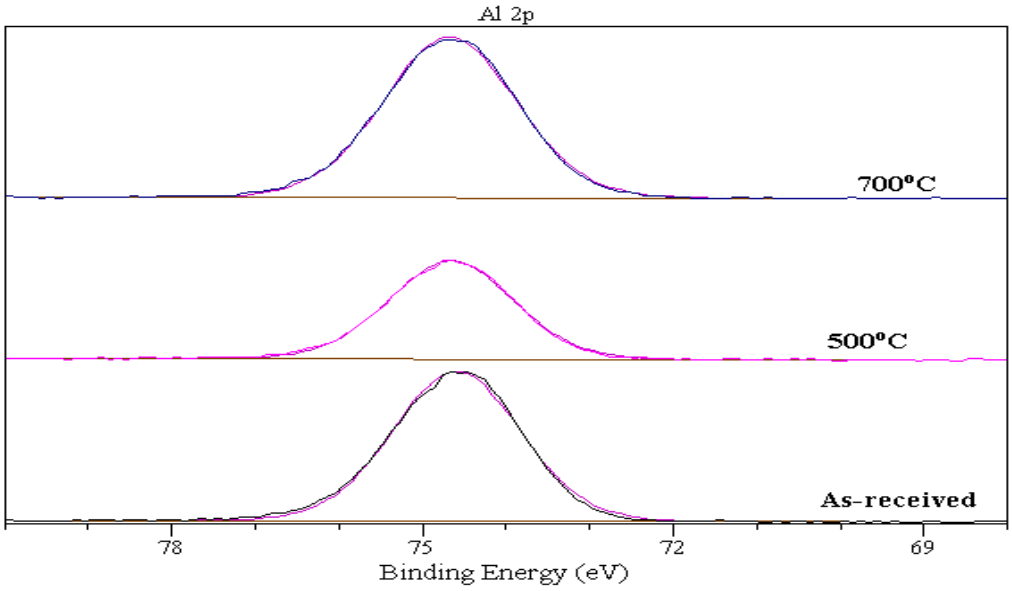

Fig. 4.21 ***XPS spectra of γ-Al_2O_3 samples calcined at different temperatures***

The XPS spectra of γ-Al_2O_3 calcined at different temperatures in Fig. 4.21, which depicts Al 2p binding energy of 74.6 ± 0.2 eV for as-received support, while the sample that calcined at 500 ^oC and 700 ^oC indicates a slight shift in the 2p binding energy to 74.7 ± 0.2 eV. This indicates existence of Al in highest oxidation state of + 3 on the surface, which agrees with value reported by Zingg et al [76].

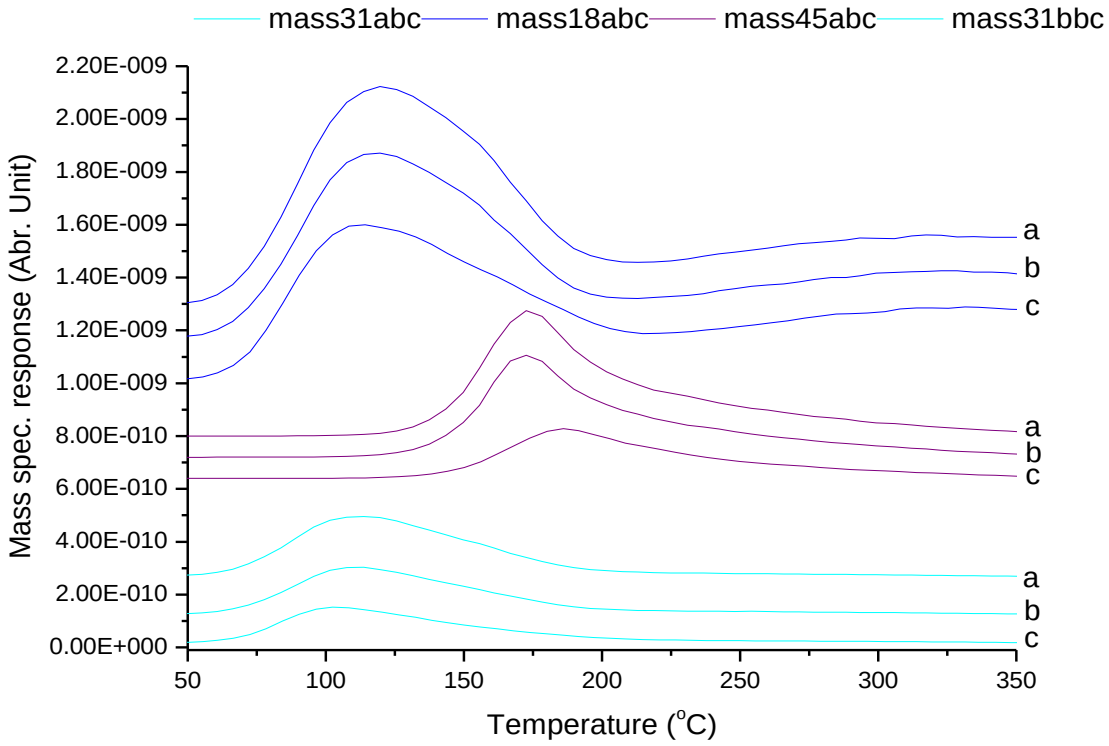

Fig. 4.22 ***TPD profile of methanol over γ-Al_2O_3 supports calcined at different temperature (a) as-received (b) 500 ^oC (c) 700 ^oC***

The comparison of TPD profile of methanol over γ-Al_2O_3 supports calcined at different temperatures in Fig. 4.22 which depicts methanol desorption peaks at 114 ^oC, 115 ^oC and 108 ^oC for as received, 500 ^oC and 700 ^oC for γ-Al_2O_3 respectively. The as received γ-Al_2O_3, reveals higher desorption temperature of water peak at 120 ^oC, which decreases with calcination temperature to 115 ^oC for 500 ^oC γ-Al_2O_3 and 102 ^oC for 700 ^oC γ-Al_2O_3. However, the main desorption product is DME, with slight variation in DME desorption temperatures for the 700 ^oC γ-Al_2O_3, 500 ^oC γ-Al_2O_3 and as-received γ-Al_2O_3 catalysts recorded at 186 ^oC, 175 ^oC and 173 ^oC respectively.

The desorption profile for alumina samples reveal variation in strength of surface acidic sites for formation of DME. The lower DME desorption temperature at 173 ^oC and 175 ^oC for the as received and 500 ^oC γ-Al_2O_3 samples respectively could be from Lewis acid sites (Al_V) on the (100) face, which is completely dehydroxylated above 327 ^oC as reported by Digne et al [50] and Kwak et al [63]. The higher temperature desorption at 186 ^oC reveals strong chemisorptions of methoxy species on strong Lewis acid sites (Al_{III}) on predominant (110) face of the catalyst calcined at 700 ^oC. Although these sites are normally hydroxylated by adsorbed water and could only be free after pre-treatment at 700 ^oC, a plausible explanation of the existence of these sites during reaction is due to partial hydration by water molecule. The water adsorption or hydroxylation of the (110) Al_{IV} surface was reported by Wischert et al [53, 54] to increases the Lewis acidity (by exposing free A_{lII} site) and basicity of the non-adjacent triple bonded O atom, which enhances chemisorptions of methanol on the surface as well as lower the adsorption energy of the surface. This could be possibly the reason for the low desorption temperature and intensity of methanol and water peaks at 108 ^oC and 102 ^oC respectively. Furthermore, the decrease in intensity of the methanol, water and DME desorption peaks of the 700 ^oC calcined γ-Al_2O_3 in comparison to other samples could indicate an increase in density of this Lewis acid-base Al_{III}-O pairs on the surface. This result is in good agreement with optimum density for Al_{III}-O species as reported by Wischert et al [54] for γ-Al_2O_3 calcined at 700 ^oC.

Table 4.8 ***Activation energies of DME desorption on as received and calcined γ-Al_2O_3 support at different temperatures***

Catalyst	DME desorption peak temperature (Tm)		Activation Energy (kJ/mol)
	^oC	K	
As received γ-Al_2O_3	173	446	115
γ-Al_2O_3 calcined at 500 ^oC	175	448	116
γ-Al_2O_3 calcined at 700 ^oC	186	459	119

Table 4.8 above shows activation energies of 115, 116 and 119 kJ/mol for DME desorption on as-received γ-Al_2O_3, γ-Al_2O_3 calcined at 500 ^oC (γ-Al_2O_3-500) and 700^oC ((γ-Al_2O_3-700) respectively. The values indicate similar activation energy barriers for DME desorption on the supports, which evidence presence of similar surface sites as well as reaction mechanism for methanol interaction over various γ-Al_2O_3 supports.

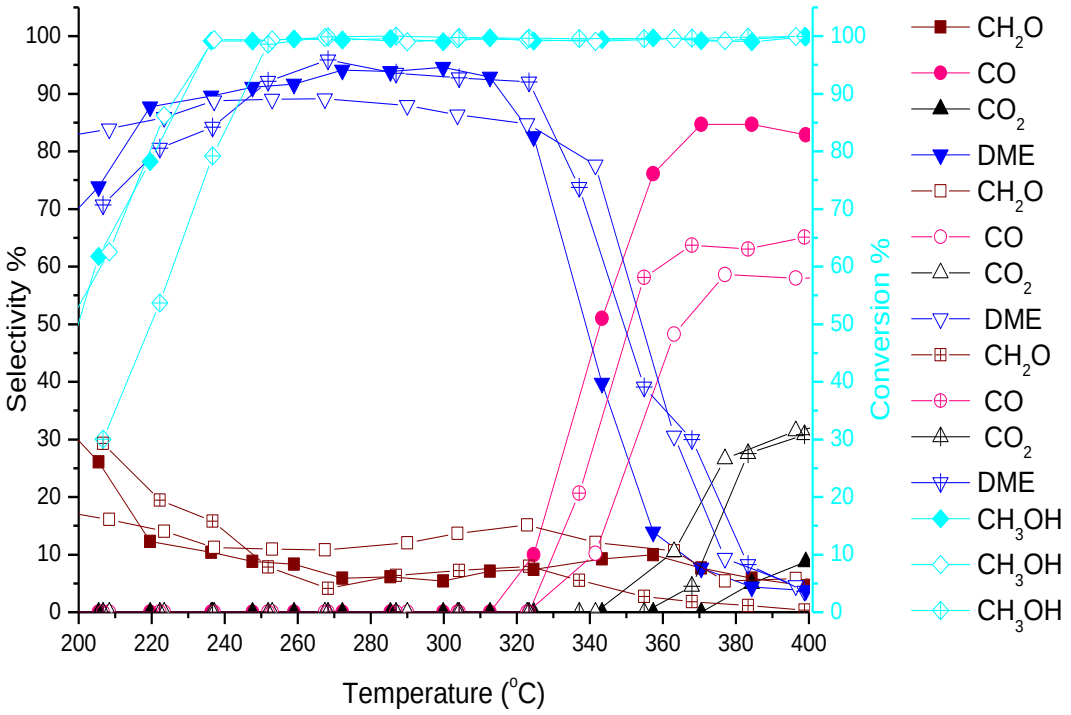

Fig. 4.23 ***Comparison of reaction profile of methanol oxidation over γ-Al₂O₃ calcined at different temperature; (a) As-received -filled symbols (b) calcined at 500 °C- unfilled symbols (c) calcined at 700 °C- crossed symbols***

The reaction profile of γ-Al_2O_3 catalysts in Fig. 4.23 reveal high to DME selectivity of 85-96 % at ~100 % methanol conversion by 268 °C. The as – received and 500 °C γ-Al_2O_3 reveal 62 % methanol conversion by 207 °C in comparison to 29 % observed for 700 °C calcined γ-Al_2O_3 catalyst, which drops rapidly above 320 °C. Formaldehyde selectivity is ~30 % for both as received and 700 °C calcined γ-Al_2O_3 by 200 °C, with 17 % selectivity recorded for 500 °C γ-Al_2O_3 catalyst. In addition, the formaldehyde selectivity declines to ~10 % and ~2 % for both as received and 500 °C γ-Al_2O_3, and 700 °C calcined γ-Al_2O_3 catalyst respectively by 360 °C. A maximum CO selectivity of 80 % and 60 % was recorded for as received and 500 °C calcined γ-Al_2O_3 respectively by 368 °C, with 65 % CO selectivity recorded for 500 °C calcined γ-Al_2O_3 catalyst at 377 °C. This is accompanied by increasing CO_2 selectivity reaching 30 % and 10 % for both 500 °C and 700 °C calcined γ-Al_2O_3, and as received γ-Al_2O_3 catalyst respectively by 400 °C.

The reaction profile reveals similar activity of 50 % methanol conversion for both as received and 500 ^oC γ-Al_2O_3 catalysts at 200 ^oC, with lower activity of 30 % conversion observed for 700 ^oC γ-Al_2O_3 catalyst at the same temperature. This is probably associated with the loss of surface area for high temperature calcined γ-Al_2O_3 catalyst as shown in Table 4.7. However, the catalysts reveal similar selectivity that declined sharply above 320 ^oC due to deactivation of the Lewis acid sites by water, a reaction product that decreases the surface acidity resulting in CO and CO_2 production. These findings are in agreement with water deactivating effect on γ-Al_2O_3 reported by Schiffino and Merrill [68], and Zuo et al [69]. Formaldehyde formation could results from β-hydrogen abstraction from methoxy species by double or triple coordinated surface oxygen sites keeping the selectivity at ~15 % below 320 ^oC.

MoO_3 supported on γ-Al_2O_3

Table 4.9 ***surface area of MoO_3/Al_2O_3 catalysts***

Catalyst	BET Surface area (m^2/g)
2wt % MoO_3/ γ-Al_2O_3 -500	51
2wt % MoO_3/ γ-Al_2O_3-700	46
10wt % MoO_3/ γ-Al_2O_3-500	35
10wt % MoO_3/ γ-Al_2O_3-700	42

The surface area of MoO_3 supported on γ-Al_2O_3 support calcined at 500 ^oC (via water impregnation) and 700^oC (via citrate impregnation) in Table 4.9 presents a surface area of 51 and 46 m^2/g for 2wt % MoO_3/γ-Al_2O_3-500 and 2wt % MoO_3/γ-Al_2O_3-700 respectively. The surface area decreases to 35 and 42 m^2/g for 10wt % MoO_3/γ-Al_2O_3-500 and 10wt % MoO_3/γ-Al_2O_3-700 accordingly.

The γ-Al_2O_3 supported MoO_3 catalyst reveals a decrease in surface area with increasing MoO_3 loading, which is quite significant in water impregnated MoO_3/ γ-Al_2O_3 catalysts. This could relate to inhomogeneous dispersion/coverage and crystallization (sintering) of the MoOx phase on the support due to rapid

evaporation of water molecules during calcination. However, the citrate impregnated MoO_3/ γ-Al_2O_3 catalysts indicates little decrease in surface area with increasing weight % loading, which indicates better dispersion of the active MoO_3 phase on the support due to chelating effect of the citrate precursor. Furthermore, addition of citrate increases the viscosity of the impregnation solution, as such resulting in slow diffusion of solvent during drying and calcination process. This effect enhances better dispersion than water-impregnated catalysts.

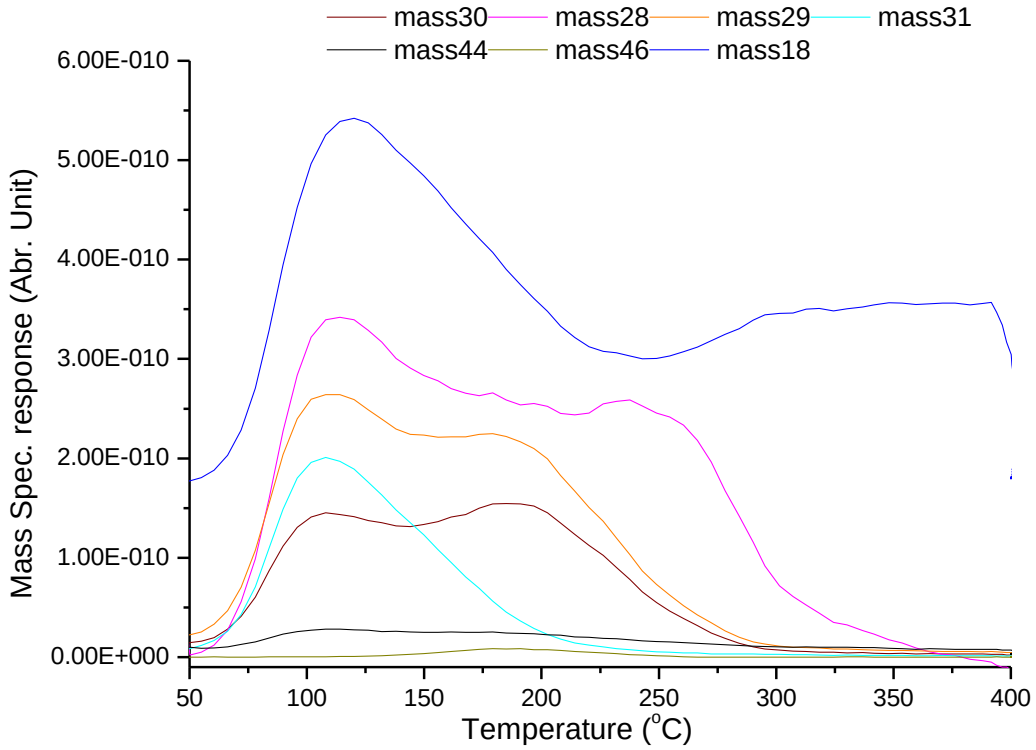

Fig. 4. 24 ***TPD desorption profile of methanol over 2wt % MoO_3/ γ-Al_2O_3-500***

The desorption profile in Fig. 4. 24 depicts a methanol desorption peak centred at 107 ^oC, preceding a broad water peak at 118 ^oC. Formaldehyde desorption peak was observed at 197 ^oC after a little DME peak centred at 185 ^oC, with a CO peak at 238 ^oC.

The methanol and water peaks at 107 ^oC and 118 ^oC respectively are attributable to molecular adsorbed methanol species and recombination of surface hydroxyl group respectively, while DME desorption at 185 ^oC could result from exposed acid sites on the γ-Al_2O_3 support. More so, formaldehyde desorption peak at 197 ^oC reveals

dehydrogenation of methoxy species on redox MoO_3 sites with further dehydrogenation resulting in CO desorption peak at 238 ^oC. The TPD profile reveals nearly complete titration of the acidic sites on γ-Al_2O_3 support by 2wt % MoO_3 loading indicating almost complete monolayer coverage.

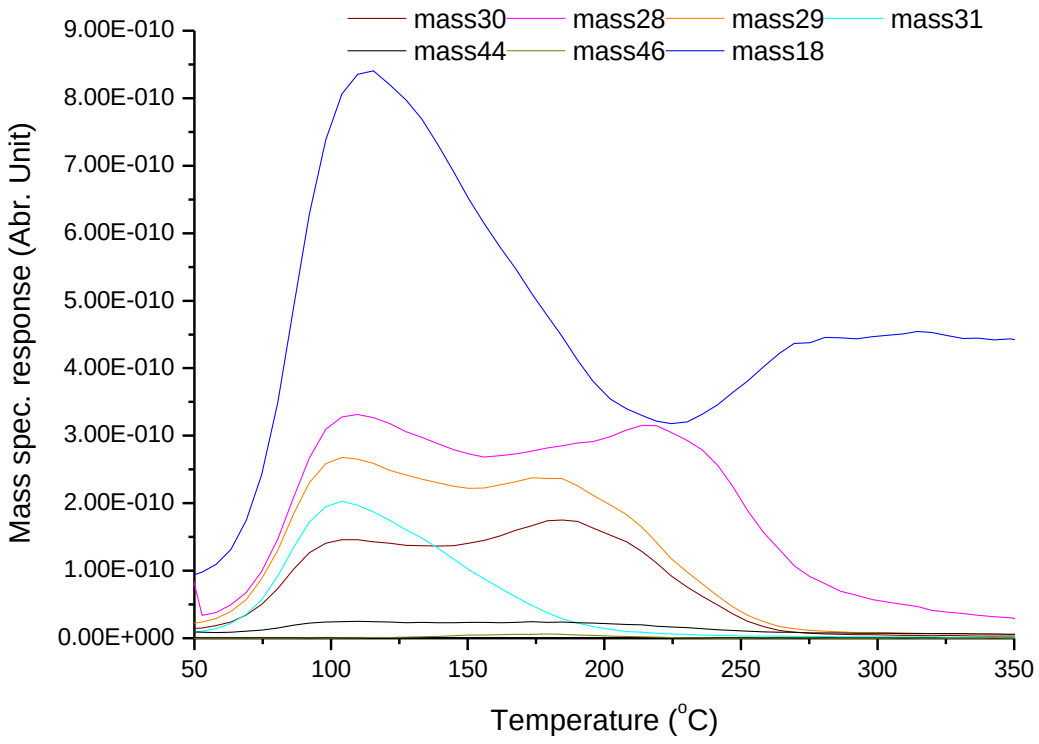

Fig. 4. 25 ***TPD profile of methanol over 10wt % MoO_3/ γ-Al_2O_3-500***

Methanol desorption on 10wt % MoO_3/ γ-Al_2O_3 in Fig. 4. 25 depicts a methanol desorption peak at 103 ^oC, before a broad water peak at 115 ^oC. A lower formaldehyde desorption temperature was observed at 185 ^oC preceding minute DME desorption peak at 179 ^oC, while a CO peak was observed at 216 ^oC.

The desorption profile for methanol on 10wt % MoO_3/Al_2O_3 indicates good coverage of MoO_3 on the support, as well revealing desorption of molecular adsorbed methanol at 103 ^oC. The water desorption at 115 ^oC results from surface recombination of hydroxyl species. However, formaldehyde is the dominant product emanating from redox Mo sites at 185 ^oC, while trace amount of DME peak at 179 ^oC indicates possible exposure of acid sites on γ-Al_2O_3 surface. The

CO desorption at 216 ^oC could be attributed to further dehydrogenation of formaldehyde.

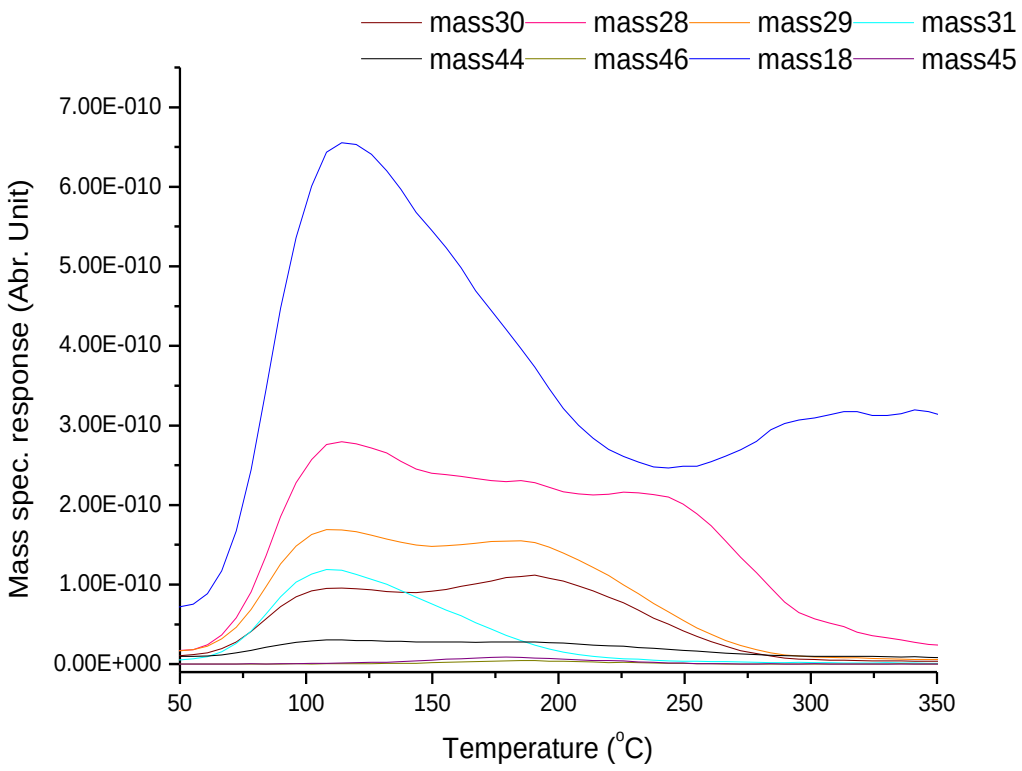

Fig. 4. 26 ***TPD profile of methanol over 2wt % MoO_3/γ-Al_2O_3-700***

The desorption profile in Fig. 4. 26 indicates molecular desorption of methanol at 108 ^oC prior to broad water desorption peak at 115 ^oC. A small amount of DME still exists with desorption peak at 179 ^oC before formaldehyde peak which centred at 191 ^oC, with a CO peak observed at 226 ^oC.

The desorption profile in Fig. 4.26 indicates recombination of surface hydroxyl species, which results in water desorption peak at 108 ^oC. The formaldehyde peak centred at 191 ^oC, emanating on redox site of MoO_3. Further dehydrogenation of formaldehyde results in CO formation at 226 ^oC. The catalysts indicates good coverage of the support, revealing only trace amount of DME desorption form from dehydration of methanol from Lewis acid sites from exposed γ-Al_2O_3 support, which is in agreement with desorption products reported by Briand et al [78] for monolayer MoO_3/ γ-Al_2O_3 catalyst.

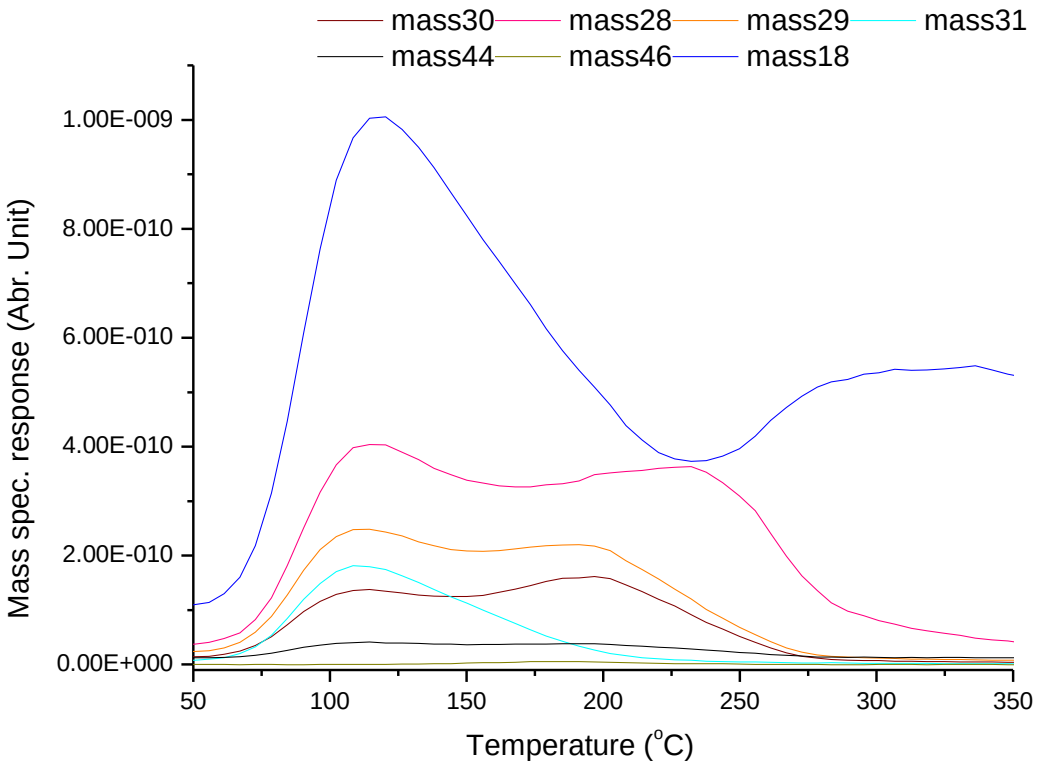

Fig. 4. 27 ***TPD profile of methanol over 10wt % MoO_3/γ-Al_2O_3-700***

TPD desorption in Fig. 4. 27 reveals a methanol desorption peak at 109 ^oC, with a broad water and very small amount of DME desorption peaks at 115 ^oC and 186 ^oC respectively. A formaldehyde desorption peak centred at 198 ^oC, preceding a CO desorption peak at 232 ^oC.

The TPD profile reveals almost similar methanol and water desorption temperature as 2wt % MoO_3/γ-Al_2O_3 catalyst, which is associated with adsorbed methanol and recombination of surface hydroxyl species. The formaldehyde desorption is related to dehydrogenation of surface methoxy on MoO_3 redox sites, while DME formation could result from under coordinated MoOx (Lewis acid) sites. The higher desorption temperature of both formaldehyde and DME is possibly due to metal support interaction between the MoO_3 phase and γ-Al_2O_3 support. Further dehydrogenation of the formaldehyde results in the formation of CO at 232 ^oC.

Table 4. 10 ***Activation energy of formaldehyde desorption over MoO_3/ γ-Al_2O_3 catalysts***

Catalyst	CH_2O desorption peak temperature (Tm)		Activation Energy (kJ/mol)
	^oC	K	
2wt % MoO_3/γ-Al_2O_3 -500	197	470	122
2wt % MoO_3/ γ-Al_2O_3-700	191	464	120
10wt % MoO_3/ γ-Al_2O_3-500	185	458	118
10wt % MoO_3/ γ-Al_2O_3-700	198	471	122

Investigation of energy barrier for formaldehyde desorption over MoO_3 supported over γ-Al_2O_3 catalysts in Table 4. 10 above shows similar energy barriers for formaldehyde desorption on the catalysts surface despite variation in calcination temperature of the support, preparation method and MoO_3 loading. This indicates that the morphology or structural coordination of MoOx species over γ-Al_2O_3 has very little effect on desorption energy for formaldehyde formation.

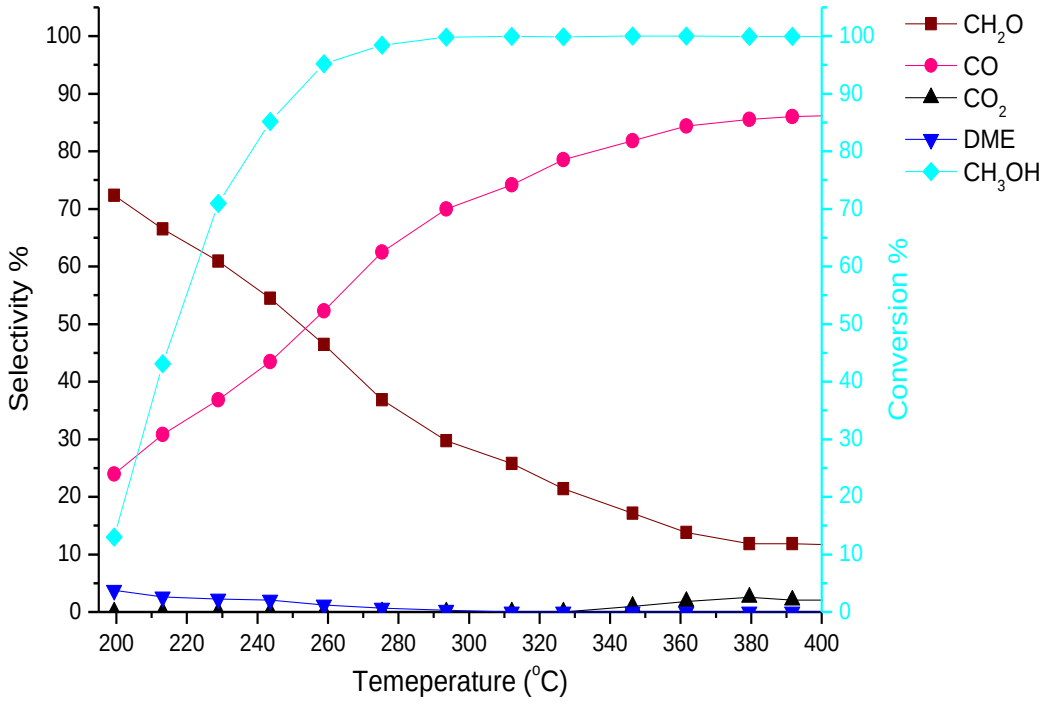

Fig. 4. 28 ***Methanol reaction profile over 2wt % MoO_3/γ-Al_2O_3 -500***

The reaction profile of methanol oxidation over 2wt % MoO_3/γ-Al_2O_3 in Fig. 4. 28 depict 66 % formaldehyde selectivity at 45 % methanol conversion by 213 ^oC, with 36 % and less than 4 % CO and DME selectivity respectively. At ~ 230 ^oC, formaldehyde selectivity reaches 61 % at 72 % methanol conversion. However, formaldehyde selectivity declines steadily to ~35 % with a corresponding increase in CO selectivity reaching 60 % at ~100 % methanol conversion by 278 ^oC. In addition, lesser CO_2 selectivity of about 2 % was evidenced above 350 ^oC.

The reaction of methanol over 2wt % MoO_3/γ-Al_2O_3 in Fig. 4.28 indicates low methanol conversion of 45 % at 213 ^oC that increases to ~100 % by 293 ^oC, whereas decline in formaldehyde selectivity with corresponding increase in CO production as temperature increases is due to further oxidation of formaldehyde. However, methanol oxidation over the catalyst indicates complete titration of Lewis acid sites responsible for DME formation, which agrees with similar effect reported by Kwak et al [94] for BaO or La_2O_3 modified γ-Al_2O_3 surface. This signifies good coverage of the support by MoOx species. Furthermore, the low

selectivity to formaldehyde of the 2wt % MoO_3/γ-Al_2O_3 catalyst in comparison to MoO_3 and $Fe_2(MoO_4)_3$ is due to ease of reducibility of MoOx species by methanol on γ-Al_2O_3 surface .

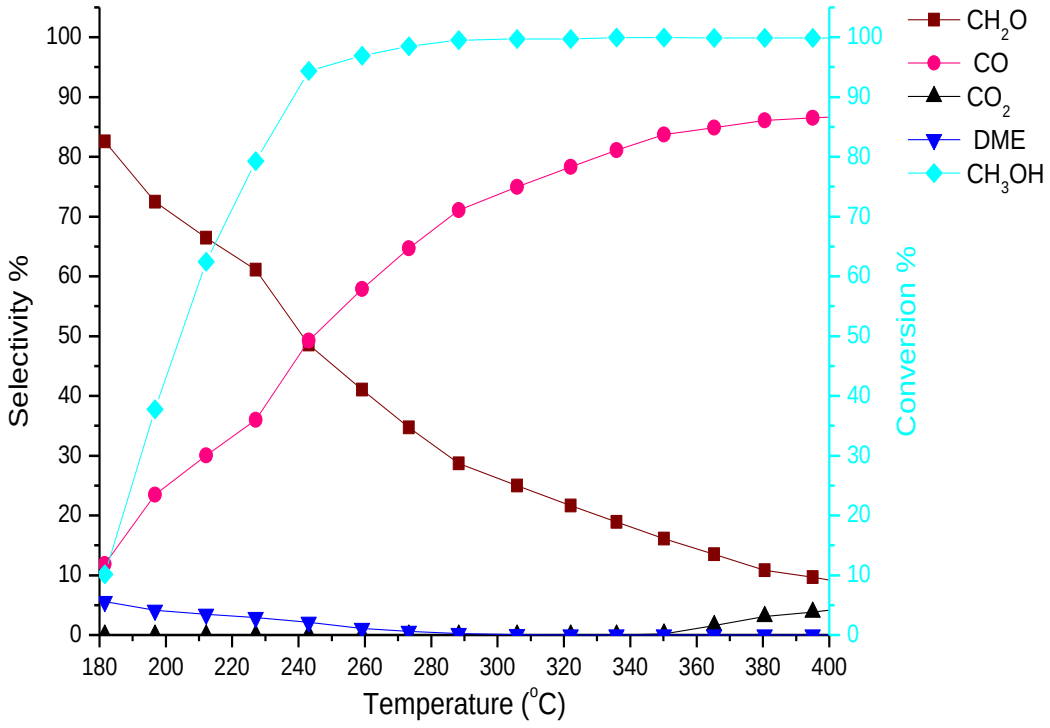

Fig. 4. 29 ***Methanol reaction profile over 10wt % MoO_3/γ-Al_2O_3-500***

Fig. 4. 29 depicts a reaction profile of methanol oxidation over 10wt % MoO_3/γ-Al_2O_3, with 73 % formaldehyde selectivity recorded at 41 % methanol conversion by 198 ^oC, with CO and DME selectivity reaching 23 % and 4 % respectively. However, formaldehyde selectivity declines to 34 % with increasing CO selectivity reaching 63 % at 99 % methanol conversion by 273 ^oC. Above 350 ^oC, CO and CO_2 selectivity reaches 85 % and less than 5 % respectively at ~100 % methanol conversion.

The slight increase in formaldehyde selectivity of 10wt % MoO_3/γ-Al_2O_3 at 198 ^oC indicates increasing Mo loading, which provides more catalytic active sites for both conversion and selectivity at lower temperature in comparison to 2wt % MoO_3/γ-Al_2O_3 (213 ^oC). Thus, indicating weak metal-support interaction due to presence

of polymeric bulk MoO_3 species, which is in good agreement with similar weak metal – support interaction as reported by Abello et al [71] for high loading MoO_3/γ-Al_2O_3 catalysts in oxidative dehydrogenation of propane to propene. The decline in formaldehyde selectivity with steady increase in CO as the temperature rises could be attributable to further oxidation of formaldehyde.

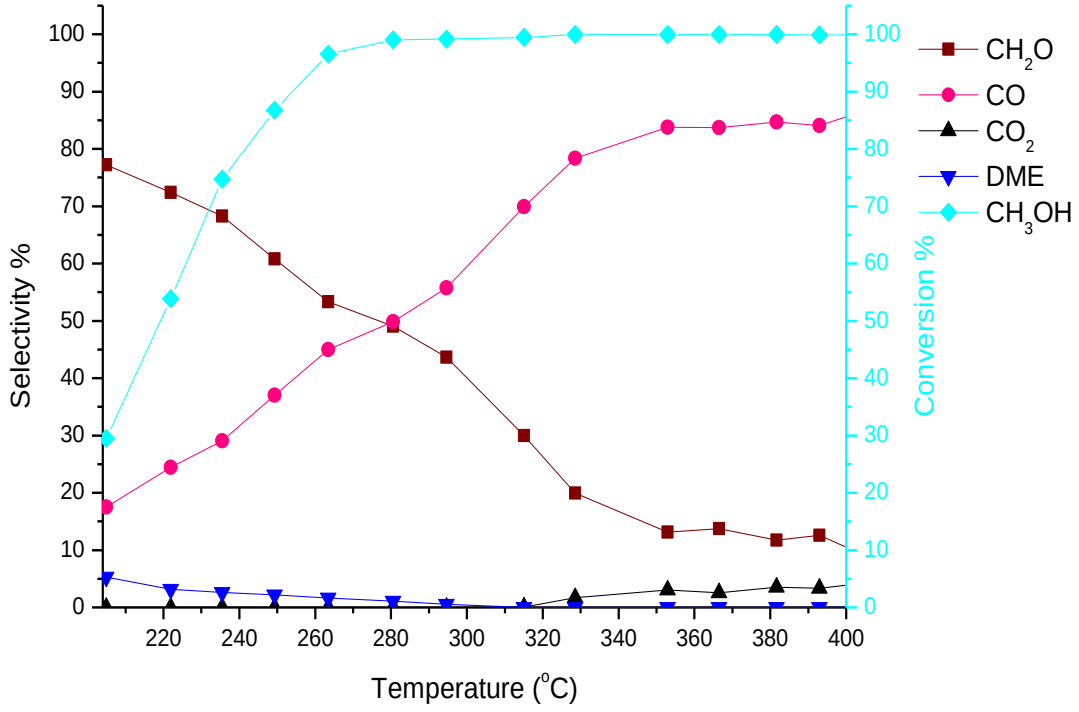

Fig. 4. 30 ***Methanol reaction profile over 2wt % MoO_3/γ-Al_2O_3-700***

The reaction profile of methanol oxidation over 2wt % MoO_3/γ-Al_2O_3-700 in Fig. 4. 30 depicts 54 % methanol conversion with formaldehyde and CO selectivity reaching ~73 % and 24 % respectively at 221 ^oC. Formaldehyde selectivity decreases to 68 % with steady increase in CO selectivity reaching 29 % at 73 % methanol conversion by 236 ^oC. However, CO selectivity reaches 84 % at maximum methanol conversion of ~ 100 %, with a decline in formaldehyde selectivity reaching 13 % by 353 ^oC. A CO_2 selectivity of less 5 % was recorded above 353 ^oC.

The catalyst depicts 75 % formaldehyde selectivity in comparison to 66 % recorded over 2wt% MoO_3/γ-Al_2O_3-500 at 213 ^oC, which decreases with increasing reaction

temperature leading to subsequent oxidation to CO. The low activity of the catalyst could be associated to a strong metal – support interaction with MoOx species. However, the catalyst revealed decrease in CO formation (50%) below 300°C due to better dispersion of MoO_3 phase on the support.

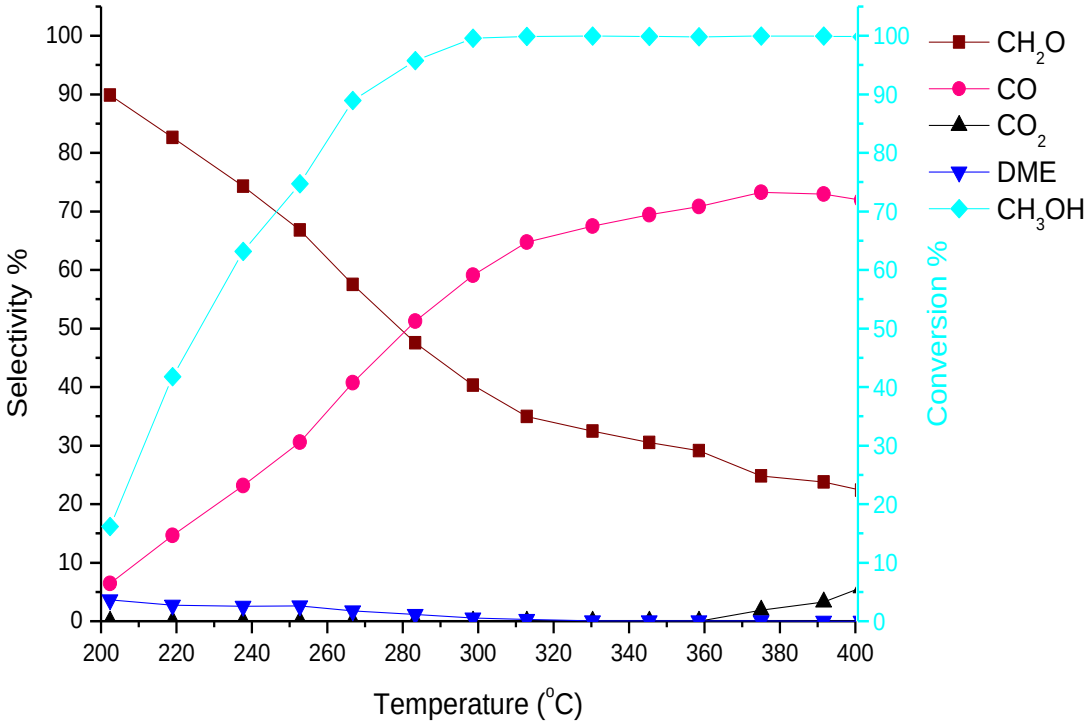

Fig. 4. 31 ***Methanol reaction profile over 10wt % MoO_3/γ-Al_2O_3-700***

The reaction profile for methanol oxidation over 10 wt % MoO_3/γ-Al_2O_3-700 in Fig. 4. 31 reveals 83 % formaldehyde selectivity at 40 % methanol conversion by 219 °C, with 14 % and 3 % CO and DME selectivity respectively. At 63 % methanol conversion, the formaldehyde selectivity declines steadily to 74 % with increasing CO selectivity reaching 23 % by 238 °C. Methanol conversion rises to ~100 % with 29 % formaldehyde selectivity by 359 °C, while CO selectivity reaches 71 % which increases to 73 % with about ~3 % CO_2 selectivity above 359 °C. The catalyst reveals highest formaldehyde selectivity of 83 % at 40 % conversion at relatively high temperature 219 °C as compared to 198 °C revealed for 10wt % MoO_3/ γ-Al_2O_3-500. This is in concordance with high density of Mo sites responsible for formaldehyde selectivity, due to increasing Mo loading.

Table 4. 11 Comparison of formaldehyde selectivity over MoO_3/ γ-Al_2O_3 catalysts at 50% methanol conversion

Catalyst	CH_2O selectivity at 50% CH_3OH conversion (%)	Reaction Temperature (^oC)
2wt % MoO_3/γ-Al_2O_3 -500	65	217
2wt % MoO_3/ γ-Al_2O_3-700	73	219
10wt % MoO_3/ γ-Al_2O_3-500	69	205
10wt % MoO_3/ γ-Al_2O_3-700	79	226

A comparison of formaldehyde selectivity at 50 % methanol conversion over MoO_3/ γ-Al_2O_3 catalysts as shown in Table 4. 11, reveals similar formaldehyde selectivity for same set of catalysts (2 and 10 wt% MoO_3). However, the MoO_3/ γ-Al_2O_3-700 catalysts prepared via impregnation using citrate solution exhibits higher selectivity in comparison to their water-impregnated counterpart (% MoO_3/ γ-Al_2O_3-500) at a slightly higher temperature. This indicates better dispersion of MoOx on γ-Al_2O_3 for citrate prepared catalyst. The formaldehyde reaction temperature could be attributable to absence of Mo-O-Al interaction (weak support interaction) above monolayer coverage resulting in polymeric octahedrally coordinated MoO_3 species. These dispersed MoO_3 species are prone to reduction by methanol, which supports the findings reported by Hu and Wachs [73], and Matsuoka et al [74] on methanol reaction on MoO_3 supported catalysts and TPR study of supported MoO_3 on γ-Al_2O_3 by del Arco et al [95] . However, increase in CO selectivity at high reaction temperature is due to oxidation formaldehyde, which is typical of selective oxidation reaction over supported MoO_3 catalysts as reported by Hu and Wachs [73].

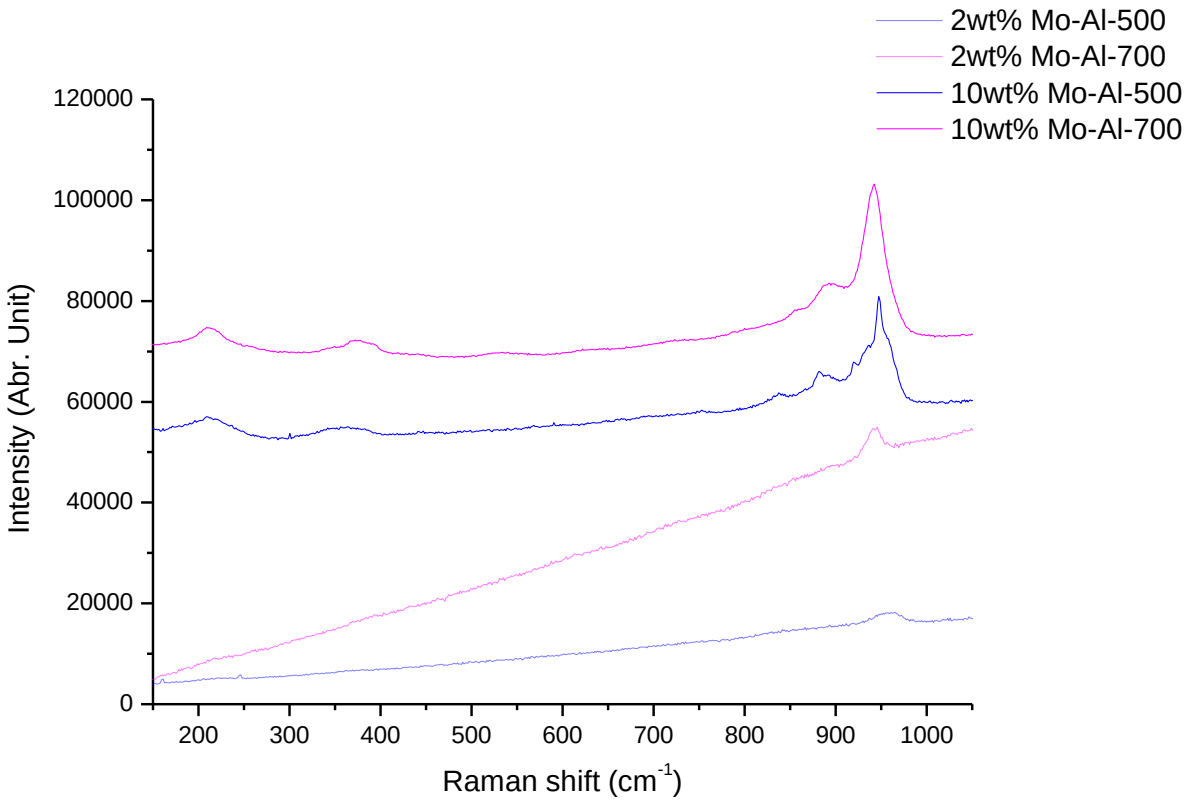

Fig. 4. 32 ***Raman spectra of varying weight loading of MoO_3/Al_2O_3 catalysts dried at 120 ^oC***

Fig. 4. 32 depicts Raman bands at 955 and 942 cm^{-1} for 2wt % Mo loading for water and citrate prepared catalysts respectively, with a weak band at 841 cm^{-1}. The 10wt % MoO_3 loading on alumina for the water prepared catalyst reveal sharp intense band at 947 with shoulder peaks at 937, 920, 892 and 859 cm^{-1}, with lower bands observed at 753, 356 and 209 cm^{-1}. However, the citrate prepared catalyst of same loading reveals a broad intense Raman band at 942 cm^{-1}, with shoulder peak at 893 cm^{-1} and 859 cm^{-1} alongside lower bands at 622, 532, 372 and 212 cm^{-1}. However, γ – alumina revealed no Raman bands due to white coloration of the sample, which reflect most of the laser beam and fluorescence caused by surface hydroxyl group.

The Raman band at 965 cm^{-1} and 942 cm^{-1} for the 2wt % loading is assignable to $[Mo_7O_{24}]^{6-}$ species, while the 841 cm^{-1} is associated with isolated $[MoO_4]^{2-}$ species as reported by Tian et al [77] and Wachs and Robert [96]. The increasing Mo loading to 10 wt % reveals formation of cluster, monomeric and polymeric species

with bands ranges of 942-947 cm^{-1}, 859-893 cm^{-1} and 356-372 cm^{-1}, with an additional band at 523 cm^{-1} for citrate prepared catalyst, attributed to symmetric, asymmetric stretching and bending of Mo-O-Mo in $[Mo_7O_{24}]^{6-}$ species. Furthermore, the bands from 209 and 212 cm^{-1} are assigned to surface dioxo Mo=O in monomeric $[MoO_4]^{2-}$ species. Moreover, the sharp intense peak of the 947cm^{-1} peak of the water prepared catalyst evidences formation of large polymeric Mo cluster on the support, with a complementary shoulder peak at 920 and 937 cm^{-1} with a lower band at 753 cm^{-1} assigned to Keggin structure. The citrate catalysts reveals better dispersion of MoO_3 on the support as indicated by the broadening of the intense 940 cm^{-1} band, although the existence of the Raman band at 622 cm^{-1} is assignable to aluminomolybdic acid Keggin structure which decomposes at 300 ^oC.

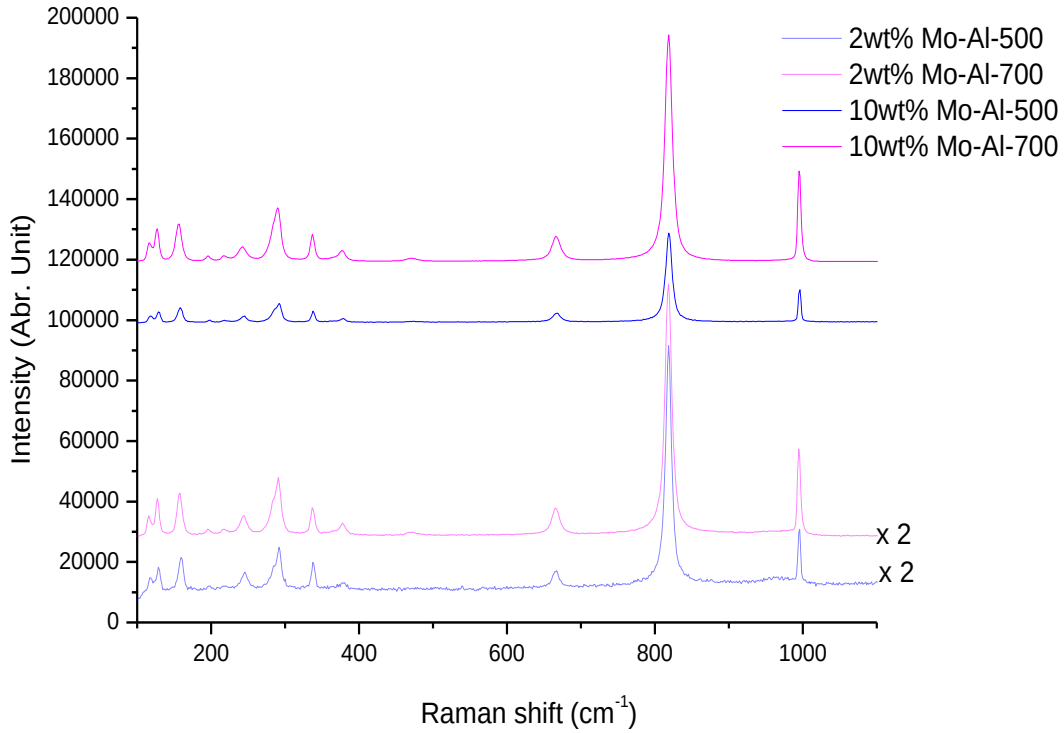

Fig. 4. 33 ***Raman spectra of MoO_3 supported over γ-Al_2O_3 calcined at 500 ^oC***

Raman spectra of samples calcined at 500 ^oC in Fig. 4. 33 reveals Raman bands at 996, 819 and 666 cm^{-1}, with lower bands at 379, 337, 290, 245, 218, 196, 158, 129 and 116 cm^{-1} for all samples. However, 10 wt % Mo loading reveals extra bands at

469 or 471 cm^{-1}. This band is present on 2wt % citrate catalyst, but exhibits weak signal, while the 2wt % Mo water prepared catalyst reveals a shoulder broad peak at 961 cm^{-1}.

The Raman bands at 996, 819 and 666 cm^{-1} observed for all samples are attributable to M=O asymmetric, symmetric stretching, and Mo-O-Mo symmetric stretching, while the band range of 469-470 cm^{-1}, 379, 337, 290, 245-218, 196 and 129-116 cm^{-1} are ascribed to Mo-O-Mo bending, wagging, twisting, rigid chain MoO_4 vibration modes respectively. The appearance of the 470 cm^{-1} band for 10 wt % and 2wt % Mo-Al-700 Mo loading for citrate prepared catalyst reveals good dispersion of the active Mo phase on the alumina support. The appearance of a shoulder band at 961 cm^{-1} on 2wt % Mo-Al catalysts which is assigned to symmetric stretching of isolated dioxo $(=O)_2MoO_2$ species, reveals the existence of monomeric species bounded to alumina surface. These findings are in agreement with those reported by Tian et al [77] and Wachs and Robert [96] for low MoO_3 coverage on alumina.

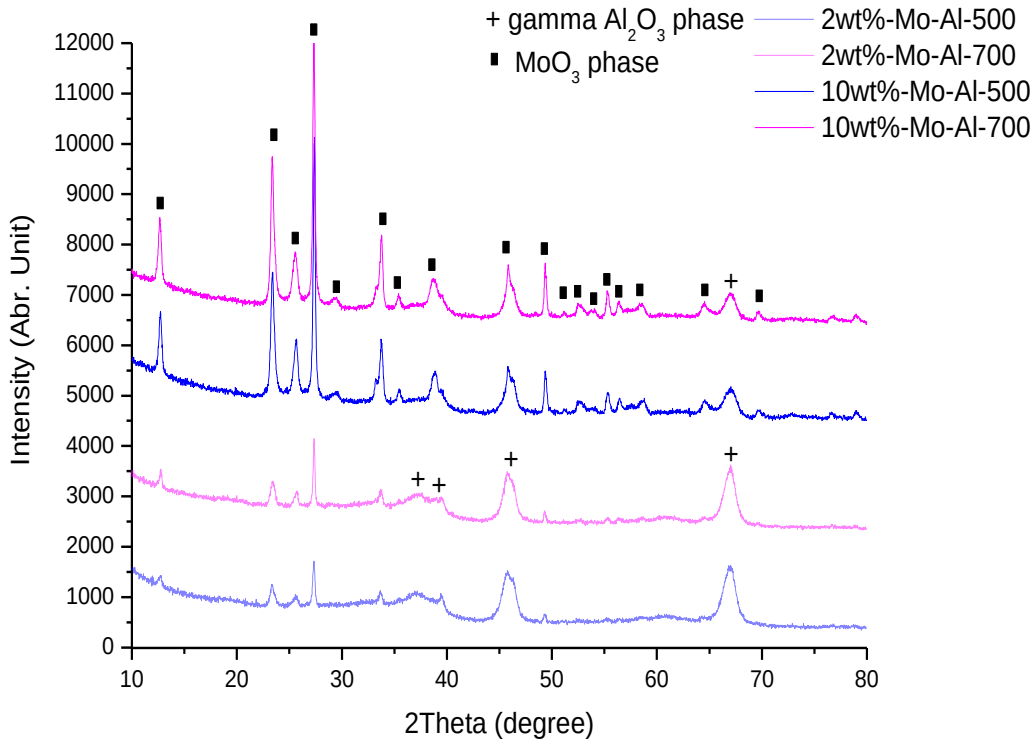

Fig. 4. 34 ***Diffractogram of MoO_3/γ-Al_2O_3***

The diffractogram of MoO_3/γ-Al_2O_3 catalysts in Fig. 4. 34 depicts 2θ value at 12.7 °, 23.4 °, 25.7 °, 27.4 ° , 29.5 ° , 33.8 °, 35.5 ° and 49.5 ° (corrected to a deviation of ± 0.2), attributed to crystalline MoO_3 phase as indexed in JCPDS card no 00-005-0508 [90]. More so, the 2θ value of 38.9 °, 45.9 ° and 67.1 ° are attributable to γ-Al_2O_3 phase in accordance with JPCDS indexing in card no.01-080-0956. Additionally, no peak related to $Al_2(MoO_4)_3$ phase was evidenced on all the catalysts. In addition, increase in MoO_3 loading from 2-10 wt % results in emergence of the 29.5 °, 35.5 ° peaks and increasing intensity of MoO_3 peaks, with corresponding decrease in γ-Al_2O_3 peaks intensity at 45.9 ° and 67.1 °.

The increasing intensity of the MoO_3 peaks for 10wt % Mo-Al catalysts indicates good coverage and the formation of crystalline phases on the support. However, the decrease in intensity of the 25.7 ° attributed to (010) reflection of the MoO_3 basal plane in comparison to the 23.4 ° and 27.4 ° peaks, could reflects decrease in exposure of the (010) phase of MoO_3 phase influenced by the distorted octahedral

or tetrahedral structure of the γ-Al_2O_3 support which exposes the predominantly (110) plane.

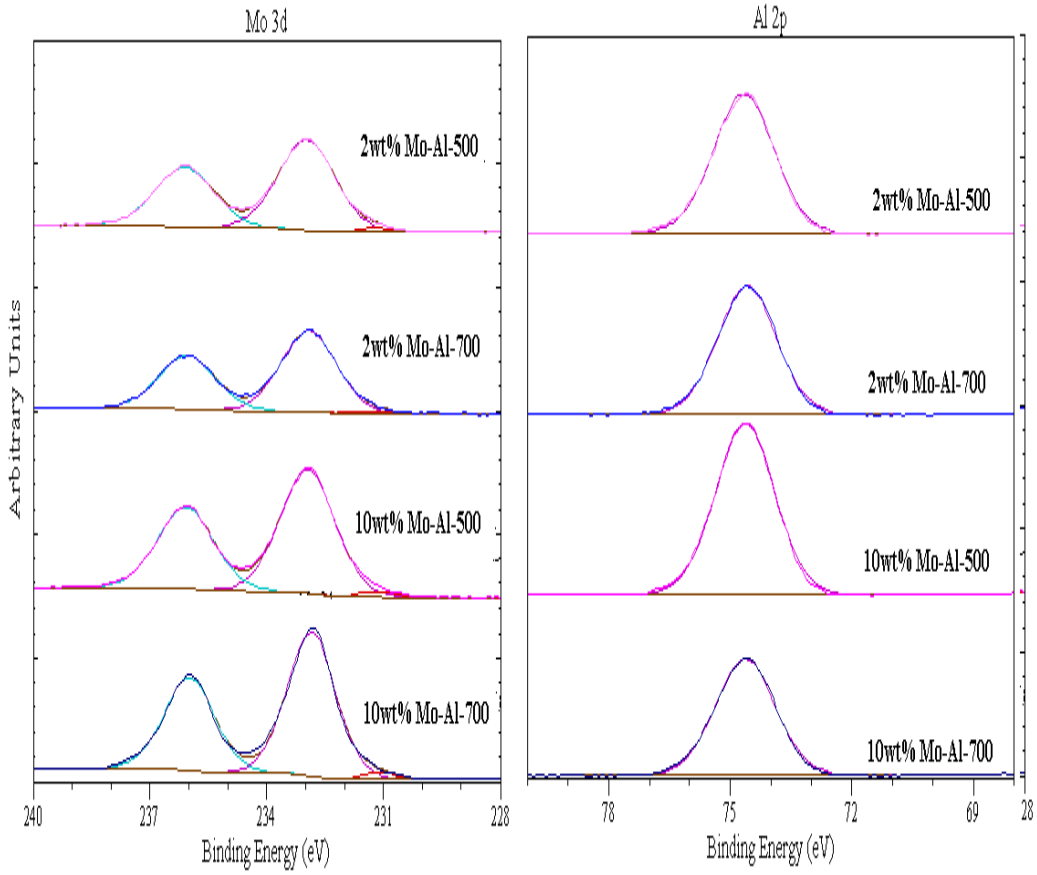

Fig. 4. 35 ***XPS spectra of Mo 3d and Al 2p of MoO_3/γ-Al_2O_3***

An XPS spectra in Fig. 4. 35 depicts binding energies of Mo 3d doublet at 233 ± 0.2 eV and 236 ± 0.2 eV assigned to Mo $3d_{3/2}$ and $3d_{5/2}$ respectively. The Al 2p reveals a binding energy at 74.6 ± 0.2 eV. The Mo 3d doublet binding energies at 233 ± 0.2 eV and 236 ± 0.2 eV for all samples indicates Mo in its highest oxidation state of Mo^{6+} for all catalysts, while binding of 74.6 ± 0.2 eV reveals Al 2p in highest oxidation state of Al^{+3}. These results are in close agreement with those reported by Zingg et al [76] for MoO_3 supported over γ-Al_2O_3.

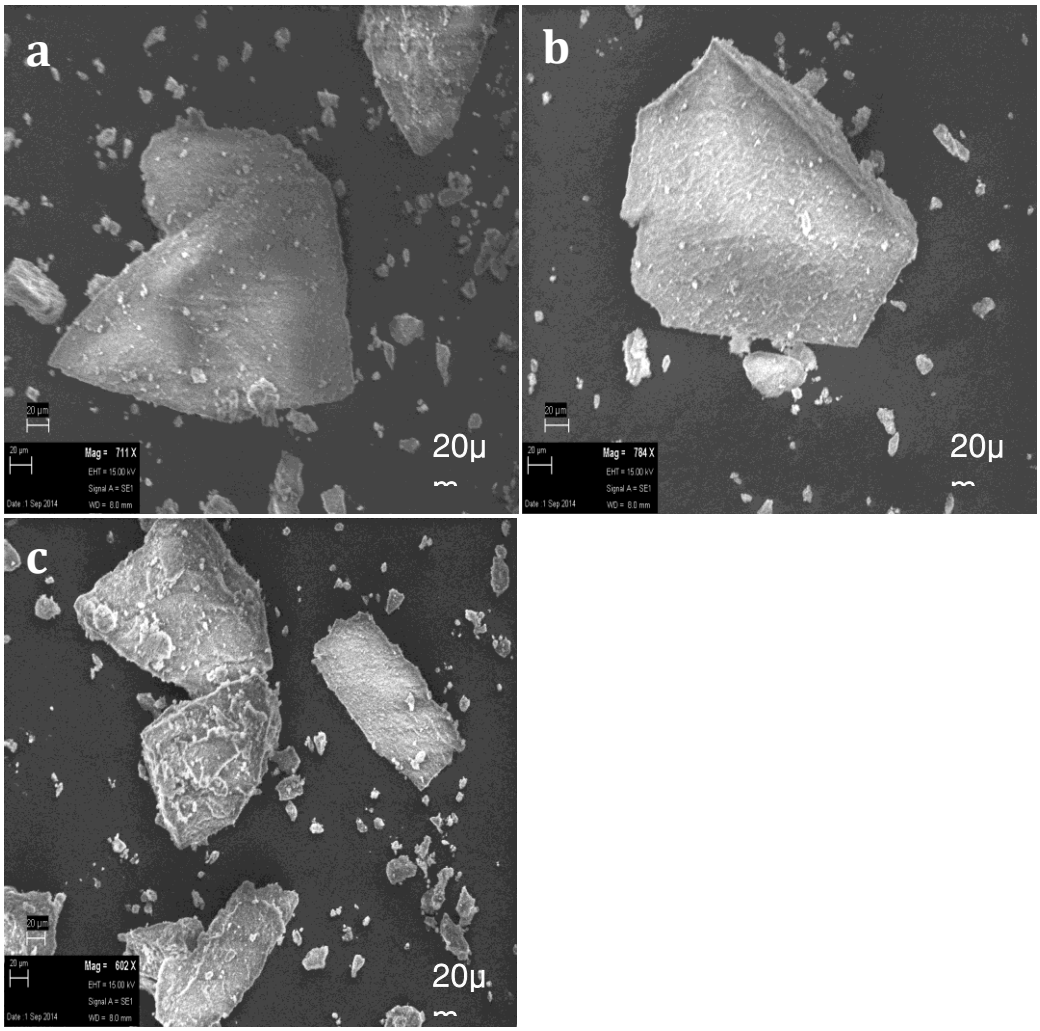

Fig. 4. 36 ***SEM micrographs of γ-Al_2O_3 support calcined at different temperatures (a) As received γ-Al_2O_3, (b) γ-Al_2O_3 calcined at 500 ^oC, and (c) γ-Al_2O_3 calcined at 700 ^oC, scale: 331 x 332 µ***

The SEM micrographs of both as received, 500 ^oC and 700 ^oC calcined γ-Al_2O_3 in Fig. 4. 36 reveals a plate-like morphology as shown in Fig. 4.36 a – c.

The SEM images of as received, 500 and 700 ^oC calcined γ-Al_2O_3 reveals no morphological changes due to increasing calcination of the support, which is in line with observation reported by paglia et al [52] on calcined γ-Al_2O_3 at different temperature from room temperature – 900 ^oC.

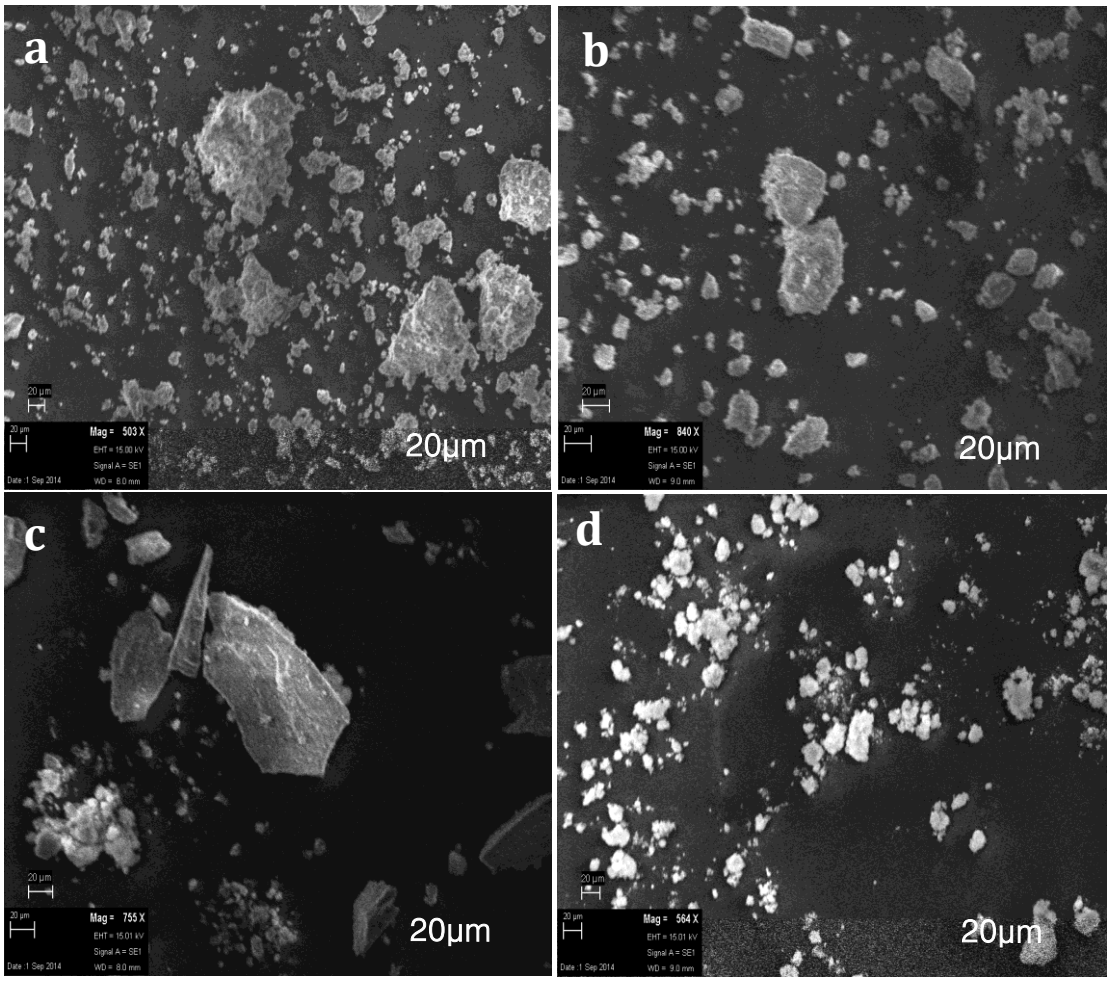

Fig. 4. 37 ***SEM micrographs of MoO_3/ γ-Al_2O_3; (a) 2wt % MoO_3/ γ-Al_2O_3, (b) 2wt % MoO_3/ γ-Al_2O_3-700, (c) 10wt % MoO_3/ γ-Al_2O_3, (d) 10wt % MoO_3/ γ-Al_2O_3-700, scale: 275 x 310 µ***

The micrographs in Fig. 4. 37 reveals crystalline aggregates of MoO_3 on both 2 and 10 wt % Mo loading, which are similar to supported MoO_3 on γ-Al_2O_3 reported by del Arco et al [95]. The 2wt % MoO_3 catalyst in Fig. 4.37 a and Fig. 4.37 b shows dispersed MoO_3 crystallites indicating good coverage of the support, with relatively bigger crystallite on the Fig. 4.37 a in comparison to Fig. 4.37 b. Furthermore, at higher MoO_3 loading of 10wt %, Fig. 4.37 c reveals both region of dense and less dense crystalline MoO_3 phase, while Fig. 4.37 d depict well dispersed surface of crystalline MoO_3 on the support.

The SEM micrographs of catalysts indicate good coverage with the citrate prepared catalysts in Fig 4.37 b and Fig. 4.37 d reveals better dispersion in comparison to water prepared catalysts, due to the chelating effect of citrate precursor. The

inhomogeneous dispersion or sintering of the water prepared catalyst had been a major drawback of the incipient wetness impregnation method.

4.3 Summary

The results of this study indicate that calcination of nanodiamond in air for 5 hours is effective in removal of amorphous carbon and oxidation (increasing surface negative charge) from its surface at 390 ^{o}C. The increase in calcination temperatures from 390 – 500 ^{o}C slightly changes the surface area, and converts the surface functionality to thermally stable carbonyl (ketone, lactone) and acid anhydride groups as evidenced by Raman spectroscopy and XPS results.

In addition, the diamond peak (Raman band at 1331cm^{-1}) intensity signal increases with oxidation temperature up to 500 ^{o}C, with corresponding destruction of the graphitic sp^2 ring structure to olefenic group of medium or short chain length.

Complete burning of the nanodiamond support into dark-brown residue (likely metal carbonates) at 600 ^{o}C is catalysed by metal impurities encapsulated in the lattice and core as revealed by XPS results. However, calcination of nanodiamond at 500 ^{o}C revealed no noticeable change of the bulk structure in comparison to the as-received sample.

The surface area of nanodiamond supported MoO_3 catalysts decreases with increasing Mo loading, from 55 m^2/g for 90 % monolayer coverage to 37 m^2/g at 400 % Mo loading.

Raman spectroscopy and XRD study of MoO_3/ND catalysts revealed existence of isolated tetrahedral coordinated amorphous MoOx species alongside octahedral polymeric MoOx crystallites at lower Mo coverage (90 – 100 % MoO_3 monolayer coverage) over nanodiamond, and octahedral coordinated crystalline MoO_3 phase at high Mo loading of 400 %.

Increasing Mo loading resulted in dispersion and crystallization of MoO_3 phase, which reached complete surface coverage by 400 % Mo loading, as evidenced by Raman, XRD, and SEM studies. The XPS results indicated Mo species in their highest oxidation state of +6 for all catalysts, with complete titration of surface oxygen species achieved by 100 % MoO_3 monolayer coverage.

Temperature programmed desorption (TPD) of methanol over nanodiamond revealed heterogeneity of its surface, with methanol and water desorption resulting

from molecularly adsorbed methanol and recombination of hydroxyl species. Formaldehyde and DME are produced from carbonyl oxygen functionality (ketone, lactone or acid anhydride) and defect sites on the edges respectively, whereas lower temperature CO could be from reaction of hydroxyl species with bulk defect sites on (0001) plane of graphitic shell and possible decomposition of surface epoxide or carboxylic group. However, methanol TPD over MoO_3/ND revealed structure sensitivity of the surface, with redox and Lewis acid sites responsible for formation of formaldehyde and DME respectively.

The reaction profile of methanol oxidation over nanodiamond support indicates high activity (75 % methanol conversion) and poor selectivity to formaldehyde (36 %) and DME (60 %) at 170 ^{o}C. however, the support indicates maximum selectivity for CO (95 %) and maximum conversion of 98 % above 220 ^{o}C. This indicates the dehydrating and dehydrogenating property of the support.

MoO_3 supported on nanodiamond indicates high activity and selectivity to formaldehyde at low temperature (below 200 ^{o}C), which increases with Mo loading. A maximum formaldehyde selectivity of 85 % at 81 % methanol conversion was recorded by 198 ^{o}C for 400 % Mo loading, due to increase in density of active redox sites on the support. However, 90 % monolayer coverage indicates lowest activity due to blockage of surface oxygen (active) sites via bond formation with MoOx. This indicates a synergistic effect between support and active MoOx phase, which results in relative stability of redox sites and decrease in CO production, accompanied by steady decline of formaldehyde selectivity (45 %) at higher temperature above 250 ^{o}C in comparison to higher Mo loading catalysts.

XRD study of calcined boemite (AlOOH) from room temperature to 900 ^{o}C, revealed phase evolution and transition of γ-Al_2O_3, with pure γ-Al_2O_3 phase formed at 500 ^{o}C due to collapse of the boemite structure. Phase transition of γ-Al_2O_3 begins at 800 ^{o}C, with a mixed phase consisting of both γ and δ-Al_2O_3 revealed at 900 ^{o}C.

However, calcination of the support increases the surface area to 72 m^2/g at 400 ^{o}C, due to removal of adsorbed water and dehydroxylation of γ-Al_2O_3 surface. This decreases steadily to 45 m^2/g by 900 ^{o}C owing to phase transition and sintering of the support.

Characterization of MoO_3/ γ-Al_2O_3 catalysts using Raman spectroscopy, XRD, and SEM revealed existence of crystalline MoO_3 phase on the supports, which increases with Mo loading. However, 2 wt % Mo-Al catalyst revealed presence of tetrahedral coordinated MoOx species with Raman shoulder band at 961 cm^{-1}, while better dispersion of MoOx phase on support at 2wt% Mo loading for citrate prepared catalysts (2 wt % Mo-Al-700) was established by Raman (due to presence of 470 cm^{-1} band) and SEM study. The XPS study of the supported catalysts revealed Mo and Al in highest oxidation state of +6 and +3 respectively.

Reaction measurement indicates that the as received (boehmite), 500 and 700 ^oC calcined γ-Al_2O_3 are highly selective to DME, but inhibited by water above 320 ^oC. More so, the surface acidity of the support varies with the degree of calcination, as indicated by higher desorption temperature (186 ^oC) of DME for 700 ^oC γ-Al_2O_3 in comparison to as received and 500 ^oC calcined support.

The MoO_3/ γ-Al_2O_3 catalysts revealed complete titration of acid sites on γ-Al_2O_3 support (mono layer coverage) by 2 wt % Mo loading, with good correlation between increase in activity and formaldehyde selectivity with increasing Mo loading from 2 -10 wt % at low temperature (< 250 ^oC), for support MoO_3 supported on γ-Al_2O_3 calcined at 500 ^oC. However, increasing Mo loading (10 wt %) resulted in slight decrease in activity of the citrate prepared catalyst (Mo-Al-700). However, the structural coordination of MoOx species at lower (tetrahedral) and higher (octahedral) revealed less influence on formaldehyde selectivity at 50 % methanol conversion.

4.4 Conclusion

Studying the properties of the catalyst support prior to impregnation of the active phase is essential for achieving active and selective catalysts for methanol oxidation and related processes. Our investigation of nanodiamond support revealed that the support is thermally unstable as compared to γ-Al_2O_3, with its surface contaminated with impurities. It burns completely in air at 600 ^oC leaving behind mostly metal residue.

Mo loading on both supports evidence presence of monomeric tetrahedral coordinated MoOx species at low Mo loading, and crystalline octahedral coordinated MoO_3 species at higher loading. More so, pre-calcination γ-Al_2O_3 support allows good dispersion of MoOx species, with better dispersion observed over γ-Al_2O_3 support calcined at 700 ^oC using citrate method.

Temperature programmed desorption of methanol over both supports revealed structure sensitivity, with formaldehyde and DME produces on redox and acid sites respectively over ND surface. The presence of only acid (Lewis) sites on γ-Al_2O_3 makes it selective to DME, but these sites are completely titrated at 2wt % Mo loading. Moreover, MoO_3 supported catalysts produce formaldehyde on redox sites, whereas MoO_3/ND catalysts in addition produce DME on acidic sites (possibly on (100) face).

More so, the nature of surface MoOx species (tetrahedral or octahedral coordinated) does not indicate any effect on formaldehyde selectivity for MoO_3/ γ-Al_2O_3 catalysts. The citrate prepared MoO_3/γ-Al_2O_3-700 display higher formaldehyde selectivity than their water counterpart MoO_3/γ-Al_2O_3-500 at 50 % methanol conversion.

MoO_3/ND revealed good activity and selectivity to formaldehyde at lower temperature, which increases with Mo loading. However, 90 % MoO_3/ND revealed synergistic effect between the support and active MoOx species preventing complete reducibility of MoOx species.

References

1. Danilenko VV. On the history of the discovery of nanodiamond synthesis Physics of the Solid State. 2004;46(4):678-80.

2. Dolmatov VY. Detonation synthesis ultradispersed diamonds: properties and applications. Russian Chemical Reviews. 2001;70(7):607-26

3. Vul AY, Aleksenskiy A E, and Dideykin A T. Detonation nanodiamonds: technology, properties and applications. 3rd Internation symposium on detanotion nanodiamond: Technology, properties and application; St. Peterburgh, Russia: Encyclopedia of Life Support System; 2008.

4. Mochalin VN, Shenderova O, Ho D, and Gogotsi Y. The properties and applications of nanodiamonds. Nat Nanotechnol. 2011:1-13.

5. Osawa E. Monodisperse single nanodiamondnparticulates. Pure Appl Chem. 2008;80(7):1365-79.

6. Korobov MV, Avramenko, N.V., Bogachev, A.G., Rozhkova, N.N. and Osawa, E. Nanophase of water in nano-diamond Gel. J Phys Chem C 2007;111: 7330-4.

7. Yang GW, Wang, J.B. and Liu, Q.X. . Preparation of nano-crystalline diamonds using pulsed laser induced reactive quenching. J Phys Condens Mat. 1998;10:7923-7.

8. Boudou J-P, Curmi P A, Jelezko F, Wrachtrup J, Aubert P, Sennour M, Balasubramanian G, Reuter R,Thorel A, and Gaffet E. High yield fabrication of fluorescent nanodiamonds. Nanotechnology. 2009;20:235602.

9. Osswald S, Yushin, G., Mochalin, V., Kucheyev, S.O. and Gogotsi, Y. Control of sp^2/sp^3 carbon ratio and surface chemistry of nanodiamond powders by selective oxidation in air. J Am Chem Soc. 2006;128:11635-42.

10. Petrov I, Shenderova,O., Grishko, V., Grichko, V., Tyler, T., Cunningham, G. and McGuire, G. . Detonation nanodiamonds simultaneously purified and modified by gas treatment. Diam Relat Mate. 2007;16:2098–103.

11. Shenderova O, Koscheev, A., Zaripov, N., Petrov, I., Skryabin, I., Detkov, P.,Turner, S., and Van Tendeloo, G. Surface chemistry and properties of ozone-purified detonation nanodiamonds. J Phys Chem C. 2011;115:9827-37.

12. Shenderova O, Petrov, I., Walsh, J., Grichko,V., Grishko, V., Tyler, T. and Cunningham, G. . Modification of detonation nanodiamonds by heat treatment in air. Diam Relat Mater. 2006;15:1799–803.

13. Xu NS, Chen, J., Deng,S.Z. . Effect of heat treatment on the properties of nano-diamond under oxygen and argon ambient. Diam Relat Mater. 2002;11:249-56.

14. Xu X, Yu, Z., Zhu, Y., Wang, B. Influence of surface modification adopting thermal treatments on dispersion of detonation nanodiamond. J Solid State Chem. 2005;178:688-93.

15. Xu X YZ. Influence of thermal oxidation on as-synthesized detonation nanodiamond. Particuology 2012;10: 339– 44.

16. Yushin GN, Osswald, S., Padalko, V.I., Bogatyreva, G.P., Gogotsi, Y. Effect of sintering on structure of nanodiamond. Diam Relat Mater. 2005;14:1721-9.

17. Bogatyreva GP, Voloshin, M.N., and Padalko,V.I. Detonation synthesized nanodiamond powder for the preparation of porous polycrystalline micron powders. Diam Relat Mater. 2008;17:213-6.

18. Xie FY, Xie, G.W., Gong, L., Zhang, W.H., Chen, S.H., Zhang,Q. Z. and Chena, J. Surface characterization on graphitization of nanodiamond powder annealed in nitrogen ambient. Surf Interface Anal. 2010;42:1514–8.

19. Belobrov PI, Bursill, L.A., Maslakov, K.I., Dementjev, A.P. Electron spectroscopy of nanodiamond surface states. App Surf Sci. 2003;215:169-77.

20. Dementjev AP, and Maslakov, K. I. . Chemical state of carbon atoms on the surface of nanodiamond particles
Physics of the Solid State. 2004;46(4):678-80.

21. Dementjev AP MKI. Chemical state of carbon atoms on a nanodiamond surface: Growth mechanism of detonation nanodiamond. Fullerenes, Nanotubes, and Carbon Nanostructures 2012;20 594–9.

22. Dementjev A, Maslakov, K., Kulakova, I., Korolkov , V., Dolmatov, V. State of C-atoms on the modified nanodiamond surface. Diam Relat Mater. 2007;16:2083–6.

23. Schmidlin L, Pichot, V., Comet, M., Josset, S. , Rabu, P. and Spitzer, D. . Identification, quantification and modification of detonation nanodiamond functional groups. Diam Relat Mater 2012;22: 113–7.

24. Enoki T, Kobayashi, Y., Katsuyama, C., Osipov, V.Y., Baidakova, M.V.,Takai, K., Fukui, K. and Vul, A.Y. Structures and electronic properties of surface/edges of nanodiamond and nanographite. Diam Relat Mater. 2007;16:2029–34.

25. Liu Y, Gu, Z., Margrave, J.L. and Khabashesku, V.N. Functionalization of nanoscale diamond powder: Fluoro-, alkyl-, amino-, and amino acid-nanodiamond derivatives. Chem Mater 2004;16:3924-30.

26. J. Mona J, Tu, J.-S., Kang, T.-Y., Tsai, C.-Y., Perevedentseva, E. and Cheng, C.-L. . Surface modification of nanodiamond: Photoluminescence and Raman studies. Diam Relat Mater. 2012;24 134–8.

27. Knight DSaW, W. B. . Characterization of diamond films by Raman spectroscopy. J Mater Res. 1989;4(2):385 93.

28. Wang Y, Alsmeyer, D.C., and McCreery, R.L. Raman Spectroscopy of carbon materials: Structural basis of observed spectra. Chem Mater 1990;2:557-63.

29. Yoshikawa M, Mori,Y., Obata, H., Maegawa, M., Katagiri, G., Ishida,H., and Ishitani, A. Raman scattering from nanometer-sized diamond. Appl Phys Lett. 1995;67(5):694-6.

30. Ferrari AC and Robert, J. Interpretation of Raman spectra of disordered and amorphous carbon. The American Physical Society. 2000;61(20):14095-107.

31. Chu PK, and Li, L. Characterization of amorphous and nanocrystalline carbon films. Mater Chem Phys. 2006;96:253-77.

32. Ferrari AC, and Robert, J. Raman spectroscopy of amorphous, nanostructured, diamond-like carbon, and nanodiamond
Phil Trans R Soc Lond A 2004; 362:2477–512.

33. Chu C-D, Perevedentseva, E.,Yeh, V., Cai, S.-J.,Tu, J.-S. and Cheng, C.-L. Temperature-dependent surface CO stretching frequency investigations of functionalized nanodiamond particles. Diam Relat Mater. 2009;18:76–81.

34. Mochalin V, Osswald, S. and Gogotsi, Y. Contribution of functional groups to the Raman spectrum of nanodiamond powders. Chem Mater 2009; 21:273–9.

35. Perevedentseva E, Karmenyan, A., Chung , P,-H., He, Y.-T., Cheng, C.-L. Surface enhanced Raman spectroscopy of carbon nanostructures. Surf Sci. 2006;600:3723-8.

36. Figueiredo J.L. and Pereira MFR. The role of surface chemistry in catalysis with carbons. Catal Today. 2010;150:2-7.

37. Moreno-Castilla C C-MıF, Parejo-Pe´rez C, Lo´pez Ramo´n, MV Dehydration of methanol to dimethyl ether catalyzed by oxidized activated carbons with varying surface acidic character. Carbon. 2001;39:869-75.

38. Tveritinova EA, Kulakova, I.I., Zhitnev, Y.N., Fionov, A.V., Lund, A., Chen, W., Buyanova, I., Lunin, V.V. Catalytic conversion of C(2)-C(3) alcohols on detonation nanodiamond and its modifications. Russian Journal of Physical Chemistry. 2012;86(1):26-31.

39. Zhang J, Su, D.S., Blume,R., Schlogl ,R., Wang, R.,Yang, X. and Gajovic´, A. surface chemistry and catalytic reactivity of a nanodiamond in the steam-free dehydrogenation of ethylbenzene. Angew Chem Int Ed 2010;49:1 – 6.

40. Liu X, Frank, B., Zhang, W., Cotter, T.P., Schlogl, R. and Su, D.S. Carbon-catalyzed oxidative dehydrogenation of n-butane: Selective site formation during sp^3-to-sp^2 lattice rearrangement. Angew Chem Int Ed. 2011;50:3318-22.

41. Frank B, Blume R, Rinaldi A, Trunschke A, and Schlogl R. Oxygen insertion catalysis by sp^2 Carbon. Angew Chem Int Ed 2011;50:10226 –30.

42. Chen D, Holmen, A., Sui, Z., and Zhou, X. Carbon mediated catalysis: A review on oxidative dehydrogenation. Chinese Journal of Catalysis. 2014;35:824–41.

43. Nakagawa K, Kajita, C., Ikenaga, N., Suzuki,T., Kobayashi, T., Nishitani-Gamo, M. and Ando, T. The role of chemisorbed oxygen on diamond surfaces for the dehydrogenation of ethane in the presence of carbon dioxide. J Phys Chem B. 2003;107:4048-56.

44. Okumura K, Nakagawa, K., Shimamura, T., Ikenaga, N.,Nishitani-Gamo, M. ,Ando, T., Kobayashi, T. and Suzuki, T. Direct formation of acetaldehyde from ethane using carbon dioxide as a novel oxidant over oxidized diamond-supported catalysts. J Phys Chem B. 2003;107:13419-24.

45. Suzuki T. New catalyst support material for Fischer-Tropsch synthesis. 21st Saudi Arabia-Japan Joint Symposium; November 27-28, ; Dhahran, Saudi Arabia2011.

46. Vershinin NN, Efimov, ON, Bakaev, VA, Aleksenskii, AE, Baidakova, M V, Sitnikova, AA and Vul, AY. Detonation nanodiamond as catalyst support. Fullerenes, Nanotubes and Carbon Nanostructures 2011;19(1-2):63-8.

47. Levin I, and Brandon D. Metastable alumina polymorphs: Crystal structure and transition sequences. J Am Ceram Soc. 1998;81(8):1995-2012.

48. Trueba M, and Trasatti S P. γ-alumina as a support for catalysts: A review of fundamental sspects. Eur J Inorg Chem. 2005:3393-403.

49. Digne M, Sautet P, Raybaud P, Euzen P, and Toulhoat H. Use of DFT to achieve a rational understanding of acid–basic properties of γ -alumina surfaces. J Catal. 2004;226:54-68.

50. Digne M, Sautet P, Raybaud P, Euzen P, and Toulhoat H. Hydroxyl groups on γ-Alumina surfaces: A DFT study. J Catal. 2002;211:1–5.

51. Krokidis X, Raybaud, P., Gobichon, A., Rebours, B., Euzen, P. and Toulhoat, H. Theoretical study of the dehydration process of boehmite to gamma-alumina. J Phys Chem B. 2001;105 5121-30.

52. Paglia G, Buckley, CE, Rohl, AL, Hart, RD, Winter, K, Studer, AJ, Hunter, BA, and Hanna, JV. Boehmite derived γ-alumina system. 1. Structural evolution with temperature, with the identification and structural determination of a new transition phase,γ^{I}-alumina. Chem Mater. 2004;16:220-36.

53. Wischert R, Coperet, C, Delbecq, F and Sautet, P. Optimal water coverage on alumina: A key to generate Lewis acid–base pairs that are reactive towards the CH bond activation of methane. Angew Chem Int Ed. 2011;50:3202 –5.

54. Wischert R, Laurent, P, Copéret, C, Delbecq, F and Sautet, P. γ‑Alumina: The essential and unexpected role of water for the structure, stability, and reactivity of "Defect" sites. J Am Chem Soc. 2012;134:14430−49.

55. Castro RHR, and Quach, DV. Analysis of anhydrous and hydrated surface energies of gamma-Al_2O_3 by water adsorption microcalorimetry. J Phys Chem C. 2012;116 24726−33.

56. Hindin SG, and Weller, SW. The effect of pretreatment on the activity of gamma alumina I. Ethylene hydrogenation. J Phys Chem 1956;60:1501-6.

57. Weller SW, and Hindin, SG. The effect of pretreatment on the activity of gamma alumina II. hydrogen-deutrium exchange. J Phys Chem. 1956;60:1506-12.

58. Van Cauwelert FH, and Hall, WK. The ortho-para H_2 conversion and H_2-D_2 exchnage reaction over a transition alumina. Trans Faraday Soc. 1970;66:454-68.

59. Maciver DS, Tobin, HH, and Barth, RT. Catalytic aluminas I. Surface chemistry of eta and gamma alumina. J Catal. 1963;2:485-97 (1963.

60. Peri JB. Infrared study of ddsorption of carbon dioxide, hydrogen chloride, and other molecules on "Acid" sites on dry silica-alumina and γ-alumina. J Phys Chem. 1966;70(10):3168-79.

61. Flockhart BD, Scott, AN. and Pink, RC. Electron-transfer at alumina surfaces. Part 1.-electron-acceptor properties of aluminas. Trans Faraday Soc. 1966;62:730-40.

62. Joubert J, Salameh, A, Krakoviack, V, Delbecq, F, Sautet, P,Coperet, C and Basset, JM. . Heterolytic splitting of H_2 and CH_4 on γ-Alumina as a structural probe for defect sites. J Phys ChemB. 2006;110:23944-50.

63. Kwak J-H, Peden, C.H.F. and Szanyi, J. Using a surface-sensitive chemical probe and a bulk structure technique to monitor the γ- to θ-Al_2O_3 phase transformation. J Phys Chem C. 2011;115:12575–9.

64. Roy S, Mpourmpakis, G, Hong, D-H, Vlachos, DG, Bhan, A and Gorte , RJ. Mechanistic study of alcohol dehydration on γ‑Al2O3. ACS Catalysis 2012, . 2012;2:1846−53.

65. Roy S, Mpourmpakis G, Hong D-H, Vlachos DG, Bhan A, and Gorte RJ. Mechanistic study of alcohol dehydration on γ‑Al_2O_3. ACS Catal. 2012;2:1846−53.

66. DeWilde FD, Chiang, H, Hickman, DA, Ho, CR and Bhan, A. Kinetics and mechanism of ethanol dehydration on γ‑Al_2O_3: The critical role of dimer inhibition. ACS Catal. 2013;3:798−807.

67. Greenler RG. Infrared study of the adsorption of methanol and ethanol on aluminum oxide. J Chem Phys. 1962;37(9):2094-100.

68. Schiffimo RS, and Merrill, R P. A Mechanistic study of the methanol dehydration reaction on γ-alumina catalyst. J Phys Chem. 1993;97:6425-35.

69. Zuo Z, Huang, W, Han, P, Gao, Z and Li, Z. Theoretical studies on the reaction mechanisms of AlOOH- and γ-Al_2O_3-catalysed methanol dehydration in the gas and liquid phases. Appl Catal A. 2011;408:130-6.

70. Wang B, Ding, G, Shang, Y, Lv, J, Wang, H, Wang, E, Li , Z, Ma, X, Qin, S and Sun, Q. Effects of MoO_3 loading and calcination temperature on the activity of the sulphur-resistant methanation catalyst MoO_3/γ-Al_2O_3. Appl Catal A. 2012;431– 432 144– 50.

71. Abello MC, Gomeza MF, and Ferretti O. Mo/γ-Al_2O_3 catalysts for the oxidative dehydrogenation of propane. Effect of Mo loading. Appl Catal A General. 2001;207:421-31.

72. Christodoulakis A, Heracleous E, Lemonidou AA, and Boghosian S. An operando Raman study of structure and reactivity of alumina-supported molybdenum oxide catalysts for the oxidative dehydrogenation of ethane. J Catal. 2006;242:16–25.

73. Hu H, and Wachs I E. Catalytic properties of supported molybdenum oxide catalysts: *In Situ* Raman and methanol oxidation studies. J Phys Chem. 1995;99:10911-22.

74. Matsuoka Y, Niwa M, and Murakami Y. Morphology of molybdena supported on various oxides and its activity for methanol oxidation. J Phys Chem. 1990;94(4):1477-82.

75. Brandhorst M, Cristol S, Capron M, Dujardin C, Vezin H, Le bourdon G, and Payen E. Catalytic oxodation of methanol on Mo/Al_2O_3 catalyst: An EPR and Raman/infrared operando spectroscopies study. Catal Today. 2006;113(1-2):34-9.

76. Zingg DS, Makovsky LE, Tischer RE, Brown FR, and Hercules DM. A surface spectroscopic study of molybdenum-alumina catalysts using X-ray photoelectron, ion-scattering, and Raman spectroscopies. J Phys Chem. 1980;84(22):2898-906.

77. Tian H, Wachs, I.E., Briand, L.E. Comparison of UV and visible Raman spectroscopy of bulk metal molybdate and vanadate catalysts J Phys Chem B. 2005;109:23491-9.

78. Briand LE, Farneth W E, and Wachs I E. Quantitative determination of the number of active surface sites and the turnover frequencies for methanol oxidation over metal oxide catalysts I. Fundamentals of the methanol chemisorption technique and application to monolayer supported molybdenum oxide catalysts. Catal Today. 2000;62:219–29.

79. Dupin J-C, Gonbeau, D,Vinatierb, P, and Levasseur, A. Systematic XPS studies of metal oxides, hydroxides and peroxides. Phys Chem Chem Phys. 2000;2:1319-24.

80. Lopez GP, Castner, D.G. and Ratner, B.D. XPS O1s binding energies for polymers containing hydroxyl, ether, ketone and sster groups. Surf Interface Anal 1991;17:267-72.

81. Rosenthal D, Ruta, M, Schlögl, R and Kiwi-Minsker, L . Combined XPS and TPD study of oxygen-functionalized carbon nanofibers grown on sintered metal fibers. Carbon. 2010;40:1835-43.

82. Figueiredo JL, Pereira, MFR, Freitas, MMA and Orfao, JJM. Modification of the surface chemistry of activated carbons. Carbon 1999;37:1379–89.

83. Xu SC, Irle, S, Musaev, DG and Lin MC. Quantum chemical study of the dissociative adsorption of OH and H_2O on pristine and defective graphite (0001) surfaces: Reaction mechanisms and kinetics. J Phys Chem C 2007;111:1355-65.

84. Farneth WE, McCarron III E M, Sleight A W, and Staley R H Comparison of the surface chemistry of two polymorphic forms of molybdenum trioxide. Langmuir. 1987;3(2):217-23.

85. Tatibouet JM, Germain JE, Volta JC. Structure-sensitive catalytic oxidation: alcohols on graphite-supported molybdenum trioxide. J Catal. 1983;82:245-51.

86. Tatibouet JM, and Germain JE. A structure-sensitive oxidation reaction: methanol on molybdenum trioxide catalysts. J Catal. 1981;72(2):375-8.

87. Machiels CJ, Cheng W H, Chowdhry U, Farneth W E, Hong F, Mc Carron E M, and Sleight A W The effect of structure of molybdenum oxides on the selective oxidation of methanol. Appl Catal 1986;15(1-2):249 – 56

88. Ressler T, Wienold, J, Jentoft, RE, Neisius, T. Bulk structural investigation of the reduction of MoO_3 with propene and the oxidation of MoO_2 with oxygen. J Catal. 2002; 210:67-83.

89. Abon M, Massardier J, Mingot B, Volta J C, Floquet N, and Bertrand O New unsupported [100]-oriented MoO_3 catalysts II. Catalytic properties in propylene oxidation. J Catal 1992;134(2):542 – 8.

90. JCPDS Card Number 00-005-0508.

91. JCPDS Card Number 01-074-1415.

92. JCPD Card Number 03- 065-6329

93. Maciver DS, Tobin, HH, and Barth, RT. Catalytic aluminas I. Surface chemistry of eta and gamma alumina. J Catal. 1963;2:485-97.

94. Kwak J-H, Hu, J., Lukask, A., Kim, D.H., Szanyi, J. and Peden, C.H.F. . Role of pentacoordinated Al^{3+} ion in the high temperature phase transformation of γ-Al_2O_3 J Phys Chem C. 2008;112:9486-92.

95. del Arco M, Carrazan S R G, Martin C, Martin I, Rives V, and Maletb P. Surface dispersion of molybdena supported on silica, alumina and titania. J Mater Chem. 1993;3(12):1313-8.

96. Wachs I, and Roberts CA. Monitoring surface metal oxide catalytic active sites with Raman spectroscopy. Chem Soc Rev 2010;39:5002-17.

Chapter 5 MoO_3 Based Model Catalysts Prepared on α-Al_2O_3 (0001) Single Crystal

Contents

5.1 Introduction and Literature Review:

This chapter concerns with the synthesis and characterization of MoO_3 and $Fe_2(MoO_4)_3$ thin films on Al_2O_3 (0001) single crystals. This pioneering study of model catalysts system on Al_2O_3 (0001) single crystals is intended to investigate the mechanism and catalytic active sites for selective methanol oxidation reaction.

Model Catalysts

The fabrication and study of model catalysts is an emerging field in catalysis, aimed at bridging the gap between complex bulk heterogeneous catalytic systems and surface science. This methodology enables the use of powerful surface techniques in monitoring reaction at an atomic scale. The study of metal films was pioneered by Poppa [1], in an investigation of metal particles and cluster deposition on substrates in UHV. Freund's group [2] and Bowker's group [3], had worked on various metal and oxide model catalysts. In a review by Freund [4], the authors stressed the significance of using conducting substrate, such as thin layers of alumina, silica and magnesia, in fabrication and growth of metal or oxide thin film as model catalyst. This allows the use of both microscopic and spectroscopic techniques, such as low energy electron diffraction (LEED), scanning tunnelling microscopy (STM), x-ray photoelectron spectroscopy (XPS), transmission electron microscopy (TEM), and infrared (IR) for the characterization of surfaces and investigation of adsorbate on model surface in UHV and ambient conditions.

Hoffmann et al [5], reported a molecular beam study on Pd/Al_2O_3 model catalyst. The authors revealed existence of both small and large Pd particles, with the former comprising of high density of defect sites while the latter exposes mainly (111) faces and a small fraction of (100) faces. The small particles suppressed CO poisoning as compared to the large Pd particles. In addition, transient and steady state studies on the catalyst indicate that CO oxidation is dependent on CO termination at constant O_2 flux condition. However, deviation of the reaction kinetics is attributable to heterogeneity of the model catalyst surface due to variation in particle sizes, morphology, and presence of islands and defect sites. Freund [6], reported low temperature oxidation of CO to CO_2 on Pd film grown on Fe_2O_3 (111), which is associated with delay in diffusion of O atom on Pd with oxidation of surface Pd to PdO occurring at high temperature as revealed by XPS

study. In a separate hydrogenation study on same model catalyst system by the authors [2], they revealed structure insensitivity during ethene hydrogenation, which involves reaction of weakly bonded H at top layer of Pd with π – bond in ethene. However, hydrogenation of pentene to 2- pentane indicates structure sensitivity due to reaction of weakly adsorbed H on the terrace in large Pd particles with di – s bonding. More so, oxidative dehydrogenation of methanol on Pd film prepared over alumina reported by Freund [7], evidence C – O cleavage occurring on edges and corners of Pd (111) as a precursor to both formaldehyde and formyl, which enhances formaldehyde selectivity at high temperature.

Magg et al [8], reported metal oxide catalyst based on V_2O_5 on alumina synthesised via evaporation of V_2O_5 in oxygen. An STM study of the model catalyst revealed roundish V_2O_5 particles of 20 – 30 Å particle sizes. Moreover, infrared absorption spectroscopy indicates strong particle-support interaction in thick films, with the presence of both bulk and vanadyl species on alumina film. In a separate study of V_2O_5 thin film grown on Al_2O_3 and SiO_2 reported by Freund [2, 6], the authors confirmed the presence of monomeric vanadyl (V=O) and V – O – Al species on alumina thin film at lower monolayer coverage, but polymeric V – O – V on thick film on alumina. However, Freund [7] reported granular morphology of V_2O_5 on Al_2O_3 and SiO_2 with oxidation state of +3, which increases to +5 with increasing film thickness, as well as exposure and termination of vanadyl species on the surface. Methanol dehydrogenation on V_2O_5 (0001)/ Al_2O_3 model catalyst reported by Romanyshyn et al [9] and Freund [7], revealed vanadyl species as the active and selective site for formaldehyde formation on V_2O_5 model catalyst.

MoO_3/Al_2O_3 Single Crystal Model Catalyst

Early investigation of selective oxidation reaction on MoO_3 was based on single crystal and bulk crystalline MoO_3 surfaces respectively. Smith and Rohrer [10], reported an atomic force microscope (AFM) study on MoO_3 crystal prepared using chemical vapour transport method. The reaction of hydrogen and water on the crystal surface at 400 ^oC revealed the formation of voids and removal of second layer of oxygen, which resulted in formation of crystallographic shear plane. These defects intersect the (010) plane leading to formation of steps along (001) surface, revealing maximum vacancies on the MoO_3 crystals.

In a separate AFM study of the methanol reaction on a MoO_3 crystal reported by Smith and Rohrer [11], the formation of bronze precipitate of $HMoO_3$ was revealed due to intercalation of H into MoO_3 step in (h 0 l) cleavage, which increases with size and depth of the steps and pits respectively. The steps and pits are proposed as active sites for chemisorption of methanol and formation of DME besides formation of $HMoO_3$ bronze. However, Spevack and McIntyre [12] reported an XPS and Raman study of MoO_3 thin film prepared by sputtering method on alumina substrate. The authors proposed that the film thickness could be estimated from the increase in FWHM of Mo 3d doublet spectra. In addition, they attribute reduction of Mo(VI) on film thickness, but found the presence of $Al_2(MoO_4)_3$ that is irreducible at 350 ^oC. More so, vacuum reduction of MoO_3 thin films under H_2/N_2 flow at 500 ^oC revealed the existence of both MoO_2 and MoO_3 species, while the unsupported MoO_3 was completely reduced to Mo metal.

Zou and Schrader [13] reported α-MoO_3 and $NiMoO_4$ multi-component thin films formed on a Si wafer using reactive sputtering techniques. The authors revealed preferential orientation of basal plane (010) on smooth surface of α- MoO_3 thin film, whereas $NiMoO_4$ exhibits non-uniform multi crystalline morphology and monoclinic α- $NiMoO_4$, with formation of new reactive phase (β- $NiMoO_4$) at interfacial region between α- MoO_3 and α- $NiMoO_4$. This phase indicates high reactivity and selectivity for the conversion of 1 – 3 – butadiene to furan, and blocks sites responsible for complete oxidation of products. However, they reported a synergistic effect between α- MoO_3 and α- $NiMoO_4$ phases. More so, Haro – Poniatowski et al [14] reported crystalline MoO_3 film of different sizes synthesized by laser irradiated techniques. The authors revealed formation of metastable β-MoO_3 structure on the underlying films.

Gunther et al [15], reported a photoelectron spectroscopic study of MoO_3 spreading on titania and alumina model supports prepared by the deposition of MoO_3 at 320 K prior to heating at 720 K for 6 hours. The authors revealed the formation of MoO_3 thin films of thickness between 20 nm - 1μ at 720 K, with inhomogeneous islands with no specified orientation attributed to defect structure on alumina support. The defects on the alumina support are proposed to control both mobility and the adsorption energy of MoO_3 species. In addition, an XPS study on the film revealed Mo in its highest oxidation state of +6, with variation in surface potential from 2 – 10 eV due to increasing thickness of the film.

Hsu et al [16], reported increase in grain size of MoO_3 thin film synthesized via spin coating of MoO_3 sol-gel with increasing calcination temperature from 100 – 500 ^oC. More so, calcination of the film at 350 ^oC exhibits excellent electrochromism, with good optical transmittance and reversibility after 100 CV cycles. Similarly, Xie et al [17] reported electrochromism on MoO_3 nano belt grown on silica substrate via evaporation of Mo foil. An XRD and Raman study of the nano belt discerned presence of orthorhombic MoO_3 crystallite with thickness between 50 – 400 nm, as determined by AFM analysis. The nano belt indicates colour variation due to MoO_3 film thickness. Wolden et al [18], reported the presence of a polycrystalline MoO_3 thin film of 100 – 500 nm thickness synthesized via plasma enhanced chemical vapour deposition (PECVD), which was further reduced to β- Mo_2C on reduction with CH_4/H_2.

The presence of steps and terraces on Al_2O_3 (0001) single crystal surface as evidenced by AFM studies reported by Gan and Franks [19] made the surface a good model for comparison with bulk heterogeneous catalysts surface. We attempt a pioneer synthesis and characterization of MoO_3 thin film on Al_2O_3 (0001) single crystal surface using novel wet techniques, for study as model catalyst for selective oxidation of methanol to formaldehyde.

$Fe_2(MoO_4)_3$/ Al_2O_3 Single Crystal Model Catalyst

Iron molybdates used industrially for methanol oxidation to formaldehyde, have been extensively studied by various research groups [20-22], but only recently surface science investigation on model catalyst systems was reported by Bowker's group [3, 23] in collaboration with Freund's group. Uhlrich et al [23] reported a study of iron molybdate model catalysts synthesized by deposition of Mo on Fe_3O_4 (111) thin films grown on Pt (111) surface in UHV. The Fe_3O_4 (111) surface is dominated by Mo=O termination from Mo nanoparticles at low annealing temperature (300 K) as evidenced by infrared absorption spectroscopy (IRAS), whereas substitution of Fe and migration of Mo into Fe_3O_4 (111) structure resulted in formation of new bonding with oxygen at 900 K. Furthermore, the film retains the crystal structure of Fe_3O_4 (111), while its surface undergoes ($\sqrt{3}$ x $\sqrt{3}$) R30 ^{o} reconstruction as revealed by STM and LEED study.

Bamroongwongdee et al [3], reported the fabrication of iron molybdates model catalyst grown by hot-filament metal oxides deposition techniques (HFMOD) of MoO_3 film and nanoparticles on Fe_3O_4 (111) single crystal. LEED, XPS, and STM studies revealed highest oxidation state of +6 for the MoO_3 film on the crystal, which is thermally stable at about 973 K. However the authors observed cation diffusion and formation of iron molybdates at about 573 K. Studies on iron molybdate model systems for investigation of methanol oxidation to formaldehyde are scanty. We report for the first time the fabrication of iron molybdate model catalyst on Al_2O_3 (0001) single crystals using a novel wet chemical method, exploring both the steps on the crystal surface as well as same catalyst precursors used in the synthesis of bulk catalyst, to mimic bulk heterogeneous surface on a model scale.

5.2 Results and Discussion

MoO_3/Al_2O_3

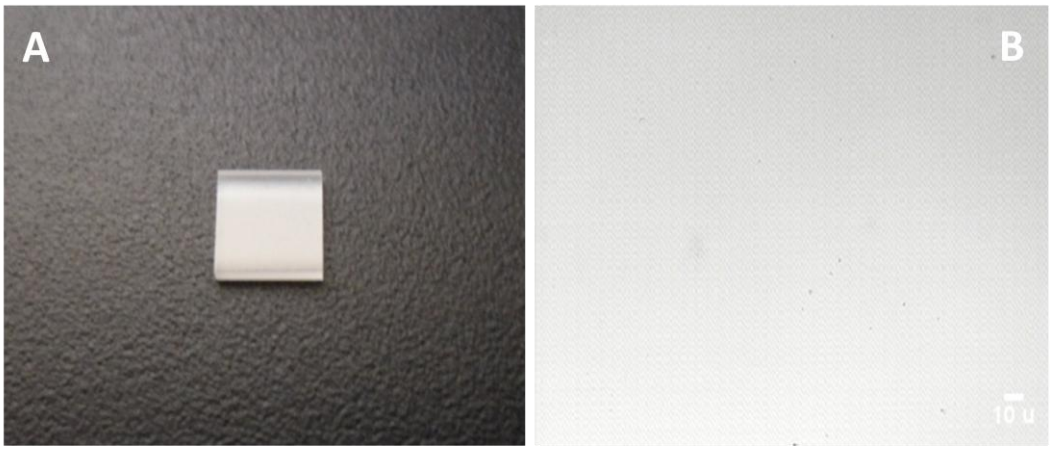

Fig. 5. 1 ***Images of α – Al_2O_3 (0001) single crystal 5 mm^2 (A) photographic (B) microscopic (light) image scale (270 x 250 µ)***

Fig. 5. 1 depicts cleaned surface of both photographic and microscopic images of the polished side of α – Al_2O_3 (0001) single crystal. The images in Fig. 5. 1 A and B reveal the polished surface to be reflective to light.

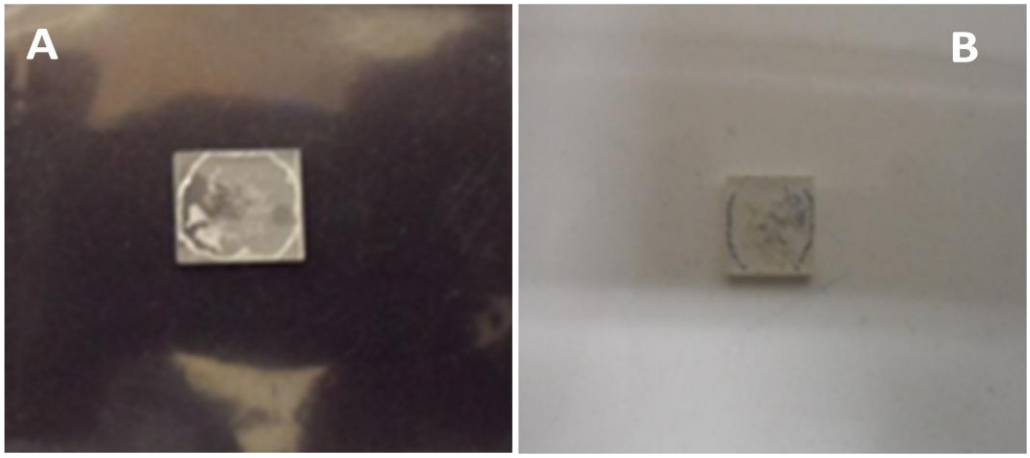

Fig. 5. 2 ***Images of AHM precursor 700 monolayer (ML) MoO_3 on Al_2O_3 (0001) crystal 5 mm^2 using water as solvent (A) dried AHM precursor (B) calcined at 200 ^oC***

The images of 700 monolayer coverage MoO_3 deposited on Al_2O_3(0001) crystal using a solution of ammonium heptamolybdates (AHM) in water as shown in Fig. 5. 2 and reveal the formation of white rounded polygon with patches of islands, which change to grey colouration after calcination in air for an hour at 200 ^oC as depicted in Fig. 5. 2 B. The white roundish structure is due to the surface tension effect of water. A drop of

AHM solution on Al_2O_3 (0001) crystal formed a dome like structure, which shrinks inwards as it evaporates on the surface leaving behind deposit of AHM salt.

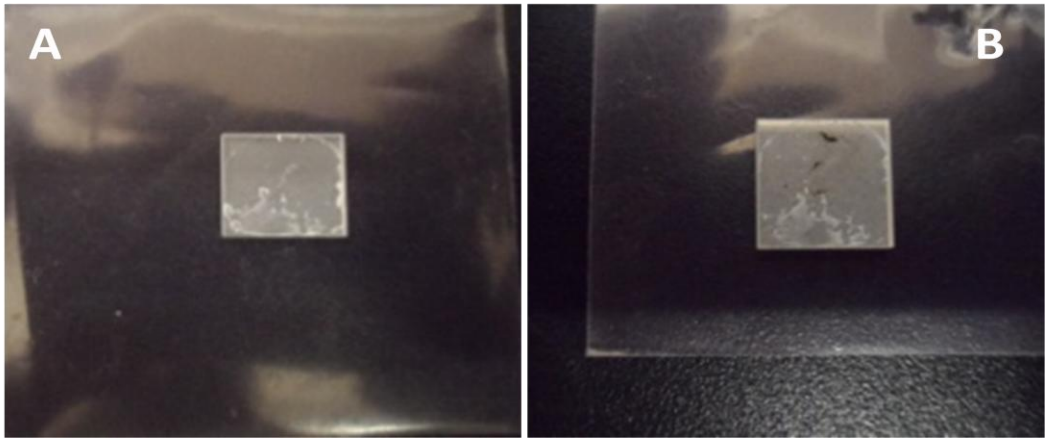

Fig. 5. 3 ***Images of AHM precursor -70 ML MoO_3 on Al_2O_3 (0001) crystal 5 mm^2 using water as solvent (A) dried AHM precursor (B) calcined at 200 ^oC***

Fig. 5. 3 depicts images of 70 ML of dried AHM precursor deposited on Al_2O_3 crystal (5.3A) and the calcined sample at 200 ^oC in Fig. 5. 3 B. Both images reveal the formation of conspicuous white island patches within a ring like structure resulting from a similar water surface tension and evaporation effect as the 700 ML coverage. The white AHM precursor turns greyish on heating to 200 ^oC for an hour. However, water does not seem a good solvent for wetting and spreading of MoO_3 on the alumina single crystals.

Fig. 5. 4 ***Images of AHM precursor- 700 ML MoO_3 on Al_2O_3 (0001) crystal 5 mm^2 using acidified water/ethanol solution (A) dried precursor (B) calcined at 200 ^oC***

The images in Fig. 5. 4 reveal a much better coverage of the Al_2O_3 (0001) crystal with polymolybdate precursor in water/ethanol solvent (5.4 A), which turns greyish after calcination in an oven for an hour as shown in Fig. 5. 4 B.

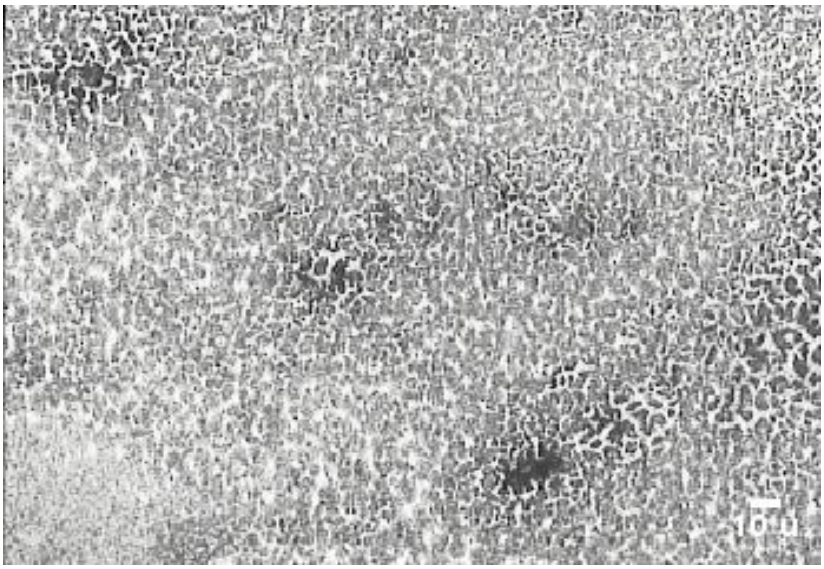

Fig. 5. 5 ***Microscopic image of 700 ML MoO_3 on Al_2O_3 (0001) 1 mm^2 crystal after calcination at 500 ^oC, scale (170 x 250 μ)***

The microscopic image in Fig. 5. 5 above reveals leopard skin-like patches of dense and less dense crystalline MoO_3 islands of $\leq 10\mu$ with no specific orientation, which is in accordance with findings reported by Gunther et al [15] for MoO_3 film grown alumina substrate. The cracking of the surface may be attributable to possible irregularity of the crystal surface due to defects and steps.

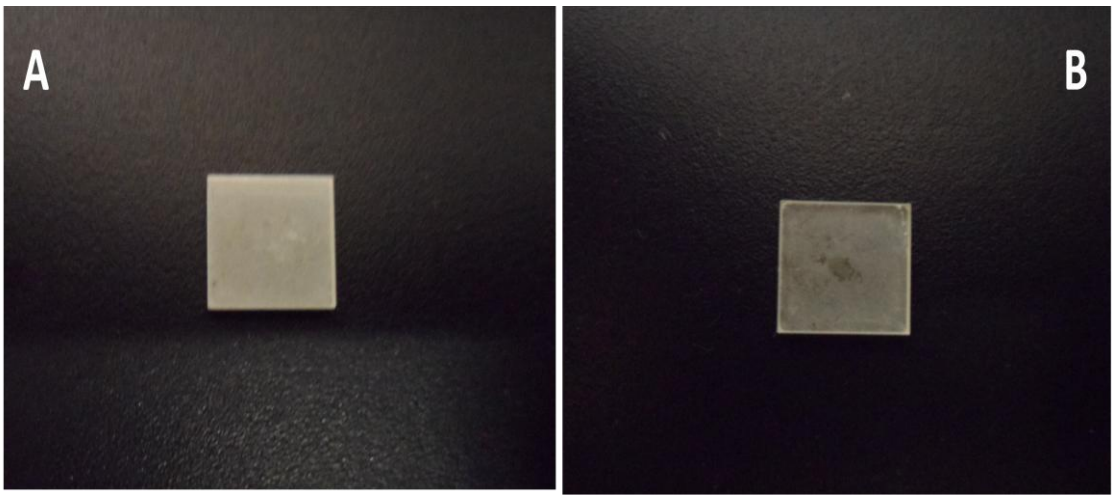

Fig. 5. 6 ***Images of polymolybdate precursor with 350 ML MoO_3 on Al_2O_3 (0001) crystal 5 mm^2 using acidified solution of AHM in water/ethanol (A) dried precursor (B) calcined at 200 ^oC***

The hydrated polymolybdate precursor on Al_2O_3 crystal at room temperature is shown in Fig. 5. 6 (A), and after calcination at 200 ^oC (B). The sample indicates good covering of MoO_3 on the single crystal alumina.

Fig. 5. 7 ***Microscopic image of 350 ML MoO_3 on Al_2O_3 (0001) crystal 1 mm^2 after calcination at 500 ^oC scale (170 x 250 μ)***

The microscopic image of 350ML MoO_3 coverage in Fig. 5. 7 depicts the formation of needle–like MoO_3 nano-rods of different sizes, thickness, and length. The nano-rods cover the entire surface of the Al_2O_3 (0001) single crystal. This finding is in close agreement with TEM and SEM images of α- MoO_3 nano rod synthesised using dilute HNO_3 and peroxomolybdic acid solution reported by Xie et al [17] and Fang et al [24] respectively.

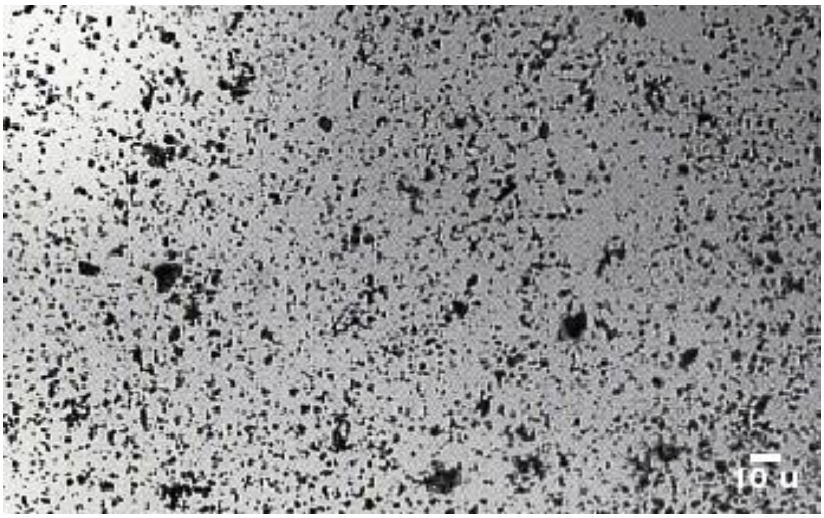

Fig. 5. 8 ***Microscopic image of 100 ML MoO_3 film on Al_2O_3 (0001) 5 mm^2 single crystal calcined at 500 ^oC, scale (170 x 250 μ)***

The microscopic image of 100 ML MoO_3 coverage on Al_2O_3 crystal prepared using dilute HNO_3 acid in Fig. 5. 8 reveal crystalline MoO_3 particles of varying sizes. This indicates good spreading of MoO_3 film over alumina crystal surface after calcination at 500 ^oC in air oven.

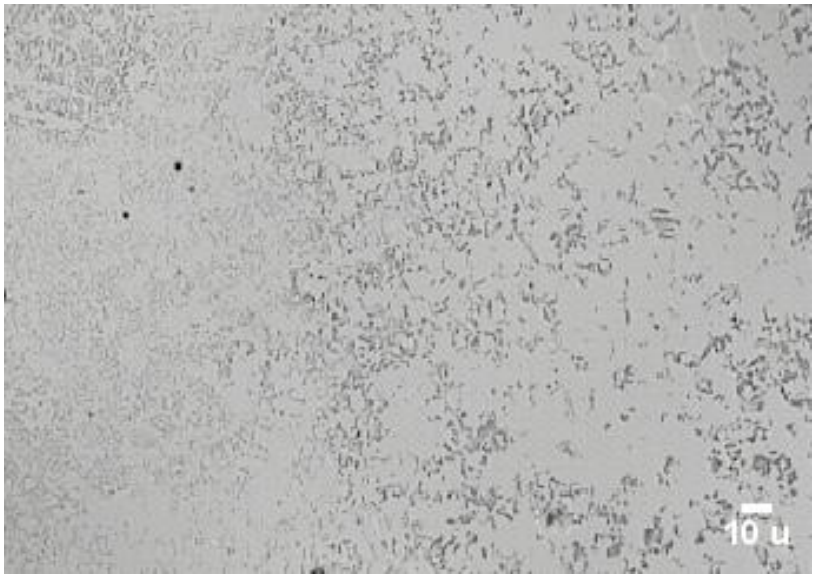

Fig. 5. 9 ***Microscopic image of 100 ML MoO_3 on Al_2O_3 (0001) crystal 5 mm^2 calcined at 500 ^oC, Scale (170 x 250 µ)***

Fig. 5. 9 depicts image of MoO_3 thin film on Al_2O_3 crystal prepared by acidifying water/ethanol solution containing AHM precursor with citric acid. The image reveals good dispersion of crystalline MoO_3 on the alumina surface, forming a mesh like structure with small crystallite sizes ($\leq 2\mu$) in comparison to nitric acidified precursor. Moreover, the image indicates region of intense and light grey colouration, which could be attributable to different density of crystalline MoO_3 on the crystal surface due to variation of adsorption energy of defect or steps on the alumina (0001) crystal surface, as previously observed by Gunther et al [15].

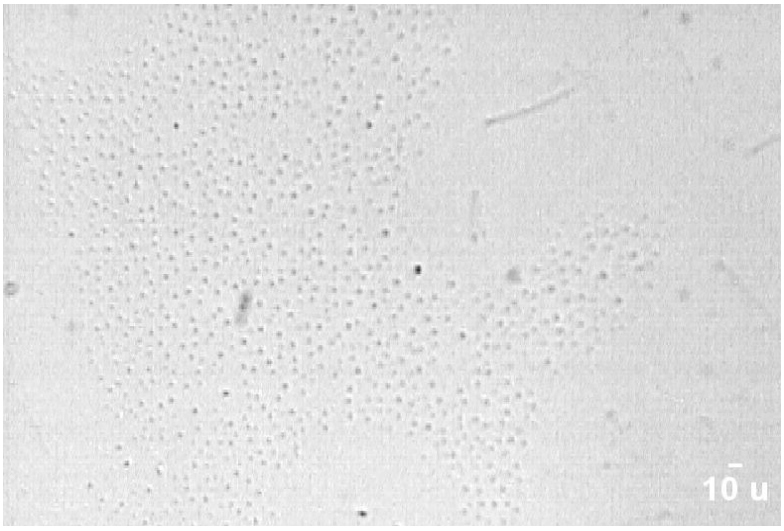

Fig. 5. 10 ***Microscopic image of 70 ML MoO_3 on Al_2O_3 (0001) 5 mm^2 crystal calcined at 500 ^oC, scale (270 x 400 μ)***

The microscopic image 70 monolayer coverage of MoO_3 thin film on single crystal alumina (0001) using wet deposition method calcined at 500 ^oC in oven for an hour in

Fig. 5. 10, reveals formation of disperse dotted greyish crystalline MoO_3 islands of varying particle sizes ($\leq 2\mu$). The islands are well spaced and covers most parts of the crystal, although some parts of the crystal remain exposed. However, the exposed region of the crystal may contain very small particle sizes beyond the limit of imaging with light microscope or possibly unequal spreading of MoO_3 on the surface. More so, the particle size distribution is evenly consistent, which could be attributable to the chelating property of citrate known to enhance metal or metal oxide dispersion on catalyst supports.

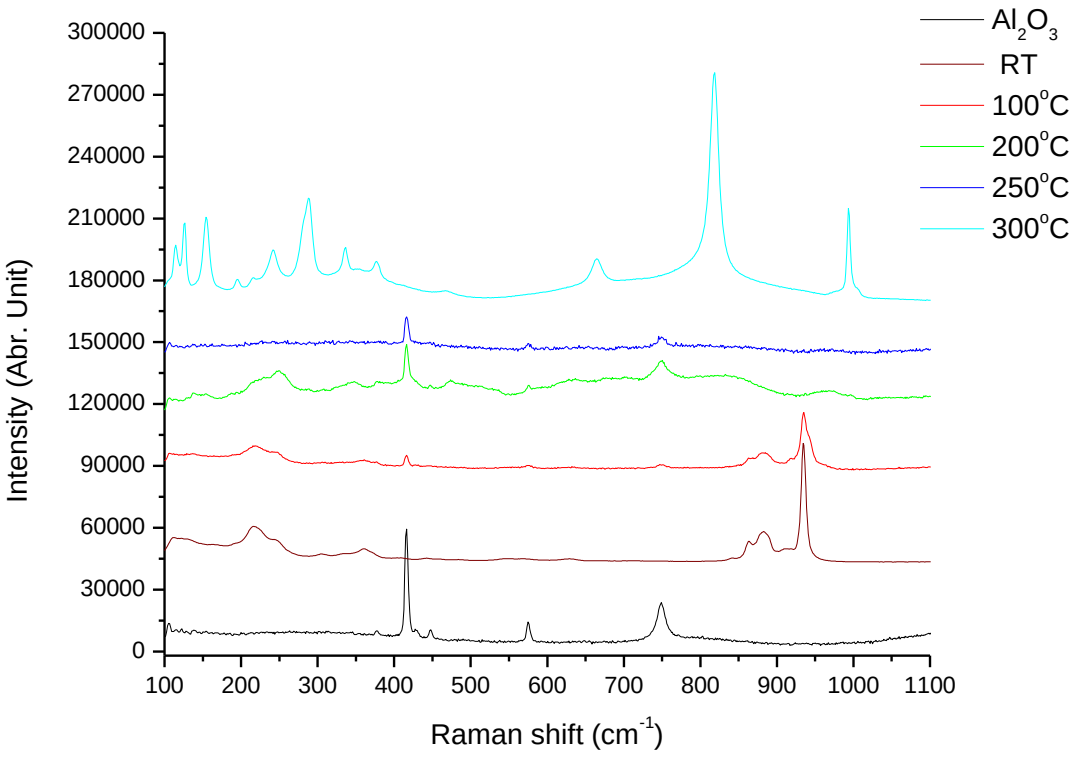

Fig. 5. 11 ***Raman spectra of MoO_3 evolution on α-Al_2O_3 (0001) crystal prepared using solution of AHM salt in water (700 ML MoO_3)***

The Raman spectra in Fig. 5. 11 reveal the evolution of MoO_3 phase on α-Al_2O_3 (0001) crystal with increasing calcination temperature. The cleaned α-Al_2O_3(0001) single crystal reveals Raman bands at 416, 377, 428, 488, 575, and 749 cm^{-1} assigned to A_{1g}, E_g (external), E_g (external), E_g (internal), E_g (internal), and E_g (internal) vibration mode respectively, which are consistent with bands reported for α-Al_2O_3 by Porto and Krishnan [25], and Aminzadeh and Sarikhani-Fard [26] . The sample calcined from room temperature (RT) to 100 ^oC reveal Raman bands at 934 cm^{-1} relative to 883 and 863 cm^{-1} attributed to asymmetric stretching of crystalline AHM with heptahedral vertex edge-corner sharing of MoO_6 in Mo_7O_{24} cluster, as reported by Wachs and Robert, Vuurman and Wachs [27, 28]. More so, increasing calcination between 200 – 250 ^oC results in disappearance of the sharp Raman band at 934 $cm^{-1}$with corresponding broadening and shifting of the band to 965 cm^{-1}, which is a typical Raman band associated with $Mo_8O_{26}^{4-}$ (polymeric species) as reported by Wachs [29], in addition to bands at 138, 158, 249, 308, 348 and 379 cm^{-1}. These bands indicate the

spreading and transformation of the crystalline AHM into polymeric MoOx species on the α-Al_2O_3 crystal at high coverage. The Raman bands discerned at 993, 819, 665, 470, 377, 337-288, 242-195, 154 and 127 cm^{-1} by 300 ^oC are attributable to υ_{as} Mo=O, υ_s O-Mo-O, υ_{as} O-Mo-O, υ_{as} O-Mo-O bending, (B_{1g}) scissoring, (A_{1g}) scissoring, δ O=Mo=O wagging, twisting vibration, A_g/B_{1g} and $B_{3g,}$ translational rigid MoO_4 chain mode respectively in crystalline MoO_3. The Raman spectra are in good agreement with reported spectra of MoO_3 thin film by Haro-Poniantowski et al [14] and Illyaskutty et al [30].

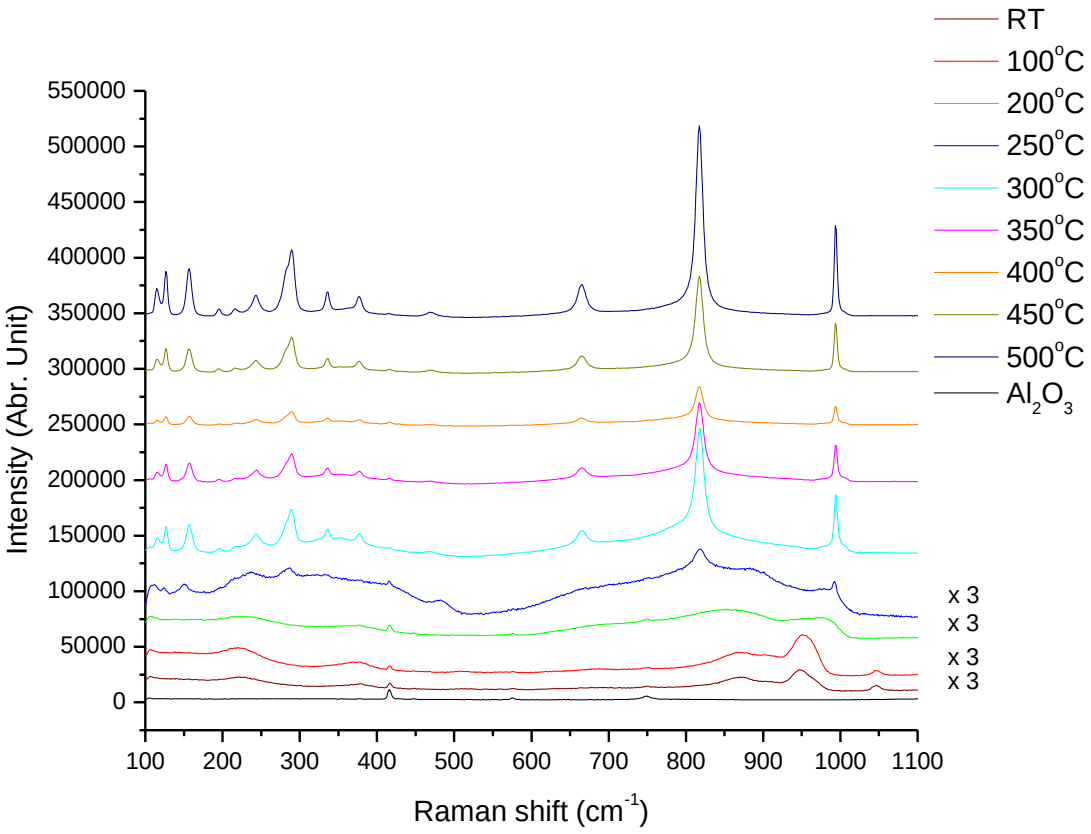

Fig. 5. 12 ***Raman spectra of MoO_3 evolution on Al_2O_3 (0001) crystal prepared using acidified solution of AHM in water/ethanol mixture (700 ML MoO_3)***

Raman spectra indicating the evolution crystalline MoO_3 thin film on α-Al_2O_3 crystal on calcination from 100 ^oC to 500 ^oC as shown in Fig. 5. 12 reveal similar Raman bands for both films at room temperature and those calcined at 100 ^oC. The bands at 950 cm^{-1} with a shoulder at 908 cm^{-1} assigned to asymmetric stretching, with additional bands at 871, 377 and 219 cm^{-1} attributable to $[Mo_7O_{24}]^{6-}$ polymeric species, which concur with monolayer Mo coverage (20wt %) on bulk MoO_3/Al_2O_3 catalyst at

ambient condition reported by Tian, Robert and Wachs [31]. However, the band at 1045 cm^{-1} is associated with NO_3^- species, which disappears completely at 200 ^oC with corresponding broadening and shifting of the 950 cm^{-1} to higher band of 981 cm^{-1} and 871 cm^{-1} to lower band of 854 cm^{-1}. Evolution of Mo=O band at 992 cm^{-1}, and Mo-O-Mo bridging band at 818 cm^{-1}, and other lower vibration bands are evidenced at 250 ^oC. A crystalline MoO_3 film formed between 300-500 ^oC reveals similar Raman bands as those discerned in figure 5.11 above for sample calcined at 500 ^oC.

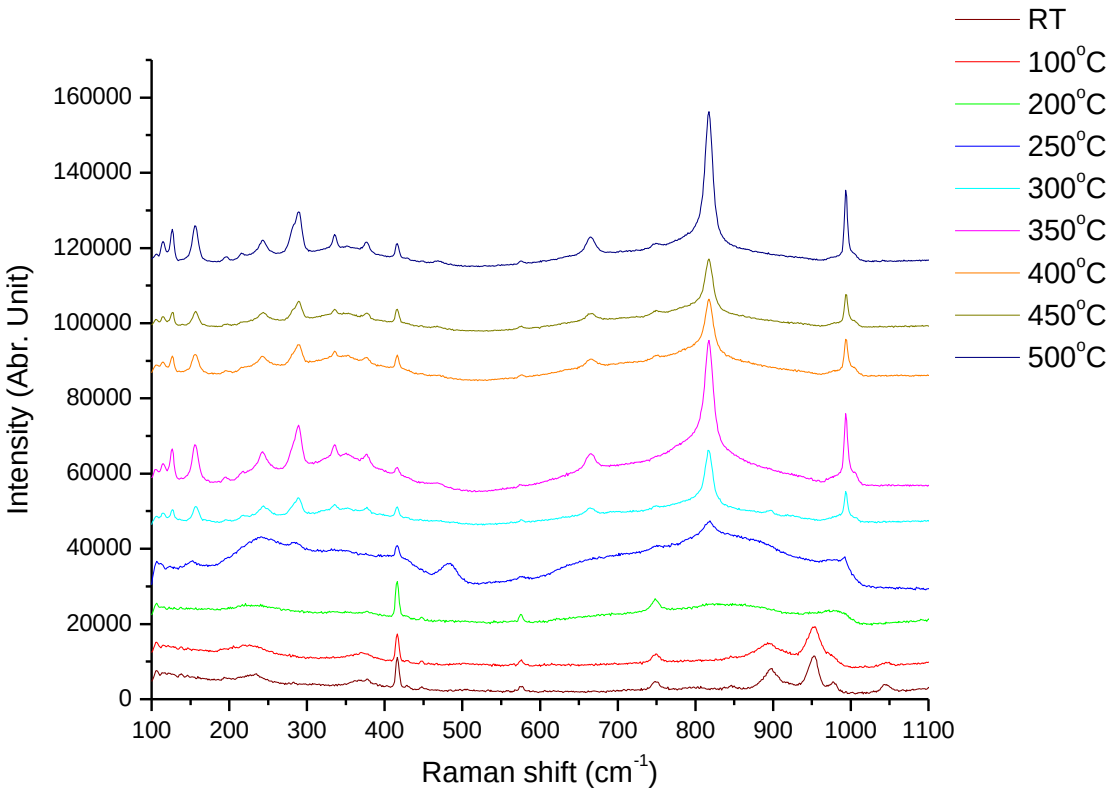

Fig. 5. 13 ***Raman spectra of MoO_3 evolution on Al_2O_3 (0001) crystal prepared using acidified solution of AHM in water/ethanol mixture (350 ML MoO_3)***

Raman spectra in **Fig. 5. 13** reveal bands at 964, 896, 377 and 218cm^{-1} for both films at RT and sample calcined up to 100 ^oC, which are characteristic bands for $[Mo_7O_{24}]^{6-}$ species. In addition, the band at 847, 975 and 1043 cm^{-1} could be assigned to $[MoO_4]^{2-}$ species, aluminomolybdic Keggin cluster, and NO_3^- species respectively, which is in agreement with Raman bands for tetrahedral $(O=)_2MoO_2$ species reported by Wachs and Robert [27], and knozinger and Jeziorowski [32]. The bands at 750 and 416 cm^{-1} are associated with Al_2O_3 single crystal. This indicates the presences of both tetrahedral and octahedral polymeric MoOx species for 350 monolayer coverage.

However, calcination of the films at 200 ^oC reveals similar broadening and shifting of the 964 cm^{-1} band to 992 cm^{-1} with transformation of the polymeric MoOx species to crystalline MoO_3 beginning at 250 ^oC and complete at 300 ^oC. Increasing calcination temperature to 500 ^oC results in well-defined Raman bands similar to those in Fig. 5.11 and 5.12 assigned to different vibration modes in crystalline MoO_3.

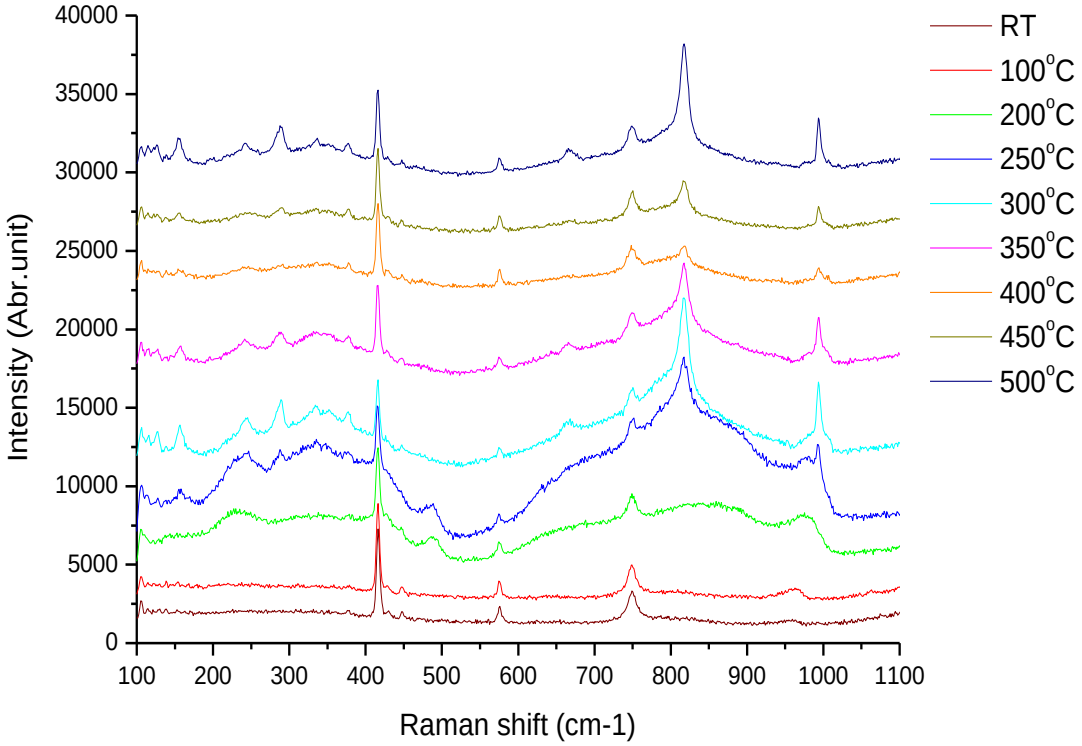

Fig. 5. 14 ***Raman spectra of MoO_3 evolution on α-Al_2O_3 (0001) crystal prepared using solution containing AHM and citric acid in water/ethanol mixture (100 ML MoO_3)***

The Raman spectra for 100 ML coverage of MoO_3 film on Al_2O_3 crystal for citrate prepared precursor in Fig. 5. 14 revealed only single Raman band at 961 cm^{-1} for films at RT and 100 ^oC attributable to MoO_6 symmetric stretching vibration, whereas the bands at 750, 575, 447 and 416 cm^{-1} assigned to α-Al_2O_3 crystal. The Raman band at 961 cm^{-1} shifted to 986 cm^{-1} with corresponding bands at 842, 489 and 241 cm^{-1} assigned to symmetric stretching of dioxo $(O=)_2MoO_2$ species, Mo-O-Al stretching , MoO_4 bending, and Mo-O-Mo deformation mode respectively at 200 ^oC. This result is consistent with 0.05 monolayer MoO_3 coverage for dehydrated MoOx species on

Al_2O_3 reported by Tian, Robert and Wachs [31]. At 300 ^oC, formation of crystalline MoO_3 species is evidenced by Raman bands at 993, 818, 666, are attributable to υ_{as} Mo=O, υ_s O-Mo-O, and υ_{as} O-Mo-O respectively, while lower bands at 377-335, 241, 196, 154, and 127 cm^{-1} are associated with scissoring, δ O=Mo=O wagging, twisting vibration, and translational rigid MoO_4 mode respectively. The Raman bands at 750, 575, 447 and 416 cm^{-1} are associated with Al_2O_3 crystal. However, the spectra at 500 ^oC reveal small shoulder band at 975 cm^{-1} assigned to asymmetric stretching of dioxo species $(O=)_2MoO_2$, which is in agreement with Raman band for asymmetric stretching of $(O=)_2MoO_2$ reported by Tian, Robert and Wachs [31].This indicates the presence of tetrahedral coordinated MoOx species at 100 monolayer coverage of MoO_3 film on Al_2O_3 crystal.

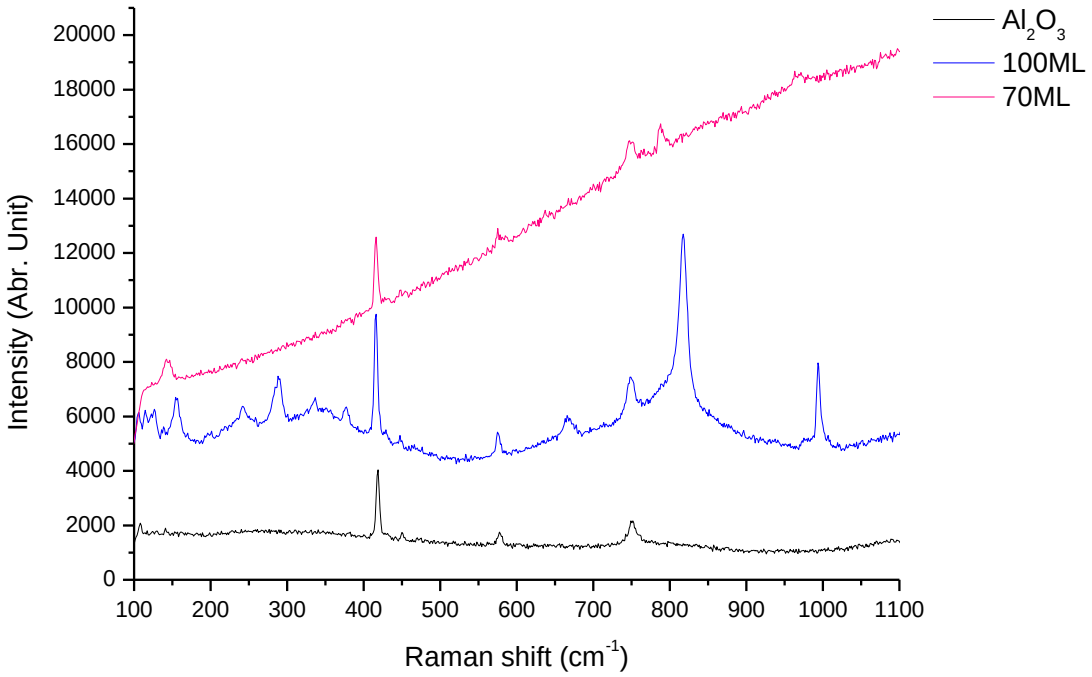

Fig. 5. 15 ***Comparison of Raman spectra of MoO_3 thin film on Al_2O_3 (0001) prepared using solution containing AHM and citric acid in water/ethanol mixture calcined at 500 ^oC***

The spectra of MoO_3 thin films calcined at 500 ^oC in air oven in Fig. 5. 15 depict Raman bands at 993, 818, 666 and a weak shoulder at 975 cm^{-1} attributable to υ_{as} Mo=O, υ_s O-Mo-O, and υ_{as} O-Mo-O and $(O=)_2MoO_2$ asymmetric stretching respectively. In addition, the lower bands at 377-335, 241, 196, 154, and 127 cm^{-1} are associated with scissoring, δ O=Mo=O wagging, twisting vibration, and translational

rigid MoO_4 modes respectively for 100 monolayer MoO_3 on Al_2O_3 crystal. The 70 monolayer coverage revealed bands at 967 and 789 cm^{-1} assigned to $(O=)_2MoO_2$ asymmetric stretching and Mo-O-Mo symmetric stretching respectively, which confirms the existence of both isolated dioxo and polymeric tetrahedral coordinated MoO_4^{2-} species at lower monolayer coverage. These findings concur with MoOx species at lower coverage on Al_2O_3 support reported by Vuurman and Wach [28], and Tian, Robert and Wachs [31]. However, bands at 750, 575, 447 and 416 cm^{-1} are associated with Al_2O_3 single crystal.

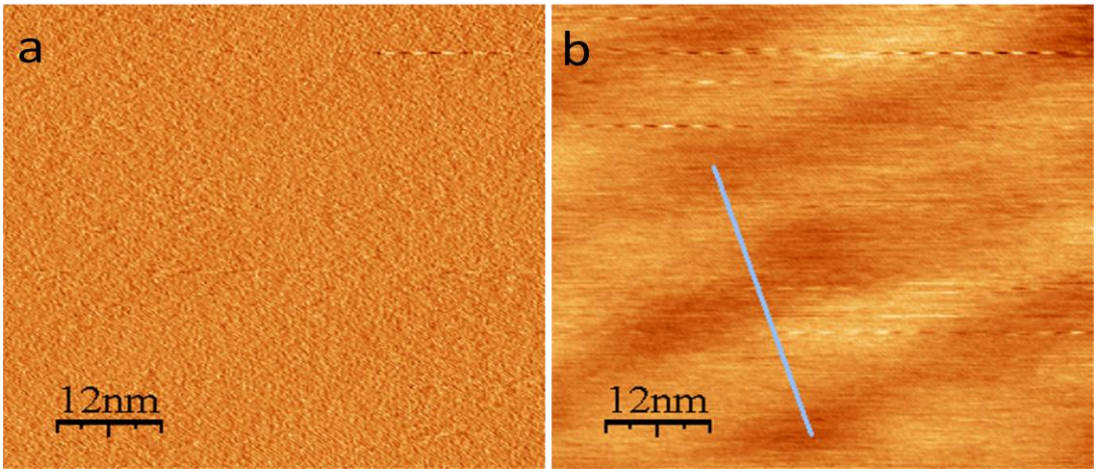

Fig. 5. 16 ***AFM image of cleaned Al_2O_3 (0001) 5 mm^2 single crystal. Right (Topographic image), left (Phase image), scale (600 x 720 nm)***

.

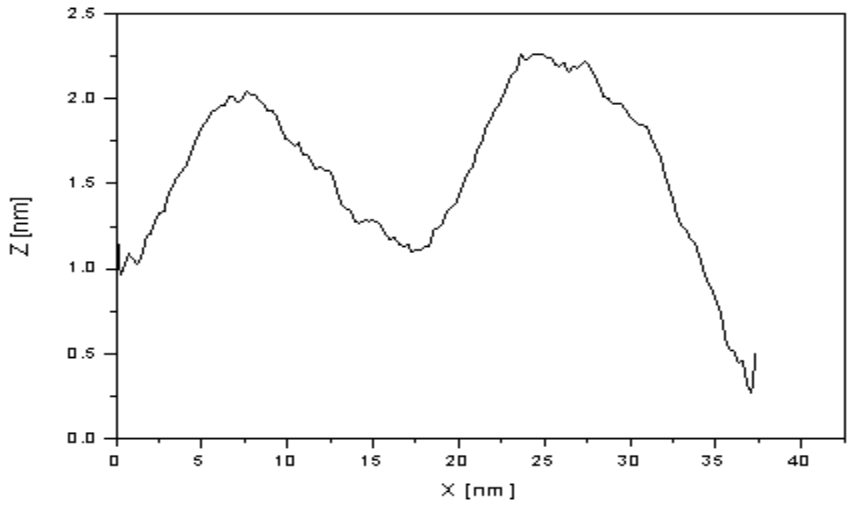

Fig. 5. 17 ***The AFM depth profile image of Al_2O_3 (0001) crystal analysed in ambient conditions***

The AFM images in Fig. 5. 16 a and b depict the cleaned Al_2O_3 (0001) single crystal, while depth profiling of the surface in Fig. 5. 17 revealed it to be very smooth with height variation of < 2nm, in close agreement with that reported by Gan and Franks [33] for AFM analysis of an Al_2O_3 (0001) crystal surface in water.

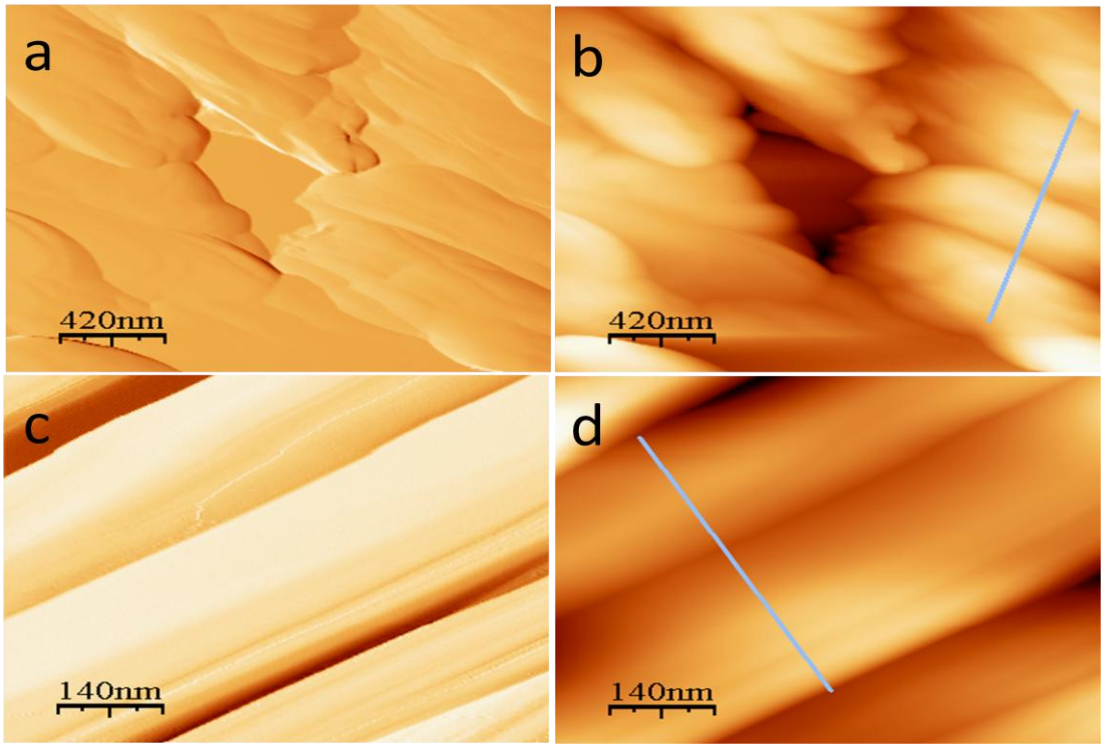

Fig. 5. 18 ***AFM images of 100 ML MoO_3 thin film on α-Al_2O_3 (0001) 5 mm^2 crystal calcined at 500 ^oC analysed in ambient conditions. Right (Topographic image), left (Phase image). Scale top (1680 x 2520 nm), bottom (560 x 840 nm).***

The MoO_3 thin film on α-Al_2O_3 (0001) crystal in Fig. 5. 18 a to d, reveals stacks of MoO_3 nano rods with flat terraces and edges of varying length that form layers. This finding is consistent with previous AFM images of MoO_3 crystals and thin films reported by Smith and Rohrer [10] and Illyaskutty et al [30] respectively.

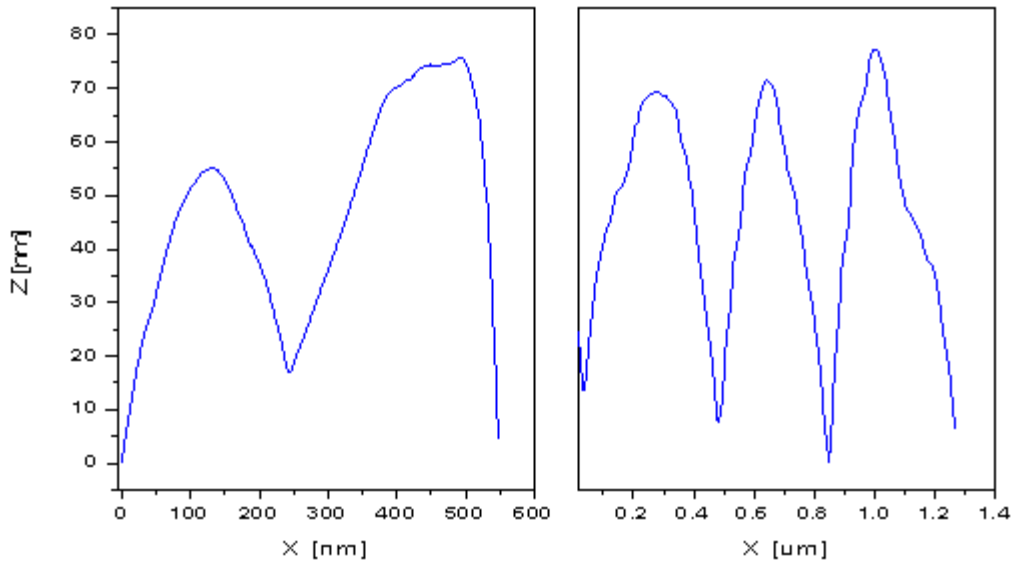

Fig. 5. 19 ***AFM depth profile image of 100 ML MoO_3 thin film on α-Al_2O_3 (0001) crystal shown in fig 5.19 d (left) and b (right).***

The depth profile images of MoO_3 thin film on α-Al_2O_3 single crystal in Fig. 5. 19, shows the surface to be much rougher than the clean surface. They consist of rod-like crystallites with height of ~ 70 nm, which is in concordance with values reported by Xie et al [17] and Illyaskutty et al [30], for MoO_3 thin film grown on silicon substrate and alumina (0001) single crystals respectively.

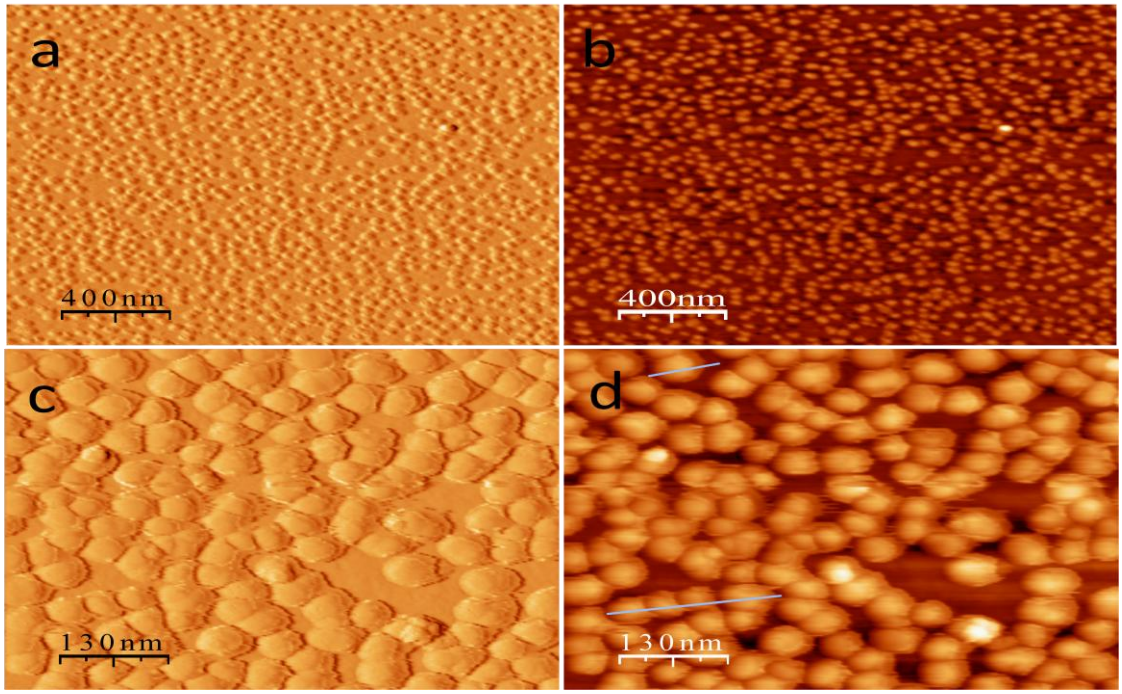

Fig. 5. 20 ***The AFM image of 70 ML MoO_3 thin film on Al_2O_3 (0001) crystal analysed in ambient condition. Right (Topographic image), left (Phase image), scale top (1600 x 2400 nm), bottom (520 x 780 nm)***

The AFM images of 70ML MoO_3 film on Al_2O_3 crystal as shown in Fig. 5. 20 a-b top image reveal 400 nm magnification, while Fig. 5. 20 c-d indicates 130 nm magnification. The Fig. 5. 20 a-d depicts well dispersed MoO_3 roundish nanoparticles of fairly uniform sizes of ~ 40 nm analogous to those observed by Magg et al [8] for V_2O_5 film grown on Al_2O_3 (0001) single crystal.

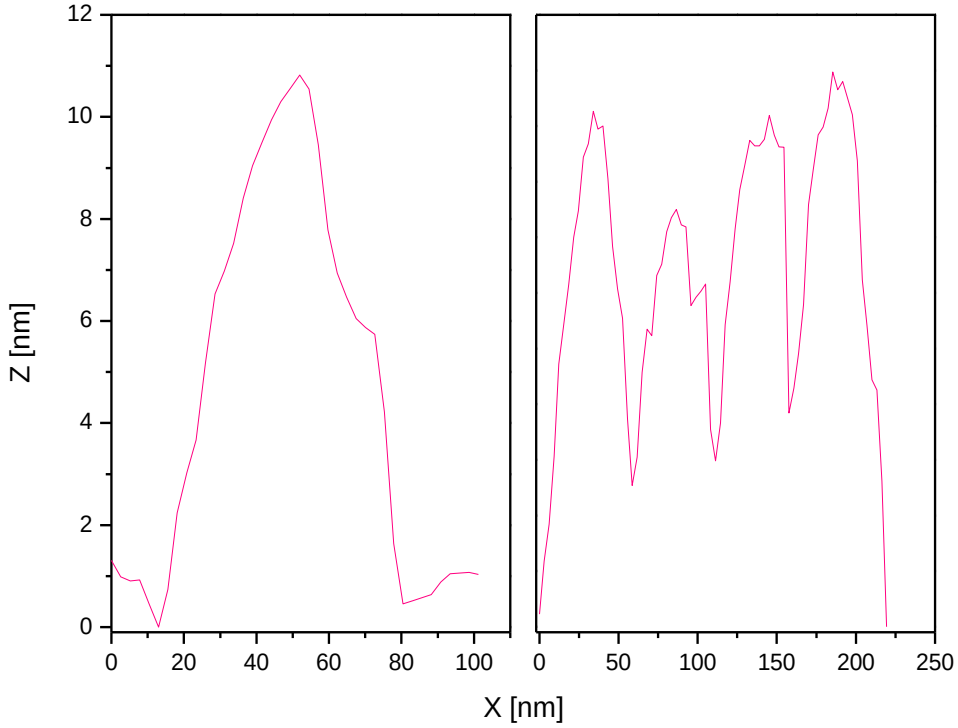

Fig. 5. 21 ***AFM depth profile image of 70 ML MoO_3 thin film on Al_2O_3 (0001) crystal analysed in ambient condition from image 5.20 d***

The profile image of the 70 ML coverage of MoO_3 thin film in **Fig. 5. 21** depicts formation of roundish polyhedron crystals uniformly dispersed on the Al_2O_3 crystal, with individual crystal sizes within 40 – 60 nm, in conformity with thickness of MoO_3 thin film particles fabricated using plasma-enhanced chemical vapour deposition technique as reported by Wolden et al [18]. However, the particles do not show any pattern of arrangement.

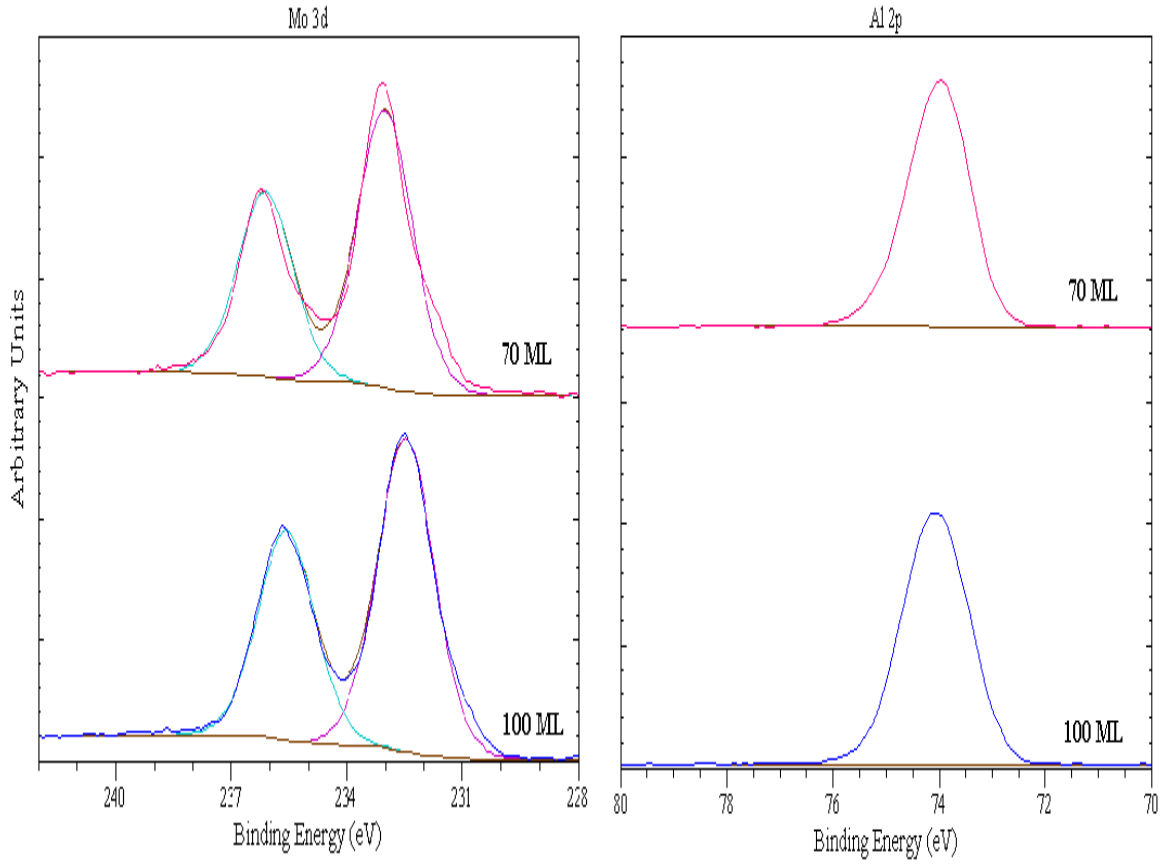

Fig. 5. 22 ***Comparison of XPS spectra of MoO_3 thin film on Al_2O_3 crystals***

The XPS spectra in Fig. 5. 22 depict Mo 3d binding energies of 232.5 ± 0.2 and 235.8 ± 0.2 eV assigned to Mo $3d_{5/2}$ and $3d_{3/2}$ respectively for both 100 and 70 monolayer MoO_3 thin film on Al_2O_3, and binding energies of 74.5 ± 0.2 eV attributed to Al 2p. The XPS data revealed Mo and Al in their highest oxidation state of +6 and +3 respectively, which is in good concordance with value reported by Spevack and Mcintyre [12] for MoO_3 thin film on Al_2O_3. The broadening of Mo $3d_{5/2}$ spectra of 70 monolayer MoO_3 thin film, with a FWHM value of 1.8 in comparison to 1.5 of 100 monolayer MoO_3 coverage is indicative of the variation in thickness of the films.

$Fe_2(MoO_4)_3$/ Al_2O_3

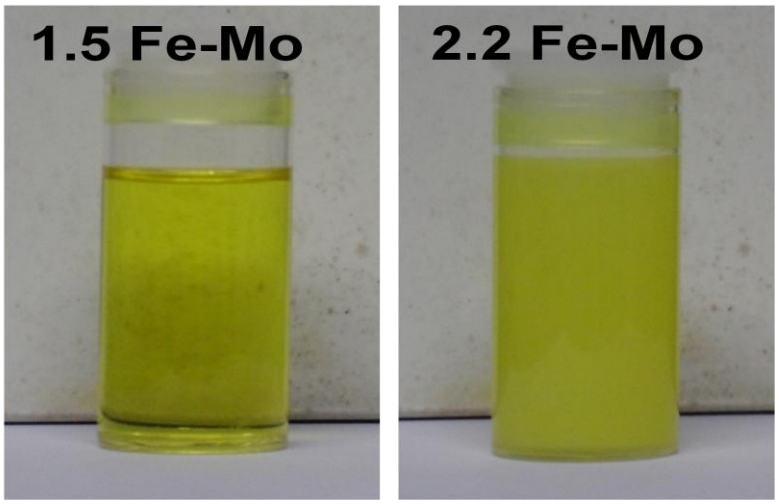

Fig. 5. 23 ***Image of iron molybdates precursor in water/ethanol mixture acidified using dilute HNO_3 acid***

The iron molybdates precursors indicate a canary yellow solution and cloudy sol for 1.5 and 2.2 Mo:Fe ratio respectively as shown in Fig. 5. 23, which is a typical colouration observed for iron molybdates precursor obtained via the co-precipitation method used for preparation of bulk catalysts as reported by Bowker's group [34, 35] and others [21, 36] . This precursor indicates that Fe and Mo species remain in same form as the co-precipitation precursor solution, with acidified water/ethanol mixture aiding dissolution, and formation of sol for 2.2 Mo ratio.

Fig. 5. 24 ***Images of 100 ML 1.5 $Fe_2(MoO_4)_3$ thin film on Al_2O_3 (0001) 5 mm^2 single crystal calcined at 500 ^oC (a) photographic image (b) microscopic image, scale (350 x 450 µ)***

The images in Fig. 5. 24 reveal good coverage of the Al_2O_3 crystal with crystalline granular structure in Fig 5.24 a with particles size of ≤ 10μm as depicted in Fig. 5.24 b for 1.5 Fe : Mo ratio.

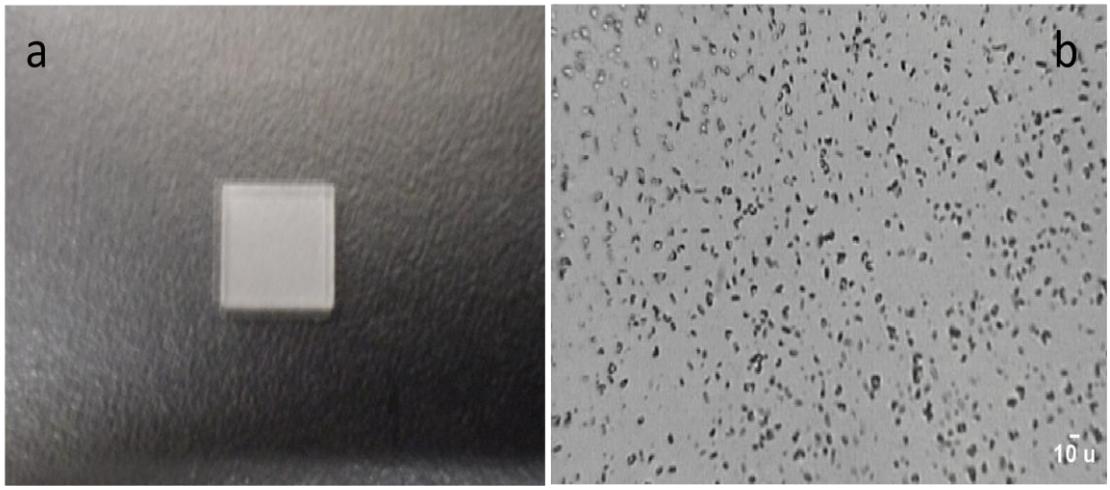

Fig. 5. ***25 Images of 100ML 2.2 $Fe_2(MoO_4)_3$ thin film on Al_2O_3 (0001) 5 mm^2 single crystal calcined at 500 ^oC (a) photographic image (b) microscopic image, scale (350 x 450 μ).***

The image in Fig. 5. *25* a depicts good coverage of Al_2O_3 crystal by 100 monolayer of 2.2 Fe_2 $(MoO_4)_3$ thin film, consisting of granular particles of sizes ≤ 10μ that are sparsely distributed as revealed in the microscopic image in Fig. 5. 25 b.

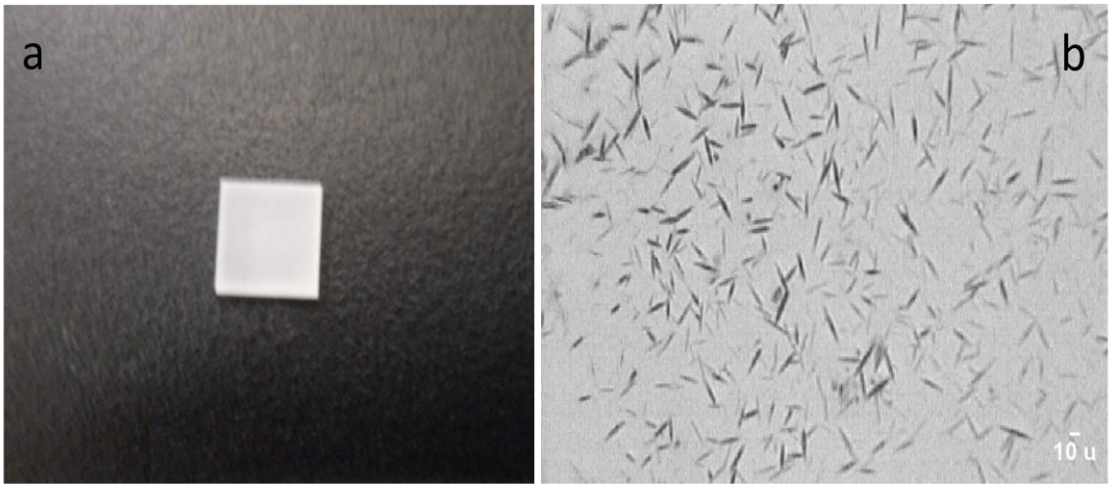

Fig. 5. 26 ***Images of 25 ML 2.2 $Fe_2(MoO_4)_3$ thin film on Al_2O_3 (0001) 5 mm^2 single crystal calcined at 500 ^oC (a) photographic image (b) microscopic image , scale (350 x 450 μ).***

Fig. 5. 26 a depicts lesser coverage of the Al_2O_3 crystal by 25 monolayer of 2.2 $Fe_2(MoO_4)_3$ thin film, which forms a needle-like structure of approximately 10µm width at varying length distributed on the entire surface as depicted in Fig. 5. 26 b.

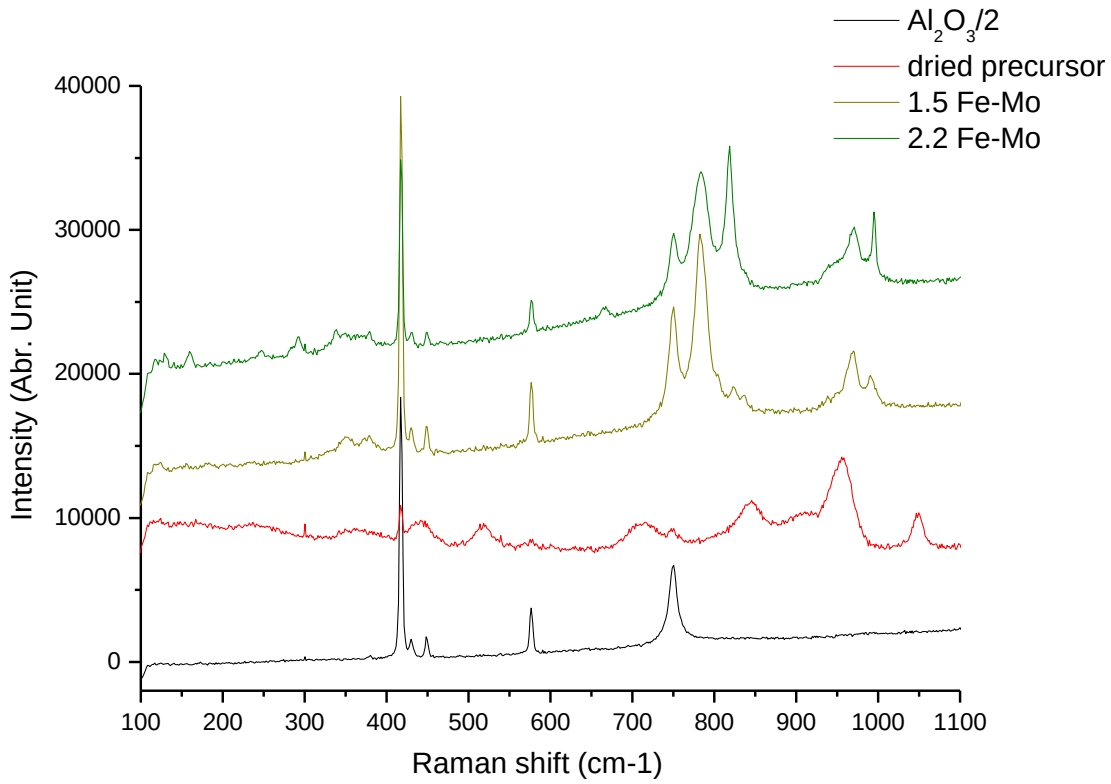

Fig. 5. 27 ***Comparison of Raman spectra of 100 ML coverage $Fe_2(MoO_4)_3$ thin film calcined at 500 ^oC and precursor on Al_2O_3 (0001) single crystal (model catalysts)***

The 1.5 and 2.2 Fe-Mo spectra in Fig. 5. 27 reveal a Raman band at 958, shoulder at 919 cm^{-1}, amidst other bands at 846, 710, 518, 436, with broadening of bands at 360 and 237 cm^{-1} attributed to iron molybdates precursors dried at ambient condition (room temperature). These bands are similar to those reported by Hill and Wilson [37, 38] for molybdates precursor on unsupported and supported bulk catalysts prepared by co precipitation method, while the band at 1049 cm^{-1} is assigned to NO_3^- species, which is completely absent after calcination at 500 ^oC. The 1.5 Fe:Mo ratio thin film reveals Raman bands at 991, 970, 940 (weak shoulder), 784 and 823 cm^{-1} attributable to υ_s Mo=O terminal stretching, υ_s distorted Mo=O terminal stretching in MoO_4, υ_s Mo=O terminal stretching, υ_{as} O–Mo–O stretching and υ_{as} O–Mo–O stretching in

MoO_4 of $Fe_2(MoO_3)_4$ respectively. The bands at 351 and 379 cm^{-1} are assigned to terminal Mo=O bending vibration in MoO_4 and O–Mo–O scissoring vibrations respectively. This is in conformity with Raman bands reported for stoichiometric bulk iron molybdates reported by House et al [34] and Soares et al [39]. However, the 2.2 Fe : Mo ratio thin film depicts increasing intensity and sharpness of Raman bands at 995, 819 and 666 cm^{-1} associated with υ_s Mo=O terminal, υ_s O–Mo–O and υ_{as} O–Mo–O stretching of excess MoO_3 respectively. In addition, the film reveals Raman bands at 379-349, 338, 292, 247, and 160-129 cm^{-1} assigned to O–Mo–O scissoring, δ O-Mo-O bending, δ O=Mo=O wagging, τ O=Mo=O twisting, and translational rigid MoO_4 chain mode respectively due to excess MoO_3 phase. These are in agreement with bands for Mo excess (>1.5) in bulk iron molybdates as reported by Hills and Wilson [37] and Routray et al [40]. The bands at 750, 577, 488, 430, 417 and 380 cm^{-1} are attributed to the Al_2O_3 (0001) single crystal.

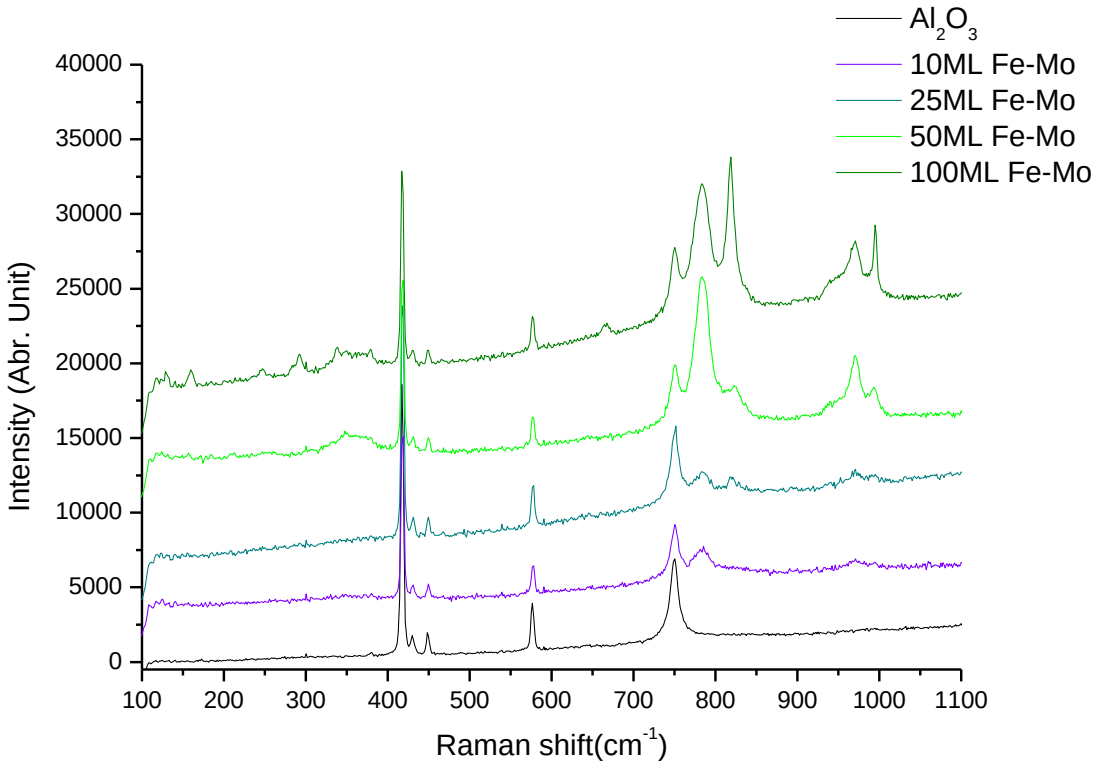

Fig. 5. 28 ***Comparison of Raman spectra of varying monolayer coverage of $Fe_2(MoO_4)_3$ thin film on α-Al_2O_3(0001) single crystal***

The Raman spectra of varying monolayer coverage of iron molybdates thin film on α-Al_2O_3 in Fig. 5. 28 reveal decreasing intensity of the band at 995, 819 and 666 cm^{-1}

assigned to υ_s Mo=O terminal, υ_s O–Mo–O and υ_{as} O–Mo–O stretching of excess MoO_3 respectively. In addition to lower bands at 379-349, 338, 292, 247, and 160-129 cm^{-1} attributable to O–Mo–O scissoring, δ O-Mo-O bending, δ O=Mo=O wagging, τ O=Mo=O twisting, and translational rigid MoO_4 chain mode for 50 and 25 monolayer $Fe_2(MoO_4)_3$ thin film. While the 10 monolayer film depicts bands at 970 and 784 cm^{-1} attributed to υ_s Mo=O terminal and υ_{as} O–Mo–O stretching in $Fe_2(MoO_4)_3$. This indicates that the excess MoO_3 phase dissolves into the water/ethanol solution during dilution to form lower monolayer coverage (10 ML).

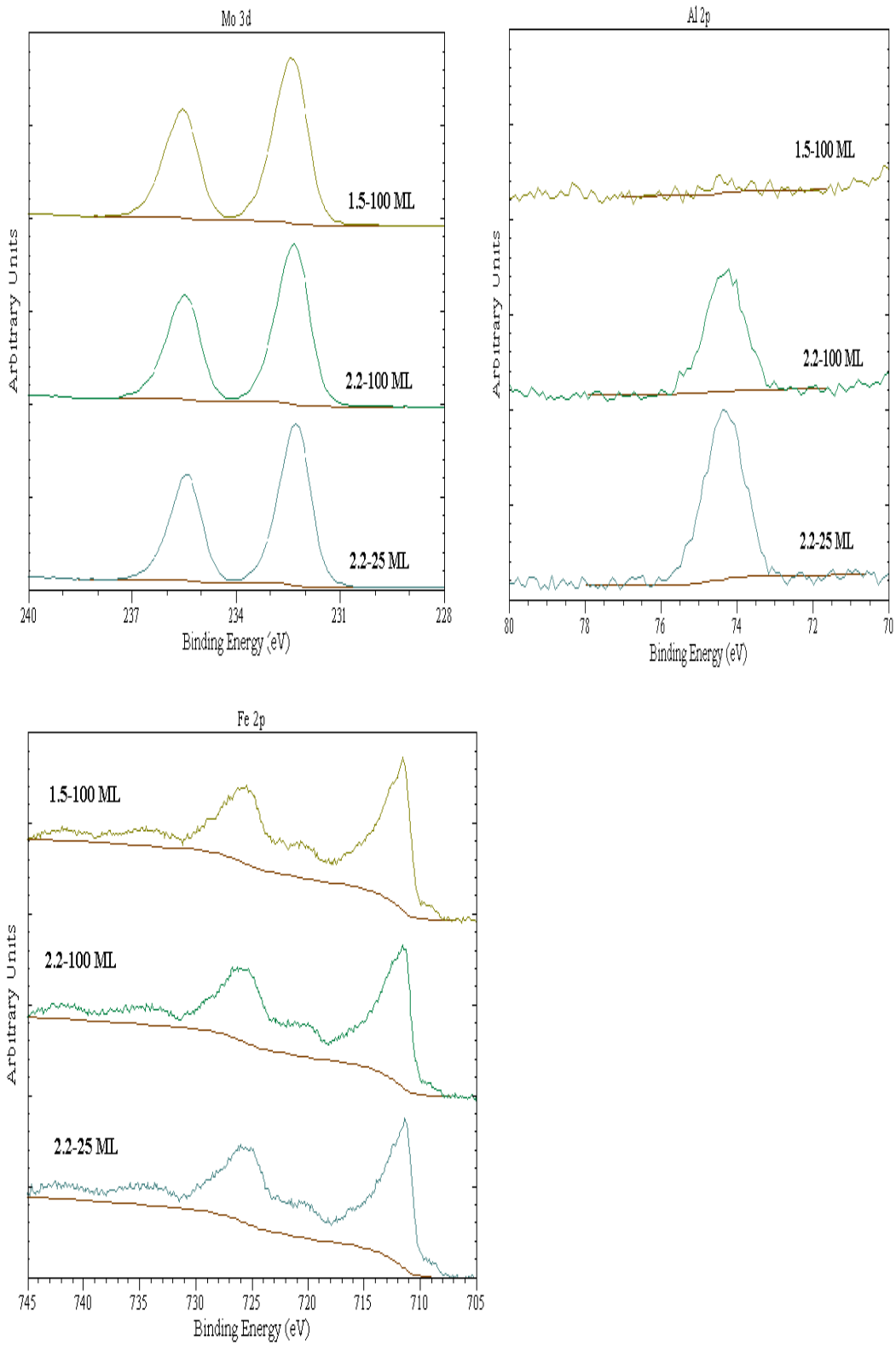

Fig. 5. 29 ***XPS spectra and binding energies for $Fe_2(MoO_4)_3$ film on Al_2O_3 (0001) crystals***

The XPS spectra in Fig. 5. 29 indicate binding energies of 232.4 ± 0.1 and 235.5± 0.1eV for Mo $3d_{3/2}$ and $3d_{5/2}$ respectively for all samples, with binding energies of 74.4 and 711.5 ± 0.1eV assigned to Al 2p and Fe 2p respectively. However the intensity of Al 2p spectra for 1.5 $Fe_2(MoO_4)_3$ film (100 monolayer coverage) was less visible in comparison to 2.2 $Fe_2(MoO_4)_3$ film on Al_2O_3 single crystal.

The data indicates that both iron and molybdenum are in their highest oxidation state of Fe^{3+} and Mo^{6+} irrespective of the Mo: Fe ratio and the thickness of the film. The lesser intensity of the Al 2p spectra in the 1.5 ratio film reveal good coverage of the Al_2O_3 crystal as well as thickness of the $Fe_2(MoO_4)_3$ film. In addition, the 2.2 ratio of 100 monolayer coverage $Fe_2(MoO_4)_3$ film indicate low intensity of Al 2p spectra when compared to 25 monolayer coverage film. This could indicate less thickness as well as distribution of $Fe_2(MoO_4)_3$ film on the crystal support, although this wet deposition technique could not produce a similar film thickness due to variation in concentration of precursor deposited on the crystal.

However, the spectra and binding energies of Mo and Fe in $Fe_2(MoO_4)_3$ films synthesized are similar to those observed on Mo deposited on Fe_2O_3 (111) single crystal and bulk iron molybdates catalyst as reported by Bamroongwongdee et al [3], Soares et al [41] and Huang et al [42].

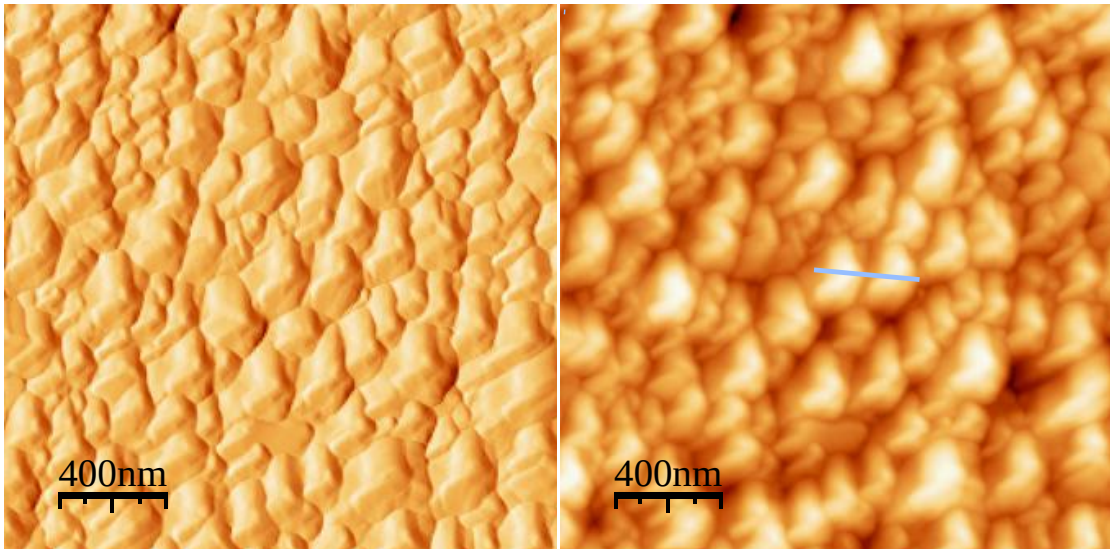

Fig. 5. 30 ***AFM image of 2.2 $Fe_2(MoO_4)_3$ thin film (100 monolayer) on Al_2O_3 (0001) single crystal. Right (Topographic image) and Left (Phase image), scale (2400 x 2400 nm)***

AFM analysis of the 100 ML $Fe_2(MoO_4)_3$ thin film on α-Al_2O_3 crystal in Fig. 5. 30 reveals the surface of α-Al_2O_3 (0001) single crystal to be densely covered with $Fe_2(MoO_4)_3$ nanoparticles, consisting of a mixture of both tetragonal and hexagonal structure truncated on edges. This is analogous to octahedral and tetrahedral structure attributed to Fe and Mo respectively in thin film $Fe_2(MoO_4)_3$ model reported by Uhlrich et al [23]. The surface of the 2.2 $Fe_2(MoO_4)_3$ thin film is dominated by the tetragonal structure.

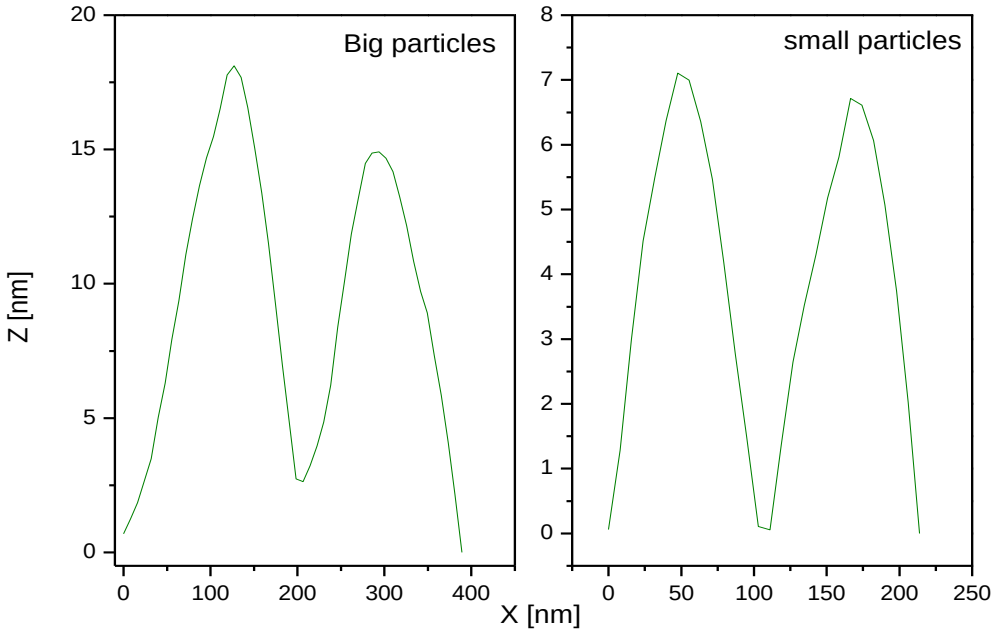

Fig. 5. 31 ***AFM particle size of 2.2 $Fe_2(MoO_4)_3$ thin film on Al_2O_3 (0001) crystals***

AFM depth profiling revealed in Fig. 5. 31 shows the iron molybdates film to consist of particles of different sizes with diameters of ~ 100-150 nm.

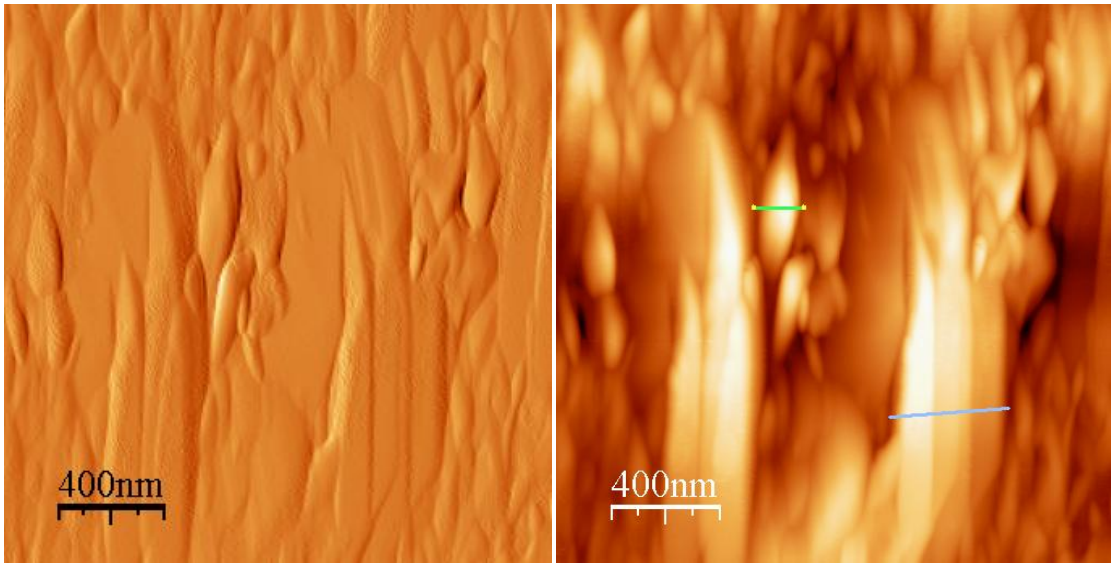

Fig. 5. 32 ***AFM image of $Fe_2(MoO_4)_3$ thin film (25 monolayer) on Al_2O_3 (0001) 5 mm^2 single crystal calcined at 500 ^oC. Right (Topographic image) and Left (Phase image), scale (2400 x 2400 nm).***

The AFM image of 25ML $Fe_2(MoO_4)_3$ thin film on α- Al_2O_3 (0001) in Fig. 5. 32 depicts formation of needle-like structures of varying length sizes.

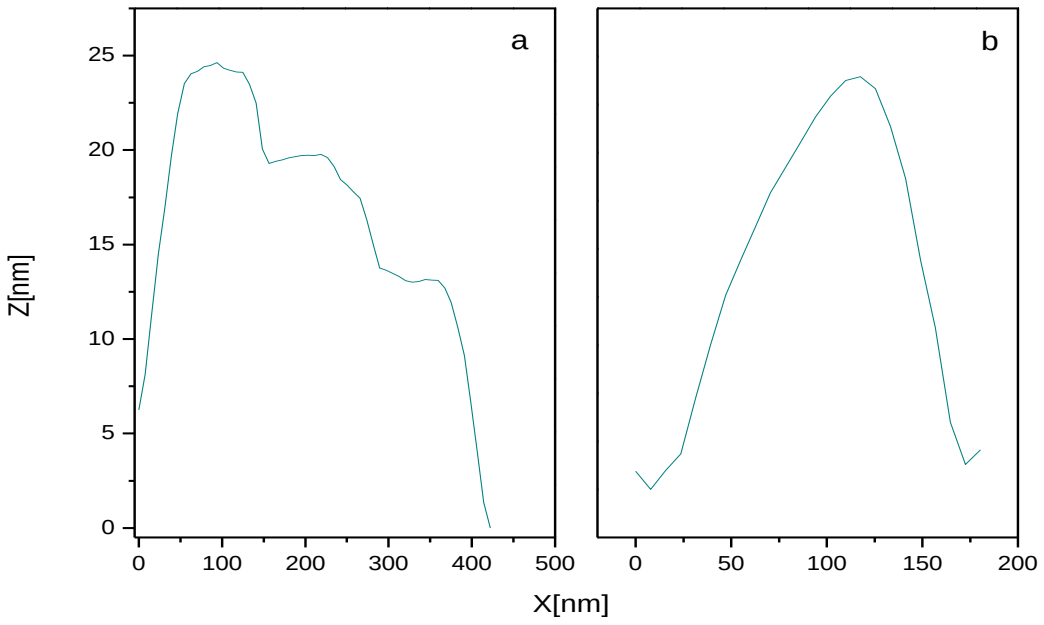

Fig. 5. 33 ***AFM particle size of 2.2 $Fe_2(MoO_4)_3$ thin film on Al_2O_3 (0001) 5 mm^2 crystals***

The depth profiling of the 25 ML $Fe_2(MoO_4)_3$ thin film indicates existence of a crystalline phase consisting of particles of diameter (in the short direction) of ~ 100 nm. These particles exist individually or overlap each other to form steps as shown in Fig. 5. 33 a.

5.3 Summary

Fabrication of model catalysts based on MoO_3 and $Fe_2(MoO_4)_3$ film on Al_2O_3 (0001) single crystal was successfully produced using novel wet chemical deposition techniques. The findings of this study revealed excellent dissolution of ammonium heptamolybdates (AHM) salt in water, but poor wetting property of the precursor on polished Al_2O_3 (0001) single crystal due to low vapour pressure and surface tension effect.

Acidified solutions of AHM in water/ethanol mixture (5/95 % v/v ratio) indicate excellent dissolution and wetting properties for synthesis of MoO_3 and $Fe_2(MoO_4)_3$ films on Al_2O_3 (0001) single crystal.

Photographic and microscopic images of 700 – 70 ML of MoO_3 film on Al_2O_3 crystal depicted good coverage of crystalline MoO_3 islands and nano particles on α – Al_2O_3 single crystal (0001).

Raman study of 700 ML MoO_3 film on Al_2O_3 single crystal revealed an intense and sharp Raman band at 934 cm^{-1} relative to 883 and 863 cm^{-1} assigned to heptahedral vertex – corner sharing of MoO_6 in Mo_7O_{24} cluster in crystalline AHM, for dried precursor at room temperature (RT) – 100 ^oC using water as solvent. The thick MoO_3 film (700 ML) prepared using HNO_3 acidified AHM precursor in mixture of water and ethanol revealed the presence of a broad Raman band at 950 cm^{-1} attributable to $[Mo_7O_{24}]^{6-}$ polymeric species between RT – 100 ^oC, whereas at lower coverage (350ML) evidenced the presence of $[MoO_4]^{2-}$ species with bands at 975 and 847 cm^{-1}. The citric acidified AHM in water and ethanol precursor gave a band at 961 cm^{-1} assigned to MoO_6 species for 100ML film dried at RT – 100 ^oC.

Raman spectra of calcined HNO_3 acidified AHM precursor film on Al_2O_3 crystal indicates complete removal of the NO_3^- band at 200 ^oC, as well as onset of transformation of polymeric MoOx species for all films on the Al_2O_3 crystal heated in air. Formation of crystalline MoO_3 films on the Al_2O_3 single crystal was seen at

300 ^oC with Raman bands at 993, 818, 666, 377-335, 241, 196, 154 and 127 cm^{-1}, which increase in intensity up to 500 ^oC.

At lower coverage (70 ML), MoO_3 films prepared using citric acid calcined at 500 ^oC revealed bands at 967 and 789 cm^{-1} assigned to $(O=)_2MoO_2$) indicating the presence of both dioxo and polymeric tetrahedral $[MoO_4]^{2-}$ species.

An XPS study of citrate prepared MoO_3 film on Al_2O_3 single crystal (100 and 70 ML), revealed Mo 3d and Al 2p in their highest oxidation state of +6 and +3 respectively. The decrease in FWHM (1.8 for 70 ML and 1.5 for 100 ML) of the Mo 3d spectra indicates variation in thickness of the MoO_3 film.

The stoichiometric $Fe_2(MoO_4)_3$ precursor revealed a canary yellow clear solution typical of that obtained for co-precipitation catalysts with formation of sol for 2.2 Mo ratio.

Photographic and microscopic images of 1.5 $Fe_2(MoO_4)_3$ film depict a dense crystalline $Fe_2(MoO_4)_3$ structure covering the entire crystal surface, whereas the 2.2 ratio revealed formation of a granular and needle –like crystalline $Fe_2(MoO_4)_3$ structure for 100 and 25 monolayer coverage respectively.

Raman bands revealed were similar to those reported by Hill and Wilson [37, 38] for $Fe_2(MoO_4)_3$ and dried precursor. The stoichiometric ratio $Fe_2(MoO_4)_3$ film revealed bands at 790, 823, 940 and 984 cm^{-1} attributable to crystalline $Fe_2(MoO_4)_3$ phase, with excess crystalline MoO_3 phase discerned due to increase in 819 and 996 cm^{-1} bands intensity and appearance of lower bands at 379, 338, 292 and 160 cm^{-1} in 2.2 $Fe_2(MoO_4)_3$ film calcined at 500^oC. Comparison of Raman spectra reveals decreasing intensity of 819 and 996 cm^{-1} bands associated with an excess crystalline MoO_3 phase, with decreasing monolayer coverage.

XPS revealed high oxidation state of +3, +6 and +3 for Fe, Mo and Al for $Fe_2(MoO_4)_3$ film on Al_2O_3 crystals, with decrease in the Al 2p spectra intensity due to increasing film thickness as observed for stoichiometric $Fe_2(MoO_4)_3$ film.

The 100 monolayer coverage $Fe_2(MoO_4)_3$ film revealed formation of tetragonal and hexagonal structure truncated on the edges and corners linked via vertex sharing. The particles have thicknesses between 100 – 200nm as indicated by AFM analysis. However, 25 monolayer $Fe_2(MoO_4)_3$ film has needle-like structures of varying length, with thicknesses between 120 – 170nm.

5.4 Conclusion

The main purpose of this study is to fabricate and characterize MoO_3 and $Fe_2(MoO_4)_3$ thin films on α-Al_2O_3 (0001) single crystal as a model catalyst system for investigation of selective oxidation of methanol to formaldehyde, exploring the novel wet chemical deposition method using solution and sol-gel of polymolybdate and iron precursors.

This study revealed successful synthesis of both MoO_3 and $Fe_2(MoO_4)_3$ thin film for the first time on Al_2O_3 (0001) crystal, with the MoO_3 film revealing inhomogeneous crystalline MoO_3 of islands at high coverage. The sizes and shapes of these films are controlled by solvent type, acid used, concentration of precursors, as well as film thickness.

Raman spectroscopic studies indicate formation of crystalline polymeric MoO_3 species at high coverage, whereas both dioxo $(O=)_2$ MoO_2 and polymeric MoO_3 species were discerned at low coverage, which occurs at 300 ^oC.

However, the films have varying particle sizes, with the large particles consisting of crystalline island of thickness between 2 – 10 μ, and small particles at low coverage indicates a thickness between 60 – 250 nm as revealed by AFM study.

XPS analysis of the films indicates high oxidation state of +6 and +3 for Mo 3d and Al 2p respectively for film calcined at 500 ^oC.

$Fe_2(MoO_4)_3$ film on Al_2O_3 (0001) crystal reveals increase in Raman band intensity of 819 and 996 cm^{-1} with increasing Mo ratio (from 1.5 – 2.2), but decreases with decreasing monolayer coverage for 2.2 Mo ratio calcined at 500 ^oC. XPS analysis of the film indicates high oxidation state of +3, +6 and +3 for Fe, Mo and Al respectively. Microscopic images of 2.2 Mo ratio film revealed formation of granular and needle-like structures for 100 and 25 monolayers coverage respectively. However, AFM study of the film indicates existence of tetragonal and hexagonal truncated structure of diameter between 100 – 200nm, whereas 25 monolayer revealed needle – like structure of varying length with thickness in the range between 120 – 170nm.

Novel wet chemical methodology is cost effective for the fabrication of thin film on Al_2O_3 (0001) single crystal, although film thickness cannot be uniformly produced using this technique. This study is limited to fabrication and characterization of the thin films intended for used as model catalysts for investigation of active sites and measurement of selective oxidation reaction of methanol to formaldehyde.

References

1. Poppa H. Nucleation, growth, and TEM analysis of metal particles and clusters deposited in UHV. Catal Rev Sci Eng. 1993;35:359 - 98.

2. Freund H-J. Model studies on heterogeneous catalysts at the atomic level. Catal Today. 2005;100:3-9.

3. Bamroongwongdee C, Bowker M , Carley A F, Davies P R, Davies R J, Edwards D. Fabrication of complex model oxide catalysts: Mo oxide supported on Fe_3O_4(111). Faraday Discussion. 2012;162:12-7.

4. Freund H-J, Ernst N, Risse T, Hamann H, Rupprechte G. Models in heterogeneous catalysis: Surface science quo vadis? Phys Stat Sol (a) ,. 2001;187(1):257–74.

5. Hoffmann J, Meusel I, Hartmann J, Libuda J, Freund H-J. Reaction kinetics on heterogeneous model catalysts : The CO oxidation on alumina-supported Pd particles. J Catal 2001;204:378–92

6. Freund H-J. Models for oxidation catalyst: Characterization and reaction at the atomic level. Catal Today. 2006;117:6-14.

7. Freund H-J. Model systems in heterogeneous catalysis: Selectivity studies at the atomic level. Top Catal. 2008;48:137-44.

8. Magg N, Giorgi J B, Schroeder T, Baumer M, Freund H -J . Model catalyst studies on vanadia particles deposited onto a thin-film alumina support. 1. structural characterization. J Phys Chem B 2002;106:8756-61.

9. Romanyshyn Y, Guimond S, Kuhlenbeck H, Kaya S, Blum R P, Niehus H, et al. Selectivity in methanol oxidation as studied on model systems involving vanadium oxides. Top Catal. 2008;50:106–15.

10. Smith RL, Rohrer GS. An atomic force microscopy study of the morphological evolution of the MoO_3 (010) surface during reduction reaction. J Catal. 1996; 163:12 – 7.

11. Smith RL, Rohrer GS. The structure sensitivity of $HxMoO_3$ precipation on MoO_3 (010) during reaction with methanol. J Catal 1999;184(1): 49 – 58.

12. Spevack PA, McIntyre NSA. Raman and XPS investigation of supported molybdenum oxide thin films. 1. Calcination and reduction studies. J Phys Chem 1993;97:11020-1 1030.

13. Zou J, Schrader G L. Multicomponent thin film molybdate catalysts for the selective oxidation of 1,3-Butadiene. J Catal. 1996; 161 667–86.

14. Haro-Poniatowski E, Jouanne M, Morhange JF, Julien C, Diamant R, Ferna´ndez-Guasti M, et al. Micro-Raman characterization of WO_3 and MoO_3 thin films obtained by pulsed laser irradiation. Appl Surf Sci 1998;127–129 674–8.

15. Gu1nther S, Marsi M, Kolmakov A, Kiskinova M, Noeske M, Taglauer E, et al. Photoelectron spectromicroscopic study of the spreading behavior of MoO_3 on titania and alumina model supports. J Phys Chem B 1997;101:10004-11.

16. Hsu C-S, Chan C -C, Huang H -T, Peng C -H, Hsu W -C. Electrochromic properties of nanocrystalline MoO_3 thin films. Thin solid films 2008;516:4839–44.

17. Xie YL, Cheong FC, Zhu YW, Varghese B, Tamang R, Bettiol A A, et al. Rainbow-like MoO_3 nanobelts fashioned via AFM micromachining. J Phys Chem C 2010;114 120–4.

18. Wolden CA, Pickerell A, Gawai T, Parks S, Hensley J, Way JD. Synthesis of β-Mo_2C thin films. ACS Appl Mater Interfaces 2011;3:517–21.

19. Gan Y, Franks G V. High resolution AFM images of the single-crystal α-Al_2O_3(0001) surface in water. J Phys Chem B 2005;205(109):12474-9.

20. Bowker M, Holroyd R, Elliott A, Morrall P, Alouche A, Entwistle E, et al. The selective oxidation of methanol to formaldehyde on iron molybdate catalysts and one component oxides. Catalysis letters 2002; 83(3-4):165-76.

21. Soares APV, Farinha Portela M, Kiennemann A, Hilaire L, Millet J M M. Iron molybdate catalysts for methanol to formaldehyde oxidation: effects of Mo excess on catalytic behaviour. Appl Catal A: Gen 2001;206: 221–9.

22. Routray K, Zhou W, Kiely C J, Grünert W, Wachs IE. Origin of the synergistic interaction between MoO_3 and iron molybdate for the selective oxidation of methanol to formaldehyde. J Catal. 2010;275:84–98.

23. Uhlrich JJ, Sainio J, Lei Y, Edwards D, Davies R, Bowker M, et al. Preparation and characterization of iron–molybdate thin films. Surf Sci. 2011;605 1550–5.

24. Fang L, Shu Y, Wang A , Zhang T. Green synthesis and characterization of anisotropic uniform single-crystal alpha-MoO_3 nanostructures. J Phys Chem C. 2007;111:2401-8.

25. Porto SPS, Krishnan RS. Raman effect of corundum. J Chem Phys. 1967;47:1009 - 12.

26. Aminzadeh A, Sarikhani-Fard H Raman spectroscopic study of Ni/Al_2O_3 catalyst. Spectrochemica Acta Part A. 1999;55:1421 - 5

27. Wachs I, Roberts CA. Monitoring surface metal oxide catalytic active sites with Raman spectroscopy. Chem Soc Rev 2010;39:5002-17.

28. Vuurman MA, Wachs IE. In situ Raman spectroscopy of alumina-supported metal oxide catalysts. J Phys Chem 1992;96:5008-16.

29. Wachs IE. Raman IR studies of surface metal oxide species on oxide supports: Supported metal oxide catalysts. Catal Today. 1996;27:437-55.

30. Illyaskutty N, Sreedhar S, Sanal Kumar G, Kohler H, Schwotzer M, Natzeck C, et al. Alteration of architecture of MoO_3 nanostructures on arbitrary substrates: growth kinetics, spectroscopic and gas sensing properties. Nanoscale. 2014;6:13882 - 94. www.rsc.org/nanoscale.

31. Tian H, Roberts CA , Wachs, IE. Molecular structural determination of molybdena in different environments: Aqueous solutions, bulk mixed oxides, and supported MoO_3 catalysts. J Phys Chem C. 2010;114:14110–20.

32. Knozinger H, Jeziorowski H. Raman spectra of molybdenum oxide supported on the surface of aluminas. J Phys Chem. 1978;82:2002-5.

33. Gan Y, Franks G V. High resolution AFM Images of the single-crystal α-Al_2O_3(0001) surface in water. J Phys Chem B. 2005;109:12474-9.

34. House PM, Carley AF, Bowker M. Selective oxidation of methanol on iron molybdate catalysts and the effects of surface reduction. J Catal 2007;252:88–96.

35. Soderhjelm E, House MP, Cruise N, Holmberg J, Bowker M, Bovin J, et al. On the synergy effect in MoO_3–$Fe_2(MoO_4)_3$ catalysts for methanol oxidation to formaldehyde. Top Catal. 2008.

36. Beale AM, Jacques SDM, Sacaliuc-Parvalescu E, O'Brien M G, Barnes P, Weckhuysen BM. An iron molybdate catalyst for methanol to formaldehyde conversion prepared by a hydrothermal method and its characterization. Appl Catal A: Gen 2009;363:143–52.

37. Hill Jr CG, Wilson III JH. Raman spectroscopy of iron molybdate catalyst systems: Part I. Preparation of unsupported catalysts. Journal of Molecular Catalysis. 1990;63(1):65-94.

38. Hill Jr CG, Wilson III J H. Raman spectroscopy of iron molybdate catalyst systems: Part II. Preparation of supported catalysts. Journal of Molecular Catalysis. 1991;67(1):57-77.

39. Soares APV, Farinha Portela M. Methanol selective oxidation to formaldehyde over iron-molybdate catalysts. Catal Rev. 2004;47:125-74.

40. Routray K, Zhou W, Kiely CJ, Grünert W, Wachs IE. Origin of the synergistic interaction between MoO_3 and iron molybdate for the selective oxidation of methanol to formaldehyde. J Catal. 2010;275(1):84-98.

41. Soares APV, Portela MF, Kiennemann A, Hilaire L. Mechanism of deactivation of iron-molybdate catalysts prepared by coprecipitation andsol–gel techniques in methanol to formaldehyde oxidation. Chem Eng Sci 2003;58:1315-22.

42. Huang Y, Cong L, Yu J, Eloy P, Ruiz P. The surface evolution of a catalyst jointly influenced by thermal spreading and solid-state reaction: A case study with an Fe_2O_3–MoO_3 system. J Mol Catal A: Chemical. 2009;302:48–53.

Chapter 6 Overall Summary, Conclusion and Recommendations for Further Research Work

Contents

This chapter outlines summaries of various results chapters, ranging from unsupported and supported to a model catalyst system, and contains general conclusions from the thesis findings and highlights possible areas for future research work.

6.1 Overall Summary

High surface area forms of MoO_3 have been prepared, and these comprise of defective (Lewis acid) sites that enhance catalytic activity as well as selectivity for methanol oxidation to formaldehyde at lower temperatures. The commercial BDH MoO_3 is highly selective to formaldehyde, but less active due to low surface area and the presence of fully saturated Mo^{6+} coordinated to a nucleophilic oxygen (O^{2-}) species.

Doping of the prepared MoO_3 surface with K modifies its electronic properties by neutralization of Lewis acid sites, as well as controlling adsorption and diffusion of gas phase oxygen within the bulk. This effect enhances formaldehyde selectivity at higher temperatures and prevents further oxidation of formaldehyde to CO_2, with consequential effect on activity for 100 % K-MoO_3 sample.

The investigation of selective oxidation of methanol on iron molybdate ($Fe_2(MoO_3)_4$) catalysts has shown that amorphous MoOx on bulk $Fe_2(MoO_3)_4$ is the active phase as evident from reactor studies of stoichiometric (1.5) ratios. However, the excess crystalline MoO_3 phase in 2.2 Mo ratio serves as Mo reservoir for replenishment of lost Mo and in maintaining catalytic activity and formaldehyde selectivity, supporting our previous findings [1, 2] and those reported by Soares et al [3, 4] and Wachs et al [5, 6].

The study of nanodiamond as a support has shown that air oxidation (calcination in air) for 5 hours is effective for the purification and oxidation of nanodiamond surface between 390 -500 ^oC. However, complete burning of the support at high temperature (600 ^oC) could be the result of a catalytic effect of metal impurities encapsulated in its matrix. The support is very active for methanol oxidation, but with poor selectivity to formaldehyde, owing to high electron density and defect sites on its surface.

The MoO_3/ND catalysts reveal the existence of dioxo $(O=)_2MoO_2$ species alongside octahedral polymeric MoOx crystallites at lower Mo coverage (90 –100 % MoO_3 monolayer coverage), and octahedral coordinated crystalline MoO_3 phase at high Mo loading of 400 % coverage in high Mo oxidation state of +6. Reaction measurement of methanol oxidation on the supported catalysts shows good activity and selectivity to

formaldehyde, which increases with Mo loading due to an increase in density of catalytic active redox sites.

The 90 % monolayer coverage of MoO_3 on ND exhibits a synergistic effect, due to bond formation with MoOx that blocks active sites on ND (defects and edges). The donation of electrons from the graphitic shell of the support prevents reduction of Mo 6+ sites.

The supported MoO_3/ND exhibits structure sensitivity during methanol oxidation with formaldehyde and DME produced on redox and acidic sites respectively.

The research has shown that calcination of Boemite from room temperature to 900 ^oC, results in γ-Al_2O_3 formation, starting at 500 ^oC as revealed by XRD analysis. Transition of γ-Al_2O_3 begins at 800 ^oC, with formation of mixed phases consisting of both γ and δ-Al_2O_3 attained at 900 ^oC.

The γ-Al_2O_3 support is highly selective to DME, with its acid – base property increasing with increasing calcination temperature from room temperature to 700 ^oC. However, water seems to inhibit DME formation above 320 ^oC leading to CO.

The study indicates that acid sites on γ-Al_2O_3 are completely titrated by 2wt % Mo loading, with better dispersion of the active phase for the citrate-prepared catalysts. Raman spectroscopy and SEM revealed tetrahedral coordinated and crystalline MoOx species at 2wt % loading respectively, with crystalline polymeric MoO_3 phase observed at 10wt % Mo loading.

The catalysts show good selectivity to formaldehyde, which increases with Mo % wt loading for the aqueous preparation catalyst, whereas the activity of the citrate prepared catalyst decreases with increasing Mo wt % loading.

The study of model catalytic systems has shown that the wet chemical deposition method using acidified water/ethanol solvent is an effective medium for fabrication of MoO_3 and $Fe_2(MoO_4)_3$ thin films on an Al_2O_3 (0001) single crystal surface. The structure and thickness of both MoO_3, and $Fe_2(MoO_4)_3$ films are influenced by solvent type, acid used, concentration of the precursor, and monolayer coverage.

Thick MoO_3 films calcined at 500 ^oC revealed inhomogeneous islands of a crystalline MoO_3 phase at 700 – 100 ML coverage, and formation of MoO_3 nano-rods at 350 ML sample acidified with HNO_3, with particle sizes $\geq 10\mu$ and diameter between 200 – 250 nm. Raman and XPS study revealed presence of crystalline polymeric $[Mo_7O_{24}]^{6-}$ in high oxidation state of +6.

At 70-monolayer coverage, the citrate acidified MoO_3 film revealed the existence of a roundish polyhedral structure of two different particle sizes with thickness of ≤ 2 μ, and 60 – 80 nm for bigger and smaller particles respectively. Raman and XPS show the presence of both dioxo and polymeric tetrahedral $[MoO_4]^{2-}$ species in oxidation state of +6.

The $Fe_2(MoO_4)_3$ film has both granular and needle-like crystalline structures for 100 ML and 25 ML respectively. The 100 ML film consists of large particles with thickness of ≤ 10 μ, whereas the small particles are made of tetragonal and hexagonal structure truncated on the edges and corners. They have thicknesses between 100 – 200 nm as revealed by AFM analysis. The 25 ML film revealed needle-like structures with larger particles size of ~10 μ, and smaller particles of diameter between 120 – 170 nm.

The film has Raman bands for a pure $Fe_2(MoO_4)_3$ phase for the stoichiometric (1.5) ratio, with 2.2 ratio also having bands at 819 and 996 cm^{-1} assigned to excess crystalline MoO_3 phase. Comparison of the Raman band intensity for 819 and 996 cm^{-1} decreases with decreasing monolayer coverage.

An XPS study of the $Fe_2(MoO_4)_3$ film indicates high oxidation states of +6, +3 and +3 for Mo 3d, Fe 2p and Al 2p respectively.

6.2 Overall Conclusion

The characterization and reaction study of methanol oxidation on molybdenum based oxides catalysts, ranging from unsupported to supported and model catalysts using BET, Raman, XRD, SEM, TPD, XPS, AFM, TPD and TPR revealed the following:

The prepared MoO_3 indicates high activity and selectivity to methanol oxidation to formaldehyde at lower temperature, due to high surface area and presence of Lewis acid sites.

The effect of potassium (K) doping on the prepared MoO_3 surface neutralizes the Lewis acid sites as well as decreases the reducibility of the Mo^{6+} sites; it also controls adsorption and diffusion of gas phase oxygen onto the surfaces, which suppresses complete oxidation of formaldehyde to CO.

The amorphous MoOx on bulk stoichiometric (1.5 ratio) $Fe_2(MoO_4)_3$ is the active phase for methanol oxidation to formaldehyde, while excess crystalline MoO_3 phase in

2.2 ratio serves as reservoir for replenishment of lost MoOx species to maintain catalytic activity and formaldehyde selectivity.

Nanodiamond (ND) support is contaminated and thermally unstable; it burns completely in air at 600 ^{o}C leaving behind metal impurities.

Oxidation of ND in air at 500 ^{o}C purifies the surface of amorphous and graphitic carbon, as well as increases the density of negatively charged surface oxygen functionalities.

ND and ND supported MoO_3 catalysts reveal structure sensitivity, making DME and formaldehyde from acid and redox sites respectively.

The 90 % surface MoO_3 coverage on ND reveal synergistic effect between the active phase and the support.

γ-Al_2O_3 support is highly selective to DME due to presence of acid sites, which are completely titrated by 2 wt % MoO_3 loading.

The supported MoO_3 catalysts discern both monomeric and polymeric MoOx species at lower coverage, but crystalline polymeric MoO_3 phase at high coverage.

The selectivity to formaldehyde over supported MoO_3 catalysts increases with increasing MoO_3 loading, due to increasing density of redox sites.

The citrate impregnated MoO_3/ γ-Al_2O_3 reveals better dispersion on the support owing to the chelating effect of citrate.

The particle size distribution, structure, and thickness of model Mo – oxides based catalysts on Al_2O_3 (0001) single crystal prepared using novel wet chemical deposition method, is influenced by concentration of precursors, solvent type, acid used, and monolayer coverage.

The MoO_3/ Al_2O_3 (0001) model catalyst reveals dispersed roundish polyhedron particles at lower monolayer coverage, with diameter between 60 – 80 nm.

$Fe_2(MoO_4)_3$ film on Al_2O_3 (0001) single crystal surface discern mixture tetragonal and hexagonal truncated structure of 100 – 200 nm in diameter at 100 monolayer coverage, but reveal needle – like structures with diameter between 120 – 170 nm at 25 monolayer.

6.3 Recommendation for Further Research Work

Further investigation on the influence of Cs and Rb doping on prepared unsupported MoO_3 surface and its effect on methanol oxidation to formaldehyde is recommended, due to their large ionic radii that allow them to remain on the catalyst surface without diffusing into the bulk, and lower electronegativity that controls acid –base properties as well as metal – oxygen bond strength.

Hydroxylation of the ND surface to ensure uniformity of support prior to MoO_3 loading, and study of V_2O_5 supported on ND should be carried out to investigate catalytic active sites in methanol oxidation reaction.

It is recommended to carry out reaction measurements on the model catalysts using mini micro pulsed flow reactor of the type shown in Fig. 6. 1 to investigate catalytic active sites and reaction mechanism of methanol oxidation on the model systems using in situ Raman diffuse reflectance infrared fourier transform (DRIFT), and infrared-visible sum frequency generation (SFG) spectroscopic techniques. However, it will be of great interest to investigate the participation of transient oxygen species currently invoked by researchers [7, 8], using isotopic-transient techniques to monitor steady state kinetics of selective oxidation reaction of methanol on molybdenum oxide-based catalyst surfaces in order to come up with a more comprehensive mechanism of selective oxidation methanol on metal oxides surfaces.

The wet chemical precursors used for fabrication of MoO_3 and $Fe_2(MoO_4)_3$ films as model catalytic system, could be a potential method for controlled preparation of thin film and amorphous bulk MoO_3 and $Fe_2(MoO_4)_3$ catalysts of high surface area using spraying drying techniques.

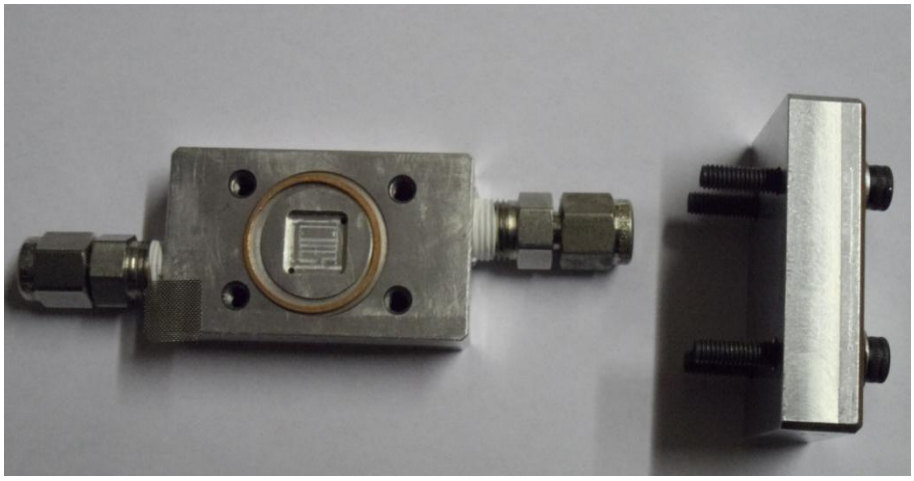

Fig. 6. 1 ***Image of mini micro pulsed flow reactor***

References

1. Bowker M, Brookes C, Carley AF, House M P, Kosif M, Sankar G, et al. Evolution of active catalysts for the selective oxidative dehydrogenation of methanol on Fe_2O_3 surface doped with Mo oxide. PhysChem Chem Phys. 2013;15:12056-67.

2. House MP, Shannon MD, Bowker M. Surface segregation in iron molybdate catalysts. Catalysis Letters. 2008;122:210–3.

3. Soares APV, Farinha Portela M, Kiennemann A, Hilaire L, Millet JMM. iron molybdate catalysts for methanol to formaldehyde oxidation: effects of Mo excess on catalytic behaviour. Appl Catal A: Gen 2001;206: 221–9.

4. Soares APV, Farinha Portela M. Methanol selective oxidation to formaldehyde over iron-molybdate catalysts. Catal Rev. 2004;47:125-74.

5. Routray K, Zhou W, Kiely CJ, Grünert W, Wachs IE. Origin of the synergistic interaction between MoO_3 and iron molybdate for the selective oxidation of methanol to formaldehyde. J Catal. 2010;275:84–98.

6. Wachs IE, Routray K. Catalysis science of bulk mixed oxides. ACS Catal. 2012;2:1235-46.

7. Carley AF, Davies PR, Robert, MW. Oxygen transient states in catalytic oxidation at metal surfaces. Catal Today 2011;169: 118–24.

8. Pradhan S, Bartley JK, Bethell D, Carley AF, Conte M, Golunski S, et al. Non-lattice surface oxygen species implicated in the catalytic partial oxidation of decane to oxygenated aromatics. Nat Chem. 2012;4:134-9.

Appendix

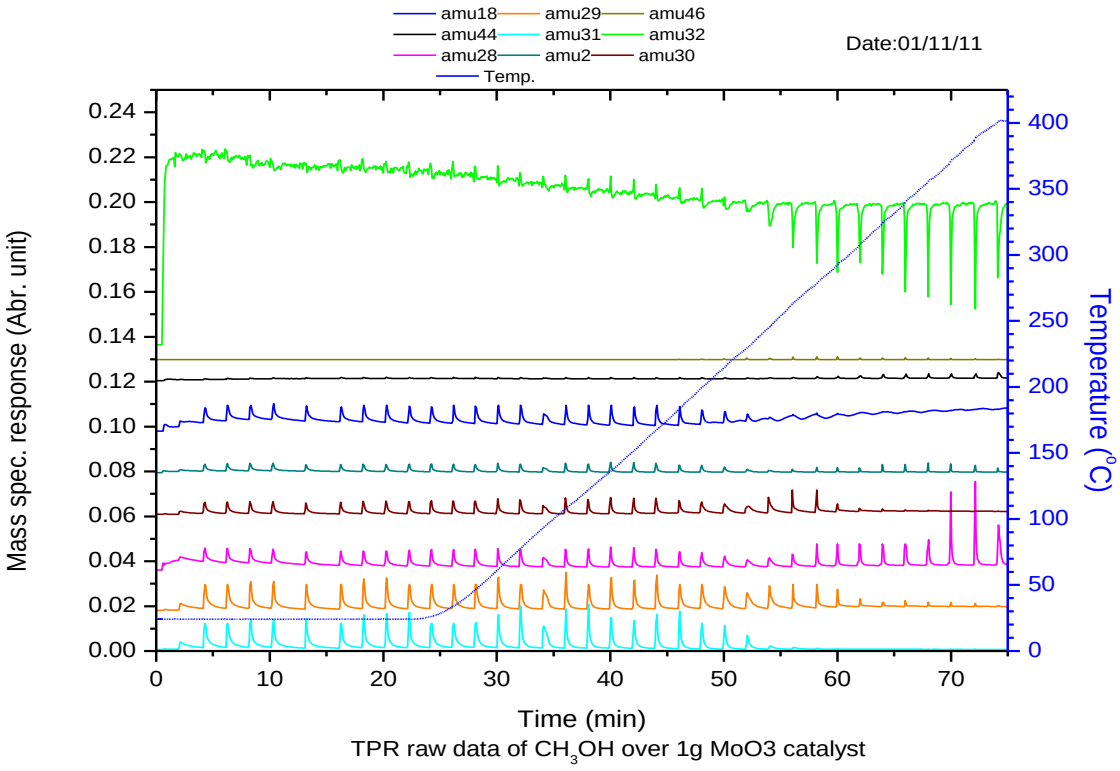

Appendix –I- Raw TPR data for methanol reaction over prepared MoO_3

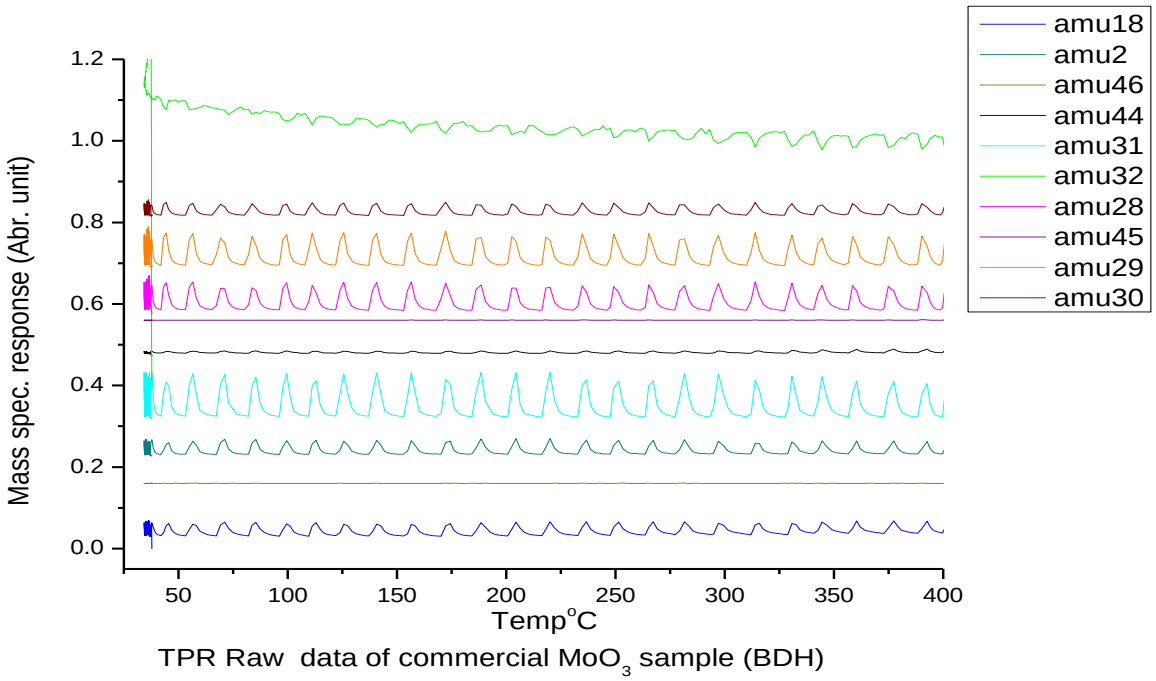

Appendix –II- Raw TPR data for methanol reaction over commercial MoO_3 (BDH)

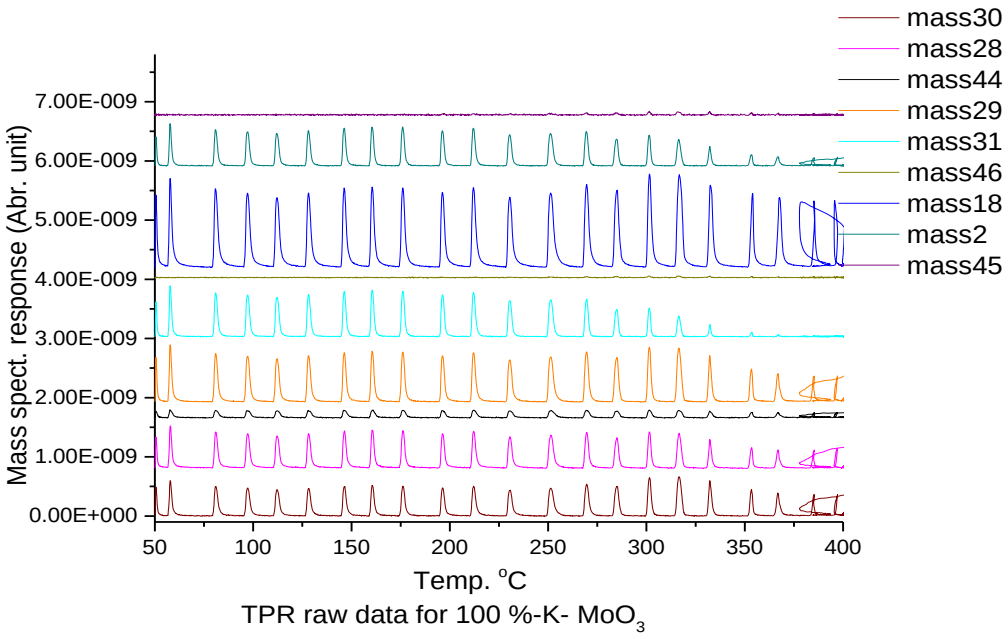

Appendix –III- Raw TPR data for methanol reaction on 100 % K/MoO_3

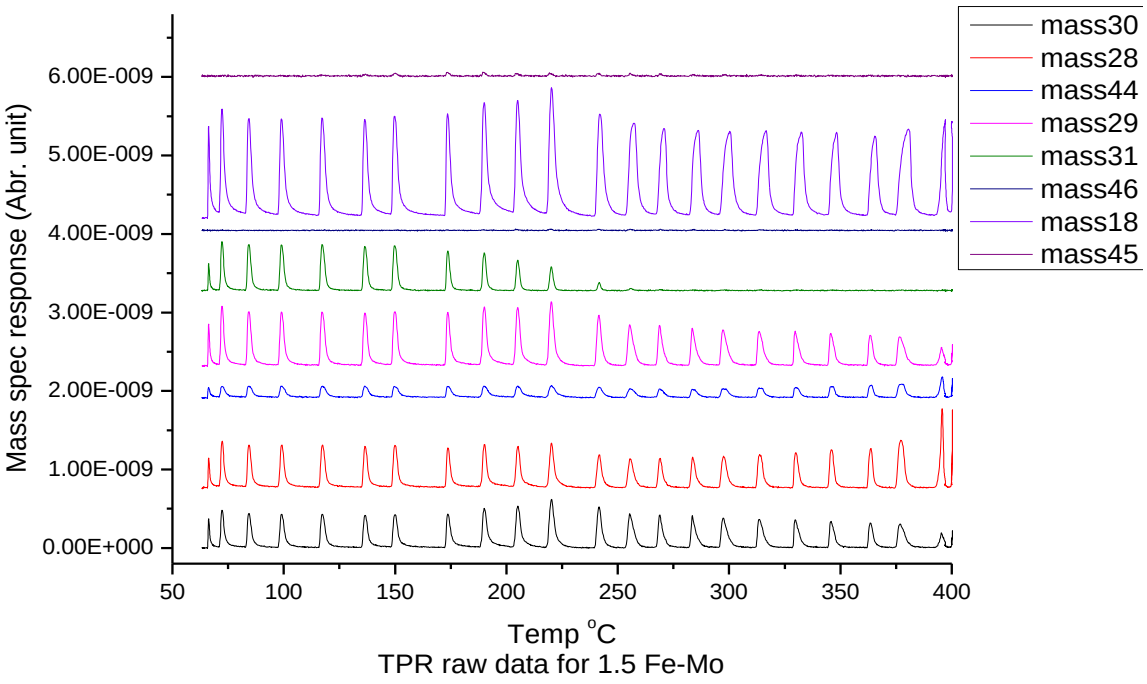

Appendix –IV- Raw TPR data for methanol reaction on 1.5 Fe-Mo

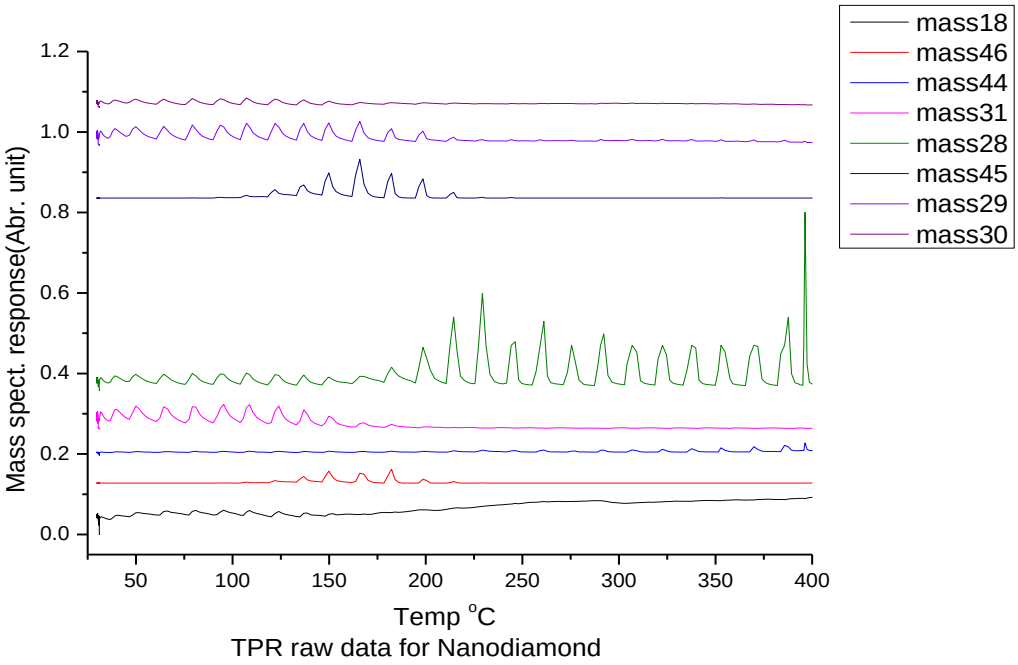

Appendix –V- Raw TPR data for methanol reaction on Nanodiamond

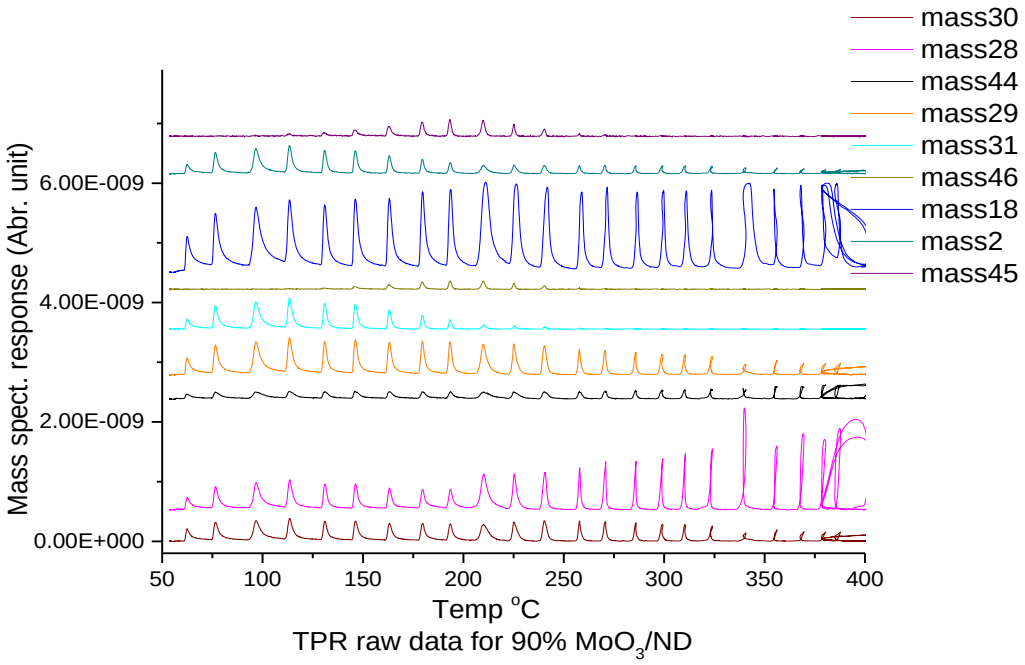

Appendix –VI- Raw TPR data for methanol reaction on 90 % MoO_3/ND

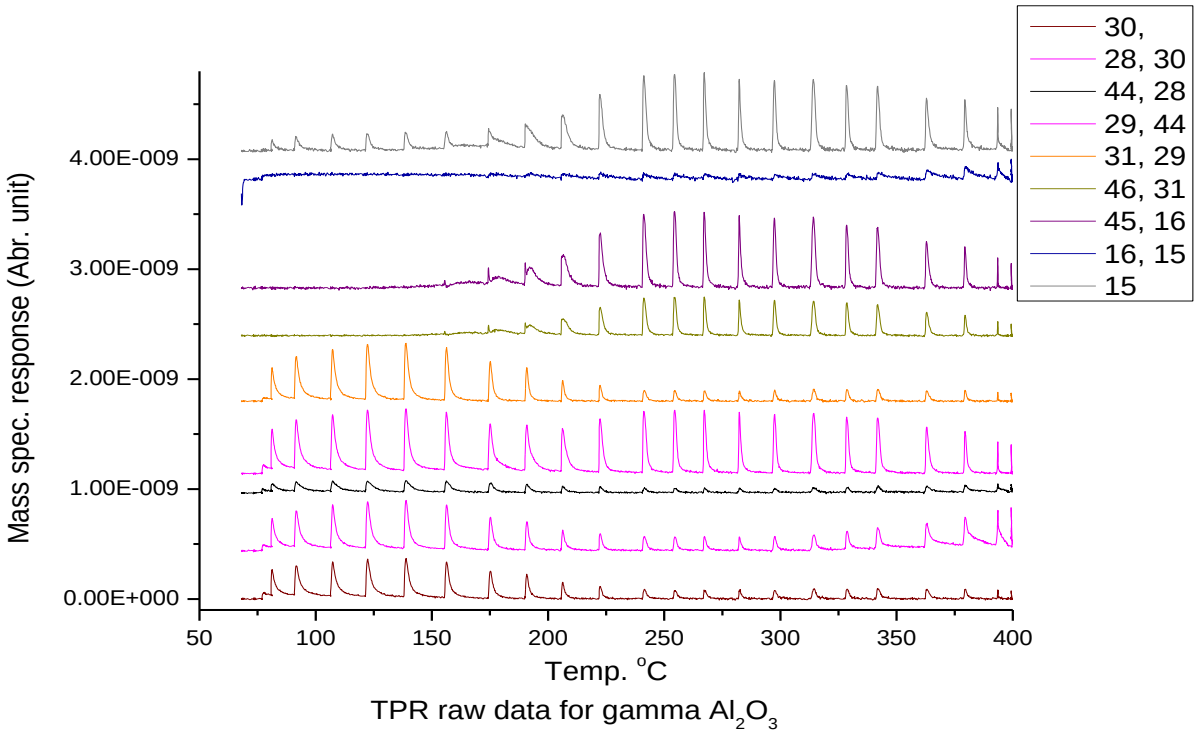

Appendix –VII- Raw TPR data for methanol reaction on γ-Al_2O_3

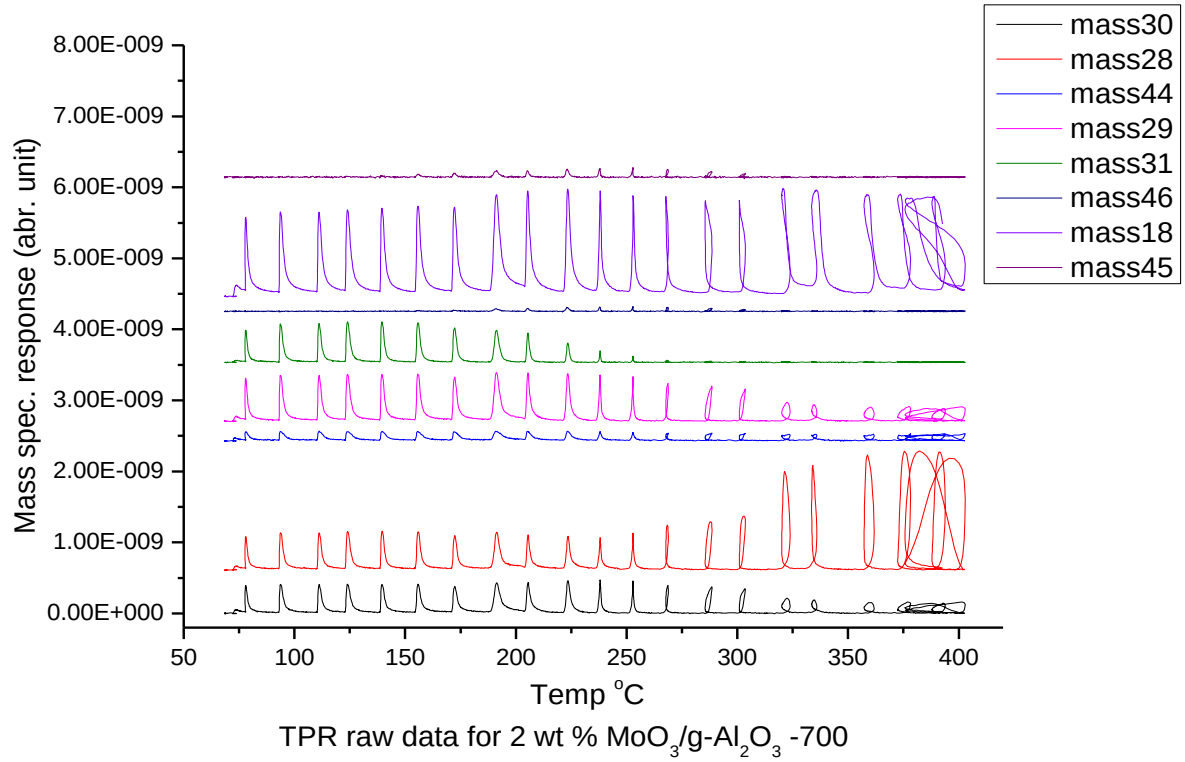

Appendix –VIII- Raw TPR data for methanol reaction over 2 wt % MoO_3/γ-Al_2O_3

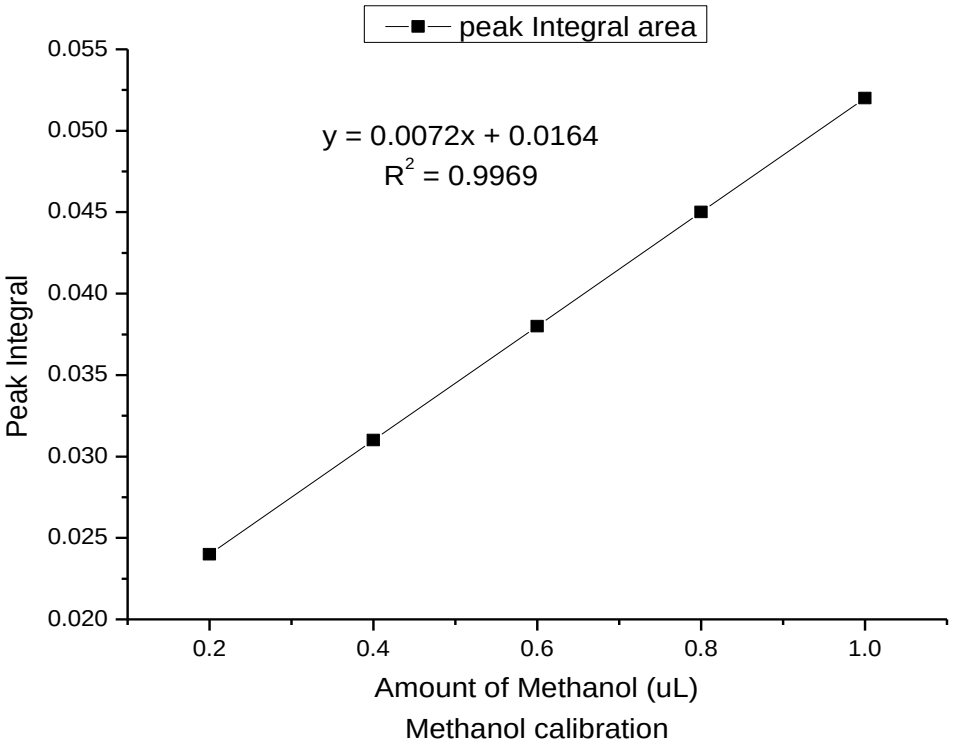

Appendix –IX- Methanol calibration plot

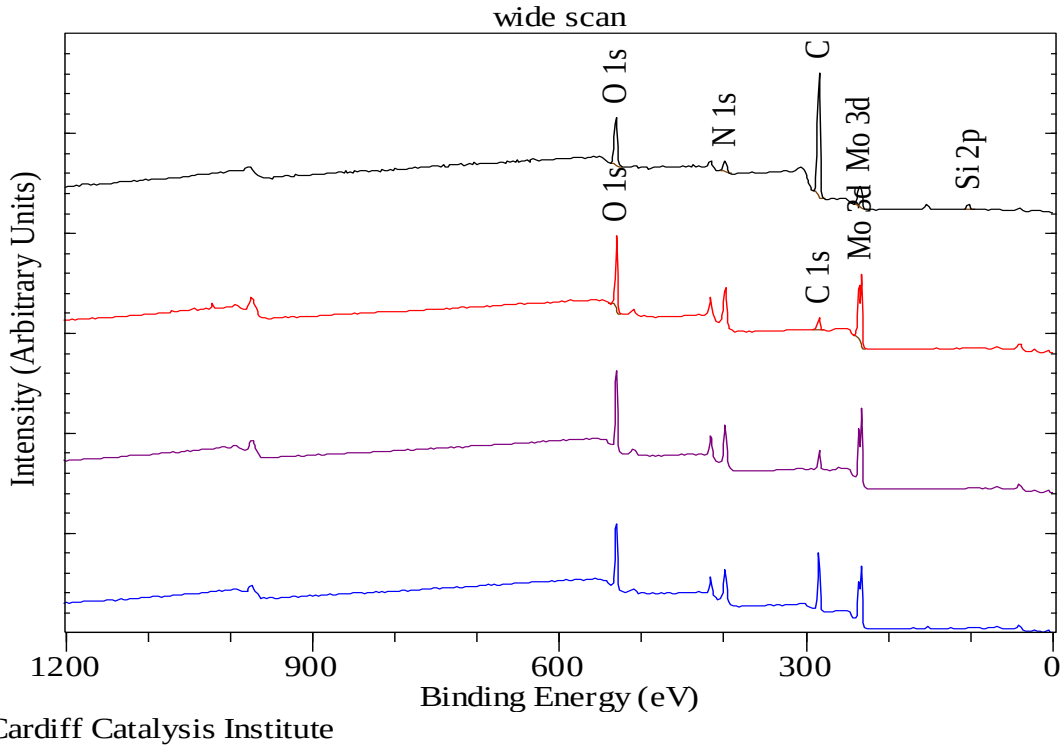

Appendix –X- XPS wide scan of MoO_3 and 100 % K-MoO_3 arranged in descending order from top , BDH MoO_3, prepared MoO_3, 25 % K-MoO_3 and 100 % K- MoO_3

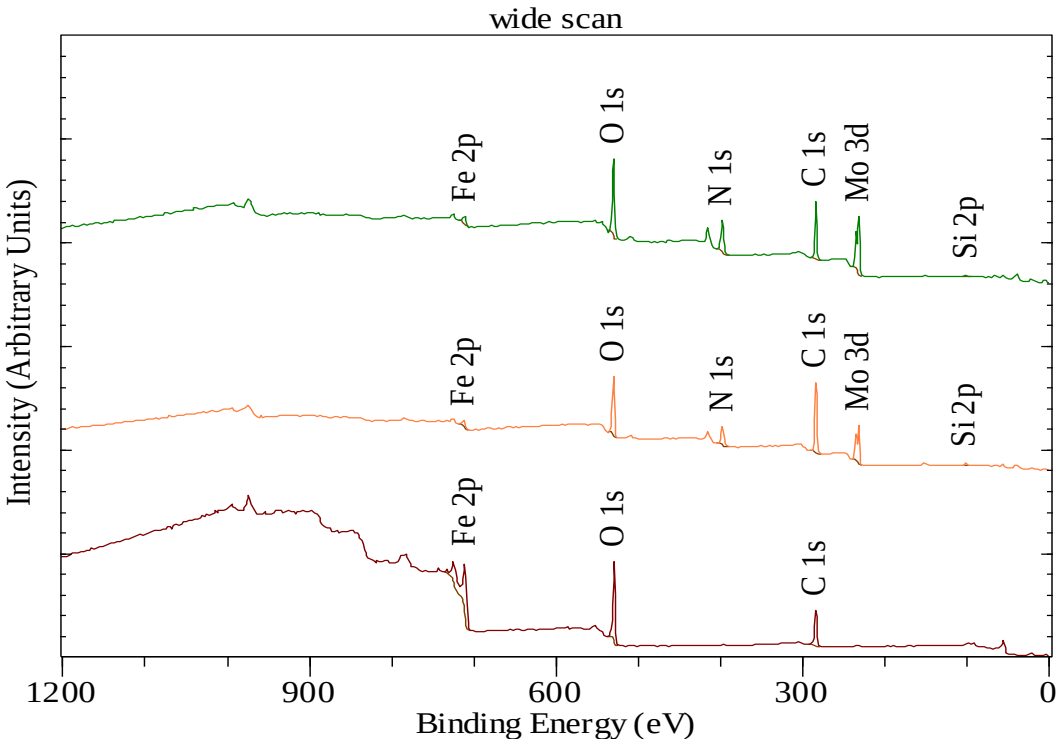

Appendix –XI- XPS wide scan of Fe_2O_3 and $Fe_2(MoO_4)_3$ arranged in ascending order from bottom, Fe_2O_3, 1.5 $Fe_2(MoO_4)_3$ and 2.2 $Fe_2(MoO_4)_3$

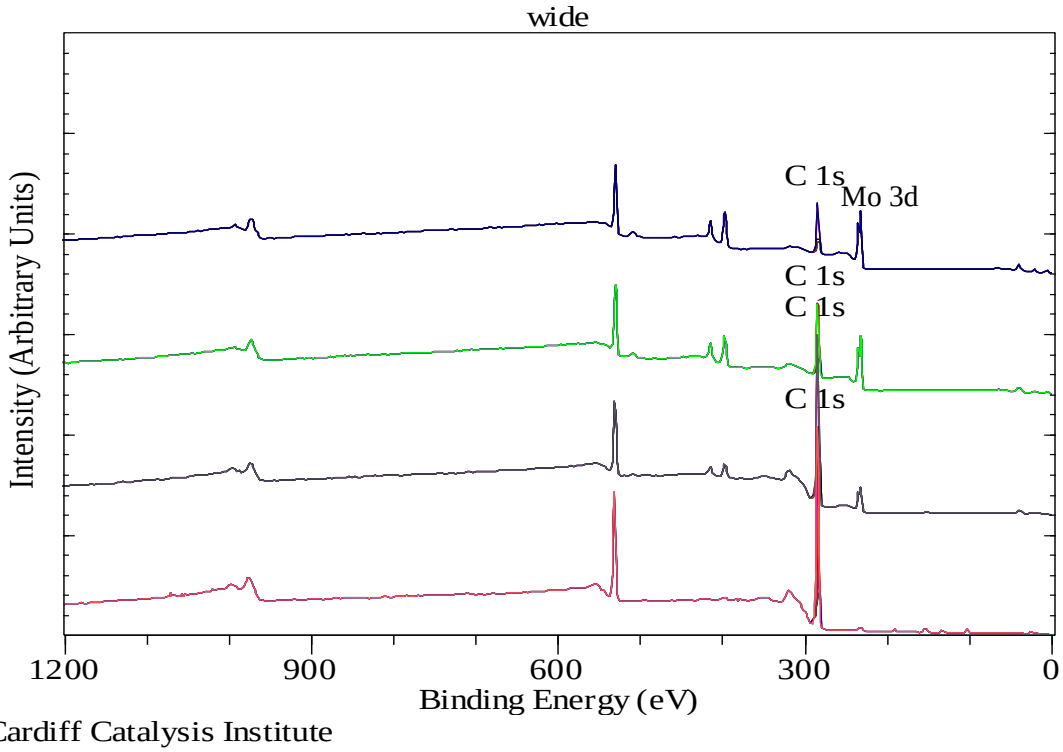

Appendix –XII- XPS wide scan of supported MoO_3/ND samples, arranged in ascending order from bottom, ND, 90 %, 100 % and 400 % MoO_3/ND

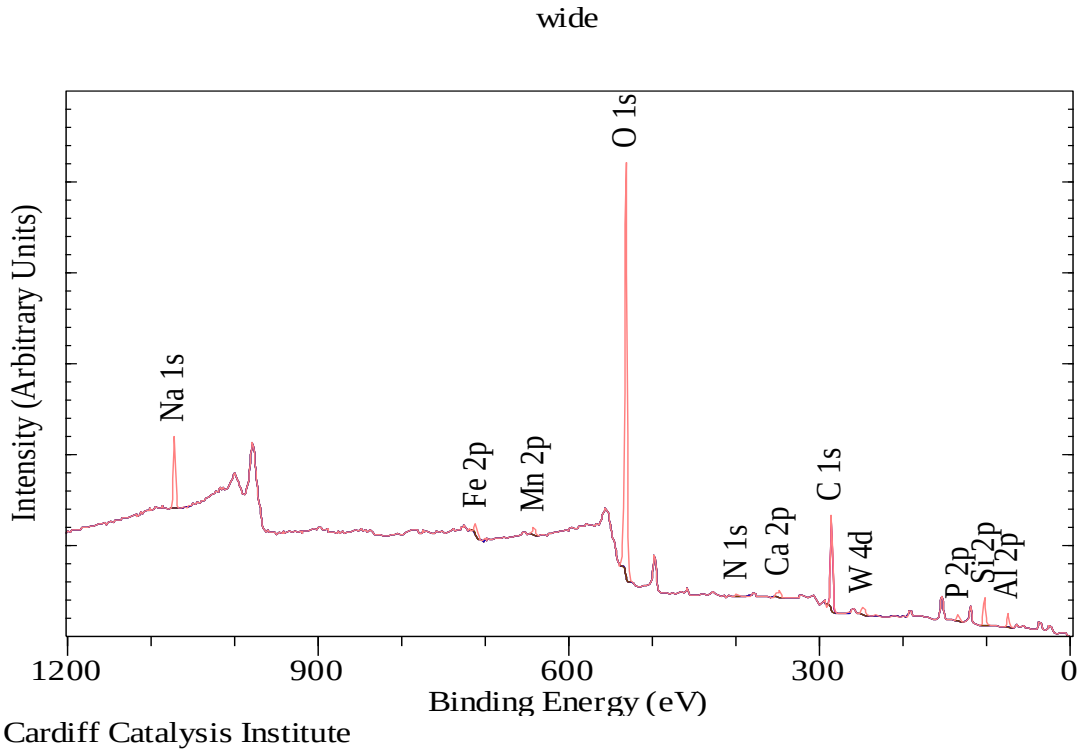

Appendix –XIII- XPS wide scan of burnt ND supported at 600 ^{o}C

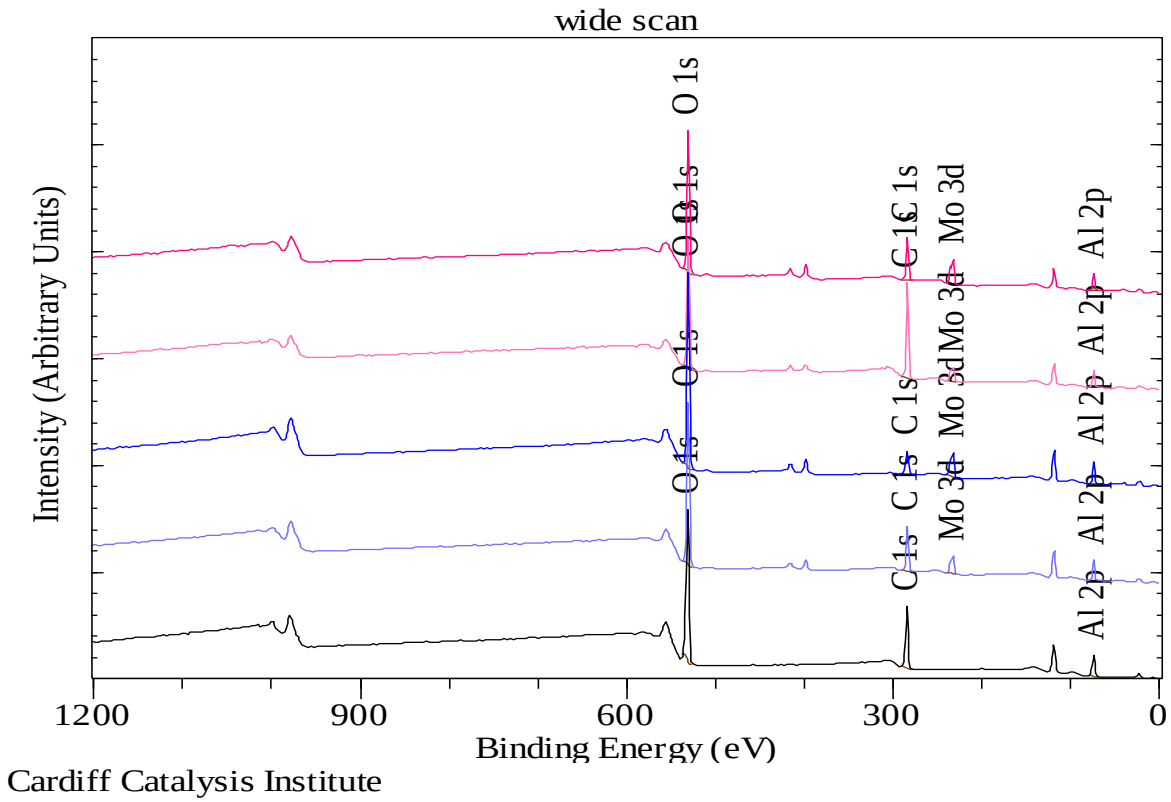

Appendix –XIV- XPS wide scan of supported MoO_3/γ-Al_2O_3 samples, arranged in ascending order from bottom, γ-Al_2O_3, 2wt % MoO_3/γ-Al_2O_3 -500, 10wt % MoO_3/γ-Al_2O_3 -500, 2wt % MoO_3/γ-Al_2O_3 -700 and 2wt % MoO_3/γ-Al_2O_3 -700